

Bilal Ahmad

# Crash Simulation of Woven Fabric Thermoplastic Composites

**Crash Simulation of Woven Fabric  
Thermoplastic Composites**

Bilal Ahmad

**Siegener Schriftenreihe Automobiltechnik**

Hrsg. von Xiangfan Fang

Band 7

# Crash Simulation of Woven Fabric Thermoplastic Composites

DISSERTATION

to obtain the degree of Doctor  
of Engineering

submitted by  
M.Sc. Bilal Ahmad

submitted to the School of Science and Technology  
of the University of Siegen  
Siegen 2021

Date of the oral examination:	27. July 2021
Supervisor and first appraiser:	Professor Dr.-Ing. Xiangfan Fang
Second appraiser:	Professor Dr.-Ing. Christian Hesch

## **Bibliografische Information der Deutschen Nationalbibliothek**

Die Deutsche Nationalbibliothek verzeichnet diese Publikation in der Deutschen Nationalbibliografie; detaillierte bibliografische Daten sind im Internet über <http://dnb.dnb.de> abrufbar.

## **Impressum**

### **Herausgeber:**

Univ.-Prof. Dr.-Ing. Xiangfan Fang  
Lehrstuhl für Fahrzeugleichtbau  
Universität Siegen  
Breite Straße 11  
57076 Siegen  
Telefon: +49 271 740 2384  
Fax: +49 271 740 3786  
E-Mail: [info.flb@uni-siegen.de](mailto:info.flb@uni-siegen.de)

### **Druck:**

Uni Print, Universität Siegen

Siegen 2021: universi – Universitätsverlag Siegen  
[www.uni-siegen.de/universi](http://www.uni-siegen.de/universi)

Gedruckt auf alterungsbeständigem holz- und säurefreiem Papier.

**ISSN: 2568-0374 (Siegener Schriftenreihe Automobiltechnik)**

**ISBN: 978-3-96182-108-2**

**[doi.org/10.25819/ubsi/10027](https://doi.org/10.25819/ubsi/10027)**

Die Publikation erscheint unter der  
Creative Commons Lizenz CC-BY-SA



*To my father*

## **Acknowledgment**

This thesis presents the work carried out during my employment as researcher at the Institute of Automotive Lightweight Design (FLB) in University of Siegen from 2014 to 2020.

First and foremost, I would like to thank my supervisor Prof. Dr.-Ing. Xiangfan Fang who not only devised the basic idea of this work but also guided me throughout my work. Alongside supervising my technical work, he also imparted a great deal of knowledge about important aspects of professional life to me. I am especially grateful to him for supporting me during difficult times. I am also thankful to Prof. Dr.-Ing. Christian Hesch who showed particular interest in the topic and made many helpful comments as second appraiser. I also thank Prof. Dr. Vladimir Kobelev and Prof. Dr.-Ing. Ulrich Stache for their willingness to act as a member and chairman of the doctoral committee and give technical feedback on this work.

I wish to extend my thanks to all of my work colleagues at the FLB, who contributed in making my time at the institute a pleasant experience. I would particularly mention Arno Reichmann for his assistance in designing and carrying out laboratory tests and Petra Kauschke for making organizational procedures very smooth.

Lastly, with all my heart, I acknowledge the selfless support of my brothers Naveed and Zahid. Their sacrifices, friendship and guardianship made it possible for me to achieve the goals of life.

## **Abstract**

Fiber composite materials are frequently being used in automotive industry to meet the growing demand for fuel efficient passenger cars. Woven fabric thermoplastic composites materials provide high stiffness-to-weight, strength-to-weight and energy absorption-to-weight ratio at affordable mass production cost. To use these materials in structural components of passenger cars, the crashworthiness requirements must be met. To fulfill the crashworthiness requirements, dynamic FEM simulations are carried out as part of the product development process. However, the composite material behavior under dynamics loads is not fully understood. Furthermore, the state-of-the-art material models fail to predict the crash behavior of woven fabric composite material accurately which leads to under-utilization of the weight-saving-potential of these materials.

The goal of this work was to develop an improved material model for the dynamics simulation of woven fabric thermoplastic composites. The material model must be independent of non-physical parameters and all parameters could be determined experimentally.

In the framework of this work, the mechanical material properties were measured experimentally. The test data was used to identify discrepancies in state-of-the-art continuum damage mechanics material models. The in-plane shear damage behavior was improved and effects of tensile and compression strain on the shear behavior were quantified. High-speed test data was used to incorporate the strain rate-dependency in material model. The improved material model was implemented as user-material subroutine and simulation results were validated with component level drop tower crash tests.

The potential for further improvements was identified by proposing the method to implement the measured size effect on the strength of materials. Stress-strain transformation was used to determine the failure points under multiaxial stress state. Finally, the viability of cohesive zone modeling approach was investigated to model the quasi-static axial crushing.

## **Kurzzusammenfassung**

Um die wachsende Nachfrage nach kraftstoffsparenden PKW zu erfüllen, werden in der Automobilindustrie heutzutage zunehmend Faserverbundwerkstoffe eingesetzt. Thermoplastische Verbundwerkstoffe bieten eine hohe spezifische Steifigkeit, spezifische Festigkeit und spezifische Energieabsorption bei erschwinglichen Produktionskosten in der Massenfertigung. Um diese Materialien in Strukturbauteilen von PKWs einzusetzen, müssen diverse Anforderungen an die Crashesicherheit erfüllt werden. Um diese Anforderungen zu erfüllen, werden im Rahmen der Produktentwicklung dynamische FEM-Simulationen durchgeführt. Das Verhalten von Verbundwerkstoffen unter dynamischen Belastungen ist jedoch noch nicht vollständig bekannt. Darüber hinaus können die aktuellen Materialmodelle das Crashverhalten von gewebten Verbundwerkstoffen nicht genau vorhersagen, was dazu führt, dass das Gewichtseinsparungspotenzial dieser Materialien nicht voll ausgeschöpft wird.

Das Ziel dieser Arbeit war es, ein verbessertes Materialmodell für die dynamische Simulation von gewebten thermoplastischen Verbundwerkstoffen zu entwickeln. Da das Materialmodell auf nicht-physikalische Parameter verzichtet, kann es vollständig mittels experimentell erhobener Daten kalibriert werden.

Im Rahmen dieser Arbeit wurden die mechanischen Materialeigenschaften experimentell ermittelt. Die resultierenden Versuchsdaten wurden verwendet, um Diskrepanzen in modernen kontinuumsmechanischen Materialmodellen zu identifizieren. Das Schädigungsgesetz für Schub wurde verbessert und die Auswirkungen von Zug- und Druckbelastungen auf das Schubverhalten wurden quantifiziert. Hochgeschwindigkeits-Testdaten wurden verwendet, um die Abhängigkeit von der Dehnungsrate in das Materialmodell einzubeziehen. Das Materialmodell wurde als User-Material-Subroutine implementiert und die Simulationsergebnisse wurden mit Fallturm-Crashtests auf Komponentenebene validiert.

Die Implementierung des beobachteten Größeneffekts auf die Festigkeit der geprüften Materialien wurde als Verbesserungspotenzial für zukünftige Arbeiten identifiziert. Die Spannungs-Dehnungs-Transformation wurde verwendet, um die Versagenspunkte unter multiaxialem Spannungszustand zu bestimmen. Zum Schluss wurde die Durchführbarkeit des Modellierungsansatzes für kohäsive Zonen untersucht, um den quasistatischen Axialcrash zu modellieren.

# Contents

1	Introduction .....	1
1.1	Potential of continuous fiber thermoplastic composites.....	1
1.2	Motivation .....	2
1.3	Objective.....	2
1.4	Procedure .....	2
2	Theoretical background .....	5
2.1	Fiber composite materials .....	5
2.1.1	Fibers .....	6
2.1.2	Matrix.....	7
2.2	Energy absorption characteristics of fiber composites .....	8
2.2.1	Flat specimens .....	10
2.2.2	Self-supporting specimens .....	11
2.3	Size effect.....	12
2.4	Lamina stress-strain law.....	13
2.5	Failure of composite materials.....	16
2.5.1	Failure surface testing .....	17
2.5.2	Failure criteria.....	18
2.6	Explicit finite element method.....	19
2.7	User-defined material modeling (VUMAT).....	21
2.8	Elasto-plasticity.....	22
3	Experimental material testing .....	27
3.1	Material.....	27
3.2	Tensile test .....	27
3.2.1	Test specimen .....	28
3.2.2	Test procedure .....	29
3.2.3	Results .....	30
3.3	Compression test.....	31
3.3.1	Test specimen .....	31
3.3.2	Test procedure .....	31
3.3.3	Results .....	33
3.4	Shear test .....	34
3.4.1	Test results.....	35
3.4.2	Cyclic shear test .....	36
3.5	Intra-laminar fracture energy .....	38

3.5.1	Tensile fracture energy.....	40
3.5.2	Compression fracture energy.....	44
3.6	Axial crushing behavior.....	45
4	Continuum damage mechanics.....	47
4.1	Basics of CDM.....	47
4.2	Ls-Dyna CDM model MAT_Laminated_Composite_Fabric.....	50
4.2.1	Fiber response.....	50
4.2.2	In-plane shear response.....	53
4.3	Abaqus CDM model ABQ_PLY_FABRIC.....	54
4.3.1	Fiber response.....	55
4.3.2	In-plane shear response.....	58
4.4	Validation.....	60
4.4.1	Three-point bending of rectangular specimen.....	60
4.4.2	U-profile.....	61
4.5	Conclusion.....	62
5	Shear modeling.....	63
5.1	Testing.....	64
5.1.1	Frame shear test.....	66
5.1.2	Rail shear test.....	68
5.1.3	Compression shear.....	69
5.1.4	Results and comparison.....	70
5.2	Improved shear modelling.....	73
5.2.1	Results.....	73
5.3	Validation.....	75
5.4	Conclusion.....	77
6	Strain-rate modelling.....	79
6.1	Test.....	79
6.1.1	Tensile strain-rate dependency.....	79
6.1.2	Shear strain-rate dependency.....	84
6.2	Strain rate-dependent modeling.....	91
6.2.1	Strain rate dependency in the fiber direction.....	91
6.2.2	Strain rate dependency along in-plane shear.....	92
6.2.3	Implementation as user-defined material subroutine.....	93
6.3	Validation.....	97
6.3.1	FEM model setup.....	98
6.3.2	Results.....	98

6.3.3	Discussion .....	99
6.4	Conclusion .....	100
7	Failure surface .....	103
7.1	Testing .....	103
7.2	Conclusion .....	108
8	Size effect .....	109
8.1	Size effect in tension .....	109
8.2	Size effect in bending .....	110
8.2.1	Pin-end buckling test .....	112
8.3	Proposed method for scaling strength in user-material subroutine .....	114
8.4	Conclusion .....	116
9	Axial crush simulation .....	117
9.1	Inter-laminar fracture energy measurement .....	117
9.1.1	DCB test .....	118
9.1.2	ENF test .....	122
9.2	Delamination modeling .....	124
9.2.1	Constitutive model of cohesive elements .....	124
9.2.2	Parameter calibration .....	126
9.2.3	Single-element simulation .....	128
9.2.4	Influence of cohesive modeling on composite response .....	130
9.3	Validation .....	132
9.3.1	DCB simulation .....	132
9.3.2	ENF simulation .....	134
9.4	Axial crush simulation .....	135
9.4.1	Conclusion .....	136
10	Summary and Outlook .....	137
10.1	Summary .....	137
10.2	Outlook .....	138
11	Bibliography .....	140
12	Annex .....	145
12.1	Test results data .....	145
12.1.1	Frame shear .....	145
12.1.2	Rail shear .....	145
12.1.3	Compression shear .....	146
12.1.4	High-speed tensile test .....	146
12.1.5	High-speed shear test .....	148

12.1.6	Off-axis tests .....	150
12.1.7	DCB test .....	152
12.1.8	ENF test .....	153
12.2	Specimen photos .....	154
12.2.1	Tensile test specimens .....	154
12.2.2	Compression tests specimens .....	154
12.2.3	Tensile-shear test specimens .....	155
12.2.4	Intralaminar fracture energy specimens .....	155
12.2.5	Axial crash of corrugated specimens .....	155
12.2.6	Rail shear tests specimens .....	156
12.2.7	Tensile shear specimens .....	156
12.2.8	Compression shear specimen .....	156
12.2.9	High speed tensile test specimens .....	156
12.2.10	High-speed shear specimen .....	158
12.2.11	Off-axis tensile test specimen .....	159
12.3	CAD drawings .....	160
12.3.1	CLC fixture .....	160
12.3.2	Clevis design for intra-laminar fracture energy .....	162
12.3.3	Frame shear fixture .....	163
12.3.4	Rail shear fixture .....	167
12.3.5	Pin-end buckling fixture .....	170

## Abbreviations

CLC	Combined Loading Compression
B.C	Boundary Condition
FEA	Finite Element Analysis
FEM	Finite Element Method
VUMAT	Explicit user material subroutine
DCB	Double Cantilever Beam
ENF	END Notch Flexure

## Symbols

$E_{11} = E_1$	Young's modulus in first in-plane principle fibre direction-1
$E_{22} = E_2$	Young's modulus in first in-plane principle fibre direction-2
$G_{12}$	Young's modulus in first in-plane principle fibre direction-2
$\sigma_{11} = \sigma_1$	Normal stress in material direction-1
$\sigma_{22} = \sigma_2$	Normal stress in material direction-2
$\sigma_{12} = \tau_{12}$	In plane shear stress in material coordinates 12
$\sigma_{xx} = \sigma_x$	Normal Stress in global direction-X
$\sigma_{yy} = \sigma_y$	Normal Stress in global direction-Y
$\sigma_{xy} = \tau_{xy}$	In plane shear stress in global coordinates-XY
$\varepsilon_{11} = \varepsilon_1$	Normal strain in material direction-1
$\varepsilon_{22} = \varepsilon_2$	Normal Strain in material direction-2
$\gamma_{12} = 2\varepsilon_{12}$	In plane shear strain in material coordinates 12
$\varepsilon_{xx} = \varepsilon_x$	Normal strain in global direction-X
$\varepsilon_{yy} = \varepsilon_y$	Normal strain in global direction-Y
$\gamma_{xy} = 2\varepsilon_{xy}$	In plane shear strain in global coordinates-XY
$\theta$	Angle between global X-direction and material direction-1



# 1 Introduction

The future of automotive sector is being driven by environmental and socioeconomic factors. European Union has decided to cap the environmental effects of vehicles by curbing the limit of CO<sub>2</sub> emissions. Vehicle manufacturers must comply with the conditions laid down in EU ETS (European Union Emission Trading System) in addition to customer's demand for more fuel efficient vehicles [1]. A lightweight vehicle design requires a smaller engine to run it with same performance at lower emission. To meet the weight reduction goals, automotive OEMs are pursuing lightweight vehicle designs besides other emissions reduction methodologies.

Vehicle weight reduction can be achieved by use of high strength steels and optimized part and assembly design. An important aspect of lightweight design is use of new lightweight composite materials. The fiber-reinforced composites are increasingly being used in automotive sector due to their high specific strength, specific stiffness and high specific energy absorption capabilities. BMW i and BMW 7 series are recent examples of use of fiber reinforced composites in structural components of modern cars [2].

## 1.1 Potential of continuous fiber thermoplastic composites

The continuous fiber thermoplastic composites, so called organo-sheets, are semi-finished products with high specific stiffness and specific strength available in the form of sheets. Their ability to be heated and formed (thermoformed) into final products makes them particularly feasible for series production. Due to short cycle time their production costs are greatly reduced in comparison to thermosetting plastic composites. The organo-sheets can be combined with short or long-fiber thermoplastics of the same matrix material to form ribs structure and edge over-molding through injection molding. Therefore, thermoplastic composites provide exceptional advantages in achieving the lightweight design of automotive parts with cost effectiveness.

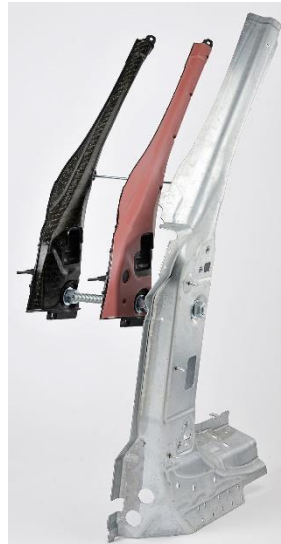


Figure 1.1 Porsche 911 Cabriolet A-pillar hybrid design using formed blank of Tepex dynalite 102-RG600(6)/47%, a woven glass fabric thermoplastic composite with PA 66 ribbed structure (black) and high-strength steel both joined by structural foam [3]

## 1.2 Motivation

The structural components of passenger cars possess extreme load bearing capacity. Beside the active safety systems installed within the vehicle which prevent accidents or otherwise reduce their severity, vehicles must also have effective passive safety measures. European New Car Assessment Program (Euro NCAP) evaluates the safety levels of cars with series of crash tests [4]. Good crash performance is required to minimize the severity in case of an accident protecting the passengers from fatal injuries and deaths. To use the composite materials in automotive applications, crashworthiness requirements must be met. Therefore, understanding the material properties and predicting the behavior during crash in finite element analysis are essential.

Crashworthiness simulation of woven fabric thermoplastic composite materials remains challenge to this day resulting in expensive and delayed product development process [5]–[7]. The material models used for crash simulations of woven fabric composite materials suffer from mesh dependency, require material parameters calibration according to particular load case and use of non-physical parameters. Using such material model, no realistic prediction can be made through simulations and the results serve no purpose in product development process.

## 1.3 Objective

The objective of this research work was to precisely characterize material properties and predict the material behavior in dynamic crash accurately through FEM simulations. The shortcoming in the state of the art material models for composite materials were identified and improvement were made. Following guidelines were followed:

- Research work focused on woven glass fabric thermoplastics because they are cheaper than carbon fiber composites and possibility of thermoforming as manufacturing process allows it to be used on large scale production.
- All material parameters used in material model must be determined experimentally or their use be backed by logical arguments
- There shouldn't be any non-physical parameters which need to be optimized for different load cases.
- The material parameters should not need to be changed depending on the loading conditions.
- The influence of mesh size on the simulation results should be minimized.
- The simulation run time should be reasonable so that simulation method and material model can be adopted for full car crash simulation.

## 1.4 Procedure

The general procedure adopted was to measure the mechanical properties of the materials experimentally at first. Then specimen level simulations were run with state-of-the-art material model and deficiencies in material model were identified. To alleviate the discrepancies in the material model, user-defined material model was developed keeping in view the experimental behavior of fiber composite material.

Chapter 2 starts with a general introduction to composite materials, mechanical properties, mathematical formulation and a review on explicit simulations.

---

In chapter 3 mechanical properties of the woven fabric composite materials are measured experimentally and input parameters for state-of-the art material models are calculated.

In chapter 4 available state of the art Continuum Damage Mechanics material models are compared along inplane shear and fiber-direction. Shortcomings in material models were identified by simulations on single element and quasi-static three-point bending of simple specimens and u-profile.

In chapter 5 the inplane shear response modeling is improved and implemented as user material subroutine. A detailed testing program was undertaken to measure the shear properties of woven fabric composites under multi-axial stress states the findings were used to improve the load-case dependent parameters. The results are validated with three-point bending on specimen level.

In chapter 6 the strain rate dependency of material is investigated. Quasi-static and high speed tests were carried out to measure the strain rate dependent material behavior. The results were implemented in user-material subroutine and validate with crash simulation on component level.

In chapter 7 off-axis tests were carried out to measure the lamina behavior under different multiaxial stress states. The experimental data was used compare the existing failure models with experimental data.

Chapter 8 includes the experimental methodology to measure the strength of material as function of size of material under stress. A method is proposed on how a user-material subroutine can incorporate the strength scaling based on the type of loading.

In chapter 9 the possibility of using interfacial cohesive elements for the delamination prediction during axial crash is investigated. Test were conducted to measure the interlaminar fracture energies and cohesive elements were modelled between the plies of composite for axial simulation of self-standing specimens.



## 2 Theoretical background

This chapter gives a brief introduction of the composite materials and its constituents. A classic elasticity law for stress-strain relation of a composite ply is described. The working principles of explicit finite element is discussed and the use of user-material subroutine is explained. Finally, the modelling of elastoplastic materials in explicit settings is discussed.

### 2.1 Fiber composite materials

Fiber composite materials are created by combining the two main constituents; (1) reinforcing fibers and (2) matrix. There can be some other constituents in the form of coupling agents, coatings and fillers to improve fiber-matrix interface bonding, load transfer between fiber and matrix, dimensional stability or reduce the cost. By combining the two materials the property advantages of individual materials are combined in one material. e.g. fibers have the property of being able to withstand tensile loads excellently and but cannot resist bending or compression which is compensated by a matrix material.

Fiber-reinforced composites are manufactured by embedding large number of fibers in thin layer of matrix material. This layer is called ply or lamina and usually has thickness of 0.1-1 mm. Fiber composites are classified on the basis of type of fiber used for manufacturing it. Fiber can be continuous or discontinuous. If the continuous fibers are aligned along one particular direction, then it is called unidirectional (UD) composite. The fiber can also be arranged in bidirectional or multidirectional orientation. Figure 2.1 illustrates the types of fiber composites.

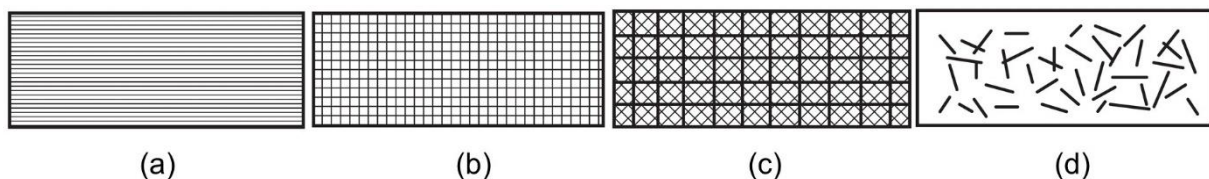


Figure 2.1 Illustration of (a) UD continuous fiber (b) bidirectional continuous fiber (c) multidirectional continuous fiber (d) discontinuous fiber composite ply [8]

In discontinuous fiber composites, the material properties are not superior in any particular direction unless the fibers are aligned by processing techniques. On the other hand, UD continuous fiber composites have highest strength and stiffness along pre-defined direction in which fibers are arranged. However, in transverse direction it has weakest strength and stiffness property. For multidirectional and bidirectional continuous fibers, due to alignment of fibers in multi-direction, there are multiple directions of higher material properties. E.g. bidirectional continuous fiber composites are not as good as UD continuous fiber composites along the fiber direction but their transverse and longitudinal material properties are equally good. Bidirectional continuous fibers are manufactured on weaving machines in the form of fabrics. The weaving pattern of the fabric can be different. Some common weaving styles are illustrated in Figure 2.2.

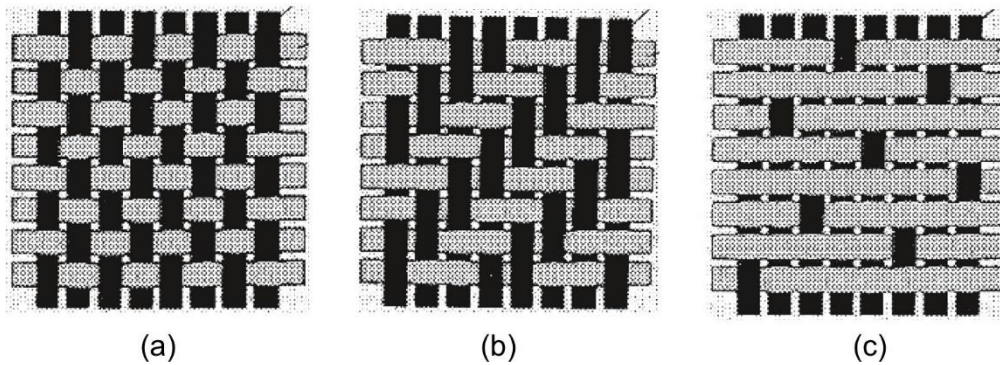


Figure 2.2 Bi-directional continuous fiber composites in (a) plain (b) twill (c) satin weaving styles [9]

In woven fabrics the fibers along the longitudinal/production are called warp. And fibers running in transverse direction are called weft. In plain woven fabric, the warp fibers pass under and over each weft alternately. In twill woven fabric, the warp fibers pass under and over two weft fibers. In satin woven fabric the warp passes under and over more number of wefts alternately. The advantage of twill woven fabric over plain woven fabric is that it can be draped without crimping the fabric. Non crimping of fabric improves the mechanical properties of composites. A satin weaving style has very good drapability due to which it can be used for relatively complex parts.

When multiple lamina/plies are stacked on one another, then it is called laminate. A laminate can have different plies oriented at different angles for optimal performance.

In following a brief overview of fibers and matrix materials is given.

### 2.1.1 Fibers

Fibers are natural or synthetic substances which have small diameter, high aspect ratio (length to thickness) and a very high degree of flexibility. They are principle constituents in composites and must always be combined with matrix material to manufacture any components. Therefore, fibers share a huge portion of volume and weight in a composite. Fibers share the major portion of load acting on a composite. Their size and volume fraction are the decisive factor in determining the density, stiffness, strength, fatigue, electrical/thermal conductivities and cost of composite material.

Filaments are the smallest unit of fibers and usually the filament size is of the order of  $\mu\text{m}$ . For practical purposes these filaments are gathered together in the form of bundle. The bundle of filaments can be twisted or untwisted. When the filaments are untwisted, the bundle of fibers is called *strand* or in case of carbon fibers *tow*. When the fibers are twisted then it is named as *yarn*. When a number of strands or tows are collected in parallel bundle with little or no twist, then it is called as *roving* (see Figure 2.3).

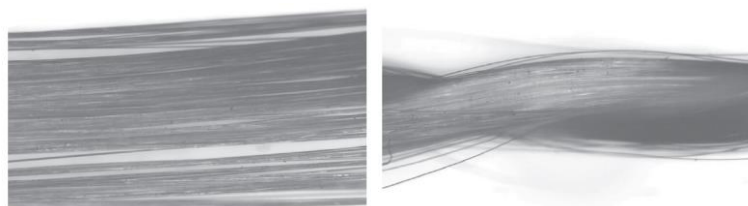


Figure 2.3 Filament bundle in form of strand (left) and yarn (right) [8]

There is variety of commercially available fibers which can be selected according the intended application of composite. Most frequently used fiber materials are

1. Glass fiber
2. Carbon fiber
3. Aramid fiber
4. Other fibers (Natural fibers, Alumina, Silica, Quartz)

Glass fibers are most commonly used fibers in composites. The diameter of glass fibers is usually in range of 5-20 $\mu\text{m}$  where the smaller diameters fibers contribute to their better performance of components. Although the specific strength of glass fibers is quite high, the specific modulus is moderate only. Glass fibers have low melting point in comparison to carbon fiber. Glass fibers do not decompose, have good chemical thermal and corrosion resistant. Glass fibers are designated according to their properties. e.g. E-glass fibers have high Young's modulus, low density and good water resistance and therefore are also used in structural applications. However, their chemical corrosion resistance against acids and alkalis is limited. S-glass or R-glass fibers have almost 35% higher strength in comparison to E-glass fibers. C-glass has better corrosion resistance.

Carbon based fibers are very lightweight fibers with very high stiffness and strength and lower failure strain. The density of carbon fibers is in the range of 1.6-2.2g/cm<sup>3</sup>. Because of low density of carbon fibers, they have very high specific stiffness and specific strength. In contrast to glass fibers, carbon fibers exhibit highly anisotropic behavior within a fiber. Their modulus along fiber axis is 200-700GPa while in transverse direction is 20GPa. Carbon fibers have high fatigue strength and thermal conductivity. In addition, carbon fibers also have chemical corrosion resistance, electrical conductivity, anti-friction properties, anti-radiation properties, damping, shock absorption, noise reduction and weave-ability. Generally, carbon fibers are more expensive than glass and aramid fibers.

Aramid fibers have low density, high tensile strength and E-modulus and lower compressive properties. Their density is 1.44g/cm<sup>3</sup> which is almost 40% lower than glass fibers and 20% lower than common carbon fibers. Their compression behavior is ductile. That is why in flexure loading, the compressive side of the material causes flexure behavior to be non-linear and causes it to absorb more energy. They have very high toughness characteristics that is why it has very high damage tolerance. Upon impact aramid fibers composites do not shatter and have very excellent vibration-damping characteristics.

### 2.1.2 Matrix

Matrix material are combined with fibers to produce the composite materials. The chemical composition and physical properties of matrix affect the processing, fabrication and properties of the composite material. Therefore, variation in composition, physical state or morphology of a matrix and the presence of impurities affect handle ability, composite material performance and long-term durability. The major role of matrix in a fiber reinforce composite are to:

- Keep fibers in place
- Transfer stress between the fibers
- Provide barrier against environmental effects such as moisture and chemicals
- Protect the surface of fibers from abrasion etc.

Under the compressive loading, the matrix provides lateral support against buckling of the fibers and hence increasing the compressive strength to a large extent. Other properties of composites which are majorly influenced by the matrix material are in plane shear and inter-laminar shear. Tensile properties however are not majorly affected by the choice of composite material. The defects in composite materials depends upon the processing characteristic of matrix materials. The interaction between fiber and matrix is also an important parameter in damage tolerant structures.

Polymer matrix materials are divided into two groups. Thermoplastics are the polymer which upon heating soften or melt. Thermosets are the polymers which do not melt or soften upon heating. Instead thermosets decompose on heating. Thermoset plastics such as epoxies, polyester and vinyl ester have low viscosity. Therefore, they are commonly used in long fiber and continuous fiber reinforced plastics. Traditionally thermoplastics were mostly used for short fiber reinforced composites. However, recently the use of thermoplastics with long fiber and continuous fibers have increased drastically. The major characteristics of thermoset and thermoplastics are summarized in Table 2-1.

	Advantage	Disadvantage
Thermoset	<ul style="list-style-type: none"> <li>• Thermal stability</li> <li>• Chemical resistant</li> <li>• Do not creep</li> <li>• Less stress relaxation</li> </ul>	<ul style="list-style-type: none"> <li>• Limited storage life</li> <li>• Long curing time</li> <li>• Low strain-to-failure</li> <li>• Lower impact strength</li> </ul>
Thermoplastic	<ul style="list-style-type: none"> <li>• High impact strength</li> <li>• High fracture resistance</li> <li>• Excellent damage tolerance</li> <li>• Higher strain-to-failure</li> <li>• Unlimited storage life at room temperature</li> <li>• Shorter fabrication time</li> <li>• Postformability (e.g. thermoforming)</li> <li>• Can be recycled</li> </ul>	<ul style="list-style-type: none"> <li>• High viscosity</li> <li>• Lower creep resistance</li> <li>• Lower thermal stability</li> </ul>

Table 2-1 Comparison of thermoset and thermoplastics

Examples of thermosetting matrix materials are epoxy and polyester. Most common thermoplastic matrix materials are PP, PA6 and PA6.6.

## 2.2 Energy absorption characteristics of fiber composites

To ensure the passive safety of passengers, the structural members must be able to absorb kinetic energy. Typically, in case for frontal crash the energy is absorbed by metallic crash box axially by folding and buckling. The metallic material deforms plastically and failure strain can reach up to 60% in strain localization area [10]. Fiber reinforced composites on the other hand undergo very small plastic strain along the fiber direction. Thermoplastic composite materials can provide higher energy absorption capability at reduced weight if designed carefully. Figure 2.4 shows a qualitative comparison of energy absorbed by constant weight of three different materials. The energy absorbed by continuous fiber reinforced thermoplastic (Tepex glass) is highest in comparison to metal (Aluminum) and plastic without fiber reinforcement (engineering polymer) [11].

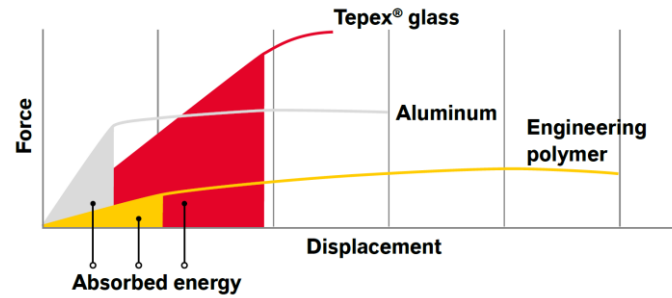


Figure 2.4 Qualitative comparison of specific-energy absorbing capacity of Tepex glass fiber thermoplastic composite with aluminum and engineering plastics [11]

The axial crushing of composites structures can result in two types of crushing (see Figure 2.5).

1. Catastrophic or unstable failure is where increase in force is followed by sudden decrease. This type of failure is common in long structures with thinner wall thickness because buckling stability is compromised and structure tends to collapse [12], [13].
2. Other type of failure is Progressive crushing where structure is crushed in a stable manner and energy absorbed is higher [13]–[15]. The front of material which deforms progressively is called “crush front”.

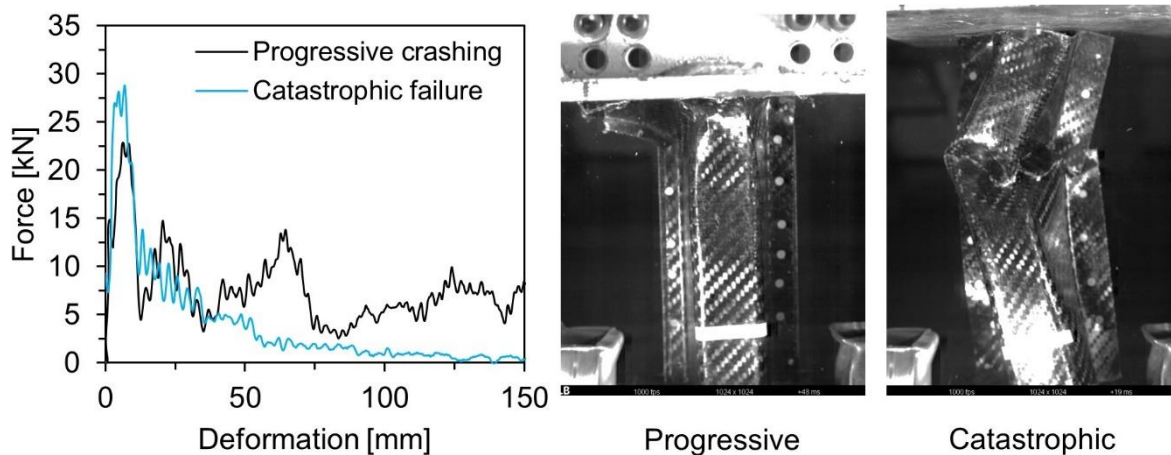


Figure 2.5 Progressive and catastrophic failure in axial crushing [6]

The area under load deformation curve gives quantitative value of total energy absorbed  $W$ . And energy absorbed per unit mass is specific energy absorption SEA.

$$W = \int_0^{\delta} F d\delta \quad (2.1)$$

$$SEA = \frac{\int_0^{\delta} F d\delta}{\rho A \delta} \quad (2.2)$$

Therefore, structural design must be designed to achieve progressive crushing behavior. There are different aspects of how to avoid composite structure failure in catastrophic manner. These factors

include effect of trigger, geometry of structure, wall thickness to diameter ratio, material type and its layup [14]–[16].

Different composite materials, if crushed axially in stable manner, absorb energy differently. And the amount of energy absorbed is dependent on the crushing mechanism. Progressive crushing of tubes can be further classified into three categories based on the crush front morphology. [17]

1. Brittle fracture with crash front breaking into debris
  - This type of crushing disintegrates fibers and matrix into small pieces and therefore absorb highest amount of energy as compared to other crushing types. (Figure 2.6a)
2. Continuous fronds formation
  - The fiber layers delaminate and splay outward. The plies remain intact but practically no structural stiffness left in the material and it can no longer bear any further load. (Figure 2.6b)
3. Accordion type folding
  - This failure type is often seen with Kevlar fiber which can undergo relatively higher amount of strains. The buckling and folding pattern is the same as in metals. (Figure 2.6c)

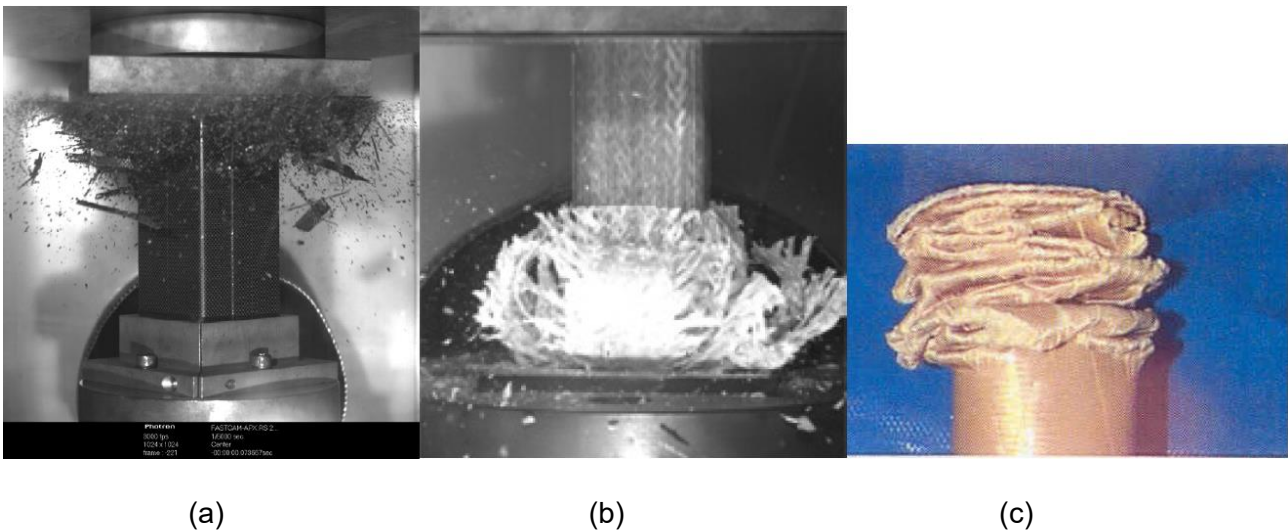


Figure 2.6 Three types of composite crushing morphologies [17]

To quantify the axial crash energy absorption of composite materials, coupon level tests are done. This determines the potential of composites materials to be used in energy absorbing structures.

Feraboli [18] has divided coupon level crush energy absorption specimens into two types.

1. Flat specimen with support fixtures
2. Self-supporting

### 2.2.1 Flat specimens

Flat specimens are just small rectangular pieces of material which need expensive/specialized fixture to stabilize them. Typically, small trigger geometry is machined on the crush front of these

specimens. Figure 2.7 shows an example of testing a flat specimen for energy absorption characteristic with a fixture. Barnes et al. [16] has given summary of all flat specimen testing fixtures. The fixture design should be such that:

- It provides lateral support for flat specimens.
- Crush Specimen does not have any knife edge or tearing of both ends which results in higher amount of measured energy absorption.
- It should provide enough unsupported distance (unsupported length of specimen on crushing end) that crushing can occur freely while avoiding buckling.

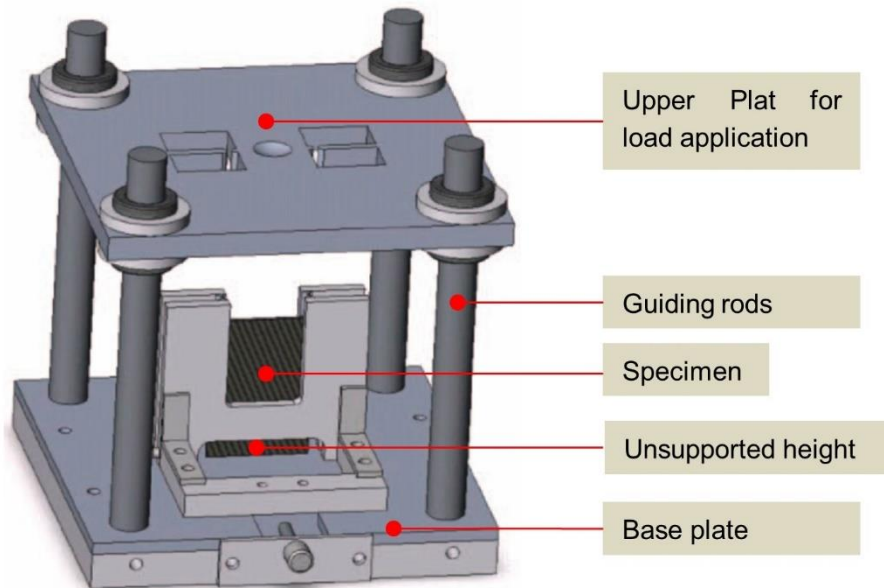


Figure 2.7 Fixture design for flat specimen crushing by Feraboli [19]

### 2.2.2 Self-supporting specimens

Self-supporting specimens have out of plane curvature which allows them to stand on ground without any external support. If the length of specimen is right, then such specimen can be crushed without any buckling failure.

Feraboli [18] conducted study on three different corrugated specimens (see Figure 2.8) to screen materials and layup design of composite material. The specimen featured low sinusoidal, high sinusoidal and semi-circle specimen having different degrees and shapes of corrugation. In tests with different layup and materials, semi-circle specimen showed highest amount of energy absorbed. Due to its three dimensional nature, corrugates specimens can capture most of failure modes seen in tubular specimens and yet it is easier to manufacture. However self-supporting specimens need special thermoforming or manufacturing tool in contrast to flat specimens.

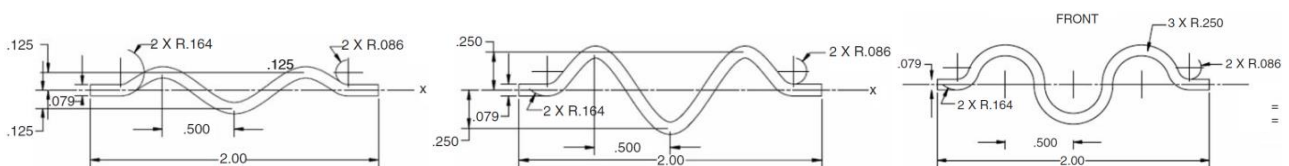


Figure 2.8 Cross section view of Low sine, deep sine and semi-circle specimen, dimensions in inches [18]

### 2.3 Size effect

In fiber composite materials, the fibers are used because the materials are stronger in their fibrous forms as compared to the bulk form. The reason being that probability of containing strength critical defects such as cracks and voids in a bigger volume of material is higher as compared to smaller volume of material. This reduces the strength of material significantly. This tendency of decreasing strength with increasing specimen volume, called size effect, is mostly observed in brittle materials including fiber. On the other hand, as the volume of the material decreases, the probability of defects decreases and hence the strength increases. Figure 2.9 shows, how the strength of glass fiber decreases with increasing size.

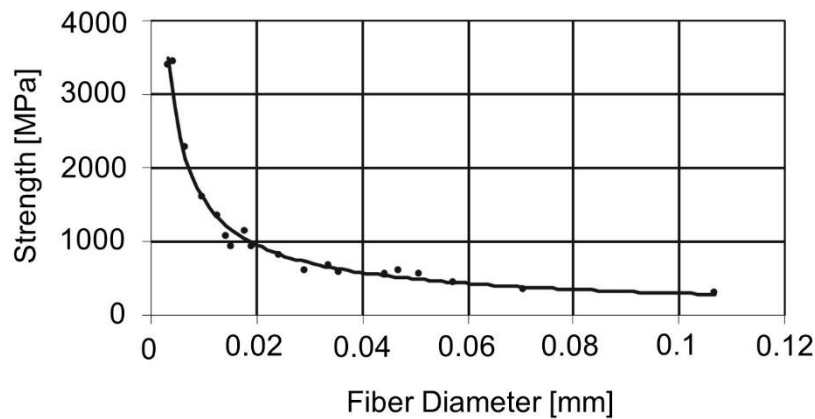


Figure 2.9 Effect of fiber diameter on the strength of glass fibers [9]

The size effect in composite materials is not limited to fiber size. Rather it is also observed on specimen and structural levels. The flexural strength of elastic brittle materials is also higher than their tensile strength. Size effect also explains the higher flexural strength over tensile strength measured in uniaxial tests. The flexural strength also increases by reducing the size of flexural specimen.

For a perfectly homogeneous material, free from defect, flexural strength and tensile strength should be the same. However, materials in reality always contain defect. When the material is subjected to the tensile loading, the deformation within gauge length is uniform. In the weakest location, crack can be initiated due to the presence of the voids, micro-cracks or manufacturing defects. Because the material at the crack location is not able to bear load, all the load has to be carried by its proximity and results in stresses concentrations. The specimen fails to reach its ideal maximum strength. In contrast to the tensile test, in the three-point bending experiment, fibers at the outer surface are under maximum stress which is not necessarily the weakest point. Therefore, the flexural strength is higher than in the tensile strength [20], [21].

The probability of survival  $P(s)$  of material volume  $V$  under stress  $\sigma$  according to Weibull statistical theory [20]–[23] is:

$$P(s) = \exp \left[ -V \left( \frac{\sigma}{\sigma_0} \right)^m \right] \quad (2.3)$$

where  $m$  is Weibull modulus and  $\sigma_0$  is strength associated with unit volume of material. Therefore, a relation between the strengths of two volumes under tensile loading can be established as

$$\frac{\sigma_2}{\sigma_1} = \left( \frac{V_1}{V_2} \right)^{\frac{1}{m}} \quad (2.4)$$

Hence if the value of  $m$  is known, then the strength of fiber composite can be calculated as function of its volume.

## 2.4 Lamina stress-strain law

Consider a ply/lamina of composite materials with fibers aligned along global x-direction as shown in Figure 2.10 under external load  $\sigma_x$ .

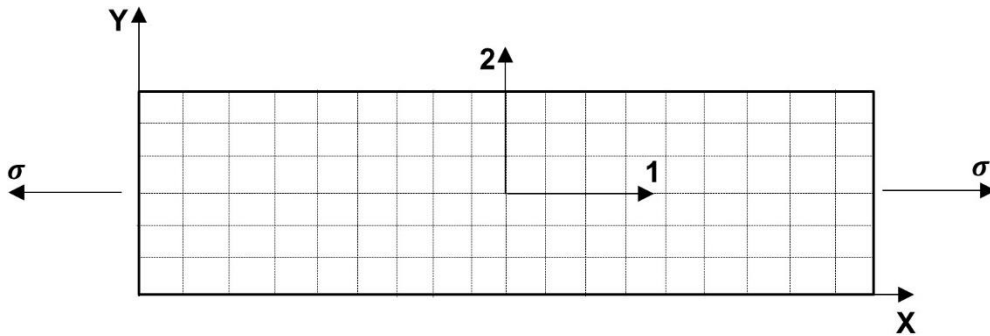


Figure 2.10 Fiber composite ply with fibers aligned along global x-direction

The elasticity modulus of composite ply along fiber direction 1 is  $E_1$  and elasticity modulus along fiber direction 2 is  $E_2$ . The stresses in the ply are related to strains as:

$$\sigma_1 = E_1 \varepsilon_1 \text{ and } \sigma_2 = E_2 \varepsilon_2 \quad (2.5)$$

Now consider the same ply is in loaded in more than one direction. The composite ply is thin in comparison to its other dimensions so the plane stress conditions ( $\sigma_3 = \tau_{13} = \tau_{23} = 0$ ) holds. The Poisson's ratio is defined as:

$$\nu_{12} = -\frac{\varepsilon_2}{\varepsilon_1} \text{ and } \nu_{21} = -\frac{\varepsilon_1}{\varepsilon_2} \quad (2.6)$$

The strains  $\varepsilon_1$  in ply is elongation due to applied load minus the contraction due to load perpendicular to it:

$$\varepsilon_1 = \frac{\sigma_1}{E_1} - \nu_{21} \varepsilon_2 = \frac{\sigma_1}{E_1} - \frac{\nu_{21} \sigma_2}{E_2} \quad (2.7)$$

Similarly:

$$\varepsilon_2 = \frac{\sigma_2}{E_2} - \nu_{21}\varepsilon_1 = \frac{\sigma_2}{E_2} - \frac{\nu_{12}\sigma_1}{E_1} \quad (2.8)$$

The shear strain  $\gamma_{12}$  is directly related to shear stress  $\tau_{12}$  through shear modulus  $G_{12}$  as:

$$\gamma_{12} = \frac{\tau_{12}}{G_{12}} \quad (2.9)$$

Due to the symmetry relationship between Poisson's ratio and elastic moduli in the two axes,  $\nu_{21}E_1 = \nu_{12}E_2$ , the Eqn. (2.7)-(2.9) can be written in matrix form:

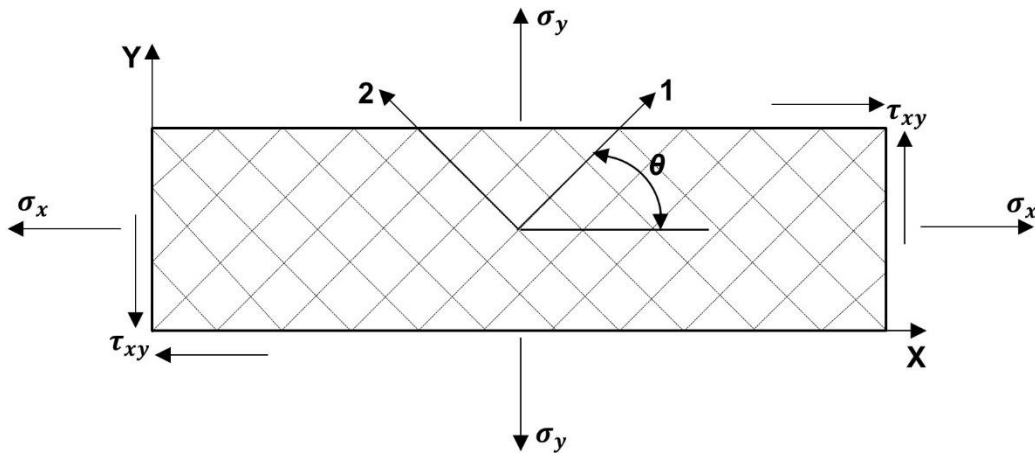
$$\begin{bmatrix} \varepsilon_1 \\ \varepsilon_2 \\ \gamma_{12} \end{bmatrix} = \begin{bmatrix} \frac{1}{E_1} & \frac{-\nu_{12}}{E_1} & 0 \\ \frac{-\nu_{12}}{E_1} & \frac{1}{E_2} & 0 \\ 0 & 0 & \frac{1}{G_{12}} \end{bmatrix} \begin{bmatrix} \sigma_1 \\ \sigma_2 \\ \tau_{12} \end{bmatrix} \quad (2.10)$$

$$[\varepsilon] = [S][\sigma]$$

$S$  is called compliance matrix for the lamina. By inverting the compliance matrix, the stiffness matrix  $K$  can be calculated for stress as function of strains.

$$\sigma = [S]^{-1}\varepsilon = [K]\varepsilon \quad (2.11)$$

Now consider a ply where the fibers are at an angle  $\theta$  from the global XY coordinate system as shown in Figure 2.11. The ply material direction does not coincide with the applied loading direction and a stress/strain transformation is needed. The transformation can be accomplished with the help of a free body diagram.



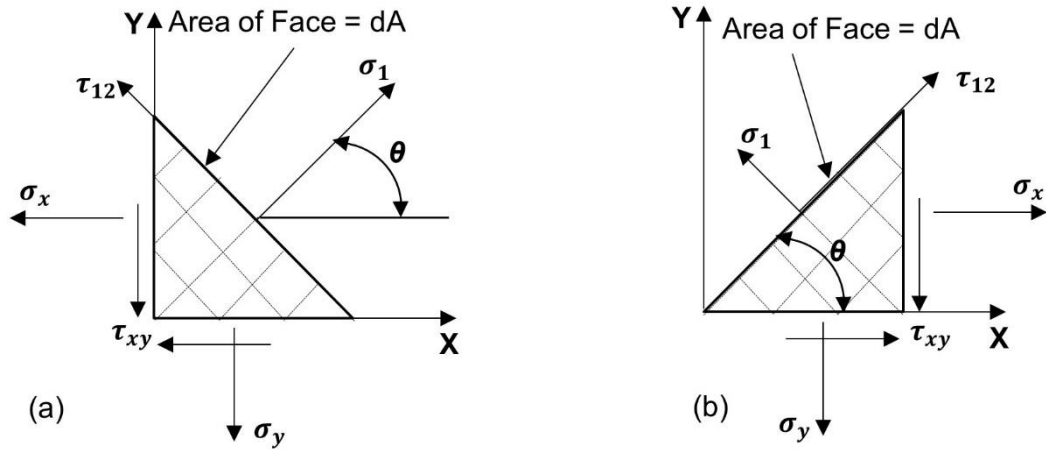


Figure 2.11 Composite ply fibers at an angle from global x-axis with free-body diagram

For an equilibrium, the sum of forces along fiber direction 1 must be zero in Figure 2.11(a).

$$\sum F_1 = 0 = \sigma_1 dA - \sigma_x (dA \cos\theta) \cos\theta - \sigma_y (dA \sin\theta) \sin\theta - \tau_{xy} (dA \cos\theta) \sin\theta - \tau_{xy} (dA \sin\theta) \cos\theta \quad (2.12)$$

Similarly, forces must be in an equilibrium in direction 2 in Figure 2.11(b).

$$\sum F_2 = 0 = \sigma_2 dA - \sigma_x (dA \sin\theta) \sin\theta - \sigma_y (dA \cos\theta) \cos\theta + \tau_{xy} (dA \cos\theta) \sin\theta - \tau_{xy} (dA \sin\theta) \cos\theta \quad (2.13)$$

Again Figure 2.11(b) can be used to write an equilibrium in direction-1.

$$\sum F_1 = 0 = \tau_{12} dA + \sigma_x (dA \sin\theta) \cos\theta - \sigma_y (dA \cos\theta) \sin\theta - \tau_{xy} (dA \cos\theta) \cos\theta + \tau_{xy} (dA \sin\theta) \sin\theta \quad (2.14)$$

The Eqn. (2.12)-(2.14) can be simplified in the following form:

$$\sigma_1 = \sigma_x \cos^2\theta + \sigma_y \sin^2\theta + 2\tau_{xy} \sin\theta \cos\theta \quad (2.15)$$

$$\sigma_2 = \sigma_x \sin^2\theta + \sigma_y \cos^2\theta - 2\tau_{xy} \sin\theta \cos\theta \quad (2.16)$$

$$\tau_{12} = -\sigma_x \sin\theta \cos\theta + \sigma_y \sin\theta \cos\theta + \tau_{xy} (\cos^2\theta - \sin^2\theta) \quad (2.17)$$

The stress transformation can be written in the form of matrix as:

$$\begin{bmatrix} \sigma_1 \\ \sigma_2 \\ \tau_{12} \end{bmatrix} = \begin{bmatrix} \cos^2\theta & \sin^2\theta & 2\sin\theta \cos\theta \\ \sin^2\theta & \cos^2\theta & -2\sin\theta \cos\theta \\ -\sin\theta \cos\theta & \sin\theta \cos\theta & \cos^2\theta - \sin^2\theta \end{bmatrix} \begin{bmatrix} \sigma_x \\ \sigma_y \\ \tau_{xy} \end{bmatrix} \quad (2.18)$$

$$[\sigma]_{12} = [T_\sigma] [\sigma]_{xy}$$

$[T]$  is called transformation matrix and can be inverted for determining global stresses in terms of local stresses as:

$$[\sigma]_{xy} = [T_\sigma]^{-1} [\sigma]_{12} \quad (2.19)$$

The same transformation matrix can be used for strain transformation.

$$\begin{bmatrix} \varepsilon_1 \\ \varepsilon_2 \\ \varepsilon_{12} \end{bmatrix} = \begin{bmatrix} \cos^2\theta & \sin^2\theta & 2\sin\theta\cos\theta \\ \sin^2\theta & \cos^2\theta & -2\sin\theta\cos\theta \\ -\sin\theta\cos\theta & \sin\theta\cos\theta & \cos^2\theta - \sin^2\theta \end{bmatrix} \begin{bmatrix} \varepsilon_x \\ \varepsilon_y \\ \varepsilon_{xy} \end{bmatrix} \quad (2.20)$$

Note that this is the transformation between tensorial shear strains  $\varepsilon_{12}$  and  $\varepsilon_{xy}$ . Figure 2.12 illustrates the difference between engineering and tensorial shear strain.

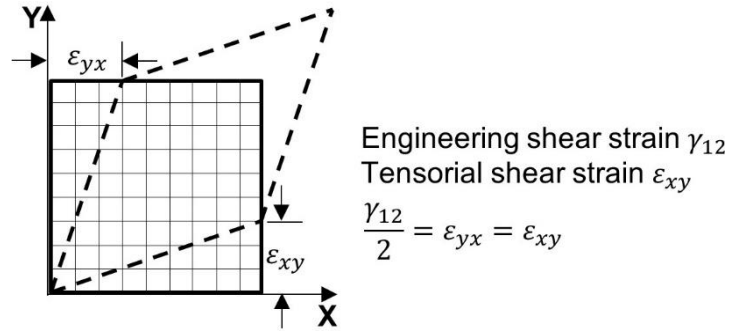


Figure 2.12 Difference between tensorial and engineering shear strain

For transformation in engineering shear strain, modification is required in transformation matrix as following:

$$\begin{bmatrix} \varepsilon_1 \\ \varepsilon_2 \\ \gamma_{12} \end{bmatrix} = \begin{bmatrix} \cos^2\theta & \sin^2\theta & \sin\theta\cos\theta \\ \sin^2\theta & \cos^2\theta & -\sin\theta\cos\theta \\ -2\sin\theta\cos\theta & 2\sin\theta\cos\theta & \cos^2\theta - \sin^2\theta \end{bmatrix} \begin{bmatrix} \varepsilon_x \\ \varepsilon_y \\ \gamma_{xy} \end{bmatrix} \quad (2.21)$$

$$[\varepsilon]_{12} = [\mathbf{T}_\varepsilon] [\varepsilon]_{xy}$$

Similar to strains, an inverse of  $\mathbf{T}_\varepsilon$  can be used to determine global strains in terms of local strains as

$$[\varepsilon]_{xy} = [\mathbf{T}_\varepsilon]^{-1} [\varepsilon]_{12} \quad (2.22)$$

A global response of ply material can be calculated by inserting Eqn. (2.11) and (2.21) into (2.19) respectively.

$$[\sigma]_{xy} = [\mathbf{T}_\sigma]^{-1} \mathbf{K} [\mathbf{T}_\varepsilon] [\varepsilon]_{xy} = [\bar{\mathbf{K}}] [\varepsilon]_{xy} \quad (2.23)$$

$\bar{\mathbf{K}}$  global stiffness matrix of 3x3 order for a single ply. Similar to previous inversions, global strains in terms of global stresses can be written with inverse of  $\bar{\mathbf{K}}$ :

$$[\varepsilon]_{xy} = [\bar{\mathbf{K}}]^{-1} [\sigma]_{xy} = [\bar{\mathbf{S}}] [\sigma]_{xy} \quad (2.24)$$

$\bar{\mathbf{S}}$  global compliance matrix of 3x3 order for single ply.

Note that the above calculations are for a lamina/single ply analysis. The equations can easily be expanded to Classical Laminate Theory (CLT) for analysis of multi-ply laminate [24].

## 2.5 Failure of composite materials

With the elastic stress-strain law, the stresses/strains in composite material can be calculated under applied external loads/deformations. When the stress/strain reaches a particular limit, the material fails. In composite material defining this limit, or fracture point is relatively complex as compared to metals due to its directional dependency. The composite materials are stronger along the fiber

direction and weaker in other directions. The complexity of analysis increases due to multi-stress state. E.g. if composite material is under load from different directions and the loading is also different. The limit of material, at which the composite material fails is called "failure surface".

### 2.5.1 Failure surface testing

Testing the composite material under uniaxial loading or along one particular direction has been standardized by ISO and ASTM. The testing of material under tensile, compression and in-plane shear is discussed in detail in chapter 3. In worldwide failure exercise [25], contributors were given material and laminate data from which they had to predict the failure behavior in different cases. The predicted data was compared against experimentally obtained failure surface data. This experimental data represented points of laminate failure on bi-axial stress space. Similarly in 2<sup>nd</sup> worldwide failure exercise, experimental data of tri-axial stress state was used to compare the failure theories [26]. Testing for failure surface/envelope for bi-axial stress states can be divided in two categories.

#### ***Biaxial failure envelope $\sigma_1/\sigma_2$ vs. $\tau_{12}$***

Bi-axial failure envelope of Longitudinal and Transverse stresses vs. Shear stress for composites can be obtained by simultaneous torsion and tension/compression of cylindrical tubes [27]. Using this method, data points of two failure envelopes can be measured.

1. Longitudinal and shear stress failure envelope  $\sigma_1$  vs.  $\tau_{12}$
2. Transverse and shear stress failure envelope  $\sigma_2$  vs.  $\tau_{12}$

The stress state depends on the direction of fibers of the tube. Data used in 1<sup>st</sup> worldwide failure exercise was obtained from circumferentially and axially filament wound tube of 60mm internal diameter and 2mm wall thickness

#### ***Biaxial failure envelope $\sigma_1$ vs. $\sigma_2$***

In-plane biaxial testing along fiber directions can be done either by tubular specimens or by cruciform specimens.

1. Tubular specimens

Biaxial failure envelope data points under longitudinal and transverse stress  $\sigma_x$  vs.  $\sigma_y$  can be obtained pressurizing a tube internally and applying axial loading [27]. In 1<sup>st</sup> worldwide failure exercise, results of a circumferentially filament-wound cylindrical tube of 100mm internal diameter, 300mm long and wall thickness of 1.2mm were used.

The hoop stress  $\sigma_\theta$  in tube can be measured by pressure P, internal radius of tube  $R_i$  and thickness  $h$

$$\sigma_\theta = \frac{PR_i}{h} \quad (2.25)$$

And axial stress using applied load  $F$

$$\sigma_1 = \frac{PR_i}{h} + \frac{F}{2\pi R_i h} \quad (2.26)$$

## 2. Cruciform Specimen

Tubular specimens do not necessarily represent actual structure. Moreover, it could also be difficult to manufacture a cylindrical tube. A cruciform specimen (see Figure 2.13) is a cross-shape specimen with is fixed from two sides and load is applied on other two sides. The arms of specimen are usually along the longitudinal and transverse direction. Any combination of in-plane stress can be introduced in specimens.

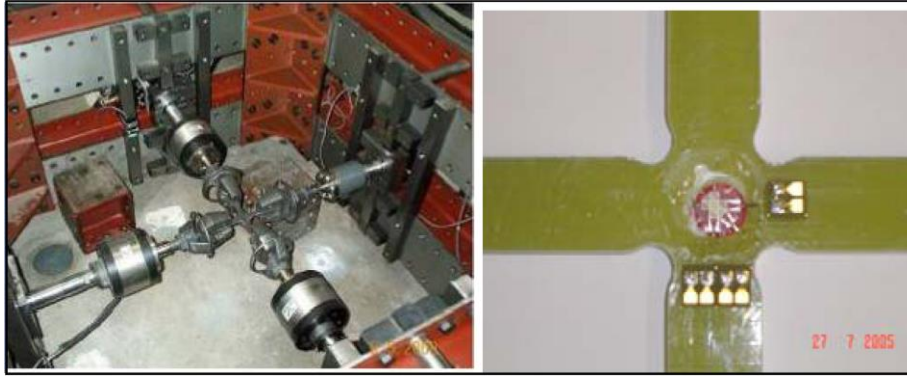


Figure 2.13 Biaxial testing machine and Cruciform specimen [28]

### 2.5.2 Failure criteria

Many works have been done to predict the failure surface of FRC. Pinho [29] classified failure criteria into “Interpolation failure criteria” and “physically based criteria.

#### *Interpolation failure criteria*

These criteria interpolate the failure surface between the experimentally obtained data points through polynomial functions. A very first interpolation criterion was proposed by Tsai [30] based on Hills yield criteria for orthotropic ideal plastic material which in turn is a generalization of yield criteria for isotropic materials proposed by Von Mises.:

$$F = \frac{\sigma_1^2}{X^2} + \frac{\sigma_2^2}{Y^2} + \frac{\tau_{12}^2}{S_{12}^2} - \frac{\sigma_1\sigma_2}{XY} < 1 \quad (2.27)$$

In which X and Y are tensile/compressive strengths in fiber direction 1 and 2 respectively.  $S_{12}$  is shear strength.

Hashin [31] pointed out that such an approximation cannot not predict the failure under isotropic stress conditions. Later Tsai and Wu [32] proposed a popular failure criteria by assuming a failure surface in stress space as a single quadratic polynomial function of the following form:

$$F = \frac{\sigma_1^2}{X_t X_c} + \frac{\sigma_2^2}{Y_t Y_c} + \frac{\tau_{12}^2}{S_{12}^2} + \frac{2\sigma_1\sigma_2 F_{12}^*}{\sqrt{X_t X_c Y_t Y_c}} + \frac{\sigma_1}{X_t} - \frac{\sigma_1}{X_c} + \frac{\sigma_2}{Y_t} - \frac{\sigma_2}{Y_c} < 1 \quad (2.28)$$

In which  $F_{12}^*$  is an interaction term which can be determined by biaxial tension or compression test of 45° specimens. Therefore, an interaction between the different stress components is considered and depend no more on normal stresses which eliminate the problems described by Hashin.

Using interpolation failure criterion is a rough approach for predicting failure in the composite because the composite constituents, fiber and matrix, fail differently under tension and compression. Using one smooth polynomial function in stress space is not exact representation of failure surface of composite materials.

### **Physically based failure criteria**

The physically based criteria distinguish between the failure modes. Therefore, they cannot be represented by a single polynomial function. Paris et.al. [33] reviewed a number of failure criteria of composite at laminate level and recommended the use of failure mechanics based criteria.

The maximum stress and maximum strain failure criteria are the simplest examples where failure is predicted when the maximum value of stress or strain in a given direction is reached:

$$F = \max\left(\left|\frac{\sigma_1}{X}\right|, \left|\frac{\sigma_2}{Y}\right|, \left|\frac{\tau_{12}}{S_{12}}\right|\right) < 1 \quad (2.29)$$

Rohwer [34] categorized such failure criteria as non-interactive criteria because no interactions between stress components are considered. The maximum stress criterion was used by many authors for fiber tensile mode prediction such as by Pinho [29]. Similarly, Davila [35] also used maximum strain criteria for his LaRC03 failure criterion.

Hashin and Rotem [36] differentiated between fiber failure mode  $F_1$  in fiber directions and matrix failure mode  $F_2$  considering shearing and tension/compression:

$$F_1 = \left|\frac{\sigma_1}{X}\right| < 1 \text{ where } X = X_t \text{ if } \sigma_1 \geq 0; X = X_c \text{ if } \sigma_1 < 0$$

$$F_2 = \left(\frac{\sigma_2}{Y}\right)^2 + \left(\frac{\tau_{12}}{S_{12}}\right)^2 < 1 \text{ where } Y = Y_t \text{ if } \sigma_2 \geq 0; Y = Y_c \text{ if } \sigma_2 < 0 \quad (2.30)$$

Modifying his previous work, Hashin [31] chose the quadratic failure criterion, as a function of stress invariants to represent the failure surface based on curve fitting. The failure criteria for the tensile, compressive fiber mode, matrix tensile and compressive mode are given in [31].

Puck [37] distinguished between fiber failure FF and inter-fiber failure IFF in unidirectional composites. The normal - in-plane shear stress envelope of the failure surface in fiber and transverse direction were different. The shear stress in compression increased the material strength as compared to tension. The results of Puck's criteria were found to be better than others [25].

## **2.6 Explicit finite element method**

For crash analysis of complex composite structures, analytical methods presented in section 2.4, section 2.5 and CLT cannot be used. From the perspective of transient dynamic simulations, finite element-based codes with explicit formulations are used. Explicit formulation has the advantage of treating instabilities and material softening, especially with problems involving contact. For a reasonable computation time, multi-layered shell elements are used to represent plies [38].

Consider a 1-d system with stiffness  $k$  and a nodal mass  $m$  attached to it under external force  $f(t)$  as shown in Figure 2.14. This is a dynamic problem where the values of displacement  $u$ , velocity  $\dot{u}$  and acceleration  $\ddot{u}$  have to be determined at every time step of the analysis.

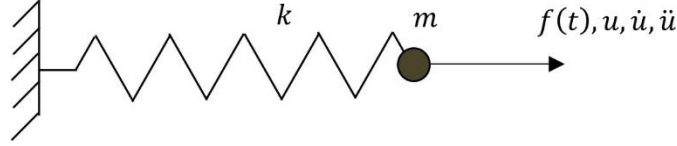


Figure 2.14 1D system under external load

The equilibrium equation of this system at time  $t = n$  can be written as:

$$m\ddot{u}_n + ku_n = f_n(t) \quad (2.31)$$

$\ddot{u}_n$  represent the nodal acceleration at time  $t = n$ ,  $ku_n$  is the internal forces and  $f_n(t)$  is the external applied forces. This equilibrium equation can be used to calculate the acceleration  $\ddot{u}_n$  by dividing the force by mass as:

$$\ddot{u}_n = m^{-1}(f_n - ku_n) \quad (2.32)$$

The time difference between two consecutive time steps  $\Delta t = t_{n+1} - t_n$  is called time increment. In explicit simulations this time step is very small. An integration scheme is called explicit if the values of unknown variables are function of the known values of previous time step. Abaqus uses explicit central difference integration rule in the explicit dynamics analysis procedure. Therefore, from the known value of acceleration, the velocity and displacement are calculated as:

$$\dot{u}_{n+1/2} = \dot{u}_{n-1/2} + \frac{\Delta t_{n+1} + \Delta t_n}{2} \ddot{u}_n \quad (2.33)$$

$$u_{n+1} = u_n + \Delta t_{n+1} \dot{u}_{n+1/2} \quad (2.34)$$

In Eqn. (2.33), the values of  $\dot{u}_{n+1/2}$  is determined explicitly as function of known value  $\ddot{u}_n$  from previous time step. If the value is defined as function of  $\ddot{u}_{n+1}$ , then it would be an implicit integration scheme. Implicit methods are used for numerically stiff problems in which stability is necessary. For the very short time steps in crash simulations, only explicit methods are used. Implicit analysis requires huge amount of computational resources at each cycle due to which they are mostly used for quasi-static analysis.

Note that the value of velocity  $\dot{u}_{n+1/2}$  at time  $t = 0$  would require known value of velocity at half step time before the start of analysis  $\dot{u}_{0-1/2}$ . Therefore Abaqus initial values of velocity acceleration at time  $t = 0$  are set to zero unless specified by user. E.g. the initial value of velocity in drop tower crash simulations is determined to save the computation time of free falling impactor unless it gets closer to the object being impacted. (see chapter 6.3)

The time increment  $\Delta t$  in explicit simulations is conditionally stable. This means that the time increment should always be less than the critical limit. This critical time limit for 1D elements is defined by:

$$\Delta t \approx \frac{L}{C} = \frac{L}{\sqrt{\frac{E}{\rho}}} \quad (2.35)$$

Here  $L$  is the length of element.  $C$  is speed of sound in the material.  $E$  is young's modulus and  $\rho$  density. So increasing the finite element size or density of the material, the stable time will increase. For a crash size FE model, the smallest finite element will determine the stable time increment. So practically only one element can affect the stable time increment of whole model. By artificially increasing the mass density  $\rho$  of the material (mass scaling) the time step can also be increased.

## 2.7 User-defined material modeling (VUMAT)

In commercial FEM codes for explicit simulations, different built in material models are available to choose from. Sometimes none of the material model is true representation of the material for which simulation is required. In such cases, user-defined subroutines are used to define the constitutive behavior of materials.

In Abaqus, the user-defined material subroutine for explicit simulations is called VUMAT. A material constitutive model is implemented in Fortran and supplied as additional file to Abaqus solver during an explicit analysis. The solver calls VUMAT at every time increment from start of the analysis till the end of analysis.

During the analysis, the strain increment information of every material point (integration point of finite element) is passed to the VUMAT. The VUMAT calculates the stresses from the strain increment and updates the stresses for every element at every time increment. e.g. if shell elements are used then at every new time increment the strain increment information  $\{\Delta\varepsilon_1, \Delta\varepsilon_2, \Delta\varepsilon_{12}\}_n$  is passed on to the VUMAT. The VUMAT calculates the new stresses and updates the stresses  $\{\sigma_1, \sigma_2, \sigma_{12}\}_n$ .

In addition to stresses, VUMAT can also update customized variable (e.g. damage, plastic strain) called State Variables. The information of stresses and state variables from previous times steps is made available during every new time increment. The information of state variables can be used for the calculation purpose during the current time step. The state variables can be output as solution dependent variables (SDV).

The VUMAT also allow to determine the internal energy and dissipated energy at the end of each increment. A flow diagram shown in Figure 2.15 gives an overview of where does the VUMAT fit in the explicit FEM analysis in Abaqus.

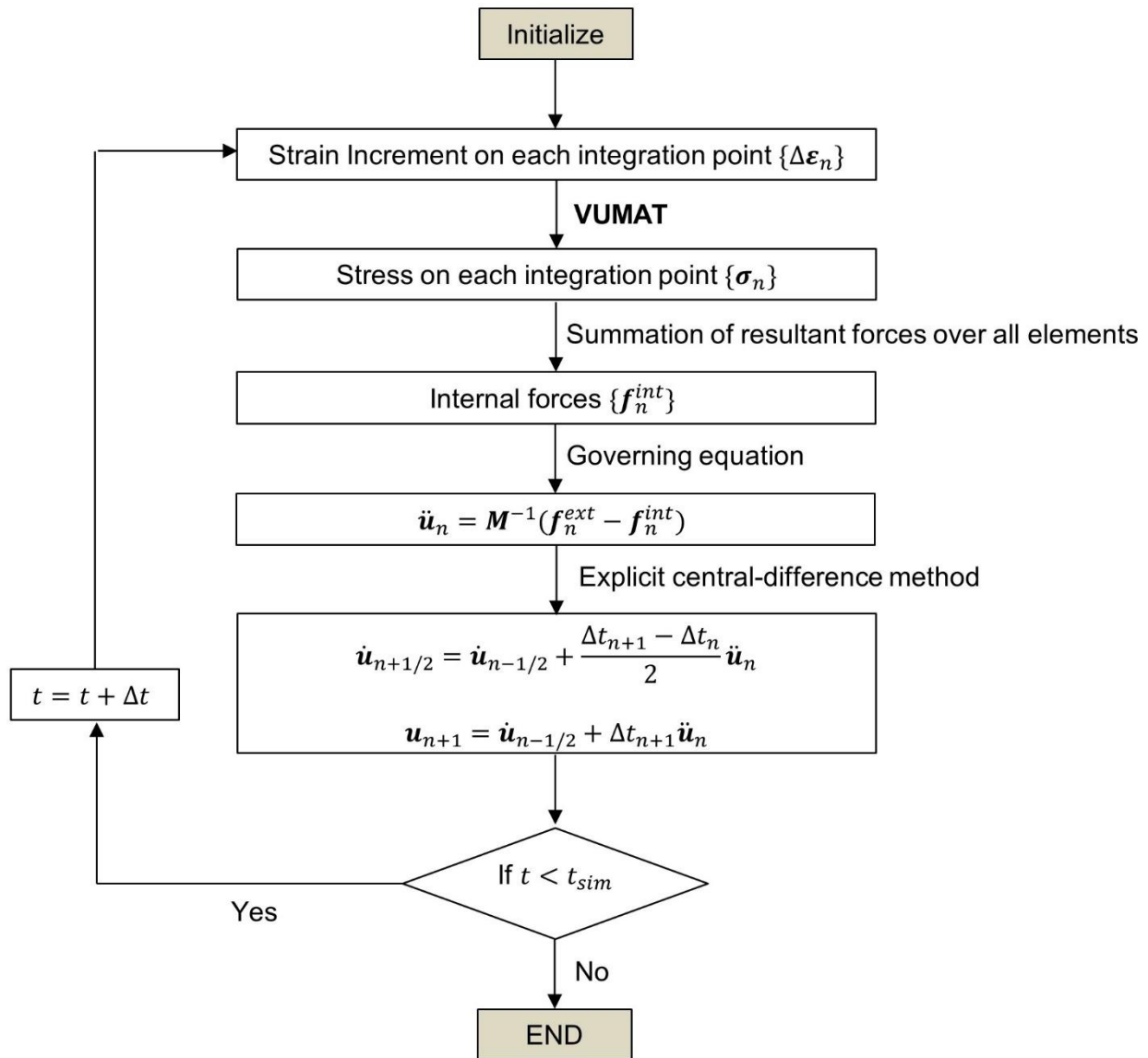


Figure 2.15 flow diagram summarizing the explicit analysis

It is important to mention that the coordinate system embedded with every element. This co-rotational coordinates means that no extra transformation between the strains and stresses is required in VUMAT.

## 2.8 Elasto-plasticity

An elastoplastic material behavior is observed in many materials including metals and angle ply laminates of composite. Typically, the in-plane shear behavior of composite materials is non-linear. This nonlinearity is attributed to the inelastic deformation of matrix and micro-cracks in matrix material[39], [40].

Elastoplastic materials behaves linearly until a certain point called yield stress  $\sigma_y$  and then deform plastically. When an elastoplastic material is loaded then it first undergo elastic strain denoted by  $\varepsilon^{el}$ . If the material is continued to be loaded, the material starts to deform plastically. Plastic strain

$\varepsilon^{pl}$  is permanent even if the load is removed. The total strain  $\varepsilon$  in the material is sum of elastic and plastic strain.

$$\varepsilon = \varepsilon^{el} + \varepsilon^{pl} \quad (2.36)$$

The stress in material is due to elastic  $\varepsilon^{el}$  strains. If the elasticity modulus of the material is  $E$  the stress can be calculated as:

$$\sigma = E\varepsilon^{el} = E(\varepsilon - \varepsilon^{pl}) \quad (2.37)$$

The stress in the elastoplastic materials is bound by yield stress  $\sigma_y$ . i.e. the stress is constrained to the elastic domain by yield stress. Since the absolute value of the stress in material cannot be greater than yield stress, it can be described as [41], [42]:

$$|\sigma| \leq \sigma_y \text{ or } F = |\sigma| - \sigma_y \leq 0 \quad (2.38)$$

in which  $F$  is called yield function defining the elastic domain. The material response for  $F < 0$  is called elastic whereas for  $F = 0$  the material response is elastoplastic.

If the material is loaded beyond the elastic domain, the plastic strain starts to increase. Even though the initial yield point  $\sigma_{y0}$  has been reached, the elastic strain can still increase. With the loading beyond initial yield point  $\sigma_{y0}$ , hardening takes place and the yield stress  $\sigma_y$  changes. The type of hardening is dependent upon the type of material. Figure 2.16 illustrates some common behavior of elastoplastic materials and their respective hardening laws.

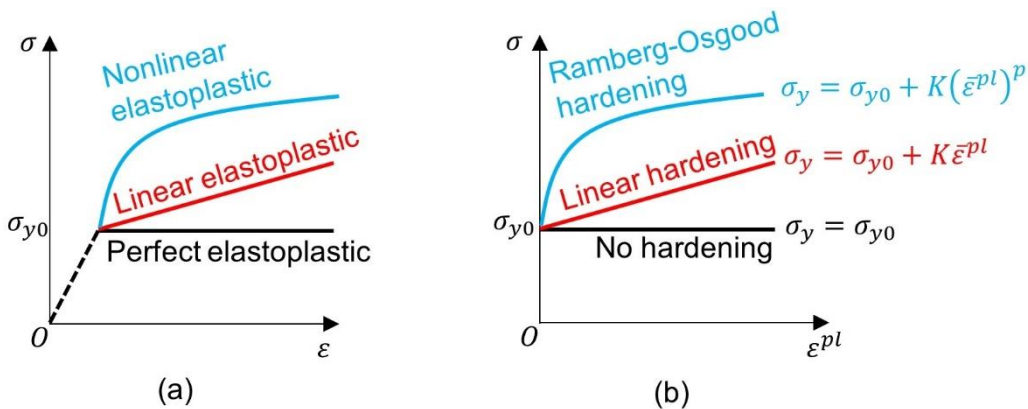


Figure 2.16 (a) Illustration of total stress-strain diagram of elastoplastic behaviors and (b) their respective plastic strain hardening laws

It is important to note that in Figure 2.16(b), the flow stress  $\sigma_y$  is defined as function of yield stress  $\sigma_{y0}$  and equivalent plastic strain  $\bar{\varepsilon}^{pl}$ . Equivalent plastic strain  $\bar{\varepsilon}^{pl}$  is an internal variable for isotropic hardening. It keeps track of the total plastic strain  $\varepsilon^{pl}$  regardless of tensile/compression loading. For a monotonic loading equivalent plastic strain and total plastic strain are equal.  $K$  and  $p$  are constants.

Now consider an explicit FEM simulation scenario where a strain increment  $\Delta\varepsilon$  is applied to the material. The information about stress, total strain, plastic strain and equivalent plastic strain

$\{\sigma_n, \varepsilon_n, \varepsilon_n^{pl}, \bar{\varepsilon}_n^{pl}\}$  at time  $t = n$  is known. To calculate the updated values  $\{\sigma_{n+1}, \varepsilon_{n+1}, \varepsilon_{n+1}^{pl}, \bar{\varepsilon}_{n+1}^{pl}\}$  at time  $t = n + 1$  an algorithm must be followed.

Strain increment gives total deformation at time  $t = n + 1$

$$\varepsilon_{n+1} = \varepsilon_n + \Delta\varepsilon \quad (2.39)$$

At first, it is assumed that strain increment was a pure elastic strain. This assumption is used to calculate a trial value of yield function  $F_{n+1}^{trial}$  as:

$$\sigma_{n+1}^{trial} = E(\varepsilon_{n+1} - \varepsilon_n^{pl}) \quad (2.40)$$

$$\varepsilon_{n+1}^{pl\ trial} = \varepsilon_n^{pl} \quad (2.41)$$

$$\bar{\varepsilon}_{n+1}^{pl\ trial} = \bar{\varepsilon}_n^{pl} \quad (2.42)$$

$$F_{n+1}^{trial} = |\sigma_{n+1}^{trial}| - \sigma_y(\bar{\varepsilon}_n^{pl}) \quad (2.43)$$

Note that for perfectly plastic material the value of yield stress  $\sigma_y$  is equal to initial yield stress but it is a function of plastic strain for linear hardening and Ramberg-Osgood hardening law which must be calculated.

If the  $F_{n+1}^{trial} \leq 0$ ; this would mean that the new strain increment  $\Delta\varepsilon$  was elastic. And the trial values calculated in Eqn. (2.40)-(2.43) are correct.

If the  $F_{n+1}^{trial} > 0$ ; this would mean that the new strain increment  $\Delta\varepsilon$  was not pure elastic. And the trial values calculated in Eqn. (2.40)-(2.43) are not correct. In this case the amount of plastic strain  $\Delta\gamma$  in the strain increment  $\Delta\varepsilon$  must be recalculated until  $F_{n+1} = 0$ .

$$F_{n+1} = |\sigma_{n+1}^{trial}| - \sigma_y(\bar{\varepsilon}_{n+1}^{pl}) - \Delta\gamma E = 0 \quad (2.44)$$

$\Delta\gamma$  is called consistency parameter because with its calculation the condition  $F_{n+1} = 0$  is fulfilled. A graphical representation of Eqn. (2.44) is shown in Figure 2.17.

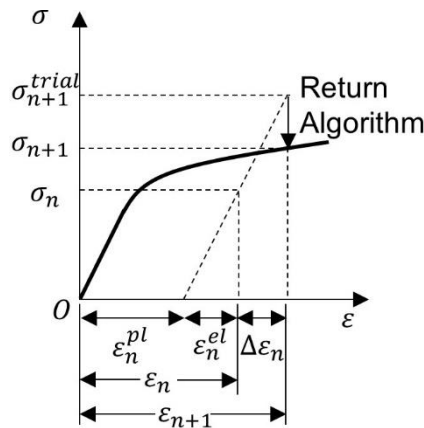


Figure 2.17 Illustration of return algorithm of plasticity [41]

The Eqn. (2.44) can be rewritten in the following form:

$$F_{n+1} = F_{n+1}^{trial} - \Delta\gamma E - \sigma_y(\bar{\varepsilon}_{n+1}^{pl}) + \sigma_y(\bar{\varepsilon}_n^{pl}) = 0 \quad (2.45)$$

For a perfect plasticity with no hardening, the Eqn. (2.45) can be solved by inserting  $\sigma_y(\bar{\varepsilon}_{n+1}^{pl}) = \sigma_y(\bar{\varepsilon}_n^{pl}) = \sigma_{y0}$  with results:

$$\Delta\gamma = \frac{F_{n+1}^{trial}}{E} \quad (2.46)$$

Similarly for linear hardening law, the Eqn. (2.45) can be solved by inserting  $\sigma_y(\bar{\varepsilon}_{n+1}^{pl}) = \sigma_{y0} + K(\bar{\varepsilon}_{n+1}^{pl})$ ;  $\sigma_y(\bar{\varepsilon}_n^{pl}) = \sigma_{y0} + K(\bar{\varepsilon}_n^{pl})$  and  $\Delta\gamma = \bar{\varepsilon}_{n+1}^{pl} - \bar{\varepsilon}_n^{pl}$  which results in:

$$\Delta\gamma = \frac{F_{n+1}^{trial}}{E + K} \quad (2.47)$$

However for Ramberg-Osgood hardening law, plugging in the yield stress into Eqn. (2.45) gives:

$$F_{n+1} = F_{n+1}^{trial} - \Delta\gamma E - K(\bar{\varepsilon}_{n+1}^{pl})^p + K(\bar{\varepsilon}_n^{pl})^p = 0 \quad (2.48)$$

The Eqn. (2.48) cannot be solved for  $\Delta\gamma$  analytically because  $\Delta\gamma = \bar{\varepsilon}_{n+1}^{pl} - \bar{\varepsilon}_n^{pl}$  and  $\bar{\varepsilon}_{n+1}^{pl}$  is not known. Therefore, iterative numerical method "Newton Raphson Method" is used for solution.

For newton Raphson method, an initial guess value of  $\Delta\gamma$  for iteration number  $j = 0$  is set. e.g.  $\Delta\gamma_0 = \Delta\varepsilon/2$  and by plugging in the guess value in Eqn. (2.48), the error value is found. Then an improved guess value with iteration number  $j = 1$ , the value of  $\Delta\gamma_1$  is determined by:

$$\Delta\gamma_{j+1} = \Delta\gamma_j - \frac{F_{n+1}(\Delta\gamma_j)}{F'_{n+1}(\Delta\gamma_j)} \quad (2.49)$$

The iterations continue unless the Eqn. (2.48) is satisfied or a minimum tolerance value is achieved.

With the values of  $\Delta\gamma$  calculated, the values of  $\{\sigma_{n+1}, \varepsilon_{n+1}^{pl}, \bar{\varepsilon}_{n+1}^{pl}\}$  are calculated as:

$$\sigma_{n+1} = \sigma_{n+1}^{trial} - \Delta\gamma E \text{ sign}(\sigma_{n+1}^{trial}) \quad (2.50)$$

$$\varepsilon_{n+1}^{pl} = \varepsilon_n^{pl} + \Delta\gamma \text{ sign}(\sigma_{n+1}^{trial}) \quad (2.51)$$

$$\bar{\varepsilon}_{n+1}^{pl} = \bar{\varepsilon}_n^{pl} + \Delta\gamma \quad (2.52)$$

The *sign* function return -1 if the value of  $\sigma_{n+1}^{trial}$  is negative, and +1 if the value of  $\sigma_{n+1}^{trial}$  is positive.

### 3 Experimental material testing

In this chapter testing methodology and results of in-plane material properties are discussed. The tests results were used as input to the material models in crash simulations. This enabled to identify the discrepancies in state of the art material models and make improvements in it.

#### 3.1 Material

In this study, the Tepex® dynalite 102-RG600(4)/47% material was investigated. This is a woven fabric thermoplastic composite material also known as an organo-sheet. The fabric is made of roving glass and the matrix material is a PA6 polymer. The weaving of the fabric is in a twill form with an equal weight percentage of fibers along the warp and weft, making the longitudinal and transverse mechanical and thermal properties almost equal (see Figure 3.1).

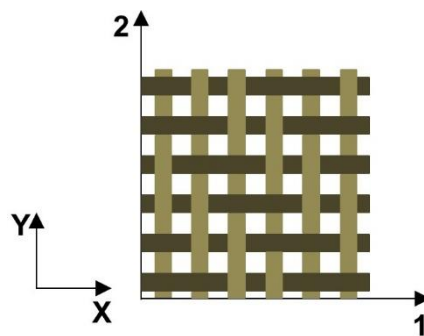


Figure 3.1 Schematic illustration of twill fabric, reinforced composite material with fibers of twill woven fabric. Direction of fibers is denoted by directions 1 and 2 also known as Local/material coordinates with reference to the global XY Cartesian coordinates system

The material has a high specific strength and stiffness along the predefined direction, combined with a high toughness and fatigue resistance. It is delivered in the form of sheets and can be thermoformed, making it feasible for mass production and rendering it cost-effective. Combining it with short or long fiber-reinforced plastic of the same type in the form of ribs/force transmission elements offers excellent lightweight potential. Some basic mechanical and thermal material properties are given in Table 3-1.

Laminate density [g/cm <sup>3</sup> ]	Fiber content [% vol.]	Ply thickness [mm]	Fabric area weight [g/m <sup>2</sup> ]	Linear density of yarn [Tex]	Melting temp. [° C]	Glass transition temp. [° C]
1.8	47	0.5	600	1200	220	60

Table 3-1 Material data of a ply of Tepex® dynalite 102-RG600/47% [11]

Hereafter, this material will be referred to as 102-RG600(x) where (x) is the number of plies. e.g. the laminate of 4 plies having thickness of 2 mm will be written as 102-RG600(4).

#### 3.2 Tensile test

Tensile tests were conducted according to ISO-527/4 [43] on a rectangular specimen with fibers aligned along the direction of loading with gauge length of 150mm x 25mm x 2mm.

### 3.2.1 Test specimen

Dog-bone shape specimen for tensile testing of woven fabric composites cannot be used because it does not break within the gauge length. Figure 3.2 shows failure of a dog-bone shape specimen in radius region under tensile loading. A static simulation of tensile loading of dog-bone shape specimen with linear elastic material parameters is also shown. The warp fibers of the specimen were aligned along the x-axis. So the material coordinates 12 and global coordinates XY are the same. Tensile loading was applied along the x-axis and simulation results show that shear stresses are produced in the radius region. Due to the presence of shear stresses along with tensile stresses the strength of material reduces significantly (see Chapter 7). Therefore, all the dog-bone shape specimen failed in radius region. Photos of more specimens are given in Annex 12.2.1.

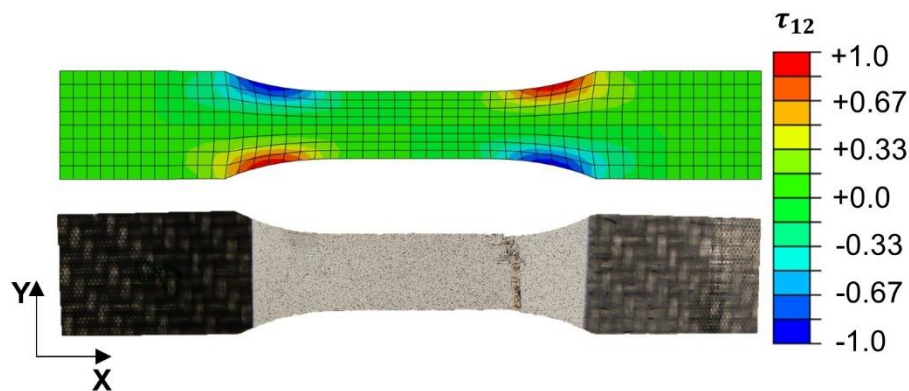


Figure 3.2 A dog-bone shape specimen failure under tensile loading outside gauge length due to shear stresses in radius region. Simulation results showing presence of shear stresses in radius region of the specimen. The legend shows normalized shear stress  $\frac{\tau_{12}}{\max(\tau_{12})}$

To get the fracture within gauge length, rectangular specimens were used. Because of high strength of composites materials, rectangular specimen must be clamped between jaws firmly. These clamping produce through-thickness stresses in material which causes the specimen to break in the grips. To lower the through-thickness stress, one possibility could be to increase the friction between the grips and specimen by roughing the specimen through sanding. With increased friction, less grip force is required to pull the specimen. But roughing the surface of material with sand paper can damage the fibers which again lead to specimen breakage in grips. So solution to this problem is use of end tabs which are glued to specimen and jaw clamps can bite into the end tab material. The end tabs transfer the forces to the material through glued material.

The specimens had dimensions of 250 mm x 25 mm x 2 mm with fiber aligned along the specimen length. Cutting organo-sheets with conventional machining processes causes delamination and damage at the edges. However, this damage was avoided with water jet cutting the specimens. Thus, all specimens were cut in the production direction with a water jet cutting machine. End tabs were also cut from the same material i.e. 102-RG600(3) with dimensions of 50 mm x 25 mm x 1.5 mm and fibers aligned at  $\pm 45^\circ$  (see Figure 3.3). Four end tabs were glued, one on each end of the specimen, with Cyanoacrylate-based glue Sicomet-77 manufactured by Henkel Germany. To glue the specimens, their surfaces and end tabs were roughened with sand paper with a grit size of P240. Then, the surfaces were washed with water to remove any remaining particles and dried. Following

this, the tabs were glued precisely and compressed in a vise so that extra glue flow outside and an even surface of glue were present between the specimen and the tabs.



Figure 3.3 Tensile test specimen with four end tabs glued. Rovings of the glass fabric are also visible indicating the direction of material

### 3.2.2 Test procedure

Tests were carried out at universal material testing machine Zwick Z100 manufactured by Zwick/Roell. It is an electromechanical controlled machine and has a testing speed range from 0.1  $\mu\text{m}/\text{min}$  to 1.5  $\text{m}/\text{min}$ . It is equipped with a piezoelectric force transducer, which can measure forces up to 100 kN in tension and compression. The strain was measured with an optical strain measuring system: ARAMIS (supplied by GOM, Germany). It is a non-contact digital image correlation (DIC) technique which uses 3D camera system to create digital camera images to measure the strain on the surface of material. Measuring strain with the ARAMIS require spraying the surface of specimen with black and white stochastic spray which was done manually. Zwick Z100 and Aramis 5M camera system were connected through a BNC cable which sent 5V TTL signal at start of test for synchronization of force and deformation measurement. Test were carried out at speed of 2  $\text{mm}/\text{min}$ . Both left and right camera took images at rate of 1 frame/second. The tensile test setup is shown in Figure 3.4.

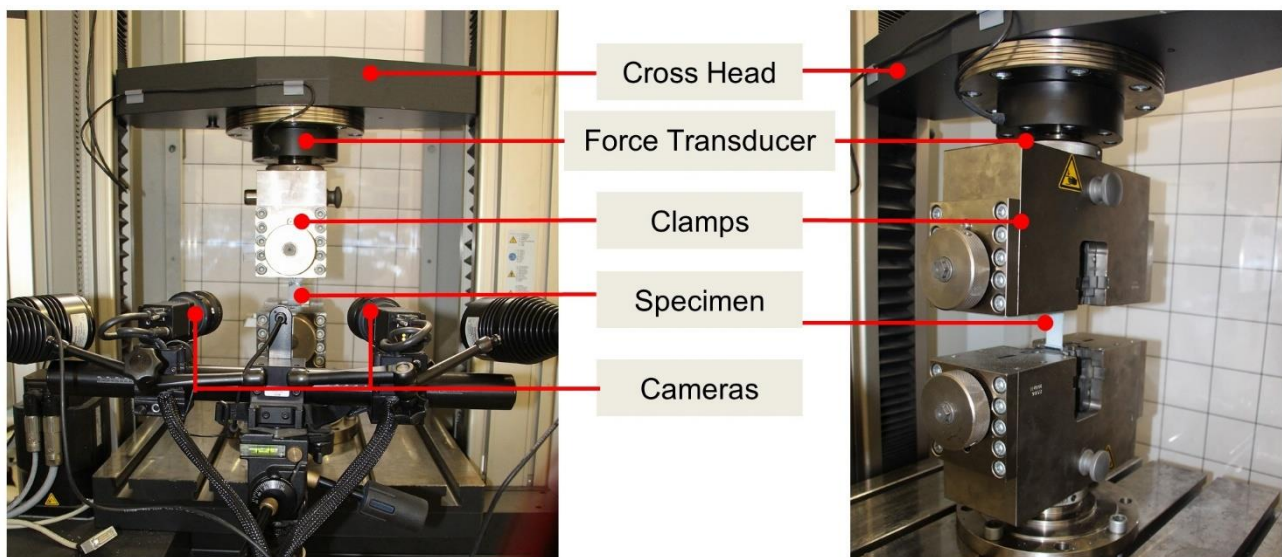


Figure 3.4 Tensile testing setup showing specimen clamped in Zwick Z100 and camera system for strain measurement

At the end of test, force data measured by Z100 was imported into ARAMIS software and synchronized with the images.

### 3.2.3 Results

The strain on the surface of material was calculated in ARAMIS software (see Figure 3.5). The measured strain was not homogenous because on the visible fiber roving was different than matrix material. So an average of the all measured strain was calculated and used for results calculation shown in Table 3-2 and Figure 3.6. For the purpose of use in FEM analysis, the data is shown as true stress strain plot. The true stress is calculated as applied load divided by actual cross-sectional area and true strain is the natural log of current length over original length.

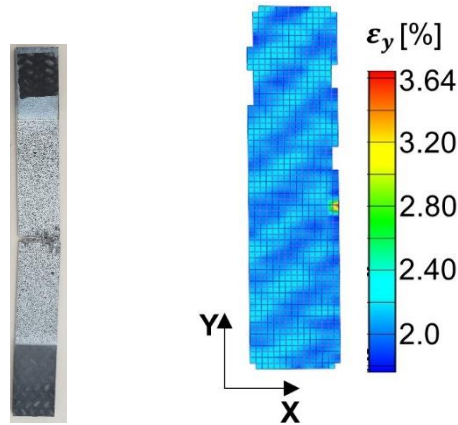


Figure 3.5 Tensile test specimen after test and strain measurement in ARAMIS at 2%

Sr. no.	Thickness [mm]	Width [mm]	E-modulus [GPa]	Poisson's ratio [-]	Tensile strength [MPa]	Failure strain [%]
1	1.96	24.88	19.14	0.057	411.24	2.09
2	1.96	24.89	18.69	0.051	409.2	2.13
3	1.98	24.92	18.73	0.041	374.5	1.95
4	1.95	24.87	18.90	0.05	387.33	1.98
5	1.97	24.83	16.95	0.052	379.65	1.97
Average	1.96	24.878	18.48	0.0502	392.38	2.02
Standard deviation			0.874	0.0058	16.93	0.08
Co-efficient of variance (%)			4.73	11.56	4.31	3.95

Table 3-2 Tensile test results of 102-RG600(4)

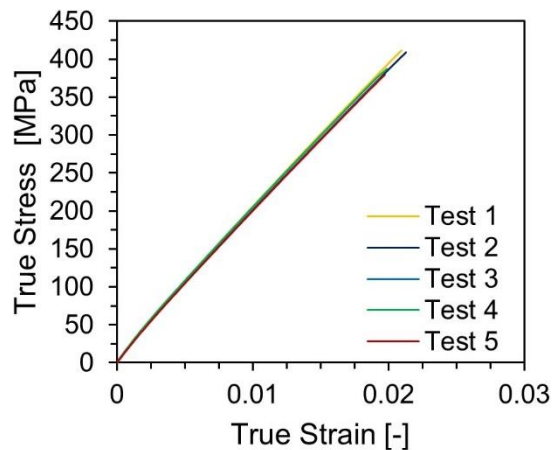


Figure 3.6 Tensile test results of 102-RG600(4)

The results show a perfect linear elastic brittle behavior. A load reversal will show that no plasticity is induced in the material. Photos of more test specimens are shown in Annex 12.2.1.

### 3.3 Compression test

It has been learned from experience that compressive testing using shear type loading, as in Calansee type [44] fixture, result in slipping of specimen in fixture. Therefore compressive tests were conducted using the combined loading compression (CLC) fixture according to ASTM D6641 [45]. In this test method, the specimen is clamped from the sides to apply frictional force much like tensile loading. This frictional loading is combined with end loading from the top of the specimen so that the ends of specimen did fail while maintaining the through thickness stress minimum.

#### 3.3.1 Test specimen

Compression test require specimen gauge length and thickness such that no buckling occurs under compression. To avoid Euler buckling of specimens, following formula is used to calculate the gauge length according to [45]:

$$h \geq \frac{L}{0.9069 \sqrt{\left(1 - \frac{1.2\sigma_c}{G_{13}}\right) \left(\frac{E_c}{\sigma_c}\right)}} \quad (3.1)$$

Here  $\sigma_c$ ,  $E_c$  and  $G_{13}$  are compressive strength, compressive E-modulus and through-thickness shear modulus respectively.  $L$  is gauge length and  $h$  is thickness of specimen. In order to calculate specimen size and thickness. the values of compressive strength and E-modulus were assumed to be equal to tensile strength and tensile E-modulus.

Preliminary tests were carried out with gauge length and thickness calculated from initial guess of values. Specimen thickness of 2 mm resulted in significant buckling but the test results were helpful in selection of new specimen dimensions for compression testing.

Finally, compressive specimens were cut from a 4mm thick panel with dimensions of 146mmx25mm corresponding to gauge length of 18mm.

#### 3.3.2 Test procedure

Compression tests were carried out on Zwick Z100. The design of CLC fixture was modified to be able to measure the strain using Digital Image Correlation system. 3D model and fixture photos are shown in Figure 3.7 and Figure 3.8. Detailed 3D drawing of fixture can be found in Annex 12.3.1.

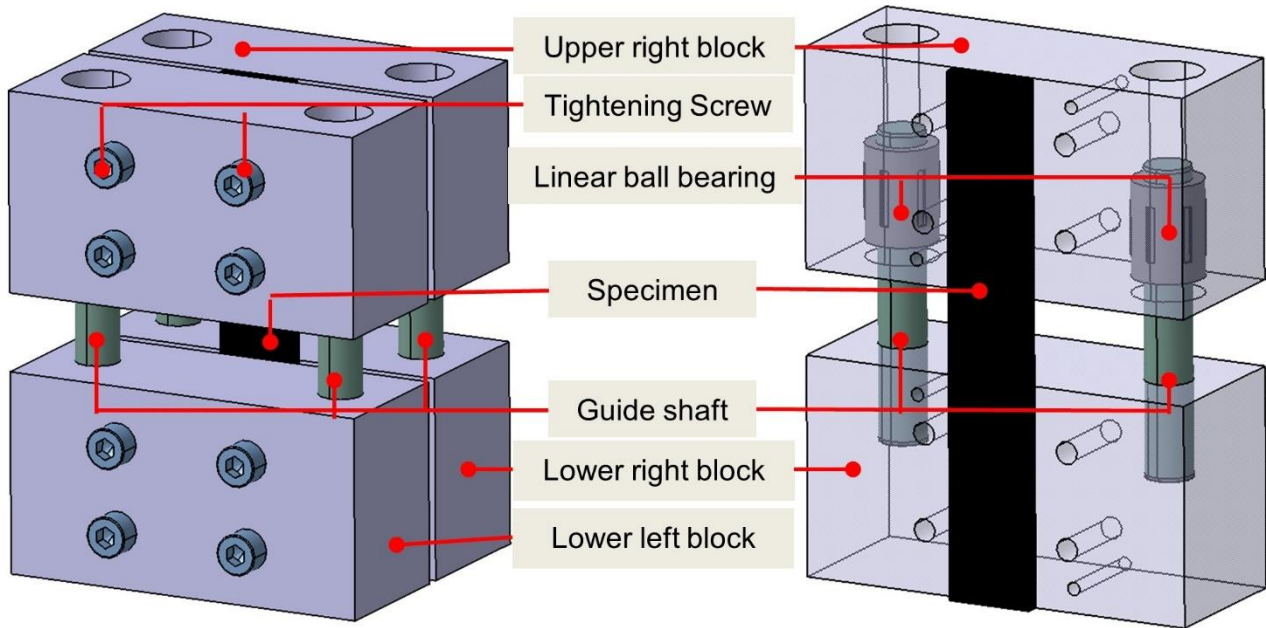


Figure 3.7 CAD Model of modified combined loading compression fixture

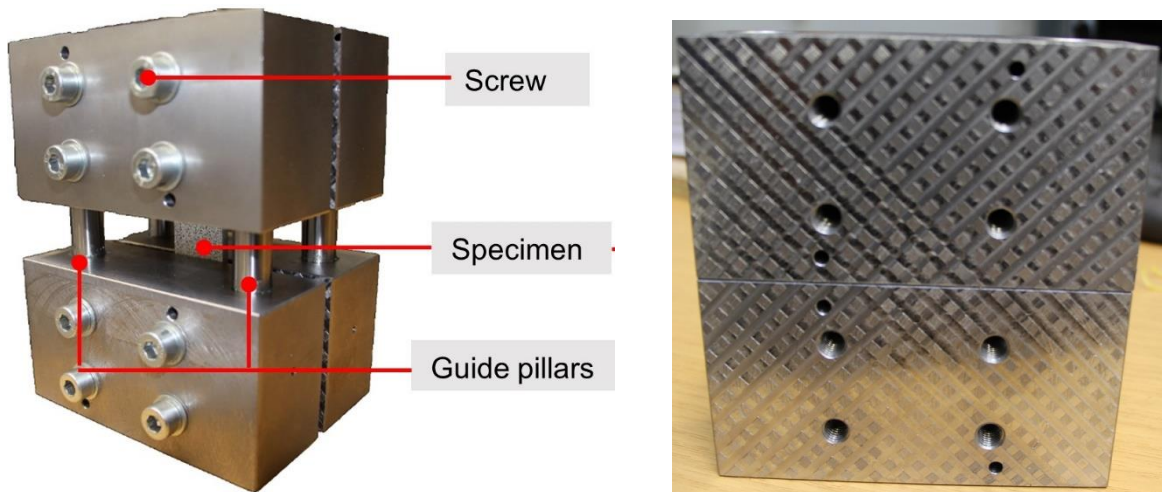


Figure 3.8 Modified combined loading compression fixture during test (left) and clamping surface (right)

This fixture had four blocks and the specimen was held between the pair of lower and upper blocks with the help of screws. The original design of CLC fixture in ASTM D6641 [45] had only two guide pillars i.e., one guide pillar in middle of left pair of blocks and one in the right. The purpose of the guide pillars is alignment between lower and upper blocks. These guide pillars are press-fit in the lower blocks and friction-free movement is made possible by the use of the linear ball bearings in the upper blocks. The presence of guide pillars in the middle of blocks restricted the view of specimen for ARAMIS camera. Therefore, four guide pillars (two guide pillars through each block) were used and positioned away from the middle. This modification provided enough space for ARAMIS cameras to measure strain on the surface of specimen. The test specimen was fixed in the fixture with eight screws tightened at 10 Nm with a torque gauge. The upper and lower ends of the specimens were made even with the blocks so that the compression load was applied through the machine head, combined with shear forces due to friction between the specimen and the fixture blocks. The screws

were tightened with help of torque gauge in a diagonal order so that specimen is tightened evenly inside clamping blocks. The length of specimen which exceeds the height of lower and upper blocks is equal to the gauge length.

The specimens for CLC testing do not require end tabs to be glued because failure inside gauge length can be achieved without end tabs. In addition, using end tabs results in an uneven surface at upper and lower ends of specimens which makes end loading impossible. The surface of gauge length was sprayed with stochastic black and white spray to measure strain. As it can be seen in Figure 3.7 and Figure 3.8 that there is enough room for camera system to take images of specimen during the test.

Test were conducted t at a speed of 1 mm/min until the specimen failed.

### 3.3.3 Results

The measured strain on the surface of material was averaged over the whole surface and shown in Figure 3.9. More specimen photos are shown in Annex 12.2.2. The test results are summarized in Table 3-3 and Figure 3.10.

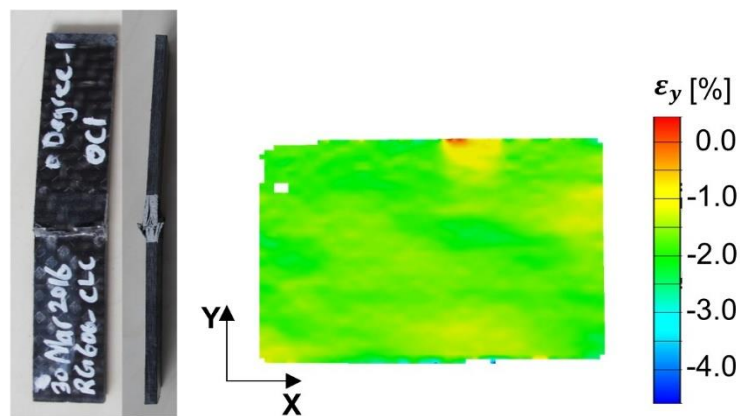


Figure 3.9 Compression test specimen after test and strain measurement in ARAMIS at compressive strain of ca. 1.7 %

Sr. no.	Thickness [mm]	Width [mm]	E-modulus [GPa]	Poisson's ratio [-]	Compressive strength [MPa]	Failure strain [%]
1	4.1	25.03	18.00	0.068	314.9	1.81
2	4.12	25.03	18.86	0.077	332.51	1.94
3	4.12	25.07	18.75	0.083	257.72	1.45
4	4.1	25.09	18.93	0.072	308.15	1.72
5	4.1	25.11	19.48	0.083	331.91	1.66
Average	4.11	25.01	18.81	0.0766	309.04	1.72
Standard deviation			0.531	0.0066	30.58	0.181
Co-efficient of variance (%)			2.83	8.69	9.90	10.53

Table 3-3 Compression test results of 102-RG600(8)

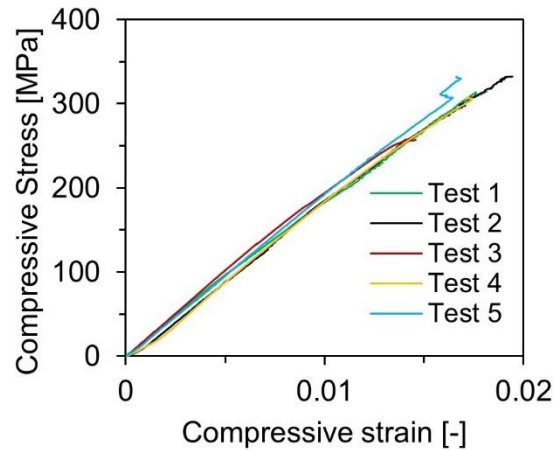


Figure 3.10 Compressive true stress strain plot of 102-RG600(8)

The results show a linear elastic compressive response of 102-RG600. The compression stress-strain results are not as linear as for those of tensile tests because of the buckling instability due to small geometrical imperfections or external perturbation loads. Testing a 4mm thick specimen with gauge length of 18mm produces acceptable results.

It is worth mentioning here that tests were also carried out with

- 2mm thick specimen with 13mm gauge length and
- 4mm thick specimen with 25mm gauge length

However, with thinner specimens and with longer gauge length, the bending of specimen cannot be prevented and stress strain plot are not linear.

### 3.4 Shear test

Shear tests was conducted according to ISO 14129 [46]. This test resembles standard tensile testing except that fibers are oriented at  $\pm 45^\circ$  from the direction of loading so it is called tensile shear test. The ease of the test and the requirement of no special fixture makes it the preferred method for measuring the shear properties of composite materials. Using this method, normal tensile stresses are also present in the material in addition to the shear stress during the testing. A complex stress state exists close to the free edges of the specimen. The resulting failure stress is not an exact representation of pure shear response. Although this test method is not recommended for shear response evaluation beyond 5% shear strain due to fiber rotations, with consideration for crash testing it is necessary to continue loading until failure occurs.

The specimen had a gauge length of 150 mm. End tabs measuring 50 mm x 25 mm x 1.5 mm with a fiber orientation of  $\pm 45^\circ$  angle were glued with fast-curing adhesive Sicomet-77 after roughening the surface. The test specimen is shown in Figure 3.11.

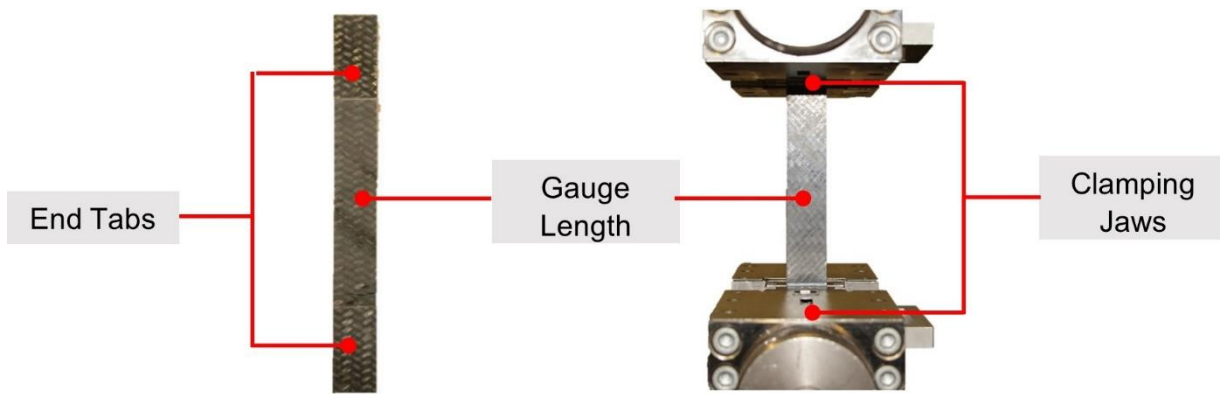


Figure 3.11 Tensile shear test

A stochastic pattern with black and white paint was used for DIC strain measurement. Tests were carried out at the speed of 2 mm/min and strain was measured optically in both the X and Y directions.

### 3.4.1 Test results

At the end, shear stress and shear strain were calculated as follows:

$$\tau_{12} = \frac{\sigma_y}{2} = \frac{F}{2bh} \quad (3.2)$$

$$\gamma_{12} = \varepsilon_y - \varepsilon_x \quad (3.3)$$

$F$ : Force applied to the specimen

$b$ : Width of the specimen

$h$ : Thickness of the specimen

$\varepsilon_y$ : Longitudinal normal strain

$\varepsilon_x$ : Transverse normal strain

Note that the expression given in Eqn. (3.2) and (3.3) can also be obtained by plugging in  $\theta = 45^\circ$  in Eqn. (2.18) and (2.21) respectively. Because the applied load was applied in y-direction only so  $\sigma_x = \tau_{xy} = 0$ . Although the fibers were aligned at  $45^\circ$  from the direction of loading, the laminate was still balanced due to the equal number of fibers in the  $+\theta$  and  $-\theta$  directions; theoretically global shear strain  $\gamma_{xy} = 0$ .

Since strains were only measured on the visible surface, for the test evaluation average value of the strain over the whole surface was calculated. Measured surface strain and shear stress-strain results are shown in Figure 3.12 and Figure 3.13.

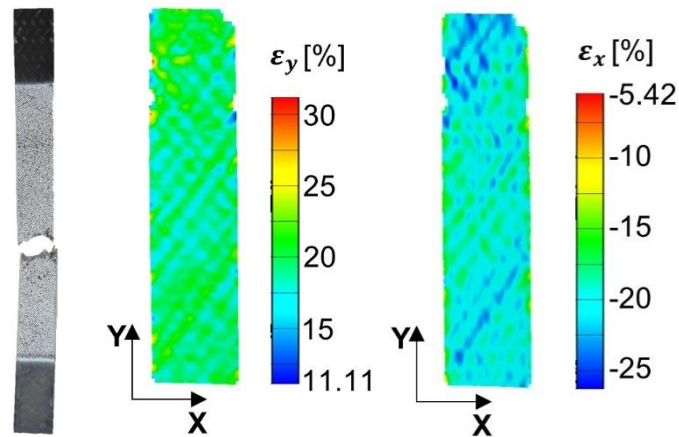


Figure 3.12 Specimen after test and longitudinal, transverse strain measured optically corresponding to 40% shear strain

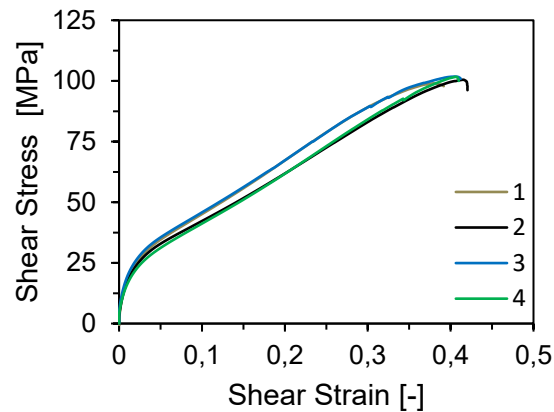


Figure 3.13 Shear Stress Strain plot of 102-RG600(4)

### 3.4.2 Cyclic shear test

It can be seen from the shear stress-strain plot in Figure 3.13 that the shear response of the material entered into a non-linear region at a shear strain  $>5\%$ . Such tests where no reversal of loading is applied are called monotonic test. To quantify the plastic deformation and stiffness reduction due to damage, monotonic tests were not sufficient [47], [48]. For this purpose, cyclic tests were carried out with the same geometry and setup. In cyclic loading, a force of 1000 N was applied in first cycle and force level was increased by 1000 N in every successive loading/unloading cycle. The test continued until the specimen could no longer take load and broke. Force-curve over the time for tests at rate of 2 mm/min and shear response of cyclic tests is shown in Figure 3.14.

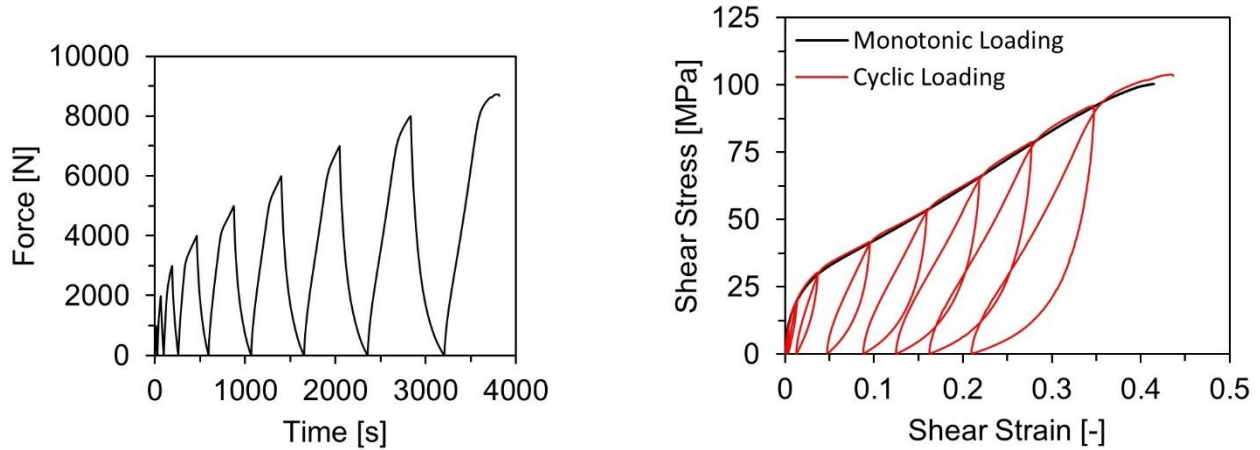


Figure 3.14 Force curve of cyclic loading/unloading test at speed of 2 mm/min (left) and cyclic shear test compared with monotonically loaded test at speed of 2 mm/min (right)

As shown in Figure 3.14, the cyclic response is similar to the quasi-static response in terms of shear stiffness, shear strength and failure shear strain. Detailed results are summarized in Table 3-4.

Sr. no.	Thickness [mm]	Width [mm]	Shear chord modulus [GPa]	Shear strength [MPa]	Failure shear strain [-]
1	2	24.82	1.83	98.99	0.39
2	2	24.81	1.63	100.49	0.42
3	2	24.84	1.67	101.80	0.41
4	2	25.06	1.46	101.66	0.41
Cyclic	2.03	24.83	2.41	103.78	0.43
Average	2.0	24.87	1.85	100.98	0.41
Standard deviation			0.36	1.81	0.016
Co-efficient of variance [%]			20.29	1.79	3.97

Table 3-4 Shear stress strain results from monotonic and cyclic shear tests

In Table 3-4, it can be seen the cyclic shear results match with monotonic results except shear chord modulus. The reason is that shear response of 102-RG600 is highly non-linear and in cyclic testing, shear modulus is measured from the first loading/unloading cycle. And the number of data points used to measure shear modulus in monotonic tests results are spread over more shear strain range which makes the difference in calculated results.

Two important things can be seen directly from the results shown in Figure 3.14. The first is that with each loading/unloading cycle, the amount of inelastic strain  $\gamma_{12}^{pl} = 2\varepsilon_{12}^{pl}$  increased; this was plastic deformation. The second is that the average slope of loading and unloading in every cycle decreased with each higher cycle. Ignoring the hysteresis, a simplified illustration is shown in the Figure 3.15.

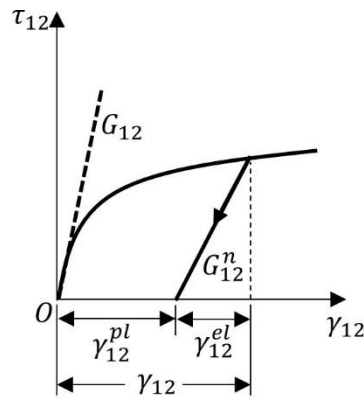


Figure 3.15 Schematic illustration of plasticity and stiffness degradation in cyclic shear testing

This stiffness degradation is termed as damage  $d_{12}$ , which is a phenomenological parameter to quantify the reduction in slope of shear modulus [47], [49], [50]. If the shear elastic modulus in the first cycle was  $G_{12}$ , corresponding to undamaged material reduced to  $G_{12}^n$  in the  $n^{\text{th}}$  cycle, then the shear damage can be calculated as [47], [49], [50]:

$$d_{12} = 1 - \frac{G_{12}^n}{G_{12}} \quad (3.4)$$

Having calculated the damage, a graphical representation of damage with respect to stress can be made as shown in Figure 3.16. A shear hardening curve from measured data is also shown.

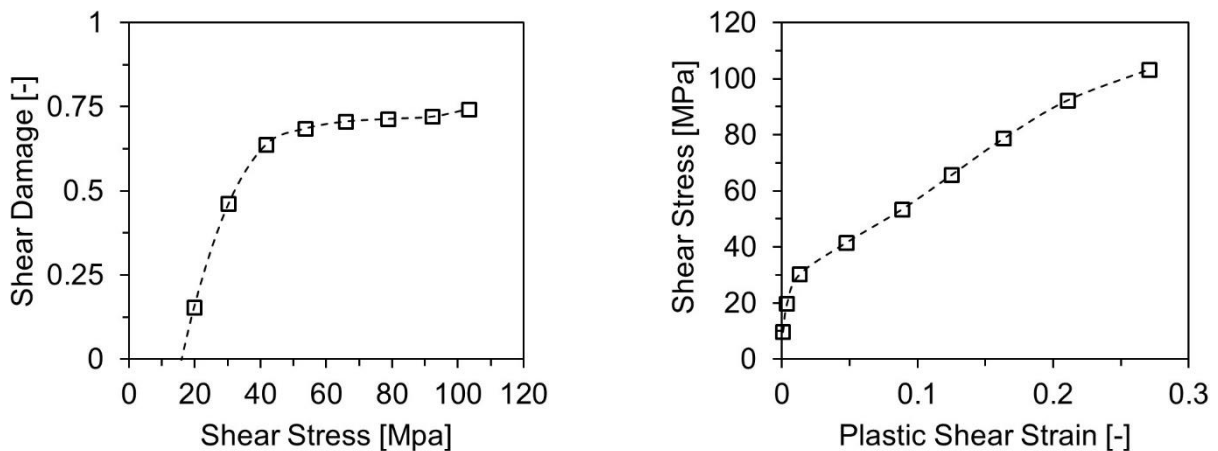


Figure 3.16 Shear damage as function of shear stress and shear hardening curve measured from cyclic shear testing

Keeping in view the results shown in Figure 3.16 it can be seen that a non-linear function to describe the damage shear as function of shear stress is needed. Further, Ramberg-Osgood equation (see Chapter 2.8) can be used for shear hardening of 102-RG600.

### 3.5 Intra-laminar fracture energy

Intra-laminar fracture energy per unit area  $G_f$  is a material property. It is the concept of fracture mechanics and is also referred to as critical strain energy release rate which is the energy absorbed

by the material per unit area of crack. A high value of  $G_f$  means that it is hard to propagate crack in that material and vice-versa. The use of intra-laminar fracture energy in material modeling for crash simulations is explained in Chapter 4.

The intra-laminar fracture energy  $G_f$  was determined for tension and compression. There are no standards yet available for measuring critical fracture energy release rate of composite materials. A method proposed by Pinho [51] was used in this work to measure fracture energy in tension and compression. The compact tension (CT) and compact compression (CC) specimens were used to measure fracture energy release rate in tension and compression respectively. Specimen geometry and dimensions are shown in Figure 3.17.

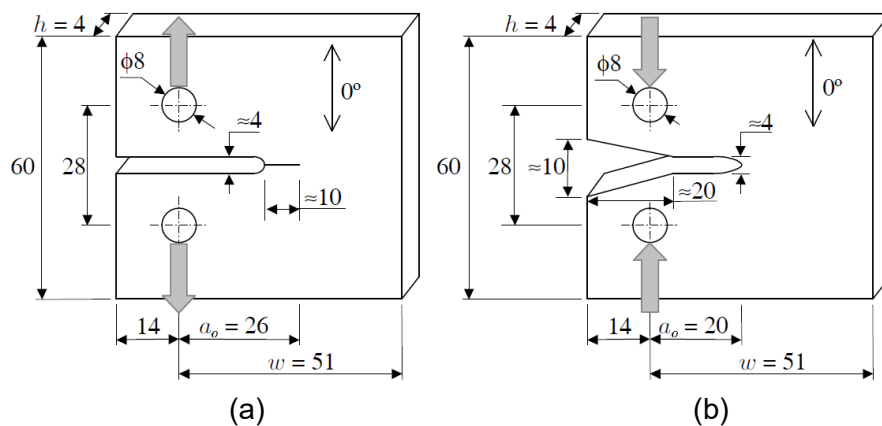


Figure 3.17 Intra-laminar fracture energy test specimen (a) compact tension for tensile critical fracture energy, (b) compact compression for compression critical fracture energy [51]

Specimens shown in Figure 3.17 feature two holes and a crack. The holes are there for applying load to the specimen using a clevis. When the tensile/compression loading is applied, stress concentration is produced at the end of crack called “crack front”. When the applied load is high enough that crack propagates, the energy absorbed by the specimen is calculated which is the critical fracture energy per unit area.

There is no analytical method available which can directly relate applied force to the energy absorbed by material in compact tension or compact compression. So the specimen was modelled in Abaqus with lamina thickness of 1 mm and ply elastic material properties were assigned to it. Then 1 N force was applied at the holes and J-integral was calculated in Abaqus. J-integral is a method of measuring the strain energy release rate. It is measured along a path completely enclosing the crack-tip/crack-front. Because J-integral is independent of path over which this value is calculated, a number of integrals can be calculated and all of the values should theoretically be equal. Therefore, if the strain energy release rate (J-integral) for 1 N force on 1 mm thick lamina is known, then strain energy release rate for any thickness and force can be calculated according to Eqn. (3.7). If the force is the critical force  $P$ , at which crack propagated, then it corresponds to the critical strain energy release rate or fracture energy per unit area  $G_f$  [51].

To summarize the above discussion, measuring intra-laminar fracture energy is a two-step process. **First step:** The J-integral around the crack front for a unit applied force on a unit thick laminate can be measured by modeling the specimens in Abaqus. A normalized fracture energy release rate value was obtained as [51].

$$f(a) = J \cdot \left( \frac{1\text{mm}}{1N} \right)^2 \quad (3.5)$$

This value was extracted for different values of crack length  $a$ . For each crack length  $a$ , a new specimen model is required and a polynomial function of the following form was assumed [51]:

$$f(a) = c_3 a^3 + c_2 a^2 + c_1 a + c_0 \quad (3.6)$$

Once the values of constants  $c_i$  were determined then for any value of force, the fracture energy could be determined.

In second step, force displacement data are experimentally determined by loading the specimen. The force value corresponding to crack propagation at a particular crack length can be recorded. At the end, the fracture energy can be calculated by using [51]:

$$G_f = \left( \frac{P}{h} \right)^2 f(a) \quad (3.7)$$

Where  $P$  is the critical force at which the crack propagated, and  $h$  the thickness of specimen.

Square-hole clevis with pin to load the specimen was used for loading the specimen. For round holes, scatter in results is seen due to variation in contact position of the pin with respect to specimen and clevis hole. With square hole, specimen is always loaded at same position. Friction introduces bending moment in specimen and introduces non-linearity and results in higher fracture toughness. Square holes clevis with hole to pin diameter ratio of 0.04 to minimize friction and scatter of results was used according to the recommendations [52]. Technical drawings of clevis are given in Appendix 12.3.2.

### 3.5.1 Tensile fracture energy

#### **Normalized J-Integral**

CT specimen was modeled using 8-node shell elements S8R5 with bolts as a rigid surface applying 1 N force to a 1 mm thick laminate. 102-RG600, elastic properties were defined with fiber direction 1 and 2 aligned along the global x-axis and y-axis respectively.

Because J-integral was to be calculated for a range of crack length  $a$  from 21 mm to 45 mm. So at first the effect of mesh size and symmetric conditions was investigated. Because the specimen is symmetric so only half of the specimen could be modelled using symmetry conditions. Figure 3.18 shows the model in Abaqus with applied B.C for full as well as symmetric B.C on half model. Figure 3.19 shows the simulation results. Ten J-Integrals were output successively around crack front. Figure 3.20 compares the results of J-integral output from full model with symmetric half model. The mesh size effect on the J-integral output is also compared.

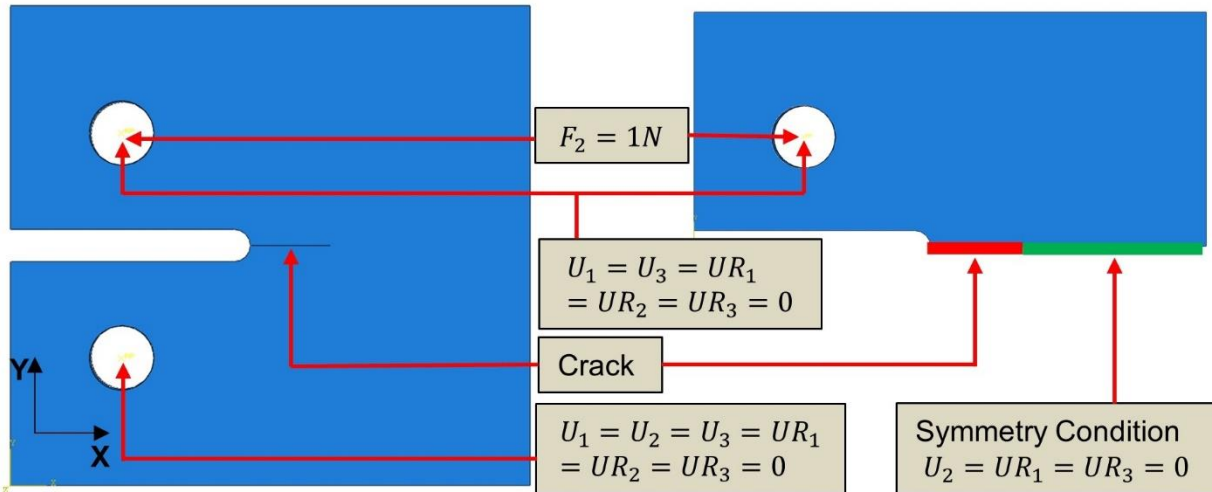


Figure 3.18 Boundary conditions for CT specimen for J-integral evaluation (full model on left and equivalent model with symmetry condition on right)

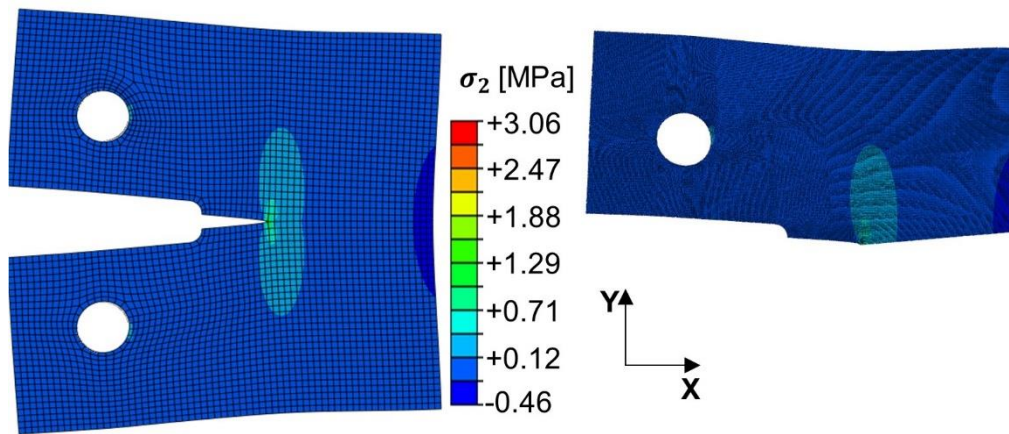


Figure 3.19 Transverse stress in CT specimen full model (left) and equivalent model with symmetry conditions (right)

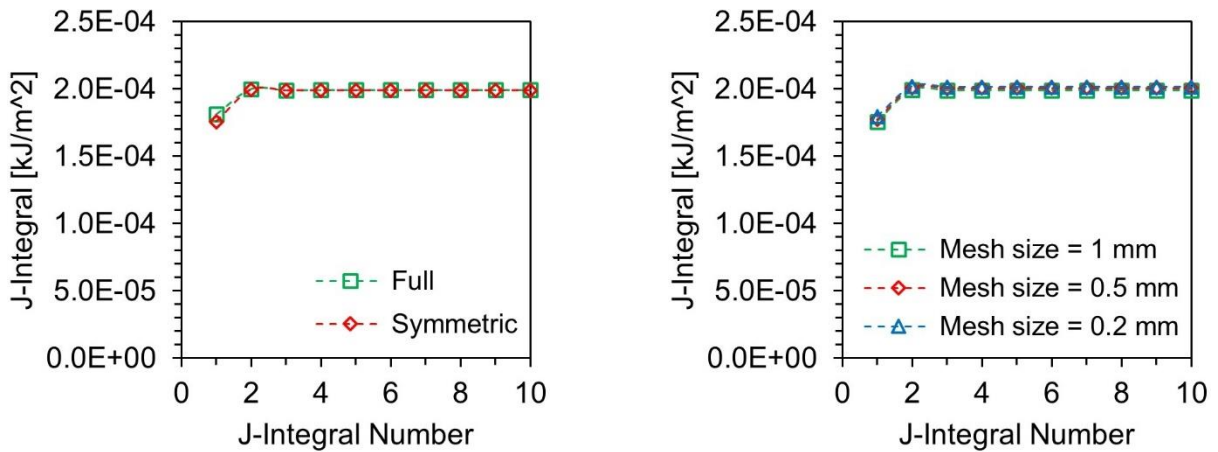


Figure 3.20 Effect of using symmetry (left) and different mesh size (right) on the J-integral output

Figure 3.20 show that using half symmetric border does not affect J-integral output. Similarly using 1 mm mesh size is also acceptable for calculating the J-integral. Therefore, simulations with varying crack lengths were carried out on a symmetric model with a mesh size of 1 mm. An average of 10 J-integrals were calculated, and the results are shown in Figure 3.21.

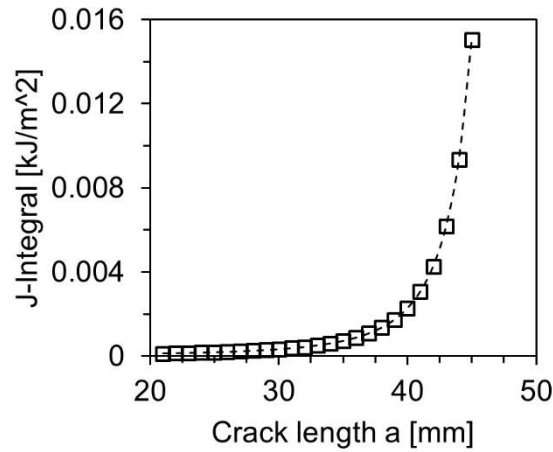


Figure 3.21 J-Integral for different crack lengths

The curve in Figure 3.21 had to be represented as a function  $f(a)$  of polynomial form according to Eqn. (3.6). However, a single polynomial function over the whole range of the crack length values requires a 6<sup>th</sup> order polynomial with 7 constants to be determined. Therefore, a piecewise polynomial function was used with same precision but with 3<sup>rd</sup> order polynomial. This required only four constants to be determined. The values of constants  $c_i$  is given in Table 3-5 and their error in estimating the exact value from Figure 3.21 is given.

	$C_3$	$C_2$	$C_1$	$C_0$	error
$21 \leq a \leq 24$	6.17393E-08	-3.34841E-06	6.99628E-05	4.39468E-04	0.001381177
$24 \leq a \leq 29$	1.40964E-07	-9.25796E-06	2.1696E-04	1.658707E-03	-0.00578683
$29 \leq a \leq 34$	5.92987E-07	-4.94288E-05	1.407886E-03	1.3436336E-02	0.00290498
$34 \leq a \leq 38$	3.00276E-06	-2.98223E-04	9.974215E-03	-0.111799531	0.080615359
$38 \leq a \leq 42$	2.07103E-05	-2.350835E-03	8.9302543E-02	1.133954915	0.212665451
$42 \leq a \leq 45$	2.0835E-04	-2.6237378E-02	1.103023201	-15.47623317	0.401035987

Table 3-5 Polynomial constant for different range of crack length

### Compact tension test

The 102-RG600(8) had to be cut into specimen shape using a water jet cutting machine. However, a sharp crack-front cannot be cut using water jet cutting. The minimum thickness of the cut with water jet machine was 0.8mm. Therefore, the specimens were cut on water jet cutting machine except the crack. 10mm long cut was created using scroll saw which had blade thickness of 0.35mm (see Figure 3.17a). And the crack front was sharpened with a 0.1 mm thin razor blade.

To identify the crack propagation during the test, the specimens were painted with Tipp-Ex water-based white correction fluid from the crack front to the opposite end. Vertical markings were drawn with a marking ruler every 1 mm (see Figure 3.22a).

The specimen were fixed in clevis through the pin and pulled at the speed of 2mm/min. Force deformation data was recorded by Zwick/Roell Z100 (see Figure 3.22b). A high-definition camera with a resolution of 2448 x 2050 pixels was used to take photos at a rate of 1 fps so that crack propagation could be tracked. Since the strain measurement was not needed, the stochastic black and white spray was not applied. After the crack has propagated around 15 mm, the specimens were unloaded.

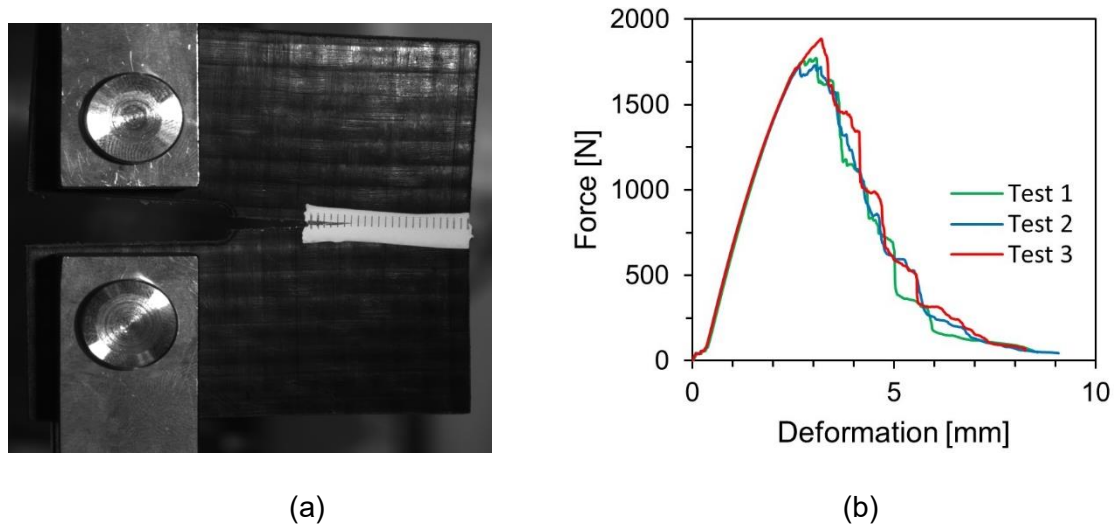


Figure 3.22 (a) Compact tension specimen during test and (b) the force-deformation curve

As the specimen was loaded, the force displacement response was quasi linear. As the crack propagates, the force drops. The crack propagated smoothly over time and therefore it was possible to identify the force value for every mm of crack length. The critical force values, at which the crack propagated were determined via synchronized imaging and force data. The crack lengths were also identified with high-resolution imaging and the 1 mm markings. With the crack length information,  $f(a)$  was calculated using the constants given in Table 3-5. Finally, using Eqn. (3.7) the fracture energy of 102-RG600(8) could be calculated.

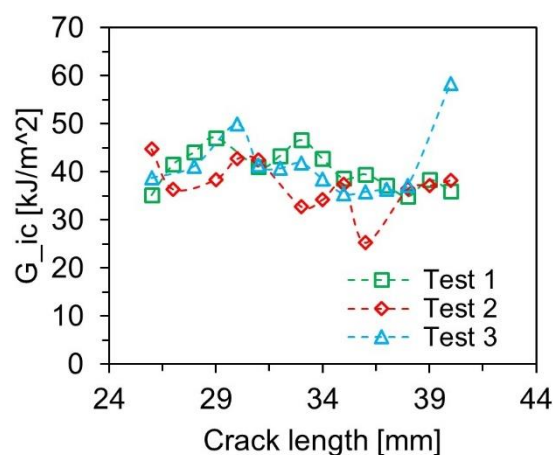


Figure 3.23 Fracture energy values determined by CT testing over crack length. The curve is also known as the R-curve

According to Figure 3.23, the average fracture energy under tension  $G_f^+$  was 39.67 kJ/m<sup>2</sup>. The corresponding standard deviation was 5.4 kJ/m<sup>2</sup>, and coefficient of variance equaled 13.72%.

### 3.5.2 Compression fracture energy

In the first step, only one normalized J-integral value for the compression fracture energy was calculated for a crack length value equal to 20. The reason is that, in contrast to the compact tension, only a limited amount of deformation can be applied before the two clevises come into contact with each other as shown in Figure 3.24. The identification of the crack front after the 1<sup>st</sup> crack propagation under compressive loading was difficult. Therefore, only one value for the compression fracture energy per specimen could be measured.

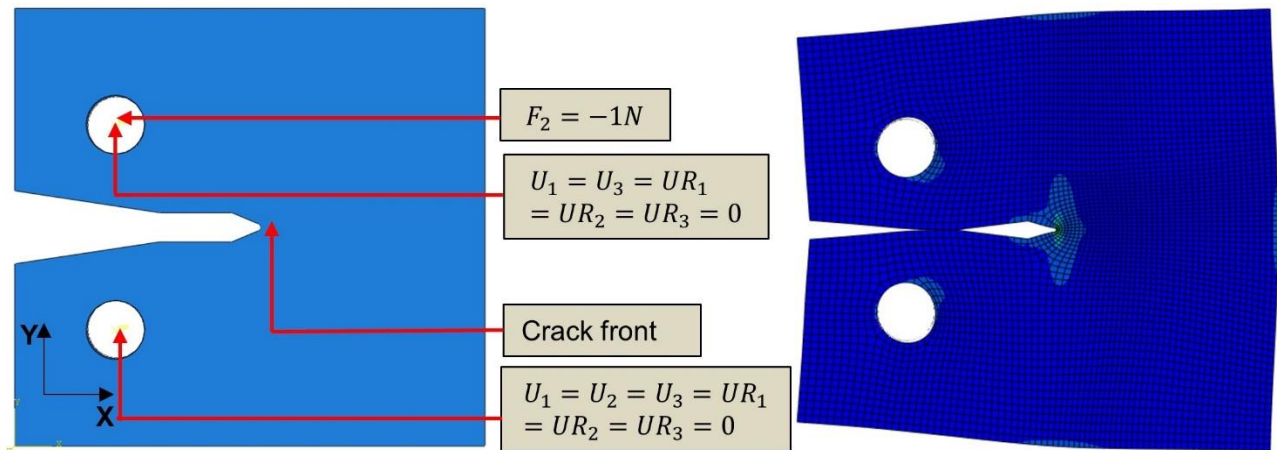


Figure 3.24 CC model for measuring the J-Integral in Abaqus and results (scaled-up deformation)

$$f(a = 20) = 1.2523E - 05 \left[ \frac{m^2}{kJ} \right] \quad (3.8)$$

#### Compact compression test

In the second step, CC specimens were loaded at a speed of 2 mm/min. The maximum deformation allowed was 5 mm, because following this, the two clevises from the top and bottom would come into contact with each other. To visualize the crack propagation, a high-definition camera was using the same setup as for CT. The test setup and force-deformation measurement are given in Figure 3.25.

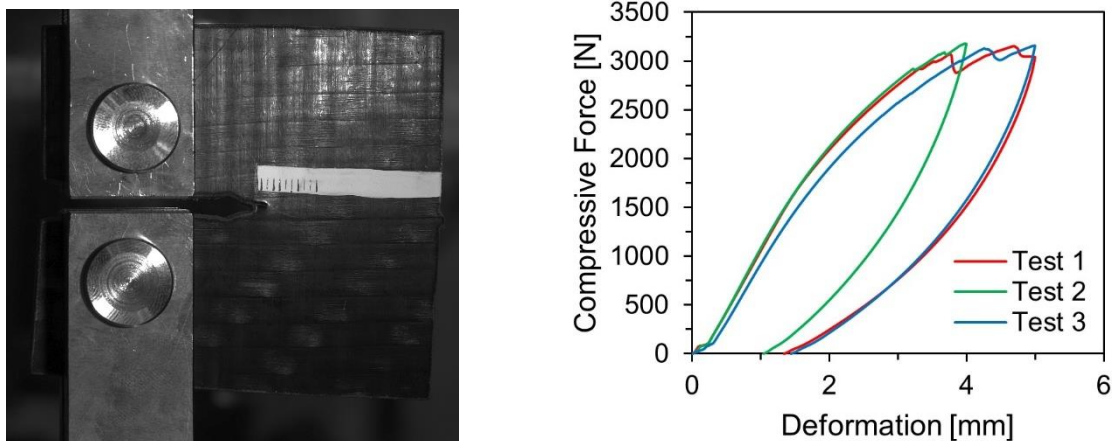


Figure 3.25 CC specimen during test and the force-deformation curve

With the synchronized images, the force value was determined at which kink due to compressive load appeared at the crack front. The force value was used to calculate the compressive fracture energy  $G_f$  according to (3.7). the results are summarized in Table 3-6.

Test no.	Crack length [mm]	Force [N]	f(a) [mm/N]	$G_{IC}$ [ $\frac{kJ}{m^2}$ ]
1	20	2910.32	1.252E-05	6.62
2	20	3099	1.252E-05	7.51
3	20	3024	1.252E-05	7.15
Average	20	3011.10	1.252E-05	7.100
Standard deviation		94.99		0.446
Co-efficient of variance (%)		3.15		6.28

Table 3-6 Test results of compressive fracture energy

Additional photos of deformed specimens are given in 12.2.4.

### 3.6 Axial crushing behavior

Energy absorption capacity of 2mm thick laminate of 102-RG600(4) was measured by quasi static axial crushing of corrugate specimen. Self-supporting corrugated specimen was manufactured from a blank in a sine wave pattern tool by heated it up to 220 °C. The specimen dimensions are given in Figure 3.26.

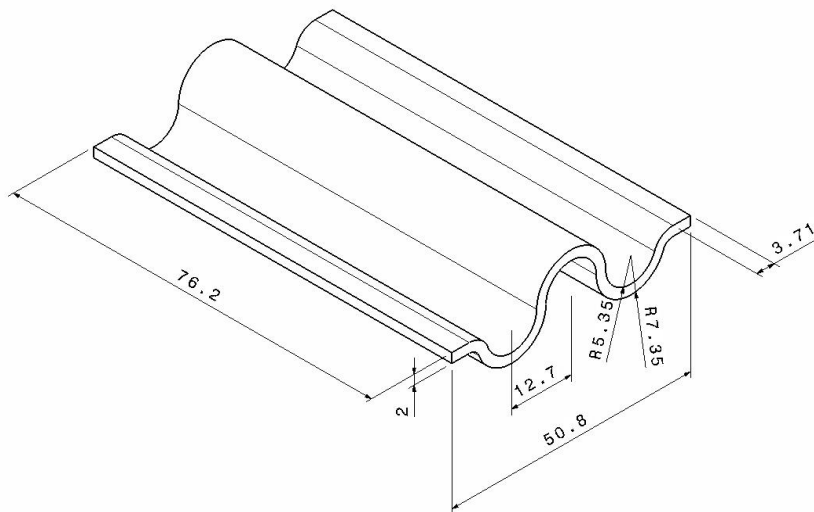


Figure 3.26 Corrugated Specimen dimensions

The specimens were placed axially in Zwick Z100 and compressed with a speed of 5mm/min. The force and deformation was measured. The tests and measured results are shown in Figure 3.27 and Figure 3.28.

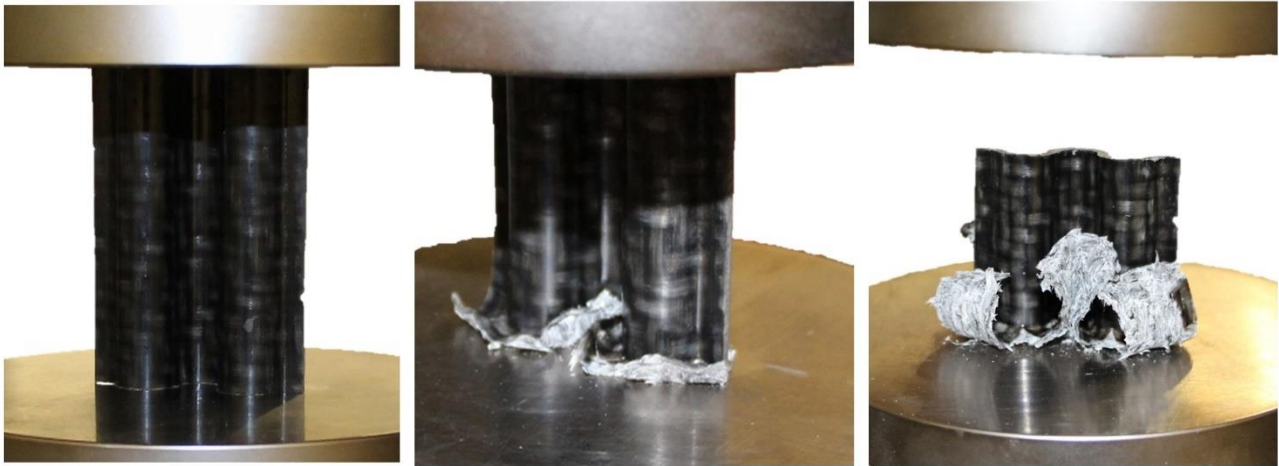


Figure 3.27 Axial crushing of corrugated specimen at different stages of testing

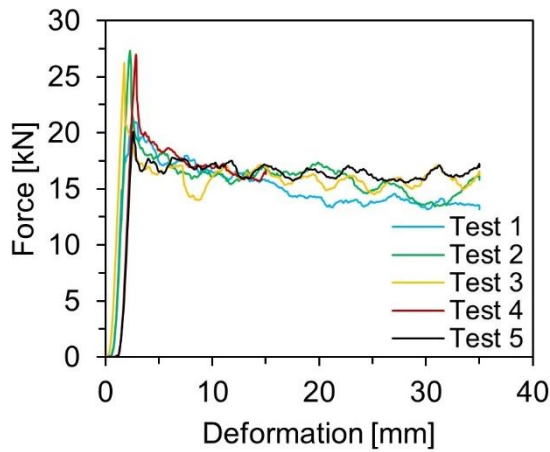


Figure 3.28 force-deformation results and a specimen after test. More specimen photos are given in Appendix 12.2.5.

Sr. no.	Length [mm]	Energy absorbed [N-mm]	Specific energy absorbed [kN-m/kg]	Sustained crush stress [MPa]
1	54.31	518058.38	55.19	100.93
2	73.47	545991.49	58.16	106.23
3	76.2	550516.92	58.65	106.30
4	77.69	233155.11	57.96	114.15
5	76.2	549617.48	58.55	111.08
Average			57.70	107.74

Table 3-7 Axial crushing of corrugated specimen

The energy absorption has resulted in a stable crushing. Fiber remain intact and delamination occurred resulting in formation of “fronds”. Compression Crush Ratio (Compressive Strength / Sustained Crush Stress  $\approx$  2.84) shows that if peak load is not too high during the start of crushing then other geometries of this material can also be successfully crushed and used to absorb energy.

## 4 Continuum damage mechanics

In this chapter openly available materials models for crash simulations are investigated. The material properties measured in chapter 3 were used as input parameters for commercially available material models and their simulation results were compared with experimental data.

Composites materials can be modeled on multiscale or mesoscale levels. In multiscale modeling, a constitutive model is defined on a microscale (fiber and fiber-matrix interface level), and the resulting stress/strain fields are transformed to the meso-level. To reduce the computational time, the periodicity of material is used. Mesoscale modeling is appropriate for crash simulations where lamina is considered as homogenized material [53]. In following a literature review of ply models with focus on Intra-laminar is described keeping in view that plane stress condition will be used.

Several orthotropic material models for modeling composite materials have been implemented in commercial FE code Ls-Dyna [54]. Current state-of-the-art material models for the crash simulation of composite materials are based on continuum damage mechanics (CDM), which is a mesoscale model that considers the orthotropic damage elastic response of a material at the homogenized level. CDM was at first proposed by Ladeveze et al [49] for UD composite materials. It was expanded by Matzenmiller [50] and Johnson [47] for woven fabric composites. Example of continuum damage modeling in commercial FE code is MAT\_Laminated\_Composite\_Fabric (\*MAT\_58) in LS-Dyna [54] and ABQ\_PLY\_FABRIC [48] in Abaqus.

In following first an introduction to CDM is given and then MAT\_58 and ABQ\_PLY\_FABRIC.

### 4.1 Basics of CDM

In composite materials the defects can occur by formation and evolution of microcracks and cavities. These defects are irreversible and can cause stiffness degradation. The damage mechanics characterize these defects by “internal variable” or damage variable denoted by  $d$ . The physical significance of scalar damage variable  $d$  can be explained by considering a one-dimensional bar under uniaxial load  $F$  as shown in Figure 4.1. The bar has cross sectional area of  $A_0$  with distributed defects measuring damage surface area  $A_d$ .

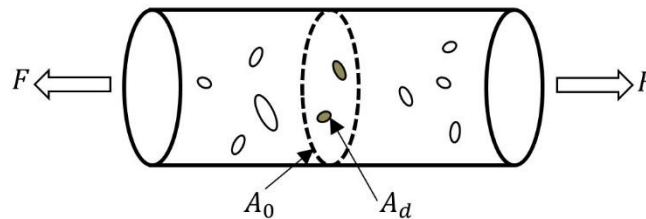


Figure 4.1 Illustration of damage in one-dimensional bar [55]

Now the ratio of “Damaged Area”  $A_d$  to the original cross-section can be defined by damage:

$$d = \frac{A_d}{A_0} = \frac{A_0 - A}{A_0} ; 0 \leq d \leq 1 \quad (4.1)$$

It is evident from this equation that for undamaged material state  $A_d = 0$  the damage  $d = 0$ . This value can reach a maximum value of One when damage area is equal to the original cross sectional

area. From Figure 4.1, it can readily be seen that  $A = A_0 - A_d$  is the “Effective Area” actually resisting the applied load. This concept is used to define “Effective Stress”  $\tilde{\sigma}$ .

$$\tilde{\sigma} = \frac{F}{A} = \frac{F}{A_0 - A_d} = \frac{\sigma}{1 - d} \quad (4.2)$$

The term Effective Stress  $\tilde{\sigma}$  is different from the “True Stress” which does not account for the damage inside the cross-sectional area  $A_0$ .

Since only undamaged part of the material will transmit the stress so the constitutive behavior of the material including failure criterion, plasticity law must be determined in terms of Effective Stress instead of True Stress. Based on the strain equivalence principle, the effective stress  $\tilde{\sigma}$  is related to the elastic strain according to Hook’s law of elasticity [55].

$$\tilde{\sigma} = E\varepsilon \quad (4.3)$$

Here  $E$  is the elasticity modulus of undamaged material. In terms of True Stress, the same expression can be written as:

$$\sigma = (1 - d)E\varepsilon = E'\varepsilon \quad (4.4)$$

Here  $E'$  is elasticity modulus of damaged material. The damage can be defined in terms of Elasticity Modulus:

$$d = 1 - \frac{E'}{E} \quad (4.5)$$

Hence, the damage of material can be calculated by measuring the elastic modulus of material at damaged and undamaged state. The elastic modulus at damaged state can be estimated from slope of unloading in stress strain plot. An illustration is shown in Figure 4.2.

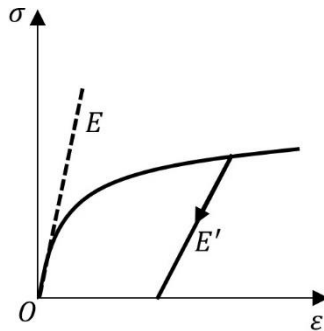


Figure 4.2 Measurement of elastic modulus at undamaged and damaged state [56]

Considering that in composite lamina, the damage along one fiber direction is independent of the other, the plane stress elasticity law of lamina from Eqn. (2.10) can be rewritten as:

$$\begin{bmatrix} \varepsilon_1 \\ \varepsilon_2 \\ \gamma_{12} \end{bmatrix} = \begin{bmatrix} \frac{1}{E_1} & \frac{-\nu_{12}}{E_1} & 0 \\ \frac{-\nu_{12}}{E_1} & \frac{1}{E_2} & 0 \\ 0 & 0 & \frac{1}{G_{12}} \end{bmatrix} \begin{bmatrix} \tilde{\sigma}_1 \\ \tilde{\sigma}_2 \\ \tilde{\sigma}_{12} \end{bmatrix} \quad (4.6)$$

[ $\boldsymbol{\varepsilon}$ ]                      [ $\boldsymbol{S}$ ]                      [ $\tilde{\boldsymbol{\sigma}}$ ]

The normal effective stresses  $\tilde{\sigma}_1$ ,  $\tilde{\sigma}_2$  and shear effective stress  $\tilde{\sigma}_{12}$  are associated to damage  $d_1$ ,  $d_2$  and  $d_{12}$  respectively:

$$\begin{bmatrix} \tilde{\sigma}_1 \\ \tilde{\sigma}_2 \\ \tilde{\sigma}_{12} \end{bmatrix} = \begin{bmatrix} \frac{1}{(1-d_1)} & 0 & 0 \\ 0 & \frac{1}{(1-d_2)} & 0 \\ 0 & 0 & \frac{1}{(1-d_{12})} \end{bmatrix} \begin{bmatrix} \sigma_1 \\ \sigma_2 \\ \sigma_{12} \end{bmatrix} \quad (4.7)$$

[ $\tilde{\boldsymbol{\sigma}}$ ]                      [ $\boldsymbol{M}$ ]                      [ $\boldsymbol{\sigma}$ ]

Inserting Eqn. (4.6) into (4.5) gives  $\boldsymbol{\varepsilon} = \boldsymbol{S}\boldsymbol{M}\boldsymbol{\sigma} = \boldsymbol{S}_d\boldsymbol{\sigma}$  which is the direct relationship between strain and true stress in the form of compliance tensor  $\boldsymbol{S}(d)$  for damaged lamina.

$$\begin{bmatrix} \varepsilon_1 \\ \varepsilon_2 \\ \gamma_{12} \end{bmatrix} = \begin{bmatrix} \varepsilon_1 \\ \varepsilon_2 \\ 2\varepsilon_{12} \end{bmatrix} = \begin{bmatrix} \frac{1}{(1-d_1)E_1} & \frac{-\nu_{12}}{E_1} & 0 \\ \frac{-\nu_{12}}{E_1} & \frac{1}{(1-d_2)E_2} & 0 \\ 0 & 0 & \frac{1}{(1-d_{12})G_{12}} \end{bmatrix} \begin{bmatrix} \sigma_1 \\ \sigma_2 \\ \sigma_{12} \end{bmatrix} \quad (4.8)$$

[ $\boldsymbol{\varepsilon}$ ]                      [ $\boldsymbol{S}_d$ ]                      [ $\boldsymbol{\sigma}$ ]

For the sake of simplicity, the degradation of Poisson's ratios also happens with the damage parameters and no additional parameter has been introduced. Inversion of the compliance tensor can be used to get stiffness matrix  $\boldsymbol{C}_d = \boldsymbol{S}_d^{-1}$  of the damaged lamina.

$$\begin{bmatrix} \sigma_1 \\ \sigma_2 \\ \sigma_{12} \end{bmatrix} = \frac{1}{D} \begin{bmatrix} E_1(1-d_1) & \nu_{12}E_2(1-d_1)(1-d_2) & 0 \\ \nu_{21}E_1(1-d_1)(1-d_2) & E_2(1-d_2) & 0 \\ 0 & 0 & G_{12}(1-d_{12})D \end{bmatrix} \begin{bmatrix} \varepsilon_1 \\ \varepsilon_2 \\ 2\varepsilon_{12} \end{bmatrix} \quad (4.9)$$

With

$$D = 1 - \nu_{12}\nu_{21}(1-d_1)(1-d_2)$$

The damaged-material strain energy in plane-stress state for homogeneous ply is written according to [47], [49]:

$$E_d = \frac{1}{2} \boldsymbol{\sigma}^T \boldsymbol{S} \boldsymbol{\sigma} = \frac{\sigma_1^2}{2E_1(1-d_1)} - \frac{\nu_{12}\sigma_1\sigma_2}{E_1} + \frac{\sigma_2^2}{2E_2(1-d_2)} + \frac{\sigma_{12}^2}{2G_{12}(1-d_{12})} \quad (4.10)$$

The so-called *thermodynamic forces*  $\frac{\partial E_d}{\partial d_i}$  can be derived by taking the differential of strain energy potential with respect to damage variables.

## 4.2 Ls-Dyna CDM model MAT\_Laminated\_Composite\_Fabric

Ls-Dyna \*MAT\_58 is a CDM based material model for fabric reinforced composites postulated by Matzenmiller et al. [50]. The damaged elasticity law of lamina response remains the same according to Eqn. (4.8) and (4.9). Because woven fabric response along the fiber direction and inplane shear is completely different (see Chapter 3) so damage initiation criterion and its evolution were defined separately.

### 4.2.1 Fiber response

Along the fiber direction there are four damage variables, namely tensile and compressive damage along every fiber direction. These damage variable are function of their corresponding effective stresses which are defined as:

$$\tilde{\sigma}_{1+} = \frac{\langle \sigma_{11} \rangle}{(1 - d_{1+})}; \tilde{\sigma}_{1-} = \frac{\langle -\sigma_{11} \rangle}{(1 - d_{1-})}; \tilde{\sigma}_{2+} = \frac{\langle \sigma_{22} \rangle}{(1 - d_{2+})}; \tilde{\sigma}_{2-} = \frac{\langle -\sigma_{22} \rangle}{(1 - d_{2-})} \quad (4.11)$$

The symbol  $\langle \cdot \rangle$  represents Macauly bracket which mean  $\langle \sigma_{11} \rangle = 0$  if  $\sigma_{11} < 0$  and  $\langle \sigma_{11} \rangle = \sigma_{11}$  if  $\sigma_{11} > 0$ . In which  $\tilde{\sigma}_{1+}$  is tensile effective stress along fiber direction 1 and  $\tilde{\sigma}_{1-}$  compressive effective stress along fiber direction 1. Similarly the damage parameters  $d_{1+}$  and  $d_{1-}$  assume different values for tension and compression as the material behavior is different in tension and compression. The Eqn. (4.11) can be written in generalized form as:

$$\tilde{\sigma}_{\alpha} = \frac{\langle \sigma_{\alpha} \rangle}{(1 - d_{\alpha})} \quad (4.12)$$

in which  $\alpha = 1(+/-), 2(+/-)$ . Depending upon the loading, the damage variable automatically assumes tensile or compressive damage value by:

$$d_1 = d_{1+} \frac{\langle \sigma_{11} \rangle}{|\sigma_{11}|} + d_{1-} \frac{\langle -\sigma_{11} \rangle}{|\sigma_{11}|}; d_2 = d_{2+} \frac{\langle \sigma_{22} \rangle}{|\sigma_{22}|} + d_{2-} \frac{\langle -\sigma_{22} \rangle}{|\sigma_{22}|} \quad (4.13)$$

Matzenmiller et al. [50] bounded the elastic range along fiber direction with damage activation function:

$$F_{\alpha} = \phi_{\alpha} - r_{\alpha} \leq 0 \quad (4.14)$$

In which  $\phi_{\alpha}$  is the damage activation function with maximum stress failure criterion.

$$\phi_{\alpha} = \frac{\tilde{\sigma}_{\alpha}}{X_{\alpha}} \quad (4.15)$$

here  $X_{\alpha}$  is the strength along fiber direction measured for uniaxial loading. Notice that damage activation criterion is postulated in terms of effective stress. MAT\_58 also allows to choose Hashin's criteria [31], [36] for damage activation function. Using Hashin's criterion the failure surface adopts a smooth shape instead of faceted failure surface with maximum stress criterion [57].

$r_{\alpha}$  is damage threshold, defining the range of elastic domain. The initial value of  $r_{\alpha}$  is equal to 1 and increase with increasing damage value according to:

$$r_\alpha(t) = \max_{\tau \leq t} \phi_\alpha(\tau) \quad (4.16)$$

This definition of  $r_\alpha$  ensures the non-reversal of damage. The value of  $r_\alpha$  at time  $t$  is equal to the maximum value of  $\phi_\alpha$  during all the time history  $\tau$ .

Matzenmiller et al. [50] assumed the damage evolution law of the form:

$$d_\alpha = 1 - \exp \left[ -\frac{1}{m} \left( \frac{\varepsilon_\alpha}{\varepsilon_f} \right)^m \right] \quad (4.17)$$

In which  $\varepsilon_f = \frac{\sigma_\alpha}{E_\alpha}$  is the nominal failure strain and  $m$  is a constant which is indirectly determined by the input parameter  $\varepsilon_q$  (strain value corresponding to maximum stress value) by user:

$$m = \frac{1}{\ln \left( \frac{\varepsilon_q}{\varepsilon_f} \right)} \quad (4.18)$$

Different values of  $m$  can be chosen to influence the stress strain curve however no method was proposed to determine this value. In Figure 4.3 tensile stress-strain outcome for different values of  $m$  from simulation of a single element is shown. In the single element model boundary conditions and fiber direction is shown with material coordinates 1 and 2.

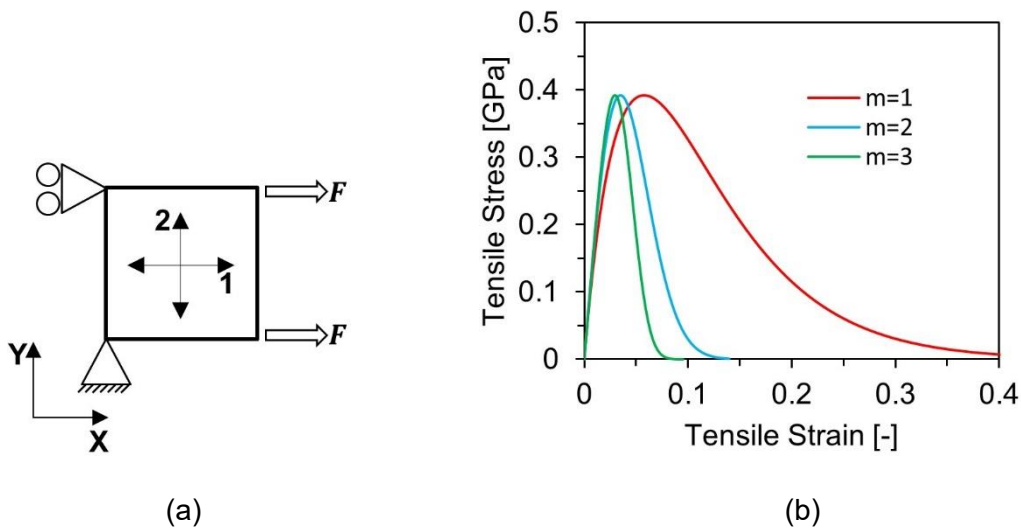


Figure 4.3 (a) Single element tensile simulation model and (b) Influence of  $m$  variable on the tensile stress-strain behavior in \*MAT\_58

Since damage is a non-decreasing function, so if cyclic loading is applied to the element, the loss of stiffness cannot be reversed. This is the advantage of CDM as shown in Figure 4.4.

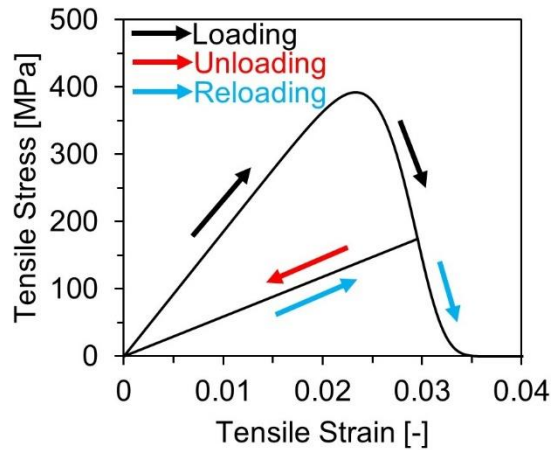


Figure 4.4 Permanent loss of stiffness due to non-reversal damage in \*MAT\_58

There is a disadvantage of classic CDM that the structural response is mesh dependent. A simple simulation model with 8 mm x 8 mm dimensions was created and meshed with 4 different mesh sizes. The boundary conditions are shown in Figure 4.5 and the results are shown in Figure 4.6.

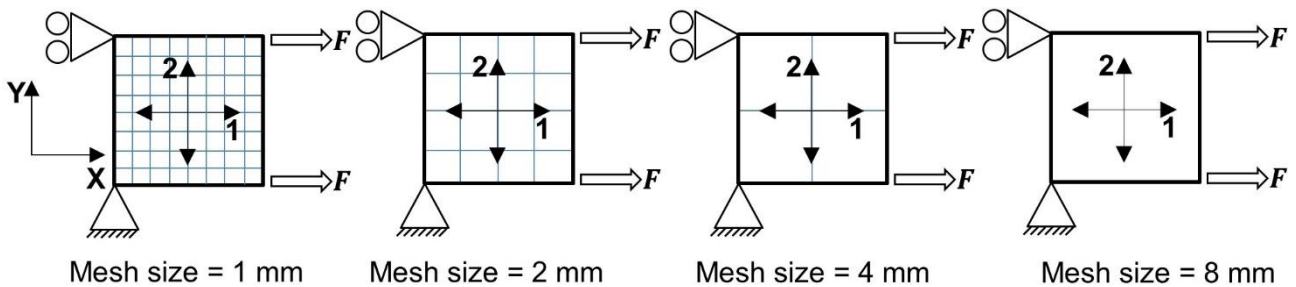


Figure 4.5 CAE model with B.C for mesh size dependency

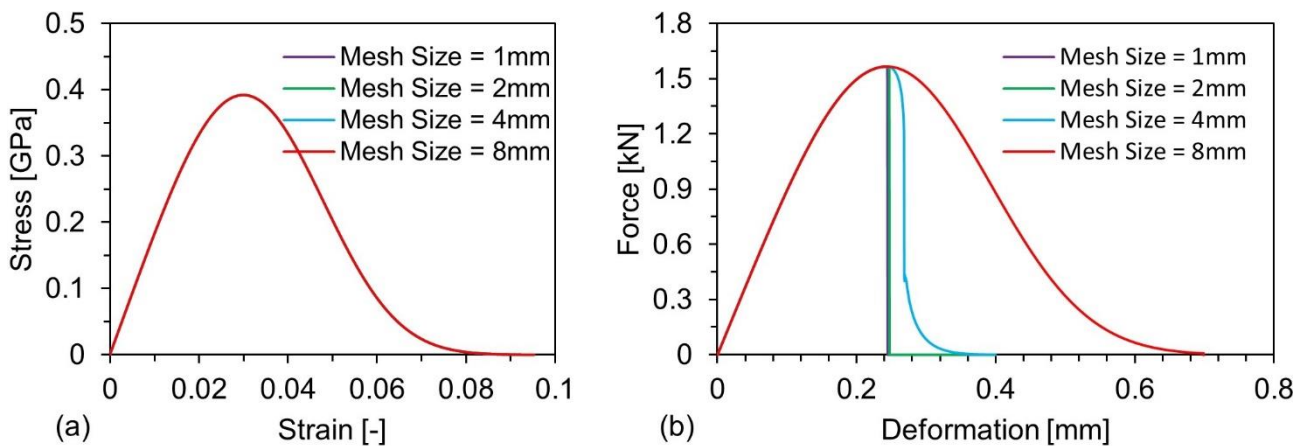


Figure 4.6 Simulation results with different mesh sizes using \*MAT\_58 showing (a) stress-strain curve and (b) force-deformation response

The results in Figure 4.6 show that even though the stress-strain response of \*MAT\_58 is the same for all element sizes, the structural response can be different.

For “tuning” the simulation results, there is also an option to limit the maximum drop of stress in an element by use of so called “SLIM” variable. The effect of using SLIM variable on stress-strain behavior is shown in Figure 4.7.

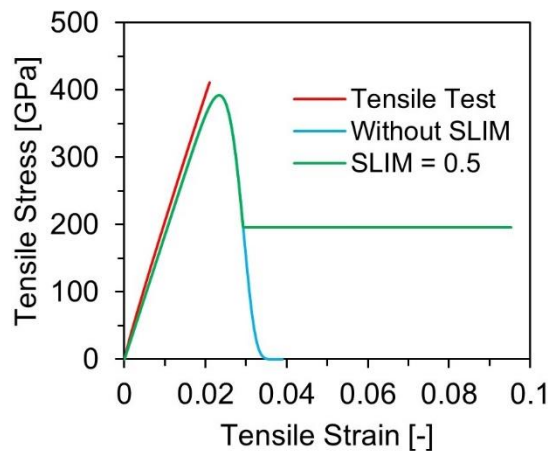


Figure 4.7 Tensile stress-strain curve of \*MAT\_58 with and without SLIM parameter compared with tensile test data

These SLIM variables can be used to “engineer” the output of results for a specific load case and specific geometry [6]. This approach however cannot be used for product development process.

#### 4.2.2 In-plane shear response

The \*MAT\_58 uses a bilinear curve defined by two pairs of shear stress-strain values  $\{(\gamma_1, \tau_1), (\gamma_2, \tau_2)\}$  to describe the non-linearity in the shear behavior of laminated fabric composites. The initial response is defined by shear modulus which continues till the first pair of data point. Then it follows linear line between first pair of shear stress-strain data point and second pair of shear stress-strain data point. Figure 4.8 shows the comparison of shear stress-strain response by use of the data points with experimental data. The simulation results were obtained by simulation of a single element with boundary conditions and fiber direction also shown in Figure 4.8.

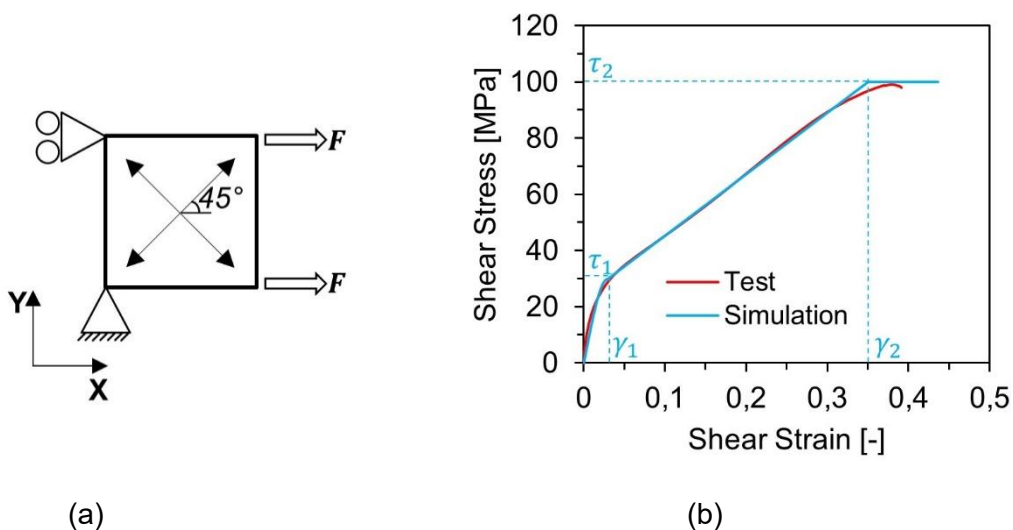


Figure 4.8 (a) single element model for with B.C and fiber direction for simulation of inplane shear and (b) shear response of \*MAT\_58 compared with experimental data

Even though the shear simulation response shown in Figure 4.8(b) looks closer to the experimental data but it is unable to account for shear plasticity. The reason is because shear curve has been obtained by calibrating with only shear modulus and two pairs of shear stress-strain data points. A cyclic simulation response is shown in Figure 4.9.

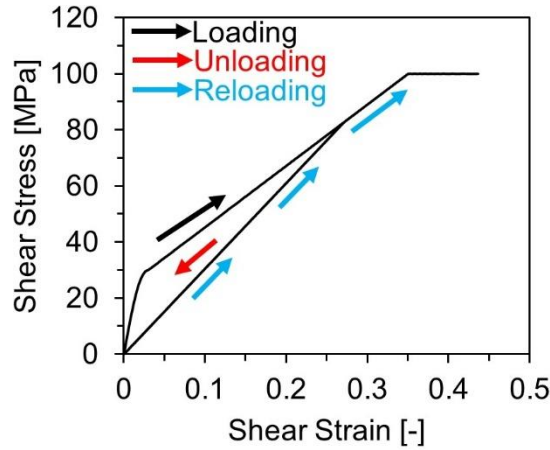


Figure 4.9 Cyclic shear response obtained by \*MAT\_58 single element simulation

By looking at the simulation results of Figure 4.9 and comparing it with cyclic shear experimental data of Figure 3.14, it can be seen that \*MAT\_58 lacks the prediction of inelastic strain. Furthermore, the stiffness degradation due to irreversible damage has also been arbitrarily calculated in \*MAT\_58.

### 4.3 Abaqus CDM model ABQ\_PLY\_FABRIC

Lapczk and Hurtado [58] alleviated the mesh dependency associated with strain localization by using the crack band model of Bazant [59]. In this model, the damage evolution is based on the fracture energy dissipation. By combining CDM and fracture mechanics the fracture energy is smeared over the entire volume of all finite elements. Thus the same amount of energy is absorbed regardless of the mesh size. Pinho et al. [60] named this method of combining CDM and fracture mechanics as “smeared formulation”. However, the maximum size of the element is restricted depending on the fracture energy value [60]. By satisfying this condition the force-displacement curve can be determined mesh independent.

Consider a composite material plate with dimensions  $L_1$ ,  $L_2$  and  $L_3$  and total volume  $V$  is under external load resulting in stress  $\sigma$  along fiber direction. The material fiber response is linear elastic until it reaches its strength  $X$  and then damage grows linearly until it fails at strain  $\varepsilon^f$ . The whole plate is modeled as single element and shown in Figure 4.10.

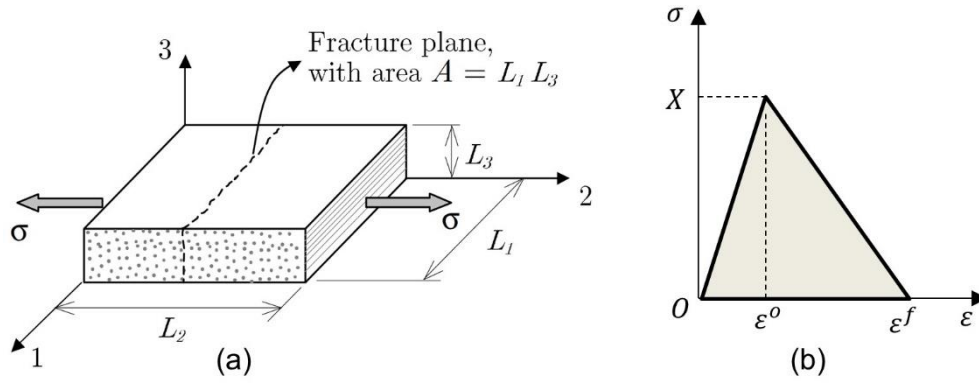


Figure 4.10 (a) Composite plate modeled as one element and (b) material response [60]

The total energy absorbed by the element till failure is:

$$U = V \times \frac{X\epsilon^f}{2} = L_1 L_2 L_3 \times \frac{X\epsilon^f}{2} \quad (4.19)$$

The total energy has been absorbed by the element to create a new crack in the middle of plate. If the cross section area of plate  $A = L_1 L_3$  then total energy absorbed  $U$  is the fracture energy per unit area  $G_f$  multiplied by the area:

$$U = G_f L_1 L_3 \quad (4.20)$$

Because  $G_f$  is a material property measured by CT and CC tests, plugging in the Eqn. (4.20) into Eqn. (4.19) gives the failure strain  $\epsilon^f$  as a function of  $G_f$ .

$$\epsilon^f = \frac{2G_f}{L_2 X} \quad (4.21)$$

So if the failure strain of the material is defined as function of fracture energy per unit area  $G_f$ , element length  $L_2$  and strength of material  $X$  then regardless of mesh size, same amount of energy will be absorbed by the element and hence the structural response will be the same. In CDM material models it is customary to define failure strain indirectly by definition of damage evolution as function of fracture energy per unit area, strength and element length.

### 4.3.1 Fiber response

In Ls-Dyna \*MAT\_58 [57] fiber response used only one elasticity modulus and Poisson's ratio regardless of tensile/compression loading was used. In Chapter 3, the results of tensile and compression tests have revealed a little difference in elasticity modulus and Poisson's ratio of tension and compression (see Table 3-2 and Table 3-3). Abaqus material model ABQ\_PLY\_FABRIC [48], incorporated these variations by calculating the trace of strain tensor and determining the loading type from it.

$$\text{sign}(\text{trace}(\boldsymbol{\epsilon})) = \text{sign}(\epsilon_1 + \epsilon_2) = \begin{cases} +ve \rightarrow & \text{Tensile} \\ -ve \rightarrow & \text{Compressive} \end{cases} \quad (4.22)$$

The initial elastic values are selected by the type of loading during simulations.

To eliminate the mesh dependency, technique explained in section 4.3 of combining CDM with fracture mechanics was employed by defining damage as function of fracture energy per unit area, strength and element length. In Figure 4.10 the damage evolution of the material was supposed to be linear after reaching the strength  $X_\alpha$  for illustration purpose. ABQ\_PLY\_FABRIC [48] defines the damage as non-linear function of the form:

$$d_\alpha = 1 - \frac{1}{r_\alpha} \exp((-A_\alpha(r_\alpha - 1))); \dot{d}_\alpha \geq 0 \quad (4.23)$$

In which  $A_\alpha = \frac{2g_0^\alpha L_c}{g_f^\alpha - g_0^\alpha L_c}$  [48] with elastic energy density  $g_0^\alpha = \frac{X_\alpha^2}{2E_\alpha}$  and element characteristic length  $L_c$ .

The stress-strain curve output of different mesh sizes is compared with experimental data in Figure 4.11(a). The structural response with different mesh sizes, for simulation model of Figure 4.5, is shown in Figure 4.11(b).

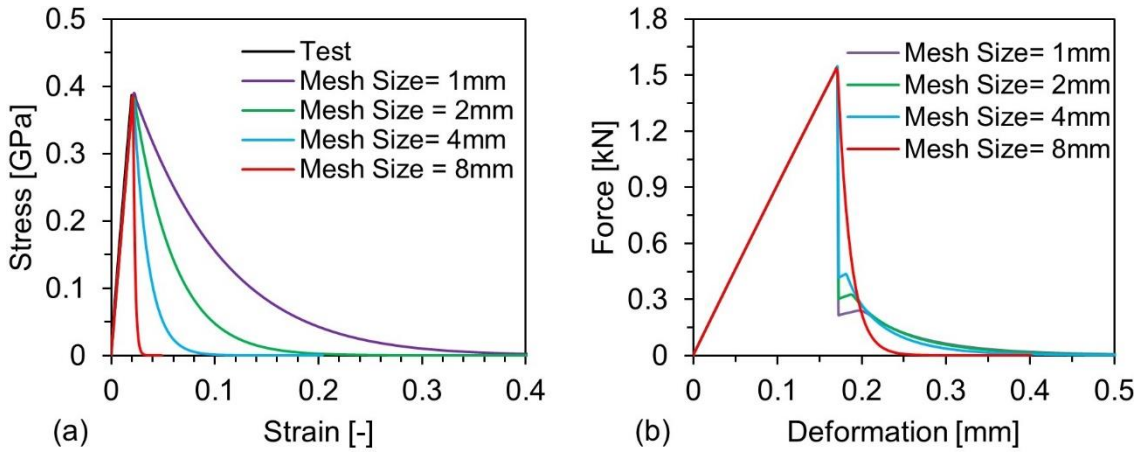


Figure 4.11 (a) Tensile stress-strain curve of ABQ\_PLY\_FABRIC for different mesh sizes and (b) structural response with different mesh sizes

The results in Figure 4.11(a) show that with the damage law defined in Eqn. (4.23) the stress-deformation behavior is linear elastic until strength value is reached. However, the softening response differs depending upon the element size because the failure strain is the function of element length. As we are interested in structural response of structures during the simulation, the force-deformation curve is almost the same irrespective of the mesh size. The reason can be explained with CAE model with 2mm mesh size shown in Figure 4.5. The simulation results are shown in Figure 4.12. When elements are elongated, initially the stress state in all elements is uniform. When the stress level reach maximum stress value, in one element damage is started before all other elements due to round of error and small time steps. Because of the damage in one element, the load bearing capability of that particular element is reduced and neighboring elements of same cross-section (elements in one vertical line) take up the load. This leads to strain concentration in one-cross section of element (red elements shown in Figure 4.12). In other elements which are still in elastic limit the load is reversed because all the deformation takes place only in one line of elements. Eventually the amount of deformation is determined by the size of element which undergo damage. Because in this formulation, the deformation at failure for all elements is same instead of failure strain, so the structural response is not affected by the element size.

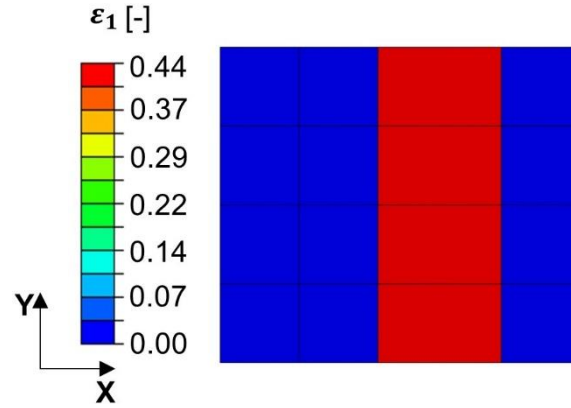


Figure 4.12 Strain concentration in elements of one-cross section. The mesh dependency is eliminated by same amount of deformation [mm] regardless of mesh size

There is one restriction to the use of smeared formulation. Consider an element under external load as in Figure 4.3a. Even though the stress-strain response is different for different mesh sizes (see Figure 4.11a), the stress-deformation curve will always be the same (see Figure 4.13). The area under stress-deformation curve of Figure 4.13a is always equal to the energy absorbed by the element which can be verified by integrating the curve over deformation (Figure 4.13b).

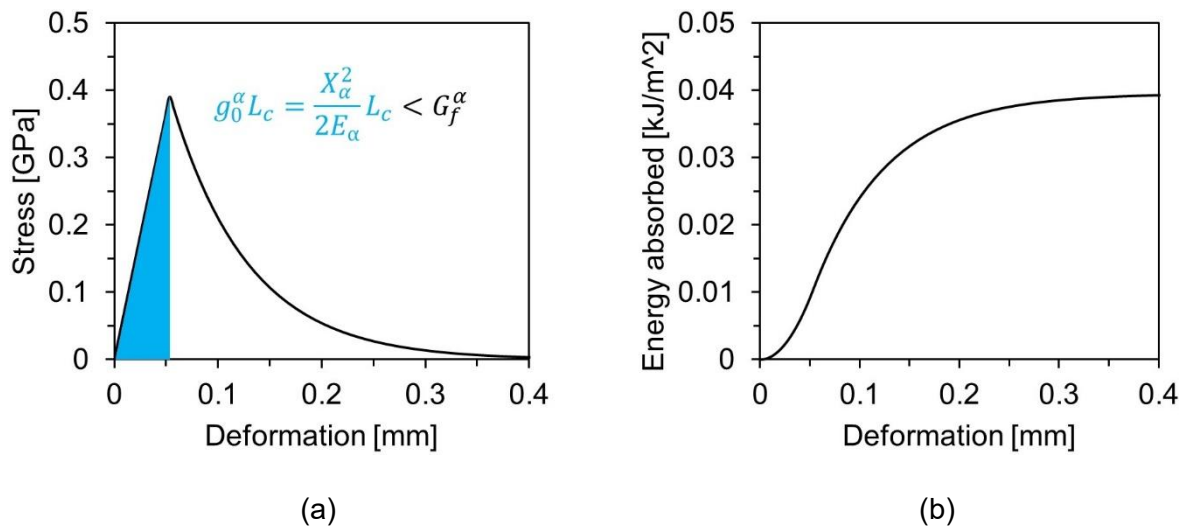


Figure 4.13 (a) Stress-deformation curve exhibited by smeared formulation and (b) Integration of the curve of which maximum value is the total energy absorbed by element

In Figure 4.13a the total area under the curve is  $G_f^\alpha$  which cannot be less than elastic strain energy  $g_0^\alpha L_c$ . This condition can be written in the following form [47], [48]:

$$G_f^\alpha - g_0^\alpha L_c > 0 \text{ or } L_c < L_{max} = \frac{G_f^\alpha}{g_0^\alpha} = \frac{2G_f^\alpha E_\alpha}{X_\alpha^2} \quad (4.24)$$

The Eqn. (4.24) leads to a condition on element characteristic length  $L_c$ . Which means that the maximum length of element is restricted by the fracture energy, strength and E-modulus. Finite elements bigger than the maximum allowable size  $L_c$  do not be dissipated equal amount of energy.

### 4.3.2 In-plane shear response

In cyclic shear tests, it is observed that under shear loading, the total shear strain is not purely elastic. Instead it is the sum of elastic and inelastic/plastic shear strain. The ABQ\_PLY\_FABRIC [48] incorporates plasticity and damage of the material according to [47].

The total shear strain is written as sum of elastic and plastic shear strain as:

$$\varepsilon_{12} = \varepsilon_{12}^{el} + \varepsilon_{12}^{pl} \quad (4.25)$$

The shear stress in material is purely due to elastic shear strain:

$$\tau_{12} = \sigma_{12} = (1 - d_{12})2G_{12}\varepsilon_{12}^{el} \quad (4.26)$$

Therefore in Eqn. (4.8) and (4.9) the shear strain terms  $\varepsilon_{12}$  are replaced with  $\varepsilon_{12}^{el}$ . Since in CDM all constitutive relations are defined in terms of effective stress so Eqn. (4.26) can be written as:

$$\tilde{\sigma}_{12} = \frac{\sigma_{12}}{(1 - d_{12})} = 2G_{12}\varepsilon_{12}^{el} = 2G_{12}(\varepsilon_{12} - \varepsilon_{12}^{pl}) \quad (4.27)$$

#### Plasticity

Since the absolute value of the stress in material cannot be greater than yield stress, it can be described as:

$$|\tilde{\sigma}_{12}| \leq \tilde{\sigma}_y \text{ or } F = |\tilde{\sigma}_{12}| - \tilde{\sigma}_y \leq 0 \quad (4.28)$$

in which  $F$  is called shear plasticity yield function. For every strain increment, the shear stress must fulfill the yield condition.  $\tilde{\sigma}_y$  is the yield shear stress due to hardening or the resistance of the material to deformation. Ramberg-Osgood hardening equation was chosen for modeling the shear plasticity of woven fabric composites because it could fit the experimental data better:

$$\tilde{\sigma}_y = \tilde{\sigma}_{y0} + K(\bar{\varepsilon}_{12}^{pl})^p \quad (4.29)$$

where  $\tilde{\sigma}_{y0}$  is the initial yield stress and  $K$  and  $p$  are material parameters which can be identified from hardening curve.  $\bar{\varepsilon}_{12}^{pl}$  is an isotropic hardening variable called equivalent plastic shear strain. Notice that  $\tilde{\sigma}_y$  is the function of tensorial shear plastic strain  $\bar{\varepsilon}_{12}^{pl}$  instead of engineering shear plastic strain  $\bar{\gamma}_{12}^{pl}$ .

Maximum value of shear plastic strain is defined for failure criterion under shear loading.

#### Damage

Similar to damaged elastic response in fiber direction, the shear damage also cannot be reversed. The state of damage remains unchanged within a domain, defined by the damage activation function  $F_{12}$  similar to Eqn. (4.14):

$$F_{12} = \phi_{12} - r_{12} \leq 0 \quad (4.30)$$

in which  $r_{12}$  is the damage threshold, defining the range of the elastic domain. The initial value of the damage threshold is set equal to 1.  $\phi_{12}$  defines the damage initiation criterion similar to Eqn. (4.15) in the following form:

$$\phi_{12} = \frac{\tilde{\sigma}_{12}}{S} \quad (4.31)$$

in which  $S$  is the damage onset stress value, measured experimentally. Since damage is a non-decreasing value, it must be monotonically increasing when damage takes place ( $\dot{d}_{12} \geq 0$ ). The damage threshold is not an independent variable, as it relates to the damage variable. It is defined by:

$$r_{12}(t) = \max_{\tau \leq t} \phi_{12}(\tau) \quad (4.32)$$

Therefore, the value of  $r_{12}$  at time  $t$  is equal to the maximum value of  $\phi_{12}$  during all the history of time  $\tau$ . This is important for implementation of the irreversible damage behavior of the material. What remains now is the definition of the shear damage variable, which was proposed by Johnson [47] as:

$$d_{12} = \min(\alpha \ln(r_{12}), d_{12}^{max}) \quad (4.33)$$

in which  $\alpha$  (not to be confused with  $\alpha$  from Eqn. (4.12)) is a constant calibrated from experimental data and  $d_{12}^{max}$  is the maximum shear damage.

By calibrating all the shear parameters from the experimental data, single element shear simulation (see CAE model in Figure 4.8a) results are compared with experimental data in Figure 4.14a. The simulation results of cyclic loading of same model is shown in Figure 4.14b.

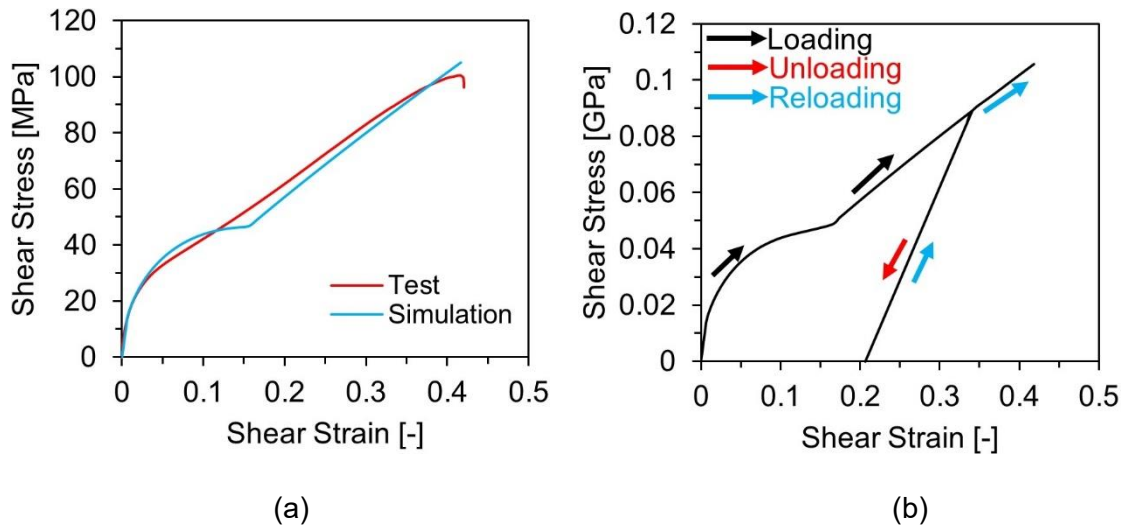


Figure 4.14 (a) Shear stress-strain simulation results compared with experimental data and (b) cyclic simulation response

The results in Figure 4.14b show that the material model is able to predict the inelastic strain which makes it a better model than Ls Dyna \*MAT\_58 (see Figure 4.9). Although shear stress-strain results in Figure 4.14a are closer to experimental data but a small kink in simulation results can be seen

which is due to logarithmic damage function defined in Eqn. (4.33). The results of damage growth from experimental data and simulation output are compared in Figure 4.15.

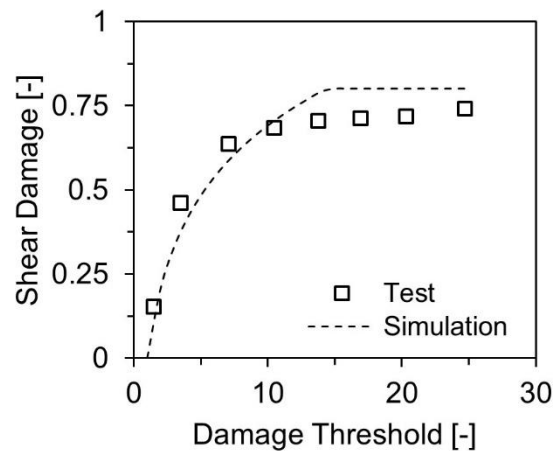


Figure 4.15 Shear damage growth as function of shear damage threshold

By looking the results shown in Figure 4.15, it can be seen why the shear stress-strain curve show a kink because the damage function described in Eqn. (4.33) does not exactly represent the experimental data. In chapter 5 a detailed study on measuring the shear properties with different test methods is discussed and the damage function is changed to improve the results.

#### 4.4 Validation

As discussed and concluded from the calibrating and verification of CDM material models on single elements in section 4.2 and 4.3, the ABQ\_PLY\_FABRIC is the relatively better material model. In this section ABQ\_PLY\_FABRIC was used to simulate the three-point bending of rectangular specimens and an open U-profile. The results were compared with experimental data.

##### 4.4.1 Three-point bending of rectangular specimen

Three-point bending test was chosen because it is the simplest tests which introduces tensile, compression and through thickness shear stress simultaneously into the specimen. Tests were conducted on specimens of two different lengths. All specimens were cut along fiber direction with 25 mm width and 2 mm thickness. Specimens were rested on two support rollers of 15 mm radius. Specimens were placed on support rollers precisely so that fiber directions remain perpendicular to impactor. Two different specimen lengths (80 mm, 100 mm) were tested. And their respective span length was 60 mm and 80 mm. The impactor had radius of 5 mm and all experiments were carried out at speed of 5mm/min. The experimental setup is shown in Figure 4.16.

The simulation model consisted of one 3D analytical rigid impactor, two 3D analytical rigid supports and specimen meshed with 2.5mm mesh size of S4R elements. S4R is 4-node shell element with reduced integration and hourglass control parameters. The supports were fixed in all degrees of freedom and impactor was fixed in all degrees of freedom except in z-direction direction. Displacement boundary condition was defined on impactor with smooth amplitude to reduce dynamic effects. The simulation time chosen was 2000ms (2s) which was more than enough to eliminate dynamic effects. Between the contacting surfaces, general contact with normal behavior (“Hard contact”) was defined which is an automatic contact type. General automatic contact is also feasible

for large scale simulation models where defining every contact surfaces manually is difficult. The simulation model is shown in Figure 4.16.

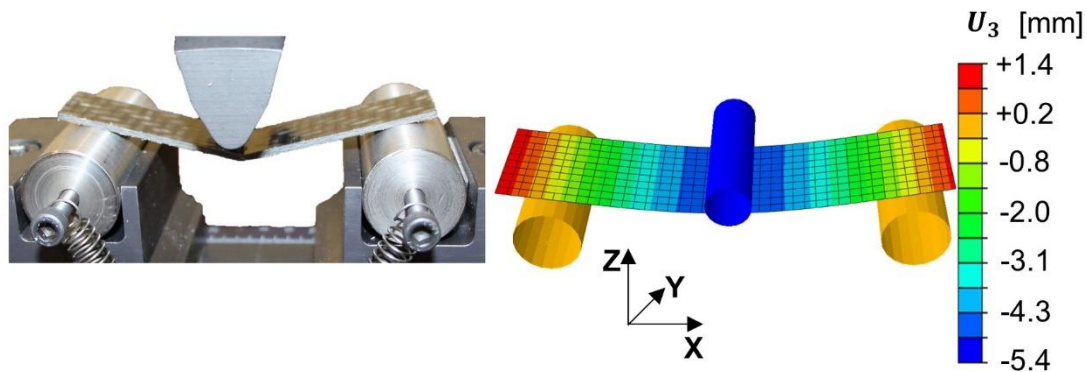


Figure 4.16 Three point bending test and simulation model

The output is a plot of vertical displacement of impactor vs. the sum of vertical reaction forces at supports. This plot was compared with experimental data in Figure 4.17.

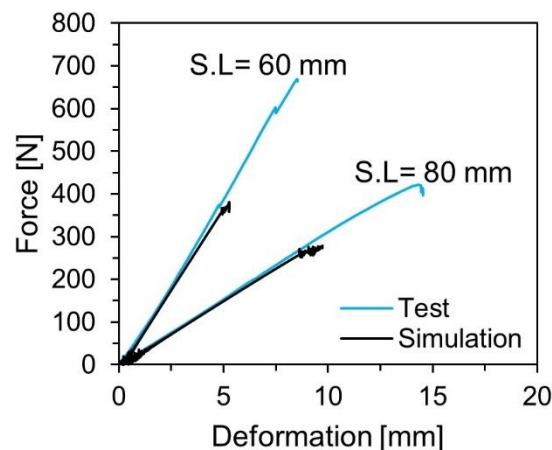


Figure 4.17 Three point bending simulation results of rectangular specimens with span length of 60 mm and 80 mm compared with experimental data

As can be seen in Figure 4.17, the bending stiffness of both specimens has been predicted correctly. However, the flexural strength is under predicted.

#### 4.4.2 U-profile

Three point bending of U-profile represent a simple component level test. The profile was thermoformed from 2 mm thick laminate of 102-RG600(4) with fiber direction along the length of profile. The profile was 260 mm long and 80 mm wide. The dimensions of cross section of u-profile are shown in Figure 4.18. The profile was placed on supports of 10 mm radius which were 200 mm apart. The profile was loaded with an impactor of 5 mm radius at speed of 10 mm/min. The test setup is also shown in Figure 4.18.

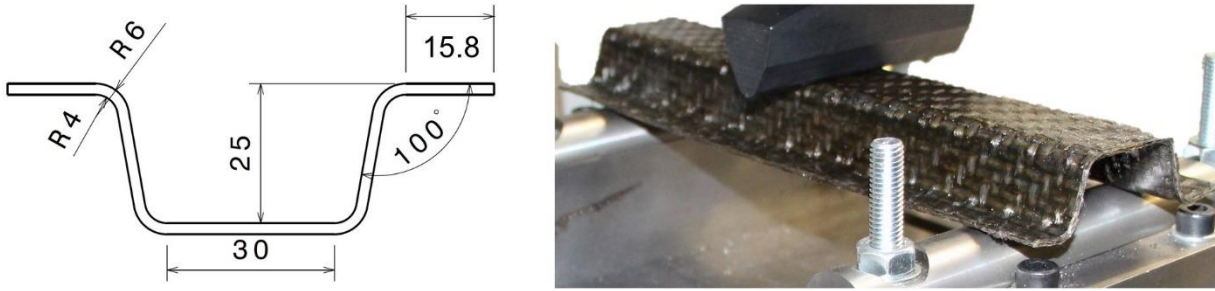


Figure 4.18 Cross-section of thermoformed profile (left) and test setup (right)

The impactor and supports were modelled as 3D analytical rigid parts. The profile was meshed with S4R shell elements with mesh size of 2.5 mm. General contact for explicit analysis was defined for all surface including self-contact with normal hard contact behavior. The simulation time was defined to be 1000 ms with smooth amplitude. The deformation and force output is compared with experimental data in Figure 4.19.

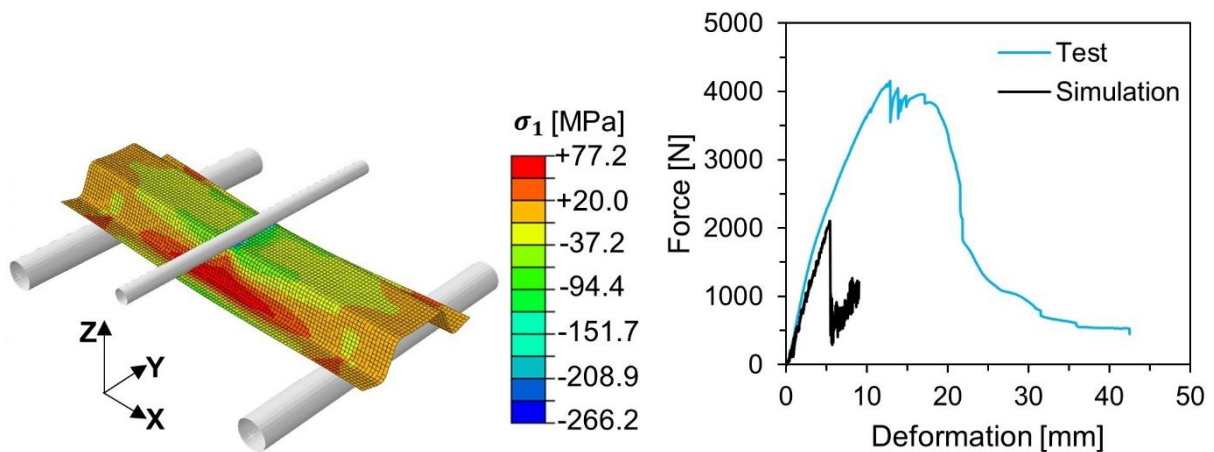


Figure 4.19 Simulation model of three point quasi-static bending of U-profile (left) and simulation results compared with test data (right)

The results in Figure 4.17 and Figure 4.19 show that ABQ\_PLY\_FABRIC can predict the bending stiffness correctly but the strength is always underpriced. The reason behind this is the size effect discussed in detail in chapter 8.

#### 4.5 Conclusion

- CDM is the state of the art material model for crash simulation of composite materials;
- Classic CDM such as Ls-Dyna \*MAT\_58 predict results which are mesh dependent;
- Mesh dependency is alleviated by combining CDM with fracture mechanics as in ABQ\_PLY\_FABRIC;
- Inplane shear response must be modeled using plasticity in addition to CDM approach;
- Damage evolution as function of logarithm of damage threshold show deviation from experimental data of 102-RG600;
- Quasi-static simulation of three-point bending of specimen as well as hat profile component under-predict the strength of material. The strength scaling is further discussed as size effect in chapter 8.

## 5 Shear modeling

The lightweight potential of composite materials is achieved by aligning the fibers in the direction of the load; this, however, leads to catastrophic brittle fracture at low strains. Sometimes, it might be desirable to achieve ductile or high failure strain behavior which can be achieved by angle-ply laminates. Furthermore, a weight-efficient design in which fibers are aligned along one particular direction might not be in the direction of crash forces. Therefore, the ability to predict the crash behavior of angle-ply laminates through FEM simulations, then, is just as important as it is along the fiber direction.

Angle-ply laminates demonstrate non-linear behavior and high strains to failure. This effect is more pronounced in the tensile/compression loading of 45° off-axis laminate. Figure 5.1 shows the ratio of shear stress in varying angle ply laminates. The shear stress-to-applied stress ratio is highest for the loading angle of 45°. Therefore, testing and modeling of the shear behavior of composite material is essential in the product development process.

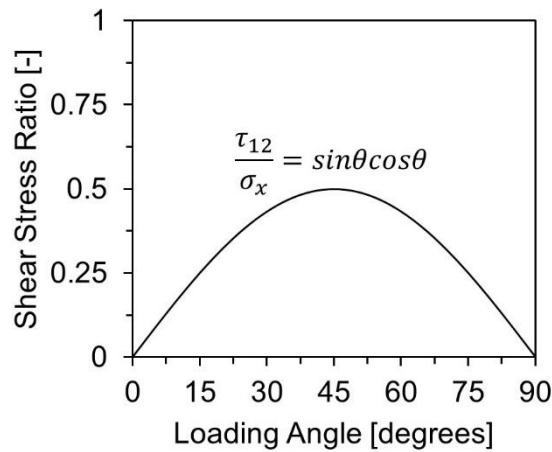


Figure 5.1 Shear stress to applied stress ratio as function of loading angle in composite ply

As discussed in chapter 4.2.2 that in Ls-Dyna \*MAT\_58 the inplane shear stress-strain curve was obtained by interpolation through two data points  $\{(\gamma_1, \tau_1), (\gamma_2, \tau_2)\}$ . Similar approach was adopted by Pinho et. al. [60] by representing the shear curve of laminated fiber composites into FE model through coefficients of polynomial. This polynomial represents the value of shear stress as function of shear strain. Thus the value of shear modulus remains constant even though the degradation of stiffness due to damage is evident from experimental data.

Paepegem et al. [61], [62] conducted an experimental program to measure the shear properties of glass fiber reinforced epoxy composites with tensile tests on  $\pm 45^\circ$  and  $10^\circ$  off-axis composite laminates. The results were used for establishing phenomenological model shear damage and permanent shear strains. Validation simulations of three point bending of rectangular  $\pm 45^\circ$  laminate have shown that measuring material parameters only for the positive normal strains affected the simulation results negatively.

Cousigné et al [63] used Ramberg-Osgood equation for interpolation and extrapolation of non-linear behavior of material and associated an unidimensional plasticity model in a separate subroutine to account for permanent deformation. The equation calculates plasticity when a difference occurs between initial and instantaneous stiffness. However, none of the four proposed damage

formulations (linear, non-linear, constant stress level, step based damage) are in agreement with measured test data of organo-sheets.

Many authors [64]–[67] have shown that effect of fiber rotation is also essential for predicting the results. However, at large strains, fiber rotation calculation for woven fabric is much more complex due to curvature and locking effect in warp and weft for which micromechanical model must be used. This in turn will very computationally expensive.

In chapter 4 it was shown that to model the shear behavior of woven fabric composites, classical CDM must be coupled with plasticity such as Abaqus material model ABQ\_PLY\_FABRIC [48] proposed by Johnson [47]. However, results produced by using this material model (see Figure 4.14 and Figure 4.15) were not satisfactory. Therefore, the focus of work shown in this chapter is the improvement in modeling of the shear behavior of 102-RG600. The material model ABQ\_PLY\_FABRIC [47] served as the basis for this work.

The improvement in material modeling were undertaken based on the detailed experimental investigation on shear behavior of 102-RG600. In section 5.1 The shear properties measured by tensile testing of  $\pm 45^\circ$  laminate from chapter 3.4 were compared with shear properties obtained by other established testing techniques to measure shear stress-strain curve of composite materials. Experimental measurements of (1) pure shear behavior and shear behavior in the presence of (2) tensile and (3) compression normal stresses were carried out. In section 5.2, improvements to the CDM model based on the experimental evidence are proposed. The improved shear model is then implemented as a user defined material model (VUMAT) in Abaqus, and the working ability of VUMAT is verified on a single element simulation. Finally, in section 5.3, the validation of simulation results on the three-point bending of  $\pm 45^\circ$  laminate is included.

## 5.1 Testing

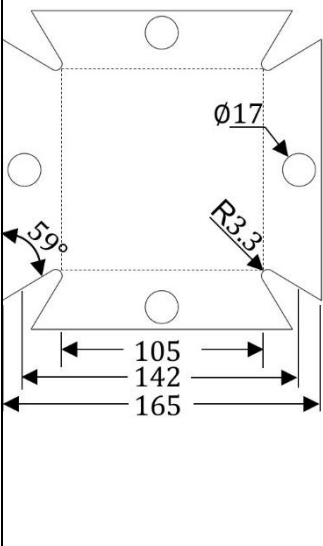
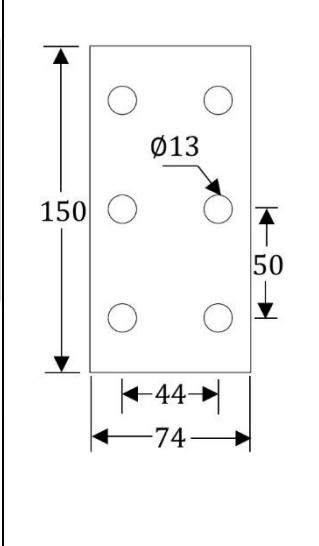
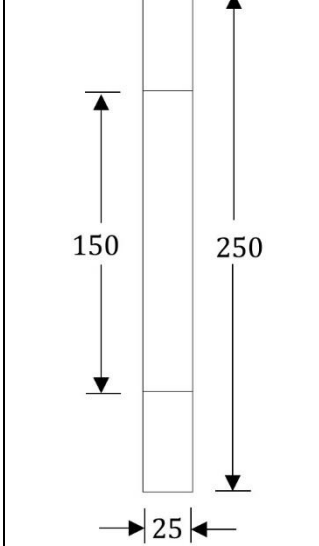
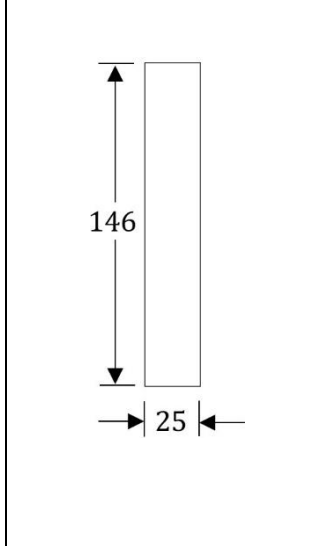
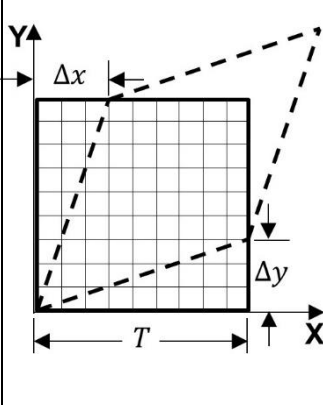
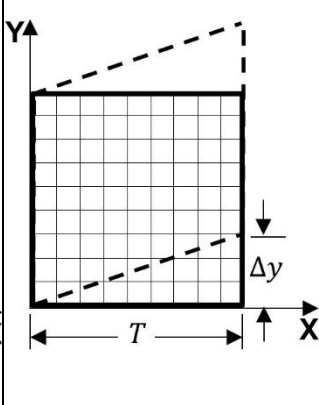
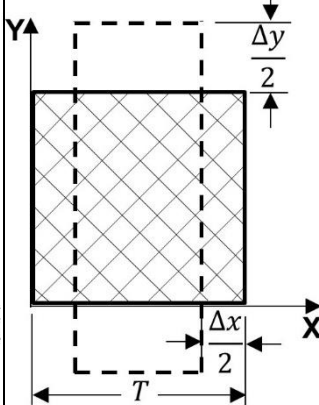
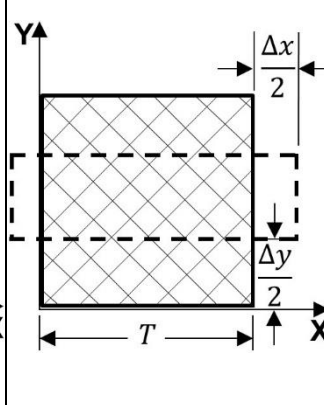
Measuring shear properties of unidirectional composites as well as those of woven fabric-reinforced composite materials are relatively complex in comparison to isotropic materials. There are various standardized test methods to determine the intra-laminar shear properties of composite materials. These methods differ in size and geometry of gauge length, complexity of fixture required, and cost. Many of these methods differ in their ability to produce the pure and uniform shear stress state in the material [46], [68]–[72].

The most suitable intra-laminar shear testing method involves the torsional testing of cylindrical samples [69]. A pure shear stress state can be achieved by twisting the tube sample with fibers oriented at  $0^\circ$  or  $90^\circ$ . This test can produce results with high accuracy. However, the manufacturing of a cylindrical specimen out of organo sheet is very difficult. Therefore, cylindrical specimens are mostly used for testing pipe components in which specimen geometry resembles the actual component.

The v-notch shear test method [70], also known as the Iosipescu shear test, is performed on a flat, rectangular specimen with centrally located v-notches. It is an asymmetric, four-point bending test in which the location of the failure is pre-determined by v-notches. A constant shear force and zero bending moment in the vertical symmetric plane of the specimen are achieved. Thus, a pure shear stress state is achieved in an infinitesimal area between the two notches. However, the shear stress state close to the notches and the middle of the specimen is not uniform. The fundamental assumption of the v-notch shear test method is that material is relatively homogeneous with respect

to the size of the specimen. The roving glass fabric has coarser fabric features with a repeating unit that is larger than the distance between the v-notches. Because of this, the Iosipescu test cannot be used for measuring the shear properties of 102-RG600.

Therefore, in this study, four types of shear testing methods were used to test the Tepex dynalite 102-RG600/47%. A schematic illustration of loading type with initial (solid lines) and deformed shapes (dotted lines) is summarized in the third row of Table 5-1. In the *Frame Shear* method [71] and *Rail Shear* method [72], the normal stress levels along the fiber direction  $\sigma_1, \sigma_2$  are theoretically equal to zero, which results in the pure shear stress-strain response. For the *Tensile Shear* method [46], in addition to the shear stress tensile or positive normal, stresses along the fiber direction are also present. In the *Compression Shear* test method [45], [68] shear deformation of the material is accompanied by compression or negative normal stresses along the fiber direction. With the *Tensile Shear* and *Compression Shear* methods, the absolute value of normal stresses is equal to shear stress.

Frame shear	Rail shear	Tensile shear	Compression shear
			
			
$\theta = 0^\circ, 90^\circ$	$\theta = 0^\circ, 90^\circ$	$\theta = \pm 45^\circ$	$\theta = \pm 45^\circ$
$\gamma_{12} = \frac{\Delta x + \Delta y}{T}$	$\gamma_{12} = \frac{\Delta y}{T}$	$\gamma_{12} = \varepsilon_y - \varepsilon_x$	$\gamma_{12} = \varepsilon_y - \varepsilon_x$

$\sigma_1 = \sigma_2 = 0$	$\sigma_1 = \sigma_2 = 0$	$\sigma_1 = \sigma_2 =  \tau_{12} $	$\sigma_1 = \sigma_2 = - \tau_{12} $
---------------------------	---------------------------	-------------------------------------	--------------------------------------

Table 5-1 Four shear test methods with specimen dimensions (in mm) in 2<sup>nd</sup> row, schematic representation of deformation in 3<sup>rd</sup> row, fiber direction in 4<sup>th</sup> row, shear strain in 5<sup>th</sup> row and multi-stress state in 6<sup>th</sup> row

Tensile shear test has already been discussed in chapter 3.4. Here test procedure of other three test methods will be discussed and results of all test methods will be compared.

### 5.1.1 Frame shear test

Shear Frame test according to DIN SPEC 4885 [71] uses a frame for the determination of the in-plane shear stress-strain response of fiber-reinforced composites. In this shear test method, the specimen is loaded in a state of pure shear without superimposing other stress states. Frame shear test can be used to measure non-linear shear properties well beyond 5% shear strain.

The shear frame has two identical halves which hold the specimen. Both halves can deform the specimen in a rhombic shape as shown in Figure 5.2. The specimen is clamped between both halves with help of bolts. When loaded in tension, this fixture introduces shear forces in specimen. Detailed machine drawing of the fixture is given in Annex 12.3.3.

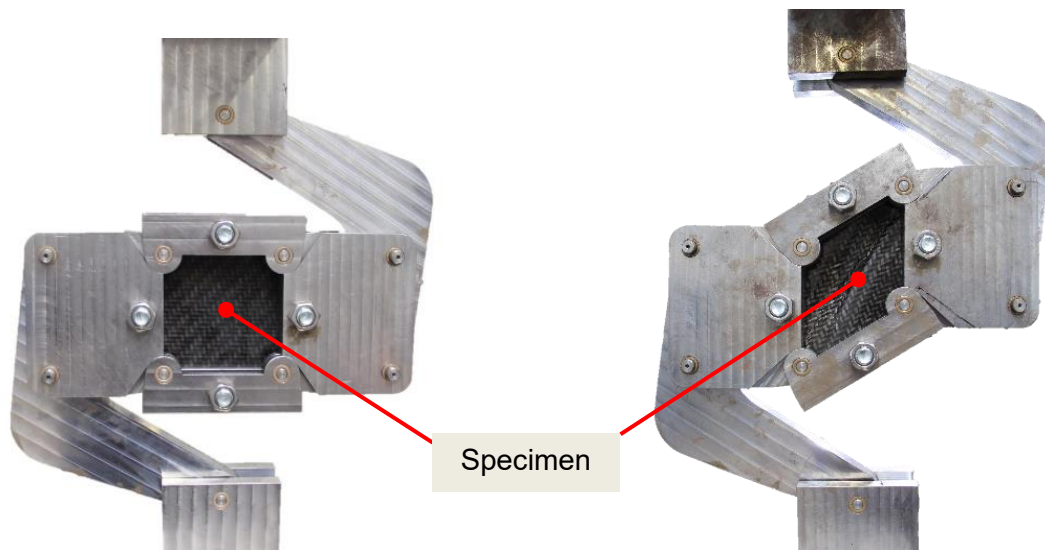


Figure 5.2 Shear Frame Test at start of test (left) and during the test (right)

#### **Test Specimen**

The specimen had flat shape measuring 165mmx165mm with 105mmx105mm load bearing area. The specimen had four holes for the fixture bolts to pass through. Specimens with two different thicknesses (2mm and 4mm) were cut with water jet cutting according to the dimensions given in Table 5-1. The fibers were aligned at 0°/90°. Due to the grip on all four sides, the specimen had no free edges. The specimen is also shown in Figure 5.3.

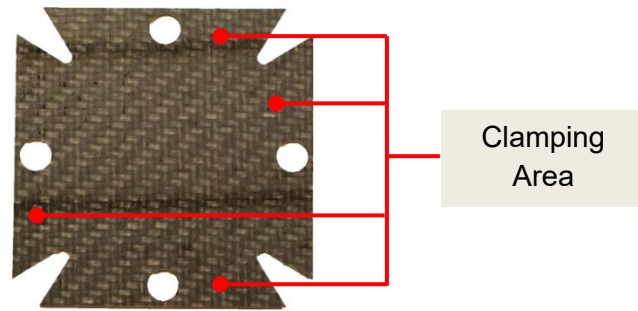


Figure 5.3 Frame shear test specimen

### Test procedure

The specimens were sprayed with black and white stochastic spray to measure the strain with digital image correlation technique. Then the specimen was clamped through bolts between the two halves of fixture. The four bolt helped in positioning the specimen by passing through the holes in addition to the tightening. A torque gauge was used to tighten the bolts at 100Nm to provide uniform grip. A displacement controlled tensile loading was applied with at a speed of 5mm/min. The Aramis 5M camera was used to take images of 105 mm x 105 mm area with resolution of 1824 x 1824 pixels at rate of 1 frame/sec. The shear strain was directly calculated by GOM Aramis software and shear stress was calculated by:

$$\tau_{12} = \frac{F}{bh} \quad (5.1)$$

Here  $F$  is the force measured by the force transducer of Zwick Z100 machine.  $b$  is the width of load bearing area of the specimen which is equal to 105mm and  $h$  is specimen thickness.

### Results

Since frame shear specimen have larger gauge area which is under loading during the test, a significant out of plane bending or buckling was observed. The measurements with specimen in buckled state are not representative of the material shear properties which rendered all these test invalid for the measurement of full shear stress strain curve. Figure 5.4 shows the buckling of the specimen measured optically at average shear strain value 14%. It can be seen that in the middle, an outward buckling amount to more than 7mm. The test was stopped after the buckling of specimen became visually obvious and the results are given in Figure 5.5.

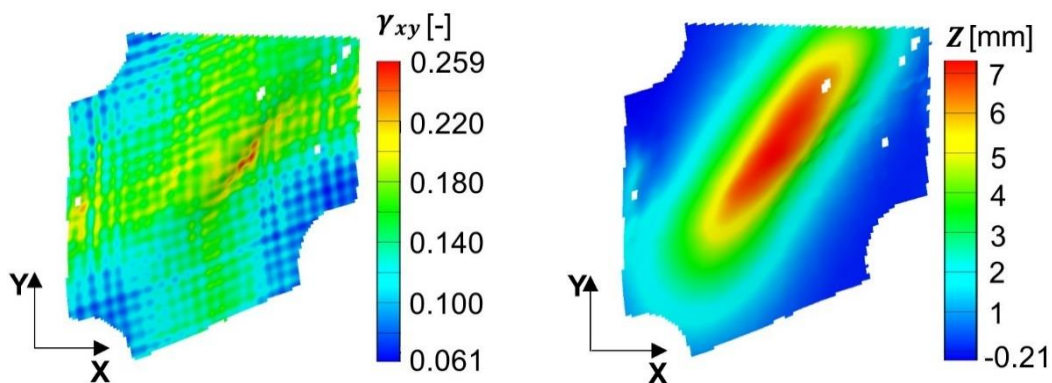


Figure 5.4 Optically measured shear strain (left) and out of plane bending (right) of 4mm thick specimen at average shear strain value of 14%

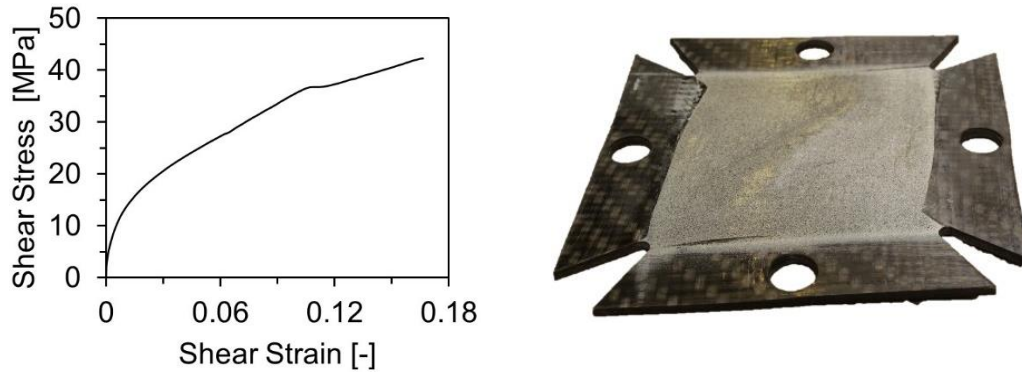


Figure 5.5 Shear Stress Strain measured by frame shear method and deformed specimens

In shear stress-strain plot (Figure 5.5) a kink can be identified at ca. 10% shear strain value which marked the onset of buckling. The results are valid for the measurements before buckling occurred which is well above the elastic region. However, this is not enough for complete failure analysis of the material. The tests were also carried out for 2mm thick specimens and in all those specimens buckling occurred at lower shear strain value in comparison to 4mm (results of other specimens are given in Annex 12.1.1). The reason of early bending in thinner specimen in comparison to thicker specimen is their lower bending stiffness which can be increased by increasing the thickness of specimen. In this case specimens of thickness greater than 4mm are desirable due to their higher buckling stability but are not available commercially. Therefore, other methods of testing shear properties were adopted for 102-RG600. Other composite materials with relatively higher through-thickness shear modulus can still be tested with frame shear method.

### 5.1.2 Rail shear test

The two-rail shear test was carried out according to ASTM D 4255 [72]. This test can be performed on a 2 mm thick flat specimen with simple geometrical features, as shown in Table 5-1. The test specimen for this study had six holes of 13 mm diameter each for bolts to pass through them. The specimens were cut with a water jet cutting machine according to the dimensions given in Table 5-1. The test fixture required is shown in Figure 5.6. The detailed 2D drawing of the fixture is given in Annex 12.3.4. The specimen was clamped between the two pairs of rails with bolt and tensile loading applied to the rails, which introduced shear strain in the laminate. Compression loading could have also been applied but larger rails would have been needed to avoid contact between the specimen's upper/lower edges with the fixture at large deformations. The bolts were tightened with a torque of 100 Nm to give a firm grip. The rails of the fixture were 30 mm wide, which covered 60 mm width of the specimen. The visible area of the specimen for optical strain measurement was 14 mm x 150 mm.

The test was done with a constant cross head speed of 3 mm/min. The strain was measured with an optical strain measuring system, Aramis. The specimen after test and the measured strain are shown in Figure 5.7. The shear stress was calculated as:

$$\tau_{12} = \frac{F}{bh} \quad (5.2)$$

Here,  $F$  is force measured during the test and  $l$  is the length of the specimen, which was equal to 150 mm.  $h$  is the thickness of the specimen.

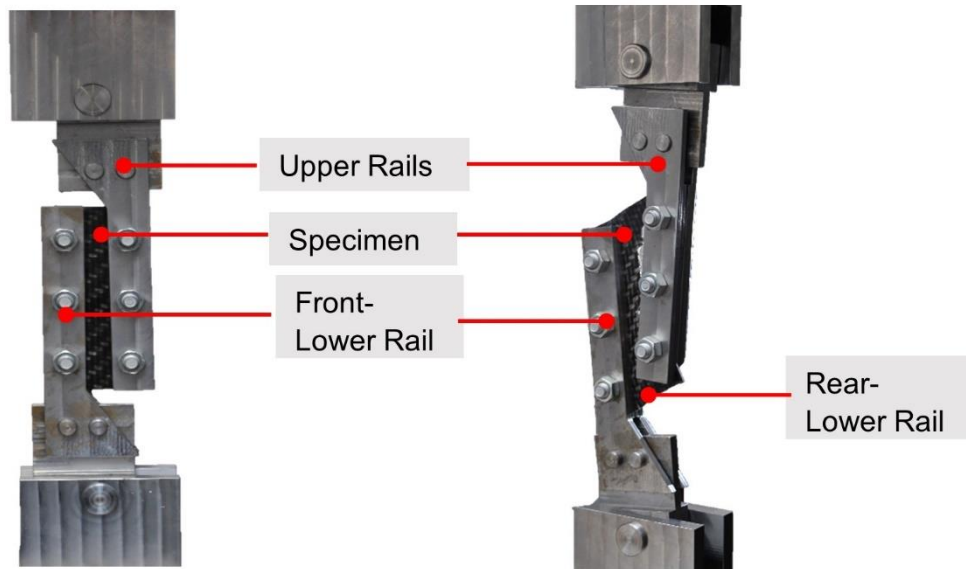


Figure 5.6 Rail shear apparatus with un-deformed specimen (left) and a deformed specimen (right)

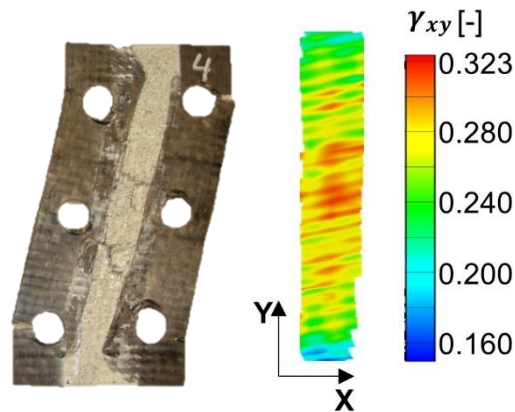


Figure 5.7 Deformed specimen after the test and optically measured shear strain measurement at ca. 27%

In this test method, the upper and lower free edges of the specimen had, theoretically, zero shear stress because those edges were not constrained. The optically measured strain in Figure 5.7 was not uniform. For results evaluation, the average value of the measured strain was calculated. This method assumes a pure shear stress state in the material, although an off-axis load of two rails introduces a small tensile load in the material. In section 5.1.4 the results are presented and compared with other methods in which multi-stress state loading was applied to the material. Detailed results are given in Annex 12.1.2 and specimen photos are given in Annex 12.2.6.

### 5.1.3 Compression shear

There is no standardized test available for compression shear testing. In ISO 14129 [46], the tensile test is performed on a specimen with diagonally oriented fibers to evaluate shear properties. From a mechanic's point of view, the same can also be obtained by performing a compression test on a specimen with diagonally oriented fibers. The only difference would be the change of normal stresses from tensile to compression. The specimen used for this test was 4 mm thick to achieve the maximum possible buckling stability. The dimensions of the test specimen were 146 mm x 25 mm x 4 mm with

a gauge length of 18 mm. The combined loading compression (CLC) fixture was used for compression testing of  $\pm 45^\circ$  laminate. The tests were carried out at a speed of 1 mm/min. The specimen after the test and measured strains are shown in Figure 5.8.

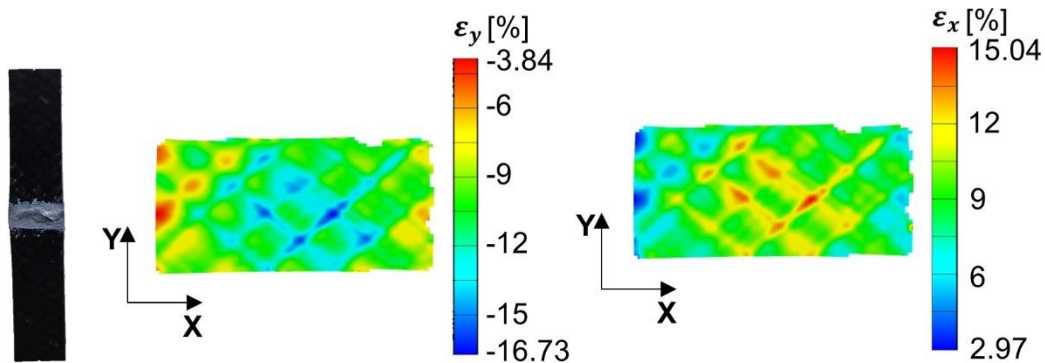


Figure 5.8 Deformed specimen after the test; optically measured, longitudinal normal strain and transverse normal strain

In Figure 5.8 the direction of the fibers in diagonal direction can be clearly seen from the measured optical strain pattern. A homogenized strain value was calculated from the average value of the strains.

The compression tests were, in general, difficult to perform in terms of getting less scattered resulting data due to the sensitivity of buckling to the fiber waviness and geometrical imperfection. In axial crash loading, since most of the materials are under compression load, it is necessary to adopt an average curve for compression shear for simulation purposes. The compression testing of off-axis laminate results in delamination due to which the plies detach from one another, thus further reducing the buckling stability of individual plies. In section 5.1.4 it will be shown how the compression shear response differs from the tensile shear response. Detailed results are given in Annex 12.1.3 and specimen photos are given in Annex 12.2.8.

#### 5.1.4 Results and comparison

The tensile shear test was explained in chapter 3.4. The frame shear test data is invalid due to buckling of specimen. Therefore, the shear properties and stress-strain curve results measured by three testing methods with valid results are summarized in Table 5-2 and compared in Figure 5.9.

	No. of tests	Shear modulus [MPa]	Shear strength [MPa]	Shear failure strain [-]
Rail shear (Standard deviation)	5	1990.58 (163.5)	80.46 (2.65)	0.33 (0.016)
Tensile shear (Standard deviation)	6	1851.78 (347.8)	100.98 (1.81)	0.40 (0.312)
Compression shear (Standard deviation)	5	1817.72 (385.9)	54.26 (14.25)	0.32 (0.013)

Table 5-2 Inplane shear properties measured by three test methods

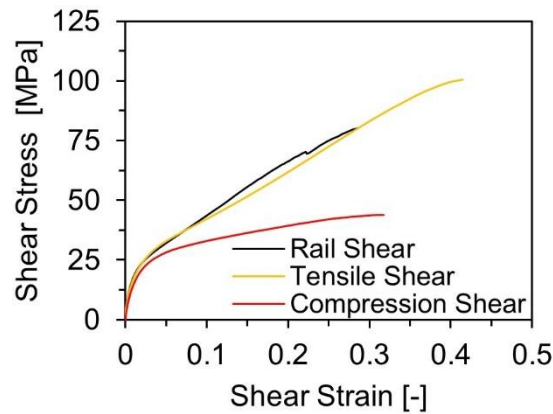


Figure 5.9 In-plane shear response measured by three test methods

It can be seen that the In-plane shear stress-strain responses were similar for the rail shear method and the tensile shear test. The effect of the multi-axial stress state in the tensile shear testing did not affect the stiffness. However, it led to an increase in the failure strength and strain value. Therefore, an appropriate failure criterion must also be chosen when dealing with complete failure of the material. However, the compressive shear curve was significantly lower than the tensile shear curve due to the difference in fiber rotation. A schematic of the fiber rotation is shown in Figure 5.10 with solid lines representing the initial position of the fibers and dashed lines representing the fiber orientation after the deformation-driven rotation of the fibers. In tensile loading, the fibers tended to rotate toward the loading direction, which increased the material's ability to bear higher loads. In contrast, under compression loading of angle-ply laminates, the fibers rotated away from the loading direction and hence reduced the load-bearing capacity.

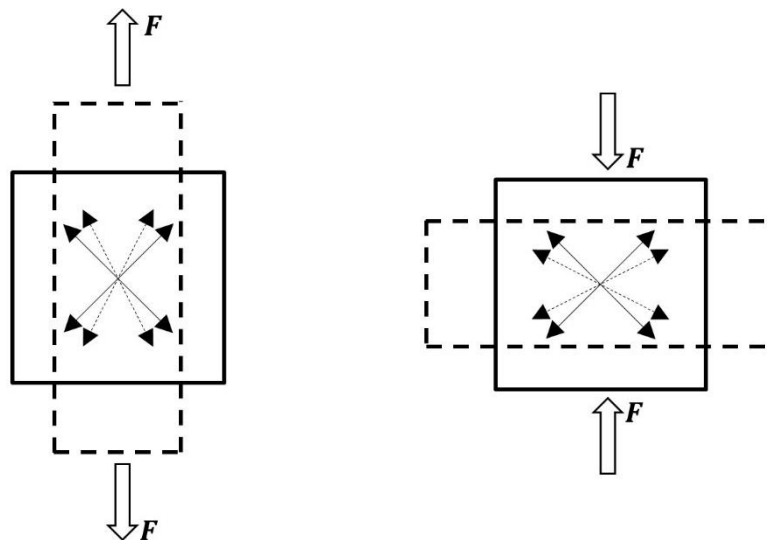


Figure 5.10 Schematic representation of the fiber rotation in the tensile shear (left) and compression shear (right) tests

### **Cyclic testing**

To quantify the plastic deformation and stiffness reduction due to damage, monotonic tests are not sufficient. For this purpose, cyclic tests were carried out with the same geometry and setup. Since the results produced by the rail shear method and the tensile shear test method produced the same results (with the exception of the failure strain and strength for modeling purpose), a full shear stress

strain was required, so cyclic tests were performed with tensile shear and compression shear methods only. In cyclic loading, a force of 1000N was increased in every cycle of loading before unloading. The results are shown in Figure 5.11.

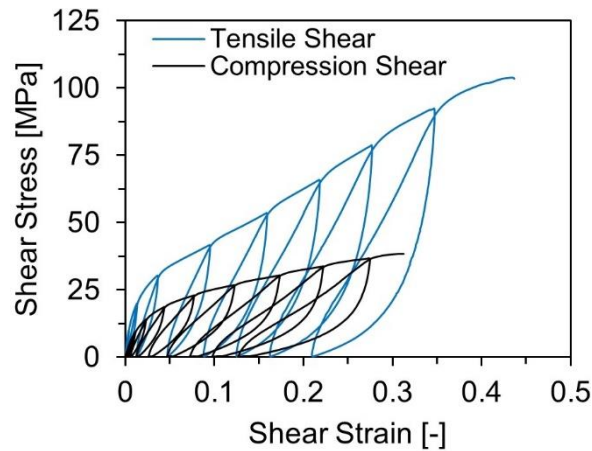


Figure 5.11 In-plane cyclic shear behavior measured by tensile and compression shear methods

To further compare the difference between tensile shear and compression shear, data acquired from cyclic testing could be used to compare the damage evolution and hardening curves of both tests, as seen in Figure 5.12.

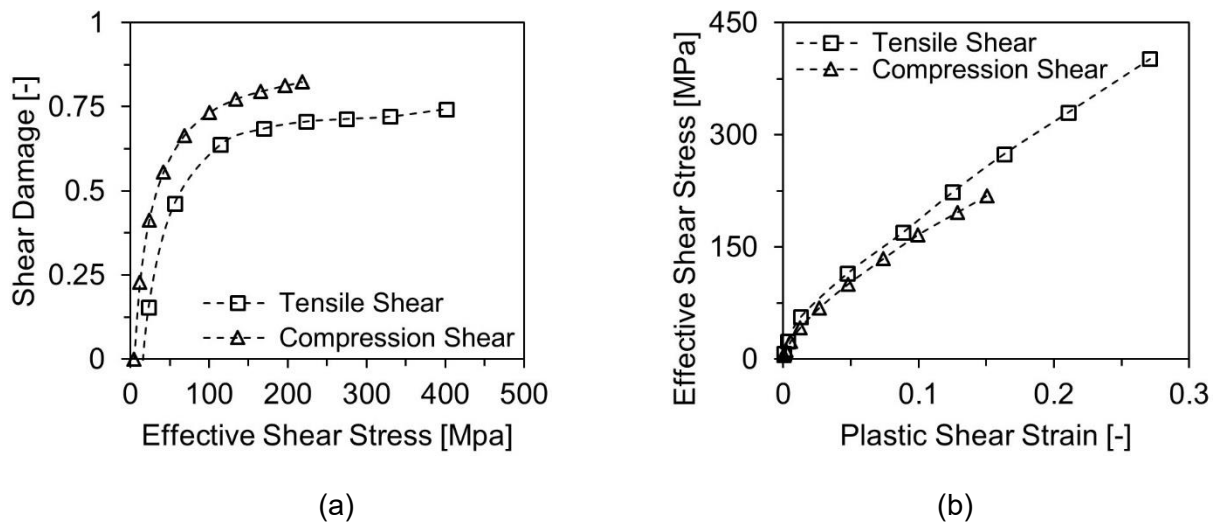


Figure 5.12 (a) Comparison of shear damage evolution measured from tensile shear and compression shear tests (b) Comparison of shear hardening curves measured from tensile and compression shear tests

In Figure 5.12(a), the curves intersecting with the x-axis corresponding to zero shear damage mark the damage onset shear stress  $S$ .

In light of the results shown in Figure 5.12 it is evident that on the macroscale, the shear curve followed two different hardening curves as well as different damage evolution laws depending upon the normal stress state in the material. A non-linear function must be used to describe the shear damage evolution law and plasticity. The material model should be able to distinguish the shear behavior in the presence of tensile or compression loading.

## 5.2 Improved shear modelling

As seen in section 5.1.4, that accumulation of plastic strain and stiffness degradation due to damage were dominating factors in the non-linear shear behavior of the woven fabric composites. It was found that the presence or absence of tensile normal stress or compression normal stress resulted in profound differences in measured shear properties. Therefore, material model must be able to distinguish between tensile shear and compression shear. A simple method, then, is proposed to detect and choose the materials' constants for shear based on the loading direction:

$$\text{sign}(\text{trace}(\boldsymbol{\varepsilon})) = \text{sign}(\varepsilon_1 + \varepsilon_2) = \begin{cases} +ve \rightarrow & \text{Tensile} \\ -ve \rightarrow & \text{Compressive} \end{cases} \quad (5.3)$$

Further, for calibration of shear damage parameters, experimental data were used, as proposed by Johnson [20] (see Figure 4.14 and Figure 4.15), in Figure 5.13.

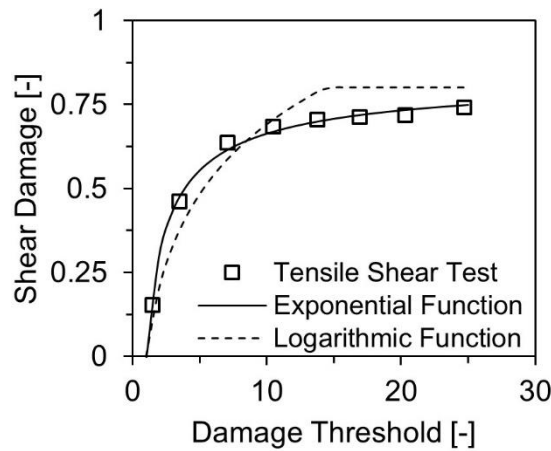


Figure 5.13 Calibration of shear damage parameters

It is obvious that the logarithmic function (Eqn. (4.33)) proposed by Johnson [20] does not fit the experimental data well. Instead, an exponential function for calibrating the damage is proposed as:

$$d_{12} = \min(m(r_{12})^n + o, d_{12}^{max}) \quad (5.4)$$

in which  $m, n$  and  $o$  are material constants measured from the cyclic shear test. This function restricts the maximum value of damage to  $d_{12}^{max}$ , which was measured experimentally. Thus, for the organo-sheet, the damage evolution function requires 3 parameters to be determined from a plot between the damage threshold and the damage.

### 5.2.1 Results

The user material model code was written as Fortran code and implemented as VUMAT in Abaqus. The verification of the results was done with cyclic loading of a single element with the fiber direction along  $45^\circ$ . The setup of the simulation model and results are shown in Figure 5.14. For better graphical presentation, only two cycles of the simulation results are shown.

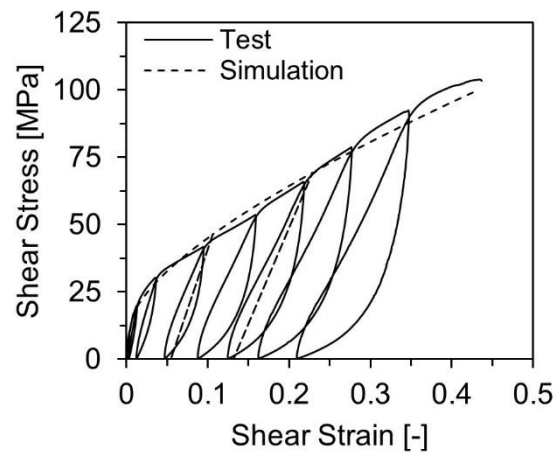
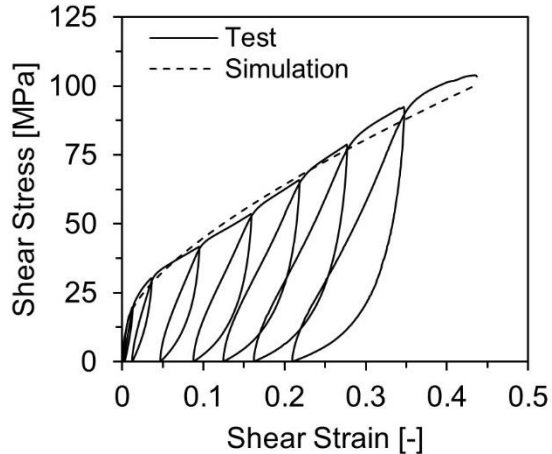


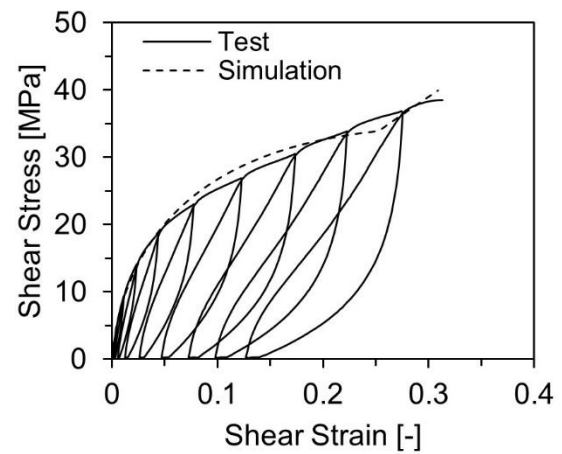
Figure 5.14 Verification of implemented user material model with cyclic loading of single element

As can be seen from the results shown in Figure 5.14, there was reasonable agreement between the simulation results and the experimental data. In simulation, the hysteresis was neglected. The plasticity and stiffness degradation were captured very well in the material model.

For further verification of the user material model, monotonic simulation results of the tensile shear and compression shear of the single element model were also compared with the experimental data shown in Figure 5.15. The output of solution-dependent variables enabled the comparison of inelastic strain and damage. The experimental data were from the cyclic tests, from which the material parameters were calibrated.



(a)



(b)

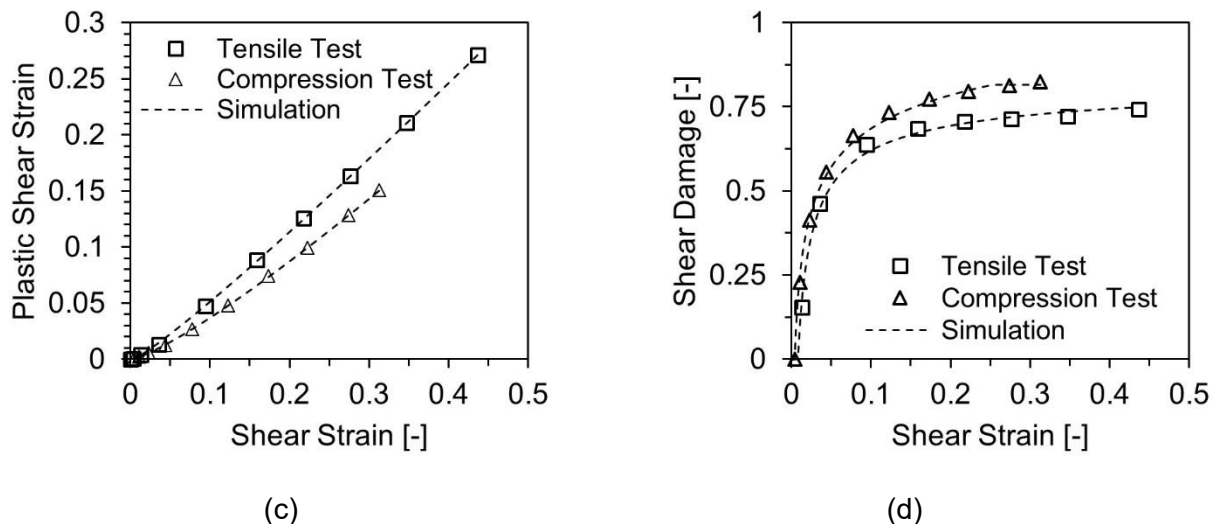


Figure 5.15 Comparison of user material model prediction and experimental data: (a) Tensile shear stress strain; (b) Compression shear stress strain; (c) Total shear strain versus plastic strains; and (d) Total shear strain versus shear damage

It was noted that the simulation results agreed with experimental results. Importantly, the use of the user material model enabled detection of the tensile/compression loading by itself; the input material parameters were then used accordingly. As such, the user-defined model can be used for the simulation of further models.

### 5.3 Validation

After verification of the model on single element simulations, simulation results were validated on three-point bending of  $\pm 45^\circ$  laminate of four plies. The test setup was the same as explained in chapter 4.4.1 and Figure 4.16 except the fiber orientation of specimen. The test specimens had rectangular dimensions of 100 mm x 25 mm x 2 mm. The impactor and two support rollers had a 10 mm diameter with supports at a distance-defining span length of 60 mm. A displacement-controlled loading was applied at the speed of 5 mm/min until the force level reached the maximum and then dropped. It was kept even at extreme bending, so that the specimen could not come in contact with the internal part of fixture other than the supports and impactor.

This test was chosen because in three-point bending, the lower half of the material was under tensile loading and the upper half experienced compression stress at the same time. Due to the diagonal orientation of the fibers, the material also underwent shear deformation. Therefore, the lower half of the sample, under bending, experienced tensile shear stress while at the same time the upper half of the sample experienced compression shear stress. Therefore, this simple and comprehensive test was used to verify whether the user material subroutine can simultaneously detect the loading type in finite elements. It also proved that user material model was able to automatically detect the compression and tensile shear loading and how it improved the simulation results.

A simulation model is shown in Figure 5.16 with a rigid impactor and supports. The impactor was modeled as a cylindrical form as only the radial part of the impactor came in contact with the specimen. To reduce the computational time of explicit simulation, the simulation time was reduced to 20 ms.

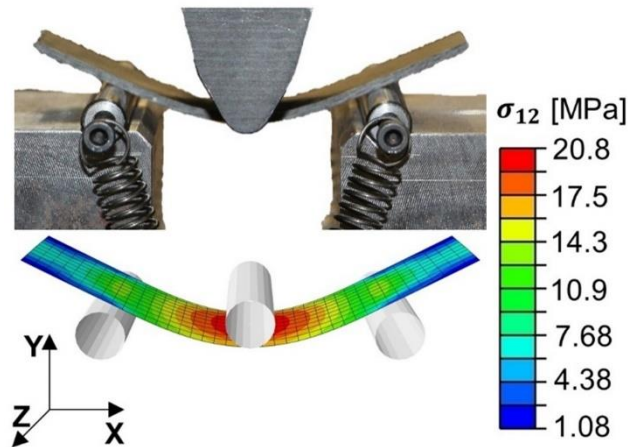


Figure 5.16 Three-point bending test and simulation showing shear strain of the bottom most ply at deformation of 8.6mm

To avoid the dynamic effects, the displacement boundary conditions were applied on the rigid impactor using *Smooth amplitude*. This method gradually ramped up the deformation and resulted in the avoidance of undesirable inertial effects (see Figure 5.17(a)). To avoid the slippage of the specimen in the z-direction, the tangential frictional coefficient was set equal to 0.03. To confirm the quasi-static response of the simulation and to avoid unwanted errors, the energy output was requested in the simulation model, as shown in Figure 5.17(b).

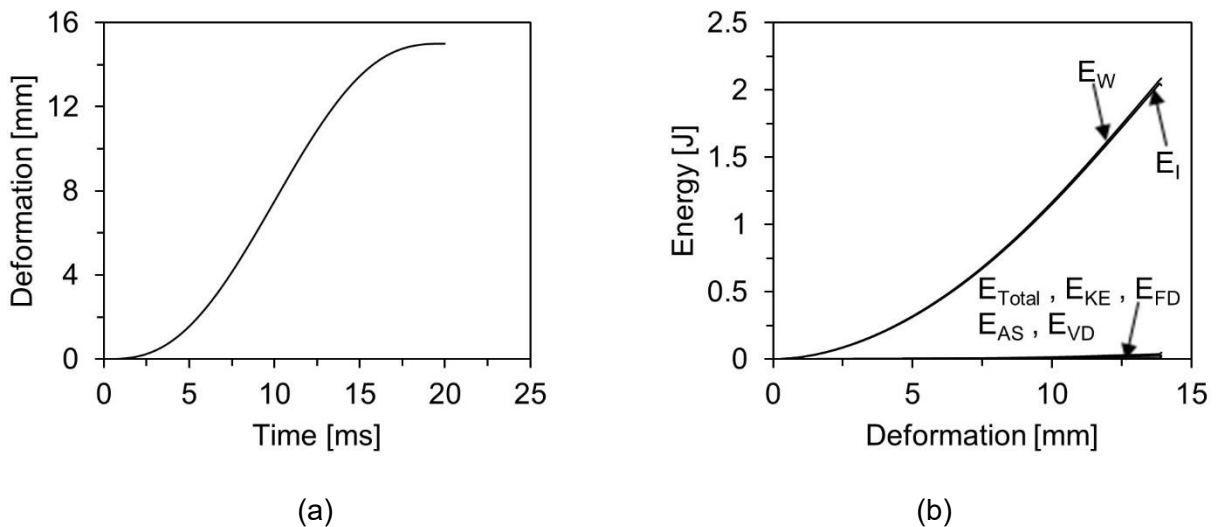


Figure 5.17 (a) Applied displacement B.C with smooth amplitude on impactor in FEM simulation  
(b) Total energy output of the simulation model

The total strain energy  $E_i$  was almost equal to external work  $E_w$ . Energy lost to kinetic energy  $E_{KE}$ , frictional dissipation  $E_{FD}$ , artificial strain energy  $E_{AS}$ , and viscous dissipation  $E_{VD}$  were negligible in comparison to external work. Finally, the simulation results were plotted against experimental results and results are shown in Figure 5.18.

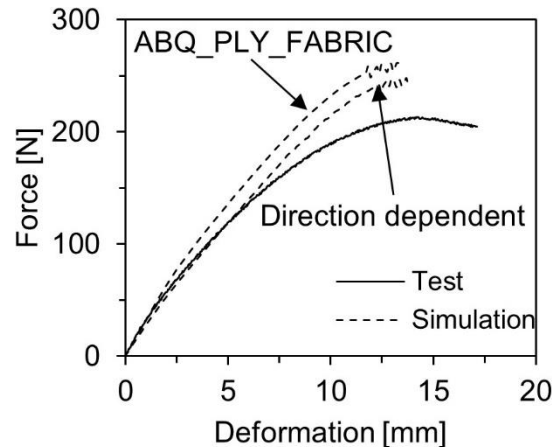


Figure 5.18 Simulation of three-point bending showing improvement in prediction results by using directional-dependent parameters in comparison to parameters measured by tensile shear only

In Figure 5.18 the simulation curve labelled as *direction dependent* shows the result where the user material model automatically chose tensile shear parameters for finite elements under tensile loading and compression shear parameters for elements under compression loading. The simulation curve labeled as *ABQ\_PLY\_FABRIC* shows results where only shear parameters measured from the *Tensile Shear Test* were used, which was generally used up to now. For deformation up to 7 mm, those test data and simulation data are in good agreement. At higher deformation, the gap between the test data and the simulation data increases but still *direction dependent* simulations results are closer to the experimental data and better than state-of-the-art. Therefore, it was noted that automatic detection of the loading direction and the selection of corresponding parameters improved the accuracy of the predictions.

The need for automatic detection of direction-dependent parameters is more important for the load cases in which off-axis laminates are subjected to compression loading, e.g. with an axial crash of cylindrical tubes.

#### 5.4 Conclusion

In this study, the influences of tensile and compression stress in the fiber direction relative to shear behavior were investigated. The rail shear method was used to measure the pure shear behavior of the composite, while tensile and compression testing of  $\pm 45^\circ$  laminate were used to measure shear behavior in the presence of tensile and compression stresses, respectively. It was found that:

- Measured shear properties of woven fabric composite are dependent upon test type;
- Shear strength and shear failure strain increase in the presence of tensile normal stress;
- Shear resistance of the material significantly reduces in the presence of compression stresses;
- The Ramberg-Osgood hardening and exponential function of damage, in terms of effective shear stress, fits well for modeling the shear behavior twill woven fabric composite material;
- Mathematically, the sign of trace of strain tensor was used successfully to detect the type of loading, so that appropriate material parameters can be selected for modeling;
- The implemented user material model predicted the shear behavior of the material perfectly on the coupon level; and

- The simulation of three-point bending of  $\pm 45^\circ$  laminate proved the effectiveness of the improved CDM model.

## 6 Strain-rate modelling

It is well known that the material properties of the composites usually show an increase in the stiffness and strength at higher strain rates. Organo-sheets also exhibit strain rate dependency but the-state-of-the-art material models ignore the strain rate effects, which have strong influence on the strength and stiffness properties of the material [5], [7]. During crash events, the material can reach deformation with strain rates of up to 500 1/s. Therefore, it is necessary to measure the material's strain rate-dependent properties and incorporate the strain rate effects into the material model for explicit dynamic simulations.

The focus of work in this chapter is on testing and modeling of the strain rate dependent behavior of 102-RG600. The results were implemented as user material subroutine which has better shear behavior prediction and is an improved version of ABQ\_PLY\_FABIRC [47], [48]. In section 6.1 an insight is provided as to how testing techniques are used to measure the strain rate dependent stress-strain curves of the material. Experimental measurements of (1) tensile stress-strain at various strain rates (2) shear stress-strain at different strain rates and (3) cyclic shear tests at different speeds are done. In section 6.2, improvements to the CDM model based on evidence of the strain rate dependent experimental data are proposed. The strain rate dependent CDM model is then implemented as a user defined material model (VUMAT) in Abaqus, and the working ability of VUMAT is verified on a single element simulation. Finally, in section 6.3, the validation of simulation results was done with crash test of u-profile in three-point bending configuration on drop.

### 6.1 Test

To investigate strain rate dependency, tests were carried out at universal material testing machine Zwick Z100 and high-speed testing machine HTM 5020 manufactured by Zwick/Roell. Z100 is an electromechanical controlled machine and has a testing speed range from 0.1  $\mu\text{m}/\text{min}$  to 1.5 m/min. HTM 50/20 has tests test speed range from 0.4m/s to 20m/s and it can measure forces up to 50 kN. Therefore, low speed tests were done on Z100 and high speed tests were carried on HTM 50/20.

The strain was measured with an optical strain measuring system, ARAMIS supplied by GOM Germany. For quasi-static tests 5M camera system was used for digital images. For high speed tests high-speed video system FASTCAM SA5 manufactured by Photron was used. Camera systems and Zwick machines were connected electronically for synchronization of force and deformation.

#### 6.1.1 Tensile strain-rate dependency

For all the tensile tests, same specimen geometry was used as discussed in 3.2.1. All the specimens had dimensions of 250 mm x 25 mm x 2mm cut with water jet cutting machine with fibers along the loading direction. Four end tabs with dimensions of 50 mm x 25 mm x 1.5 mm were glued on every specimen with industrial glue Sicomet-77 manufactured by Henkel Germany.

Tensile tests were conducted at eight different speeds. With the Z100, tests were carried at three different speeds while with HTM 50/20, they were carried out at five different speeds. Due to these different testing speeds, the digital images were recorded at different frame rates. Table 6-1 summarizes the test plan for tensile strain rate dependency of 102-RG600.

Sr. no.	Test speed	Nominal strain-rate [1/s]	Machine	Camera frame rate
1	1.5 mm/min	1.67E-04	Z100	2 fps
2	2.0 mm/min	2.22E-04	Z100	1 fps
3	27 mm/min	3.0E-03	Z100	10fps
4	1 m/s	6.67	HTM 50/20	50000
5	5 m/s	33.33	HTM 50/20	50000
6	10 m/s	66.67	HTM 50/20	50000
7	15 m/s	100	HTM 50/20	50000
8	20 m/s	133.33	HTM 50/20	50000

Table 6-1 Tensile test plan with test speed, testing machine used for test and camera frame rate for measuring strain

The nominal strain was calculated from the crosshead speed as:

$$\text{Nominal Strain Rate} = \frac{\text{Test speed}}{\text{Gauge length}} \quad (6.1)$$

In high-speed test, the resolution of the camera was 192 x 496 pixels. The strains were measured on the entire width of the sample and 80 mm gauge length. In the high-speed tests, there was a tradeoff between the resolution of the camera and the frames per second. Since the frame rate in the quasi-static tests was small, the resolution of the camera was high at 480 x 1920 pixels.

### Results

The specimen was pulled until failure, and the strain on the surface of material was calculated using ARAMIS software (see Figure 6.1 and Figure 6.2).

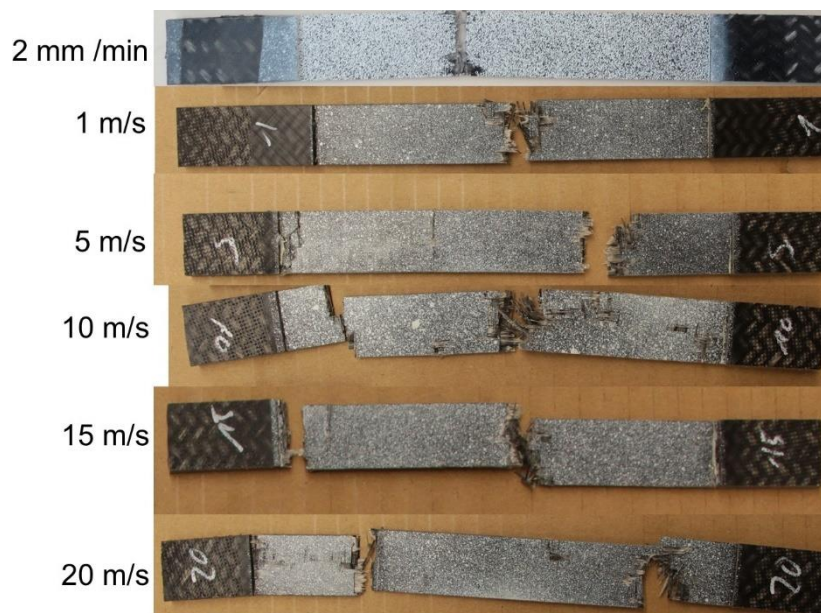


Figure 6.1 Tensile test specimens after testing at different speeds

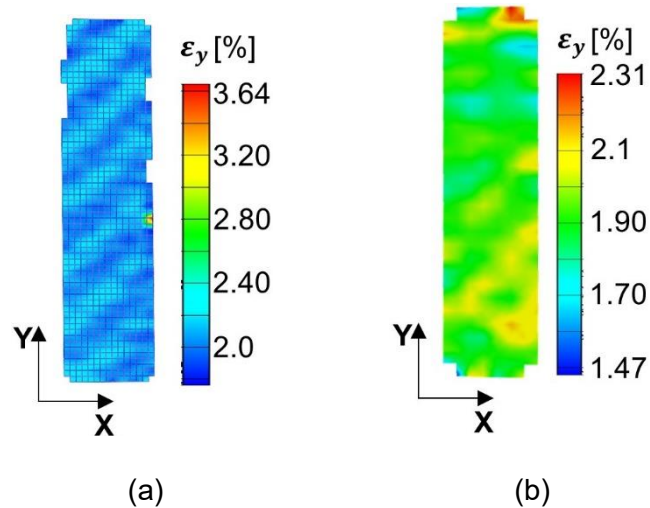
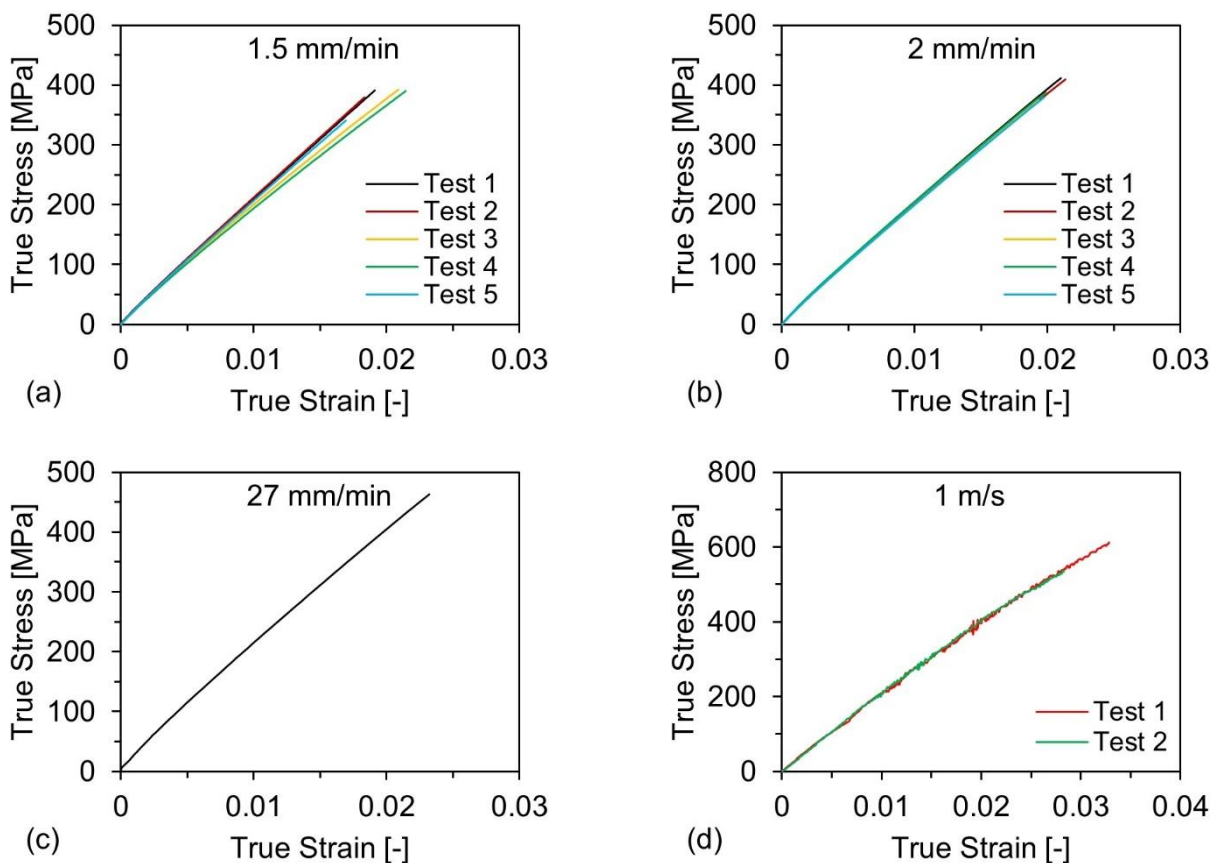


Figure 6.2 (a) Measured tensile strain of a specimen with test at a speed of 2 mm/min and (b) test with 15 m/s at an average strain value of ca. 2%. Due to inhomogeneity of the measured strain, the average of all the strain facets was calculated

Test were evaluated as explained for tensile testing in chapter 3.2. The measured stress-strain plots are given in Figure 6.3.



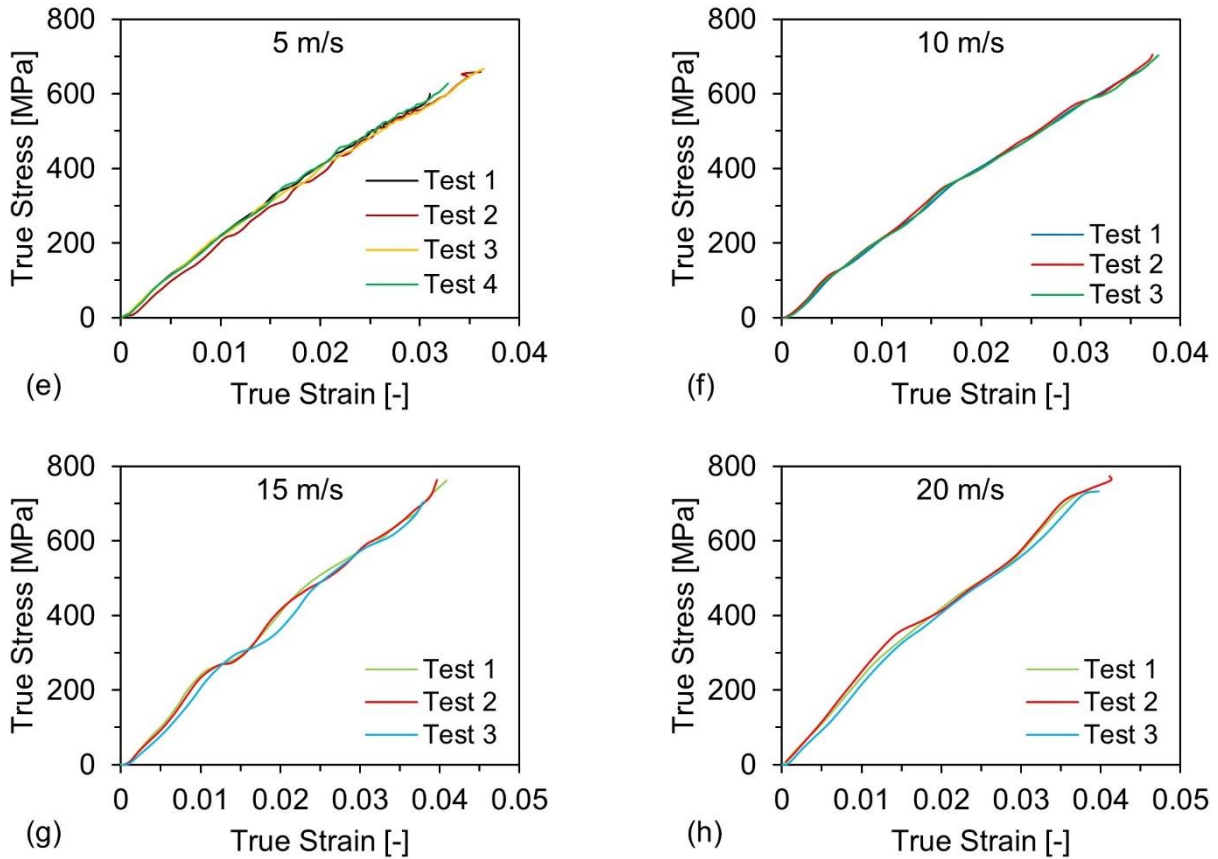


Figure 6.3 Tensile stress strain results of 102-RG600(4) at test speeds of;(a) 1.5 mm/min ,(b) 2 mm/min ,(c) 27 mm/min, (d) 1 m/s, (e) 5 m/s, (f) 10 m/s, (g) 15 m/s, and (h)20 m/s

Figure 6.3 shows that for tests at lower speeds the material exhibit perfectly linear elastic brittle behavior. A load reversal will show that no plasticity is induced in the material. As the speed of testing increases, fluctuation in stress strain curve is seen. Oscillation in the stress-strain results is due to system ringing effect associated with high speed testing. As the speed of test increases, the time between two consecutive measurement points increases. Therefore, if the same specimen could be tested at even higher speed e.g. at 50 m/s, then these fluctuations would be even more pronounced. Dedicated specimen geometries are required for testing at very high strain rates which can produce results without high oscillation of forces [73]–[75]. A constant strain rate during the tests was not achieved. Therefore, an average strain rate was calculated for every specimen individually. Nominal strain rate calculated from the test speed is not the actual strain due to small elongation machine rods pulling the specimen, slippage etc. Therefore, an average strain rate  $\dot{\epsilon}$  was calculated from the measured failure strain and test time.

$$\dot{\epsilon} = \frac{\text{Failure strain}}{\text{Test time}} \quad (6.2)$$

In Figure 6.4 the average true stress-strain curves of 8 tensile speeds are plotted together.

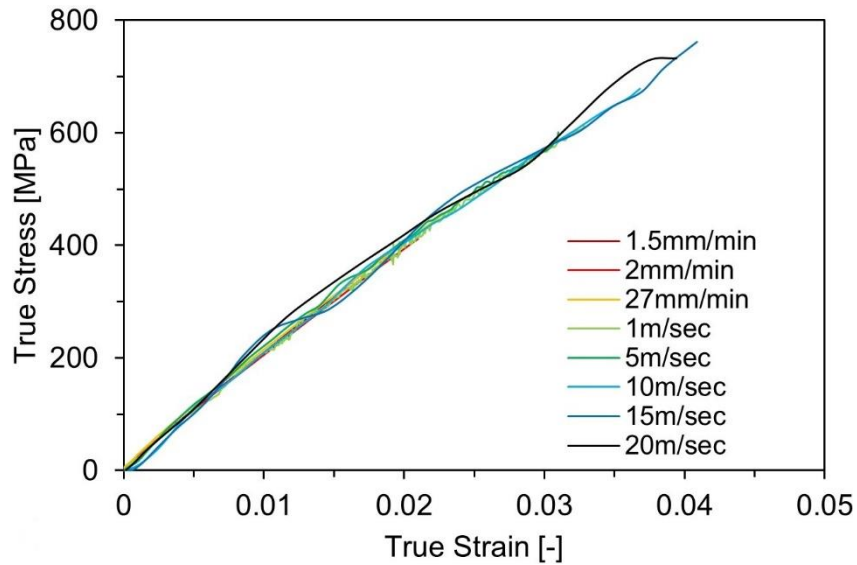


Figure 6.4 Comparison of tensile stress-strain behavior exhibited by 102-RG600 at different speeds

As shown in Figure 6.4, the tensile strength of the material increases rapidly in the range of quasi-static to measured strain rate of 23 1/s (or 5m/s). The increase in strength decreases as the strain rate increases further. Note that the number of data points also decreases with the increasing strain rate. The reason is that a constant frame rate was used for all the tests performed with the HTM 50/20. As the strain rate increases, the time to failure decreases. Therefore, in a shorter length of time, fewer images can be captured by the camera. The frame rate can be increased if the camera resolution or strain measurement is reduced. Due to the inhomogeneity of the material, a very small camera resolution and thus a small area for the strain measurement would not be acceptable. So, a compromise between the frame rate and strain measurement area was accomplished. Because the Zwick HTM 50/20 has a maximum testing speed of 20 m/s, in order to test the material at even higher strain rates, the specimen gauge length had to be smaller.

Table 6-2 gives a summary of all the tests results along with the measured material properties. Detailed test results of every speed are given in Annex 12.1.4. and specimen photos are shown in 12.2.9.

Test speed	Nominal strain-rate [1/s]	No. of tests	Measured strain-rate [1/s]	E-modulus [GPa]	Tensile strength [MPa]	Failure strain [%]
1.5 mm/min (St. deviation)	1.67E-04	5	7.60E-05 (3.68E-06)	19.02 (0.84)	378.82 (21.75)	1.93 (0.18)
2 mm/min (St. deviation)	2.22E-04	5	1.12E-04 (1.89E-04)	18.48 (0.87)	392.38 (16.92)	2.02 (0.08)
27 mm/min	3.0E-03	1	2.4E-03	19.62	473.43	2.38
1 m/s (St. deviation)	6.67	4	3.00 (0.35)	19.83 (0.13)	576.43 (30.98)	2.88 (0.38)
5 m/s (St. deviation)	33.33	4	23.03 (1.72)	20.40 (0.36)	642.69 (27.72)	3.32 (0.26)

10 m/s (St. deviation)	66.67	3	60.85 (3.86)	19.68 (0.36)	695.05 (14.25)	3.72 (0.05)
15 m/s (St. deviation)	100	4	89.77 (5.16)	22.93 (1.34)	731.56 (35.53)	3.94 (0.12)
20 m/s (St. deviation)	133.33	3	113.94 (8.15)	24.16 (1.49)	742.93 (26.60)	4.01 (0.09)

Table 6-2 Strain rate dependent tensile properties of 102-RG600(4)

The results summarized in Table 6-2 reveal that the measured strain rate is always less than the nominal strain rate. Up to 15 m/s the E-module remains almost constant and, at 15 m/s and 20 m/s it increases. However, if the curves in Figure 6.3 and Figure 6.4 are compared, this increase may be considered as a result of force or stress fluctuations in the high-speed tensile tests. Therefore, in this work, the E-module is considered to be strain rate-independent as in [5]. The tensile strength and failure strain exhibit almost a 100% increase when the strain rate increases from quasi-static to 120 s<sup>-1</sup>. The dependence of the tensile strength and failure strain on the strain rate is shown in Figure 6.5.

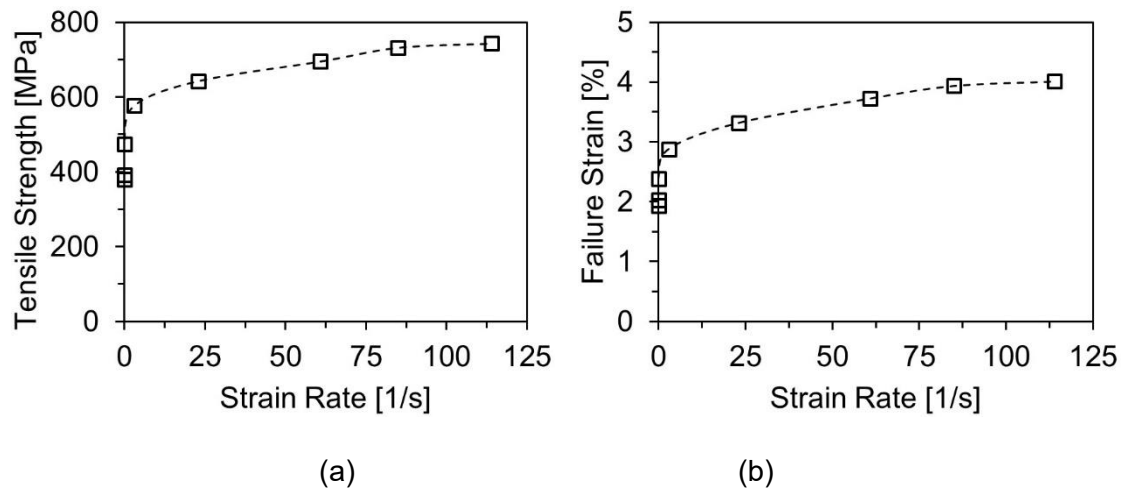


Figure 6.5 (a) Strain rate-dependent tensile strength and (b) tensile failure strain of 102-RG600

Results of Figure 6.5 show that at lower strain rate the tensile strength and failure strain increases rapidly with increasing strain rate. Then the rate of increase in strength and failure strain decreases and reaches a plateau. The reason is that at lower strain rates, isothermal conditions exist for the material. As the material undergoes deformation at higher strain rates, adiabatic heating takes place. At high temperatures, the strength of material decreases and cannot reach maximum value as it would otherwise under isothermal conditions [76]–[80]. This effect must be considered in the future.

### 6.1.2 Shear strain-rate dependency

The shear tests were conducted also just like tensile test except that the fiber orientation was at 45° along the loading direction. The specimen's geometry with gauge length 150mmx25mmx2mm and testing procedure was chosen according to ISO-14129 [46]. Shear tests were carried out at seven different speeds. The test plan, with the testing speed, machine used for testing, and frame rate, is summarized in Table 6-3.

Sr. no.	Test speed	Machine	Camera frame rate
1	1.5 mm/min	Z100	0.45 fps
2	2.0 mm/min	Z100	1 fps
3	27 mm/min	Z100	5fps
4	1 m/s	HTM 50/20	25000
5	5 m/s	HTM 50/20	25000
6	10 m/s	HTM 50/20	25000
7	15 m/s	HTM 50/20	25000

Table 6-3 Test plan for strain rate dependent shear behavior of RG600

The camera frame rate for shear testing (Table 6-3) is different from tensile testing (Table 6-1) because shear failure strain is much higher than tensile failure strain and hence longer test time was required. In order to get enough data points for shear strain measurement without exceeding the data saving limit, lesser frame rate was chosen. In quasi-static tests, the resolution of the camera was 480 x 1920 pixels. In high-speed tests, the resolution of the camera was 192 x 496 pixels.

The nominal shear strain rate could not be directly calculated from the test speed, because the shear strain of the specimen with  $\pm 45^\circ$  orientation was calculated from axial and transverse strain.

$$\gamma_{12} = \varepsilon_y - \varepsilon_x \quad (6.3)$$

Shear tests were evaluated as explained in Chapter 3.4.

The specimen were tested until failure, and the specimens after the tests are shown in Figure 6.6. The measured ARAMIS strain is shown in Figure 6.7.



Figure 6.6 Tensile shear specimens tested at different speeds. More specimen photos are given in Annex 12.2.10

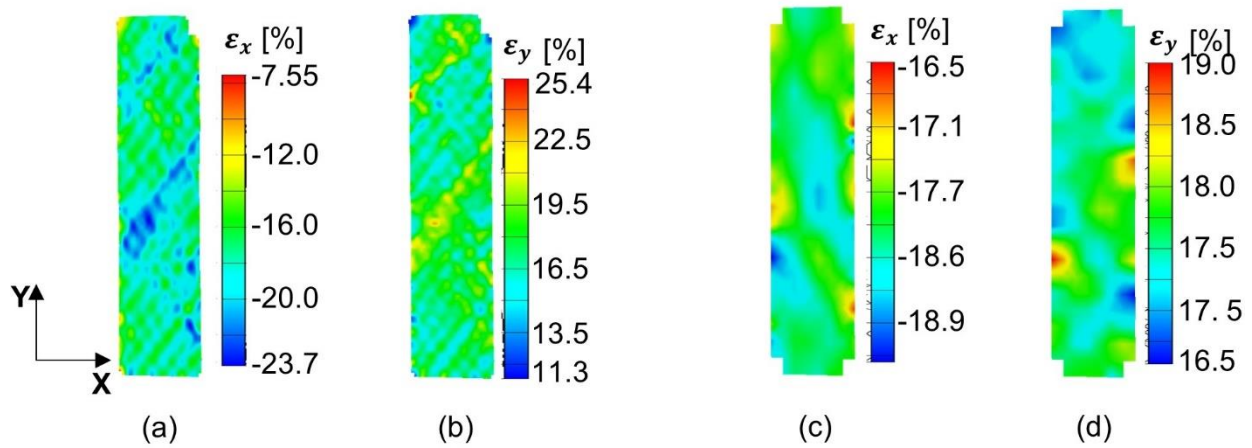
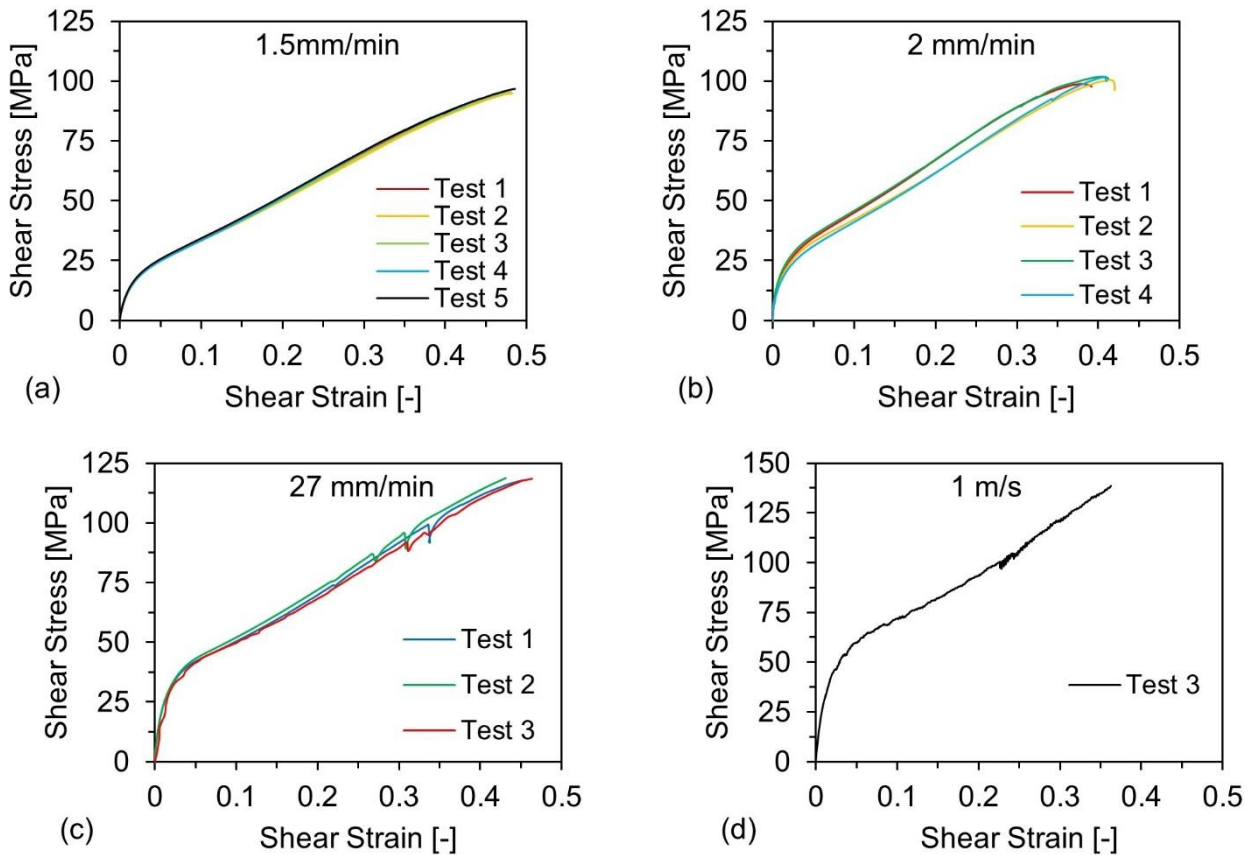


Figure 6.7 (a) Transverse and (b) longitudinal strain measured optically at test speed of 2 mm/min and (c) transverse (d) longitudinal strains measured at speed of 5 m/s corresponding to a shear strain of 36%

For the shear strain calculation, again, due to inhomogeneity, the average strain value from the whole measurement was taken. It is also visible that, at 2 mm/min, even the fiber strands could be detected running diagonally from the strain measurements of the tests. However, at a higher test speed, the degree of inhomogeneity increased. Shear stress strain plots of all the tests is given in Figure 6.8.



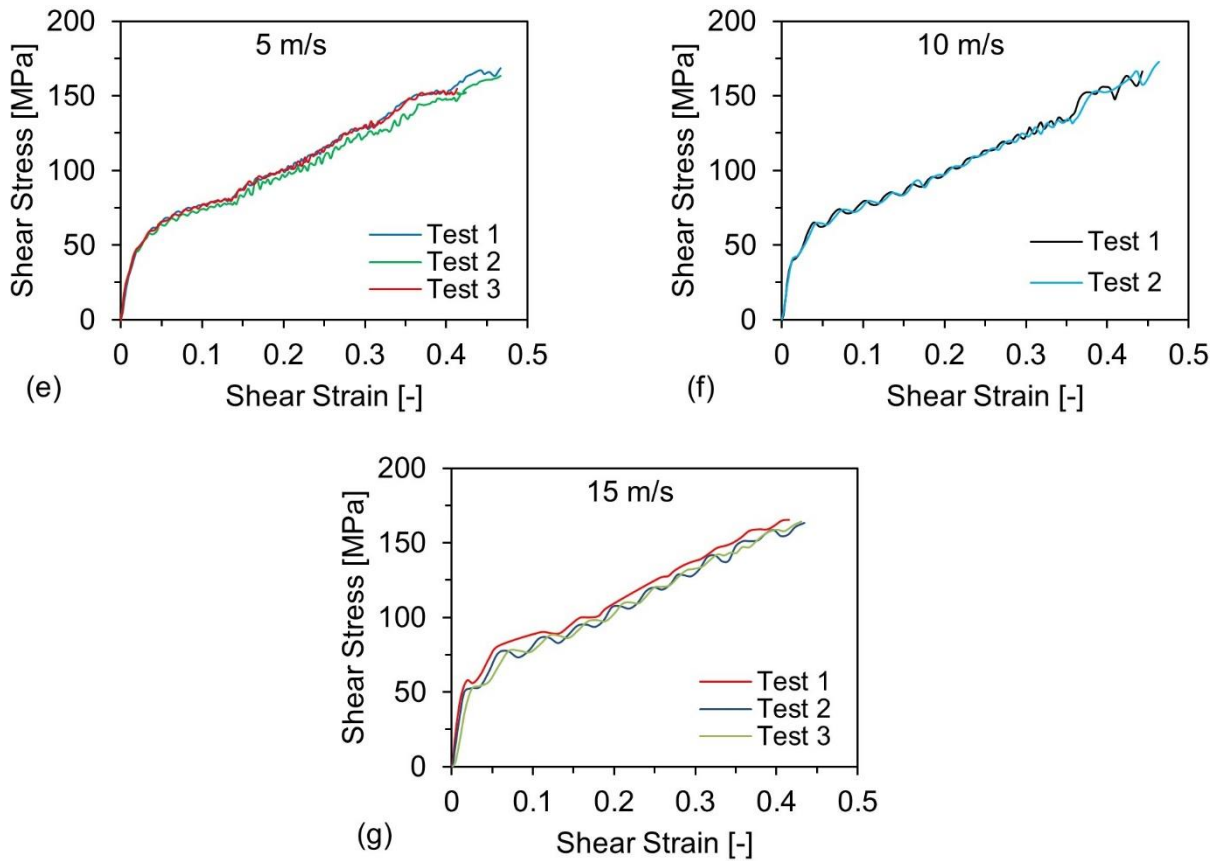


Figure 6.8 Shear stress strain results of 102-RG600(4) at test speeds of;(a) 1.5 mm/min ,(b) 2 mm/min ,(c) 27 mm/min, (d) 1 m/s, (e) 5 m/s, (f) 10 m/s, and (g)15 m/s

The oscillation pattern for shear stress-strain seen in Figure 6.8 is same as that for tensile behavior, indicating that, as the test speed increases, so do the oscillations in the force response and, eventually, stress. The average strain rate at the end of the test was calculated by:

$$\dot{\gamma} = \frac{\text{Shear failure strain}}{\text{Test time}} \quad (6.4)$$

One curve from each test speed was chosen for comparison of results at different speeds (see Figure 6.9a). And a 3D interpolated surface was created and shown in Figure 6.9b.

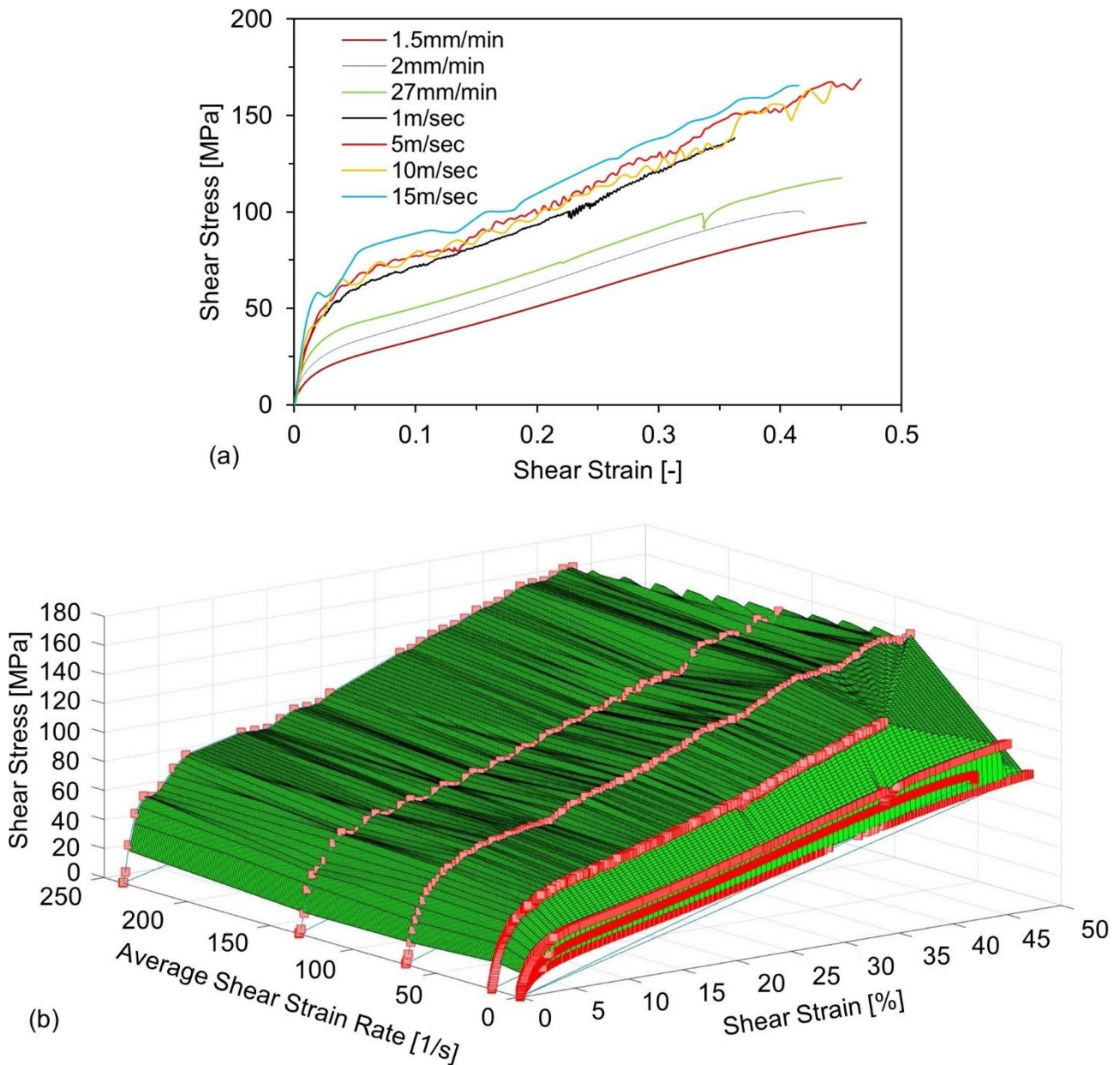


Figure 6.9 Comparison of shear stress-strain behavior exhibited by RG600 at; (a) different speeds, and (b) 3D visualization with respect to measured shear strain rate

If the rate dependent shear results shown in Figure 6.9 are compared, it is evident that the shear strength increases significantly with increasing rate of loading. However, at higher strain rates, the shear strength did not increase due to adiabatic heating effect. The non-linear region in all the tests begins at a very early stage, and using only a few data points to calculate the shear-chord modulus is difficult and inconsistent. Thus, they are not considered. In Table 6-4, the results of the measured shear properties are summarized. Detailed test results of every speed are given in Annex 12.1.5. and specimen photos are shown in Annex 12.2.10.

Test speed	No. of tests	Measured shear strain rate [1/s]	Shear strength [MPa]	Shear failure strain [%]
1.5 mm/min	5	3.15e-4	94.27	46.83

(St. Deviation)		(3.9e-6)	(2.64)	(2.5)
2 mm/min	4	4.07e-4	100.74	40.84
(St. Deviation)		(1.14e-5)	(1.3)	(1.2)
27 mm/min	3	5.11e-3	118.26	44.84
(St. Deviation)		(8.5e-5)	(0.54)	(1.6)
1 m/s	3	16.86	145.03	40.08
(St. Deviation)			(7.74)	(3.9)
5 m/s	3	68.83	162.33	44.87
(St. Deviation)		(0.61)	(6.96)	(0.03)
10 m/s	3	132.97	166.62	43.92
(St. Deviation)		(4.95)	(6.05)	(2.6)
15 m/s	3	238.84	164.21	42.66
(St. Deviation)		(4.95)	(1.18)	(1.0)

Table 6-4 Strain rate dependent shear properties of 102-RG600(4)

The shear response is non-linear, therefore, apart from the shear strength and shear failure strain, other material parameters, such as the plastic strain and damage need to be calculated to fully understand the material. Thus, for this purpose, cyclic shear tests with the same geometry and setup were carried out at three different speeds; (a) 2 mm/min, (b) 4 mm/min, and (c) 27 mm/min. Cyclic tests at higher speed with the HTM50/20 were not possible. Under cyclic loading, a force of 1000 N was applied in the first cycle before unloading and the force level was increased by 1000 N in every successive loading/unloading cycle. The test continued until the specimen could no longer take the load and broke. The results are shown in Figure 6.10.

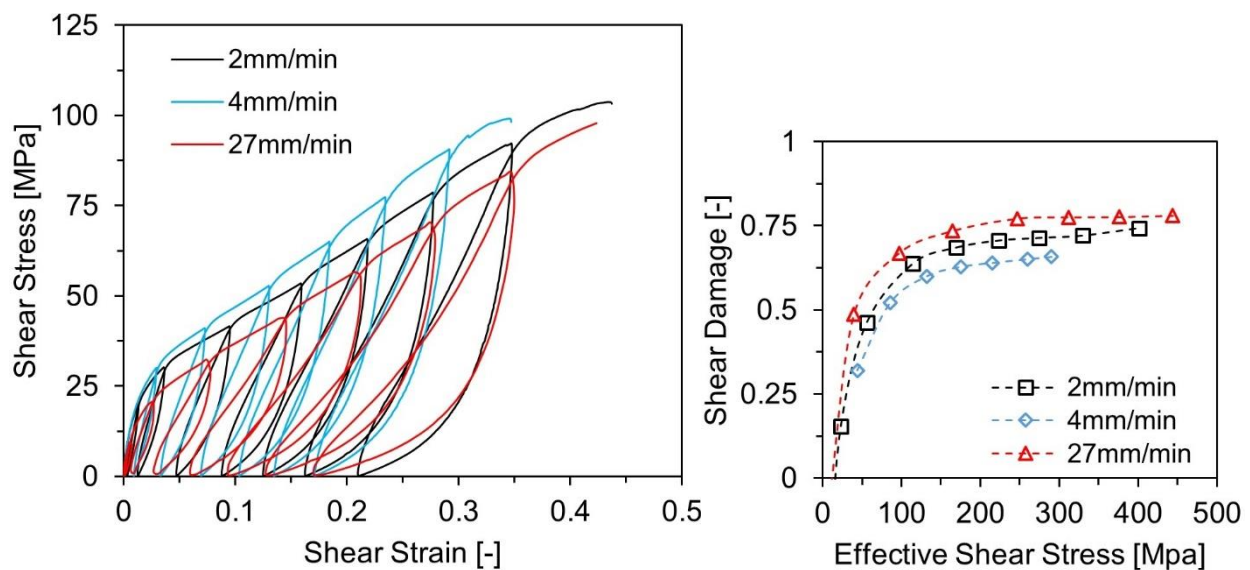


Figure 6.10 shear stress-strain response of cyclic shear tests at three different speeds

Results shown Figure 6.10 indicate that the cyclic response of material at different test speeds remains in a small range opposed to the speed dependent monotonic tests results which are strongly different as shown in Figure 6.9. The reason could be that during the unloading, material gets time to relax itself and additional stresses produced due to high speed loading are reversed. Finally, the cyclic response is similar to the quasi-static response in terms of strength, failure strain, shear elasticity modulus and damage.

In all the shear tests (cyclic, monotonic quasi-static and high speed) the shear failure strain has remained almost constant. Therefore, for any given value of shear strain  $\gamma_{12}$ , the amount of shear elastic strain  $\gamma_{12}^{el}$  and shear plastic strain  $\gamma_{12}^{pl}$  is the same for all the curves. The inelastic/plastic shear strain  $\gamma_{12}^{el}$  was measured by cyclic shear tests. And the shear stress  $\tau_{12}$  was measured by monotonic shear tests. With this information, the slope  $G_{12}^n$  and hence shear damage  $d_{12}$  can be calculated as:

$$G_{12}^n = (1 - G_{12}^o)d_{12} = \frac{\tau_{12}}{\gamma_{12}^{el}} \quad (6.5)$$

In which  $G_{12}^o$  is the initial shear modulus measured from the very first test cycle. Thus the damage  $d_{12}$  was calculated for the high-speed tests and used to determine the damage onset point. With the calculation of the shear damage, a the shear stress and shear damage curves at different speeds were calculated and are shown in Figure 6.11.

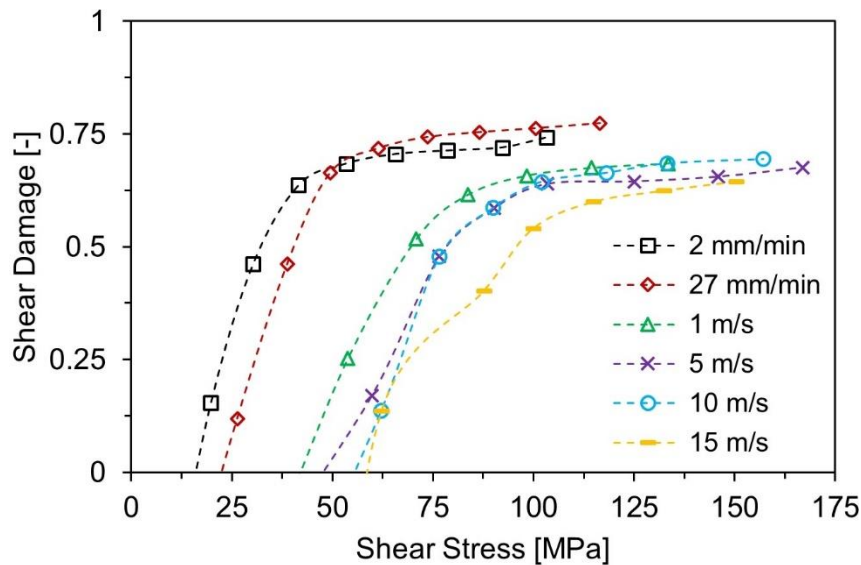


Figure 6.11 Shear damage in RG600 at different test speeds

In Figure 6.11, the point of intersection between curve and x-axis (shear stress) is where the shear damage in the material equals zero. This point corresponds to the shear damage onset point. It can be seen that with increasing test speed, the damage onset point also increases. A plot between shear strain rate and damage onset point is given in Figure 6.12. The damage onset point increases sharply in the initial strain rate range until 20 1/s and then it reaches almost a plateau.

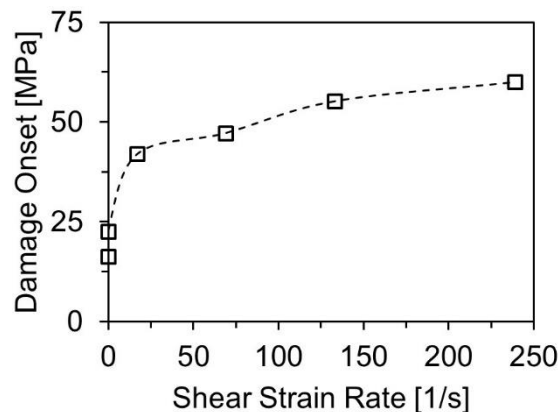


Figure 6.12 Shear strain rate dependent damage onset

## 6.2 Strain rate-dependent modeling

With strain rate-dependent material data available, the strain rate dependent material parameters could be implemented into the material model.

### 6.2.1 Strain rate dependency in the fiber direction

The experimental data shows that, along the tensile direction, the E-module remains constant and the tensile strength increases with the increasing strain. A strain rate-dependent strength in the fiber direction is thus written as:

$$X_t = X_{t0} + a(\dot{\varepsilon} - \dot{\varepsilon}_0)^b \quad (6.6)$$

Where  $X_t$  is the strain rate-dependent strength along the fiber direction,  $X_{t0}$  is the quasi-static strength,  $\dot{\varepsilon}$  is the strain rate at which the strength value is calculated,  $\dot{\varepsilon}_0$  is the quasi-static strain rate and  $a$  and  $b$  are constants which are determined from the experimental data shown in Figure 6.5.

After the implementation of the strain rate-dependent strength Eqn. (6.6) into the material model, tensile simulations with fibers aligned along the direction of loading were run on a single element model (see Figure 4.3a) at different strain rates. The stress-strain response is shown in Figure 6.13 and the maximum strength achieved in this simulation is compared with the experimental data.

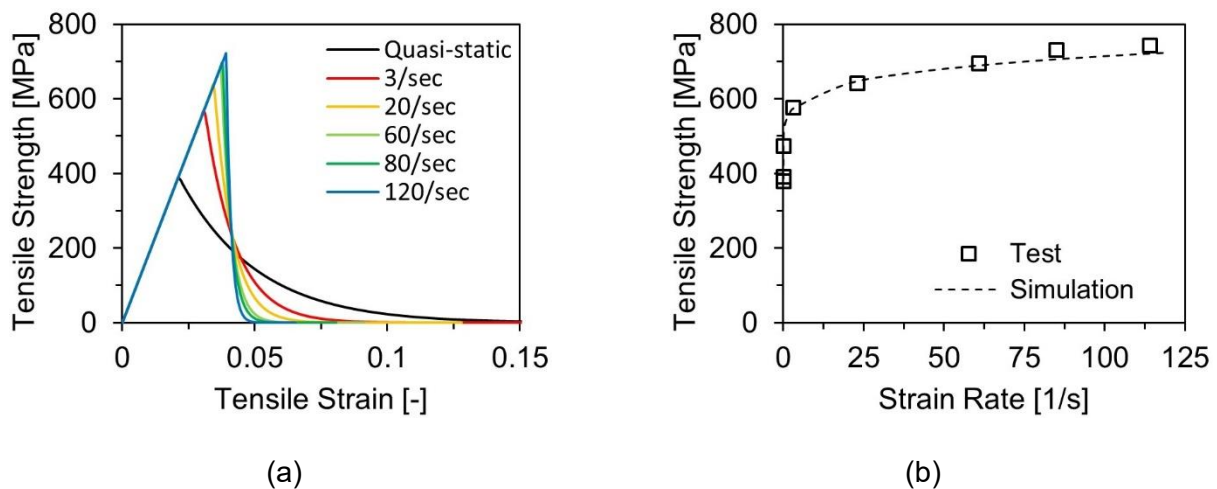


Figure 6.13 (a) Tensile stress strain response in single-element simulation model with a strain rate-dependent material model and (b) the tensile strength as function of the strain rate

It can be seen in Figure 6.13a that the elastic modulus of all the simulation remained constant. The maximum stress value however increased with the increasing strain rate, after which the damage started to increase and finally results in the full failure of element. The maximum stress values agree quite well with the experimental data. The damage curves for different strength is different because damage is a function of tensile strength according to Eqn. (4.23).

### 6.2.2 Strain rate dependency along in-plane shear

In order to incorporate the strain rate dependency for the in-plane shear a strain rate-dependent shear damage onset function similar to the Eqn. (6.6) is defined:

$$S = S_0 + C(\dot{\gamma}_{12} - \dot{\gamma}_0^{12})^g \quad (6.7)$$

where  $S$  is the strain rate-dependent damage onset point,  $S_0$  is the quasi-static damage onset point calculated from cyclic testing,  $\dot{\gamma}_{12}$  is the shear strain rate for which  $S$  is calculated,  $\dot{\gamma}_0^{12}$  is the quasi-static shear strain rate, and  $C$  and  $g$  are constants determined from the strain rate-dependent test data shown in Figure 6.12.

The implemented shear strain rate-dependent behavior was tested by single element simulation (see Figure 4.8a) at different strain rates. The simulation results were compared with experimental data. For better visualization, the comparison is shown in Figure 6.14 in two different pots, with solid lines indicating the experimental data and dotted lines indicating the simulation results.

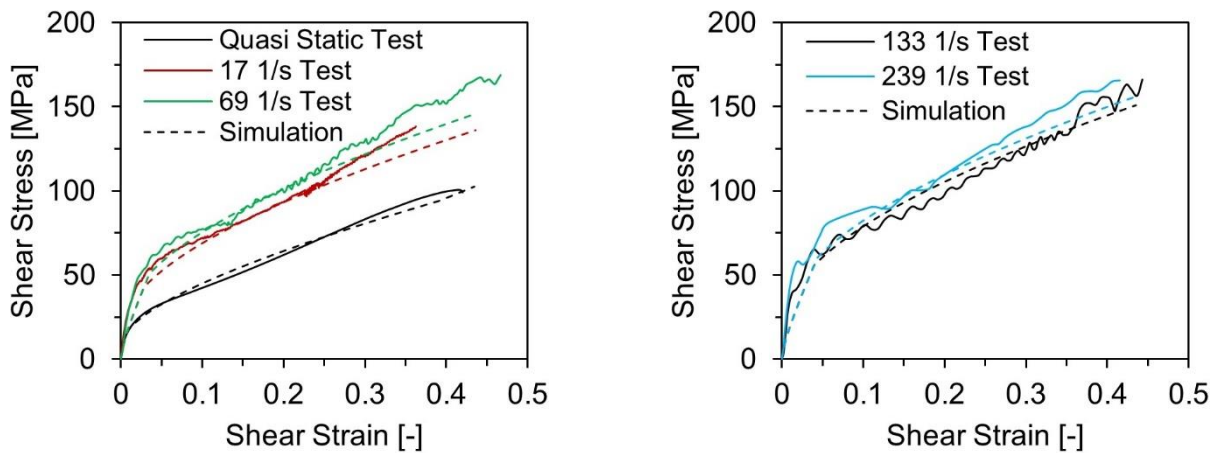


Figure 6.14 Strain rate-dependent shear behavior simulations compared with experimental data

It can be seen that the shear strain rate dependent material model predicted the results correctly. Although there are oscillations in the experimental data, the simulation shows consistency in its results. Further comparison of the shear strength and damage curves with respect to the shear strain rate can be seen in Figure 6.15.

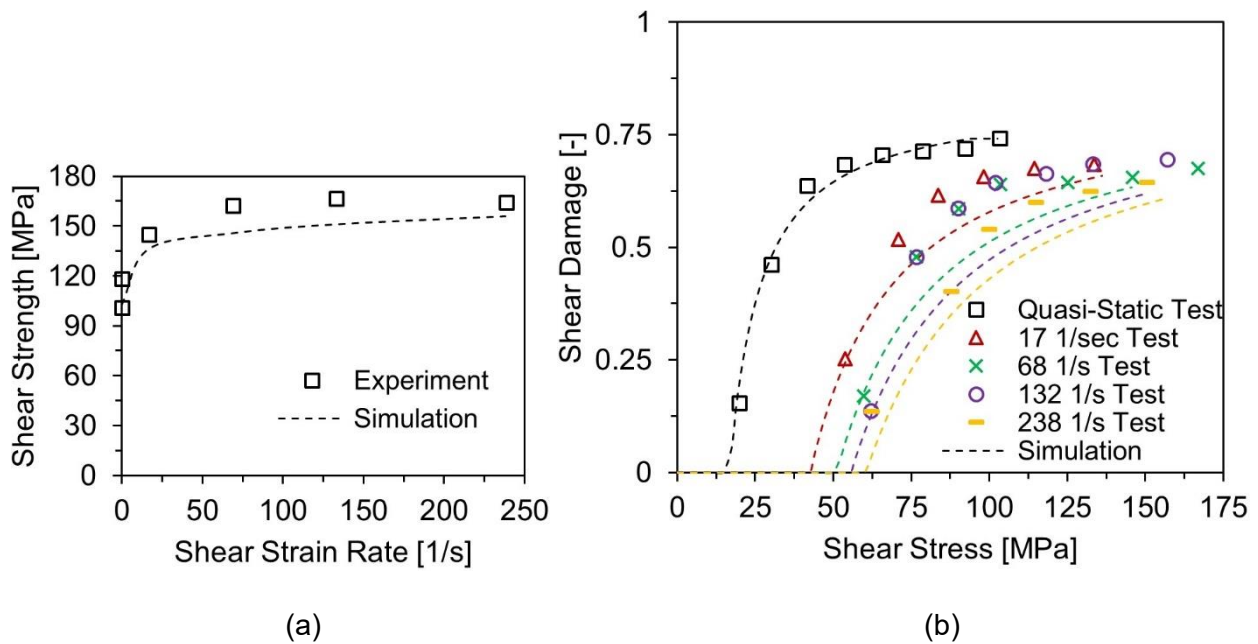


Figure 6.15 Comparison of experiment and simulation in terms of (a) shear strength and (b) shear damage at different shear strain rates

The comparison of the simulation and experimental data shown in Figure 6.15 is acceptable when the high oscillation and variation in experimental data is taken into account. Because the measured shear strength at shear strain rate of 238 1/s was smaller than the shear strength measured at the shear strain rate of 133 1/s, this could not be captured correctly in the mathematical model of Eqn. (6.7). Similarly, the shear damage onset values shown in Figure 6.11 are also not continuous, which led to the differences between the experimental data and simulation data in Figure 6.15. However, the simulation and experimental data are still in good agreement with each other.

### 6.2.3 Implementation as user-defined material subroutine

To implement the shear behavior as user-defined material subroutine VUMAT, an algorithm had to be constructed in a computational setting. A pseudo code is given in Table 6-5; this was able to take care of plasticity in inplane shear direction and damage in fiber-direction as well as in plane shear. Because damage and shear function in fiber shear direction were different, so their algorithm is also given separately.

The algorithm starts with known values of the set of parameters  $\{\sigma_n, \varepsilon_n, \varepsilon_n^{el}, \varepsilon_n^{pl}, \bar{\varepsilon}_n^{pl}, r_n, d_n\}$  at time  $t = n$ . The algorithm recalculates these values after a small-strain increment at time  $t = n + 1$ . At first, every new increment is supposed to be elastic and the corresponding stress value is termed as *Trial Stress*  $\tilde{\sigma}_{n+1}^{trial}$ . Then it is made sure that the new trial stresses comply with damage activation condition and yield criterion conditions. If the damage activation and plasticity yield conditions are not fulfilled, then corrector algorithm is applied so that yield conditions are fulfilled.

**Fiber response:** For sake of simplicity subscript 1, 2 or  $\alpha$  indicating fiber direction is removed

1. Start with the given data base of history variables  $\{\sigma_n, \varepsilon_n, r_n, d_n\}$  at time  $t = n$

2. Strain Increment gives total deformation at time  $t = n + 1$

$$\varepsilon_{n+1} = \varepsilon_n + \Delta\varepsilon_n$$

3. Compute trial value of stress

$$\sigma_{1n+1}^{trial} = \frac{E_1(1-d_{1n})}{1-\nu_{12}\nu_{21}(1-d_{1n})(1-d_{2n})} \varepsilon_{1n+1} + \frac{\nu_{12}E_2(1-d_{1n})(1-d_{2n})}{1-\nu_{12}\nu_{21}(1-d_{1n})(1-d_{2n})} \varepsilon_{2n+1}$$

$$\sigma_{2n+1}^{trial} = \frac{\nu_{21}E_1(1-d_{1n})(1-d_{2n})}{1-\nu_{12}\nu_{21}(1-d_{1n})(1-d_{2n})} \varepsilon_{1n+1} + \frac{E_2(1-d_{2n})}{1-\nu_{12}\nu_{21}(1-d_{1n})(1-d_{2n})} \varepsilon_{2n+1}$$

4. Compute strain rate

$$\dot{\varepsilon}_{n+1} = \frac{|\varepsilon_{n+1}|}{t}$$

5. Calculate strain rate dependent strength and parameters for damage evolution law

$$X_{n+1} = X^0 + a(\dot{\varepsilon}_{n+1} - \dot{\varepsilon}_0)^b$$

$$g_{n+1} = \frac{X_{n+1}^2}{2E}$$

$$A_{n+1} = \frac{2g_{n+1}L_c}{G_f - g_{n+1}L_c}$$

6. Calculate trial value of effective stress  $\tilde{\sigma}_{n+1}^{trial}$  and Fiber Failure Criterion

$$\tilde{\sigma}_{n+1}^{trial} = \frac{\sigma_{n+1}^{trial}}{(1-d_n)}$$

$$\Phi_{n+1} = \frac{\tilde{\sigma}_{n+1}^{trial}}{X_{n+1}}$$

$$F = \Phi_{n+1} - r_n$$

7. Algorithmic check for damage change

IF  $F \leq 0$  then the damage remains same

$$r_{n+1} = r_n$$

$$d_{n+1} = d_n$$

$$\sigma_{n+1} = \sigma_{1n+1}^{trial}$$

ELSE

$$r_{n+1} = \Phi_{n+1}$$

$$d_{n+1} = 1 - \frac{1}{r_{n+1}} \exp(-A_{n+1}(r_{n+1} - 1))$$

$$\sigma_{1n+1} = \frac{E_1(1-d_{1n+1})}{1-\nu_{12}\nu_{21}(1-d_{1n+1})(1-d_{2n+1})} \varepsilon_{1n+1} + \frac{\nu_{12}E_2(1-d_{1n+1})(1-d_{2n+1})}{1-\nu_{12}\nu_{21}(1-d_{1n+1})(1-d_{2n+1})} \varepsilon_{2n+1}$$

$$\sigma_{2n+1} = \frac{\nu_{21}E_1(1-d_{1n+1})(1-d_{2n+1})}{1-\nu_{12}\nu_{21}(1-d_{1n+1})(1-d_{2n+1})} \varepsilon_{1n+1} + \frac{E_2(1-d_{2n+1})}{1-\nu_{12}\nu_{21}(1-d_{1n+1})(1-d_{2n+1})} \varepsilon_{2n+1}$$

**Shear response:** In following, subscript 12 has been removed for simplicity

8. Start with the given data base of history variables  $\{\sigma_n, \varepsilon_n, \varepsilon_n^{el}, \varepsilon_n^{pl}, \bar{\varepsilon}_n^{pl}, r_n, d_n\}$  at time  $t = n$

9. Strain Increment gives total deformation at time  $t = n + 1$

$$\varepsilon_{n+1} = \varepsilon_n + \Delta\varepsilon_n$$

10. Elastic Predictor Step

Compute trial value of effective stress and the trial value of yield function

$$\tilde{\sigma}_{n+1}^{trial} = 2G_{12}(\varepsilon_{n+1} - \varepsilon_n^{pl}) = 2G_{12}(\varepsilon_n^{el} + \Delta\varepsilon_n)$$

$$F_{n+1}^{trial} = |\tilde{\sigma}_{n+1}^{trial}| - (\tilde{\sigma}_{y0} + K \bar{\varepsilon}_n^{plp})$$

11. Algorithmic check for plastic loading

IF  $F_{n+1}^{trial} \leq 0$  then the load step is elastic

$$\tilde{\sigma}_{n+1} = \tilde{\sigma}_{n+1}^{trial}$$

$$\varepsilon_{n+1}^{el} = \varepsilon_n^{el} + \Delta\varepsilon_n$$

$$\varepsilon_{n+1}^{pl} = \varepsilon_n^{pl}$$

$$\bar{\varepsilon}_{n+1}^{pl} = \bar{\varepsilon}_n^{pl}$$

ELSE  $F_{n+1}^{trial} > 0$  hence the load step is elasto-plastic

12. For the Ramberg-Osgood hardening function  $\tilde{\sigma}_y(\bar{\varepsilon}_{12}^{pl}) = \tilde{\sigma}_{y0} + K(\bar{\varepsilon}_{12}^{pl})^p$  with

$$\frac{\partial \tilde{\sigma}_y(\bar{\varepsilon}_{12}^{pl})}{\partial \bar{\varepsilon}_{12}^{pl}} = pK(\bar{\varepsilon}_{12}^{pl})^{p-1}$$

use the Newton Raphson Method to Solve

$$F_{n+1}^{trial} - 2G_{12}\Delta\gamma - \tilde{\sigma}_y(\bar{\varepsilon}_{n+1}^{pl}) + \tilde{\sigma}_y(\bar{\varepsilon}_n^{pl}) = 0 \text{ for } \Delta\gamma, \text{ as described in the following steps.}$$

i. Set the initial guess  $\Delta\gamma_j = \frac{\Delta\varepsilon_n}{2}$  for iteration  $j = 0$

ii. WHILE  $R = F_{n+1}^{trial} - 2G_{12}\Delta\gamma - (\tilde{\sigma}_{y0} + K(\bar{\varepsilon}_{n+1}^{pl} + \Delta\gamma)^p) + (\tilde{\sigma}_{y0} + K(\bar{\varepsilon}_n^{pl})^p) > tol$

Calculate an improved guess of  $\Delta\gamma_{j+1}$

$$\Delta\gamma_{j+1} = \Delta\gamma_j - \frac{R(\Delta\gamma_j)}{R'(\Delta\gamma_j)} = \Delta\gamma_j - \frac{F_{n+1}^{trial} - 2G_{12}\Delta\gamma - (\tilde{\sigma}_{y0} + K(\bar{\varepsilon}_{n+1}^{pl} + \Delta\gamma)^p) + (\tilde{\sigma}_{y0} + K(\bar{\varepsilon}_n^{pl})^p)}{-2G_{12} - pK(\bar{\varepsilon}_{n+1}^{pl} + \Delta\gamma)^{p-1}}$$

Unless  $R < tol$  is achieved

END WHILE

13. Plastic corrector step

$$\varepsilon_{n+1}^{pl} = \varepsilon_n^{pl} + \Delta\gamma$$

$$\varepsilon_{n+1}^{pl} = \varepsilon_n^{pl} + \Delta\gamma \text{sign}(\tilde{\sigma}_{n+1}^{trial})$$

$$\varepsilon_{n+1}^{el} = \varepsilon_n^{el} + \Delta\varepsilon_n - \Delta\gamma \text{sign}(\tilde{\sigma}_{n+1}^{trial})$$

$$\tilde{\sigma}_{n+1} = \left[ 1 - \frac{\Delta\gamma 2G_{12}}{|\tilde{\sigma}_{n+1}^{trial}|} \right] \tilde{\sigma}_{n+1}^{trial}$$

END IF

14. Compute shear strain rate

$$2\dot{\varepsilon}_{n+1} = \frac{2|\varepsilon_{n+1}|}{t}$$

15. Calculate Strain rate dependent damage onset

$$S_{n+1} = S^0 + a(2\dot{\varepsilon}_{n+1} - 2\dot{\varepsilon}_0)^b$$

$$\Phi_{n+1} = \frac{\tilde{\sigma}_{n+1}}{S_{n+1}}$$

16. Calculate damage activation function

$$F_{12} = \Phi_{n+1} - r_n$$

IF  $F_{12} \leq 0$  then

$$r_{n+1} = r_n$$

$$d_{n+1} = d_n$$

ELSE

$$r_{n+1} = \Phi_{n+1}$$

$$d_{n+1} = \min(m(r_{n+1})^n + o, d_{12}^{max})$$

END IF

$$\sigma_{n+1} = 2G_{12}(1 - d_{n+1})\varepsilon_{n+1}^{el}$$

Table 6-5 Pseudo code for implementation of user material subroutine

### 6.3 Validation

For validation of the strain rate-dependent material model, a high speed three-point bending test of a closed u-profile was done on a drop tower, and the results were compared with the simulation data.

For this purpose, the flat rectangular plates were cut from a 1.5 mm thick sheet of 102-RG600(3) and thermoformed into a u-profile with fibers aligned along the length direction. The profile was 85 mm in height, 118 mm in width, and 400 mm long. The flanges were 15 mm wide, and a closing sheet (also 102-RG600(3)) was joined with six rivets on the flanges of the profile (Figure 6.16).

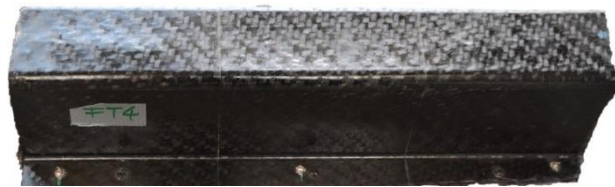


Figure 6.16 Thermoformed u-profile used for drop tower three point bending

The profile was placed on two circular steel supports with radius of 40 mm and with a span length of 300 mm. An impactor with a radius of 50 mm and a total mass of 250 kg was dropped from a height of 1 m which impacted the u-profile at a speed of 4.43 m/sec. The force was measured with force transducers at the bottom of the supports, and the deformation of the profile was measured by tracking the position of the impactor with a laser sensor. A high-speed video camera system was used to capture images of the crash at a rate of 1000 fps. The images of the crash event captured by the high-speed camera as well as the deformed specimen are shown in Figure 6.17.

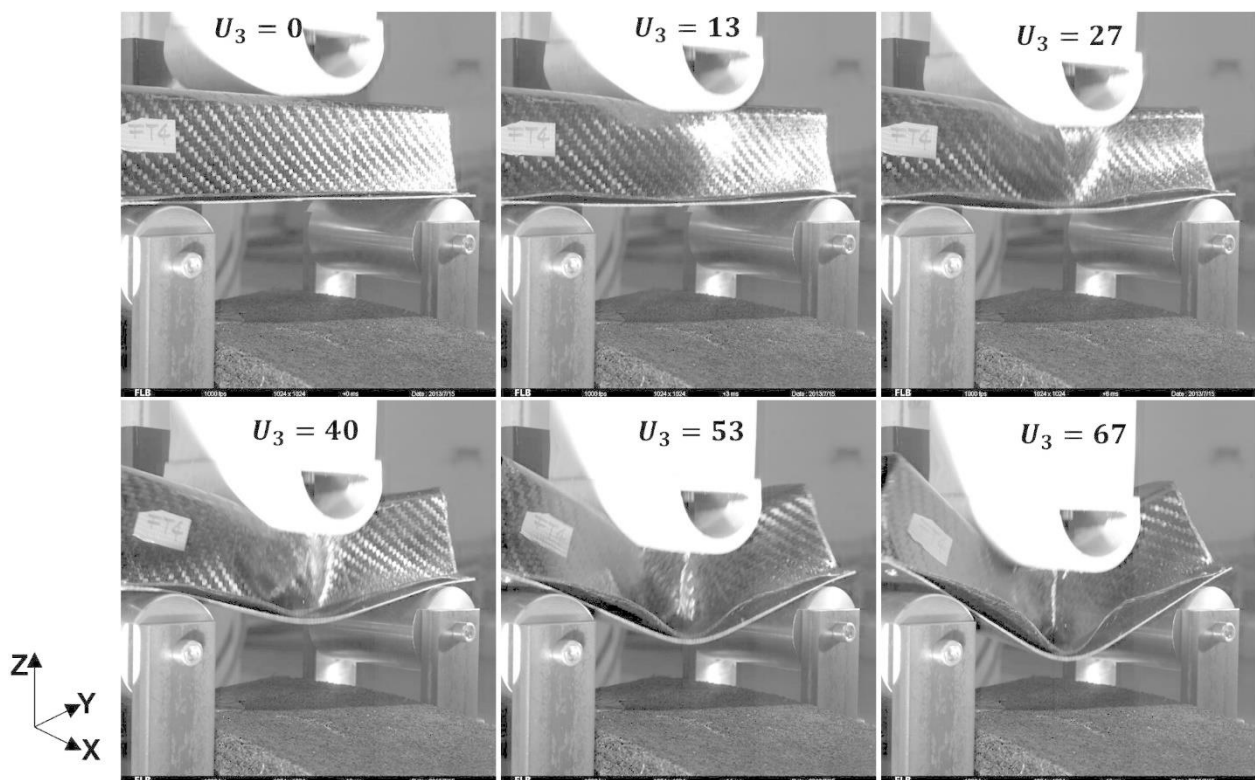




Figure 6.17 Photos of drop tower three point bending of hat profile during the test at different deformations along negative z-axis. The deformed geometry of profile after the test is also shown

### 6.3.1 FEM model setup

The FEM model for the simulation purpose was created in Abaqus as shown in Figure 6.18. The exact geometry of the impactor and supports was created and modelled as a 3D discrete rigid. A point mass of 250 kg was assigned to a reference point of the impactor. The u-profile and closing sheets were modeled with shell elements S4R with a mesh size of 3 mm. The shell elements were assigned to three plies with a thickness of 0.5 mm each. Rivets joining of the u-profile and closing sheet was modelled with tie constraints. All degrees of freedom of supports were constrained. For the impactor, all degrees of freedom, except the translational degree of freedom along the z-axis  $U_3$ , were constrained. An initial velocity of 4.43 m/s along the negative z-axis was assigned to the impactor, and a gravity load of  $9.806 \text{ m/s}^2$  was defined for the whole model. A general contact for explicit simulation was defined for the whole model, with normal behavior as “hard contact” which allowed separation after contact.

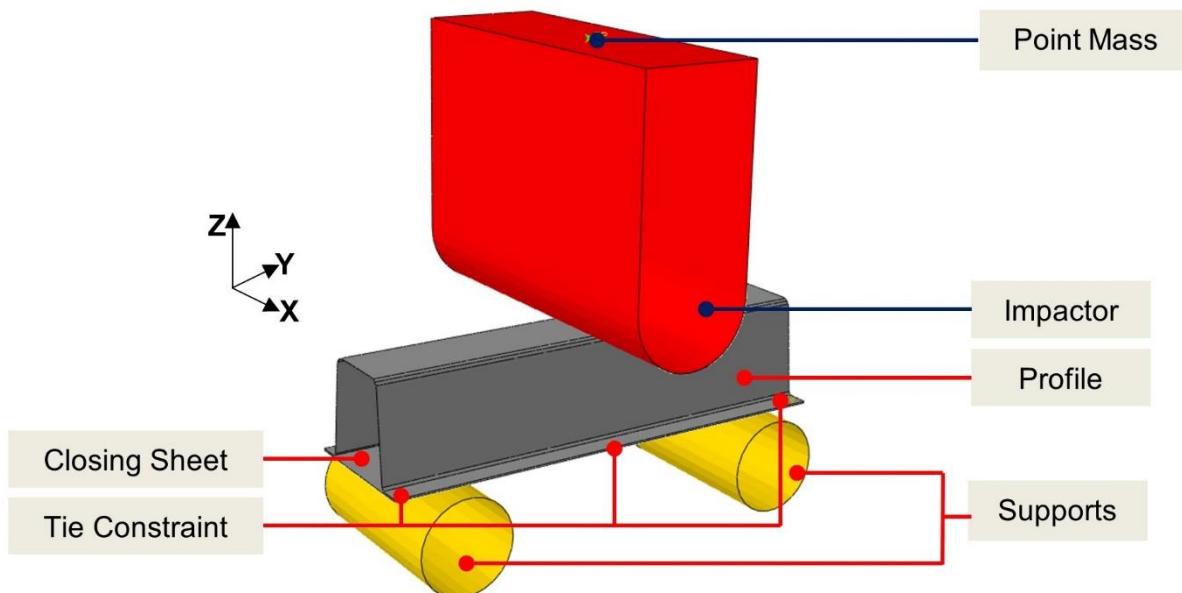


Figure 6.18 FEM Model of drop tower three-point bending

### 6.3.2 Results

Simulations were run using two different material models. (a) ABQ\_PLY\_FABRIC which is built in CDM material model for woven fabric composites without a strain rate dependency and (b) a user-material subroutine with an implemented strain rate dependency. The simulation results at the same

deformation levels are shown in Figure 6.19 and Figure 6.20 for the same deformation level as in Figure 6.17. For better visualization, the rigid impactor is hidden, and the deformation along negative z-axis is shown as positive.

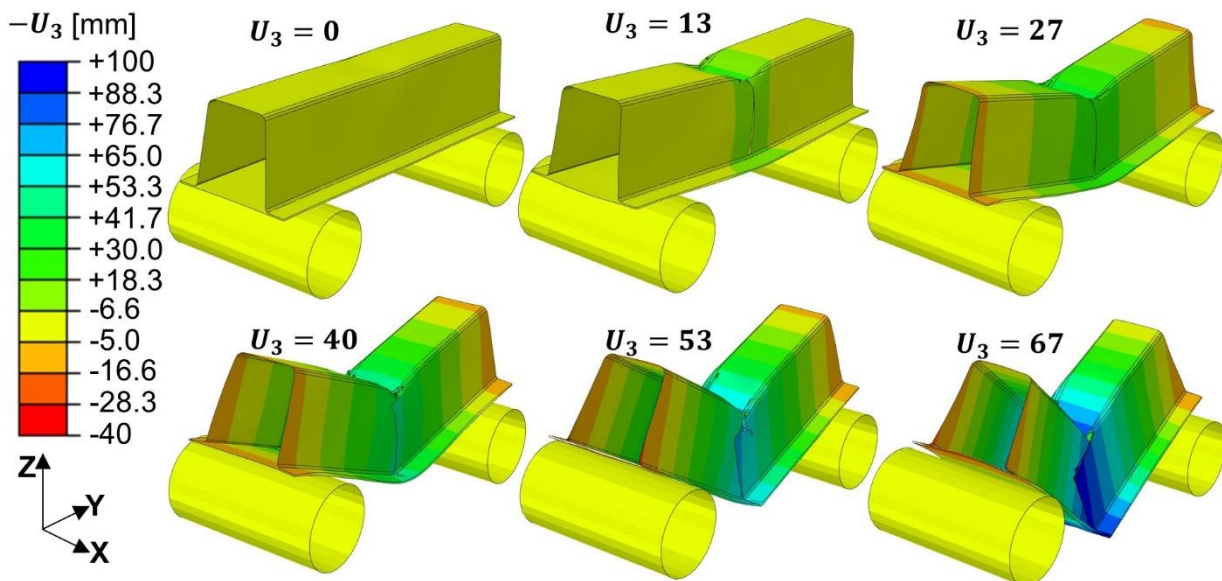


Figure 6.19 Simulation results of drop tower three point bending using Abaqus built-in material model ABQ\_PLY\_FABRIC without strain rate dependency

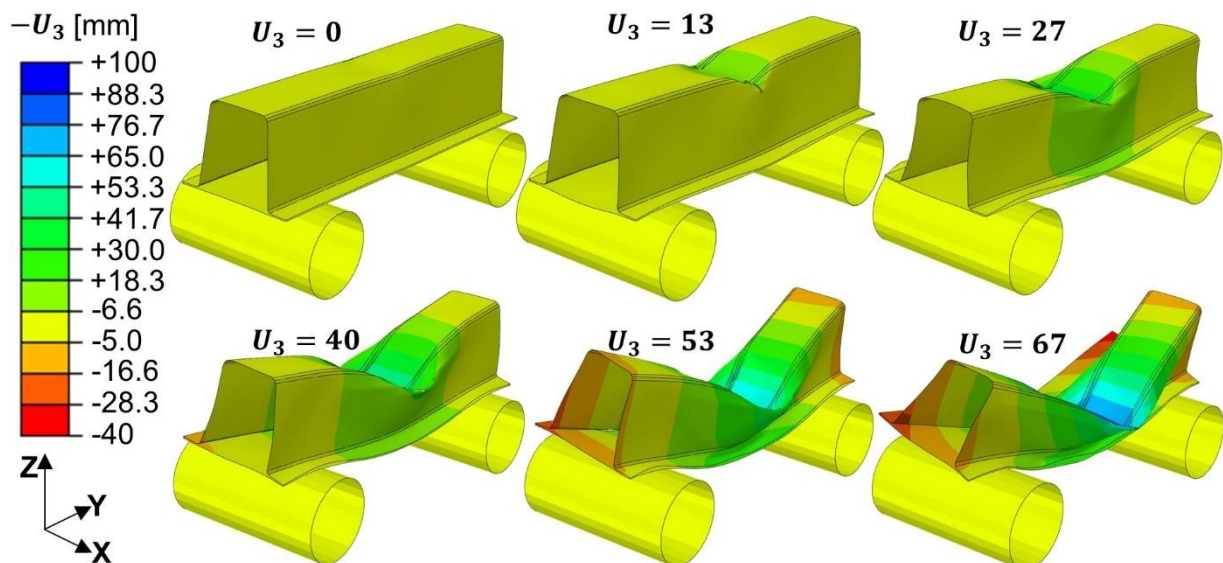


Figure 6.20 Simulation results of drop tower three point bending with strain rate dependent user-material subroutine

### 6.3.3 Discussion

By comparing the simulation results shown in Figure 6.19 and Figure 6.20 with images of experiment in Figure 6.17 it can be clearly seen that the morphology of the deformation during the crash was predicted more accurately by the strain rate-dependent user material subroutine. The simulation results in Figure 6.19 show the development of a crack in the middle of the profile running along the z-axis starting from deformation  $U_3 = 13$  mm. This is in contrast to the images captured during the

experiment, in which a buckle appears in the middle of the profile followed by the whole profile being deformed on the side. However, the new strain rate-dependent user material model predicted the failure in Figure 6.20 correctly.

For further comparison of the structural response, the force-deformation plots of both simulation models along with the test results are shown in Figure 6.21.

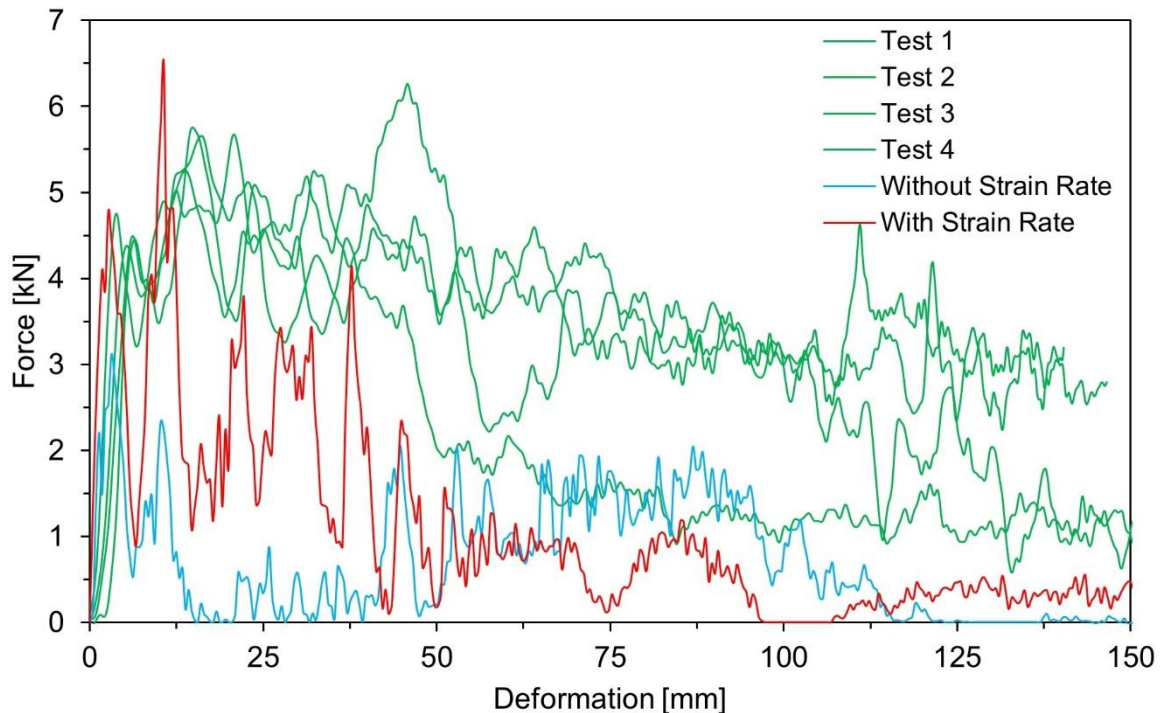


Figure 6.21 Force-deformation data of crashing u-profile in three-point bending configuration compared with simulation data produced using material models with and without strain rate dependency

Figure 6.21 shows that the force deformation levels of the simulation model with the strain rate-dependent user-material subroutine are much closer to those of the experimental data in comparison to simulation model using material model without strain rate dependency up to ca. 50 mm deformation. The user-material subroutine predicted the initial contact force quite well however, the force levels are under-predicted for deformations larger than 20 mm. The potential reasons for this under-prediction of force levels are discussed in next chapters.

## 6.4 Conclusion

In this chapter, the influence of the strain rate on the elasticity and strength properties along the fiber direction as well as in-plane shear damage and shear strength properties were investigated. Quasi-static and high speed tests were carried out using standard specimen geometries. Cyclic shear tests at different speeds were carried out to measure the shear plasticity and shear damage and then were compared with monotonically loaded test specimen data. The results of the strain rate-dependent material data were successfully implemented into the CDM material model. It was found that:

- Organo-sheet exhibits strong linear elastic behavior in the fiber direction;

- 
- The in-plane shear exhibits a non-linear ductile response;
  - Oscillations in the measured force/stress and deformation-both in the fiber direction and shear, increase with the speed of the tests;
  - The measured surface strains are not homogeneous due to inhomogeneity in the material;
  - Strain rate has no influence on the elastic modulus in fiber direction;
  - The tensile strength in the fiber direction increases approx. 100% at a strain rate of 120 1/s in comparison to the quasi-static test;
  - The in-plane shear stress and shear strength increase with increasing strain rate;
  - The exponential function of the strain rate-dependent strength in fiber direction and shear damage onset fit well for modeling the woven glass fabric composite material
  - The implemented user-material subroutine predicted the strain rate-dependent material response accurately at the coupon level; and
  - The simulation of the crash bending of u-profile through the incorporation of strain rate dependency in the material model improved the prediction of the crash results both in failure evolution and force-displacement.



## 7 Failure surface

In chapter 5 experimental results have shown that failure stress of material under pure shear stress and multi-stress state was different. The material models used for simulations in previous chapters including ABQ\_PLY\_FABRIC and user-material subroutine did not take this finding into account. A maximum stress failure criterion along the fiber direction (see Eqn. (4.15)) was used. And a maximum plastic shear strain criterion was used for inplane shear. Using such generic failure criterion contributed to wrong prediction of simulation results (see Figure 6.21).

Most of the authors addressing failure criteria, including mentioned in section 2.5, focused on UD composites. Only a few efforts have been made to study the failure behavior of woven fabric composites. Very little data has been published regarding the test results of woven fabric composites under multi-stress state. Determining biaxial failure surface with state of the art experimental methods could not be done because organo-sheets such as 102-RG600 are delivered in the form of sheets. Manufacturing a cylindrical tube out of flat sheets for biaxial failure surface testing was difficult. Moreover, testing cruciform specimens required special apparatus.

In this chapter, failure points of 102-RG600 under multi-stress state are determined experimentally by tensile tests on off-axis specimens. Stress-strain transformation was used to determine the effective of shear stress on the failure of laminate. Finally, suggestions are made for future work.

### 7.1 Testing

To measure the material behavior of 102-RG600 at different multi-stress state tests were carried out at  $0^\circ$ ,  $5^\circ$ ,  $10^\circ$ ,  $15^\circ$ ,  $30^\circ$  and  $45^\circ$ . Because the warp and weft properties of 102-RG600 are the same for  $30^\circ=60^\circ$ ,  $15^\circ=75^\circ$ ,  $10^\circ=80^\circ$ ,  $5^\circ=85^\circ$  and  $0^\circ=90^\circ$ . The specimen geometry and dimensions were the same for tensile and tensile shear property measurement. Specimen of 250 mm x 25 mm x 2 mm were glued with end tabs of 50 mm x 25 mm x 1.5 mm. Therefore, the gauge length was 150 mm. Tests were carried out on Zwick Z100 at speed of 2mm/min. The surface strains were measured with ARAMIS as explained in chapter 3.2. The specimens after tests are shown in Figure 7.1.



Figure 7.1 Specimens with fiber at various angles after tensile test

The tensile testing of specimen with fibers at 0° is exactly what tensile testing described in section 3.2 is. The tensile testing of specimen with fibers at 45° is exactly what tensile shear testing in 3.4 was discussed. More specimen photos are given in Annex. 12.2.11. The measured longitudinal stress-strain (global stress-strain along the direction of applied load) is shown in Figure 7.2 and Table 7-1. In order to compare the results only one specimen from each angle is taken so that illustration is made easier. Results of all specimens for each loading angle can be seen in Annex 12.1.6.

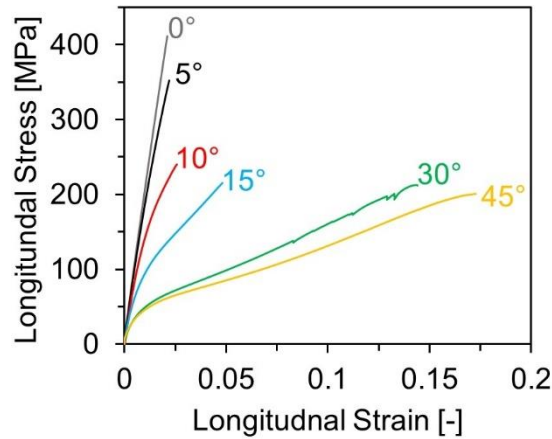


Figure 7.2 Measured longitudinal stress-strain of specimens with fiber at different angles

Fiber direction [degrees]	No. of test	Strength [MPa]	Failure strain [%]
0° (St. deviation)	5	392.38 (16.92)	2.02 (0.08)
5° (St. deviation)	5	330.83 (14.2)	1.95 (0.14)
10° (St. deviation)	5	242.86 (5.43)	2.64 (0.059)
15° (St. deviation)	5	217.28 (5.4)	4.68 (0.18)
30° (St. deviation)	4	216.35 (3.89)	14.42 (0.53)
45° (St. deviation)	4	201.47 (2.6)	17.64 (0.38)

Table 7-1 Measure longitudinal strength and failure strain of 102-RG600 at different fiber angles

As it can be seen in Figure 7.2, the material show the highest stiffness and strength when tested along the direction of fiber i.e. 0°. As the loading angle changes, the stiffness and strength decreases significantly. However, non-linearity and failure strain in the material increases. This pseudo-ductility is due to the shear stresses in material which is the highest for 45°. This is why tensile shear tests are also carried out at specimens with fibers aligned at 45°. The shear stress can be calculated according to Eqn. (2.17). The applied load was in y-direction only, so  $\sigma_x = \tau_{xy} = 0$ ; which reduces Eqn. (2.17) to Eqn. (7.1).

$$\tau_{12} = \sigma_y \sin\theta \cos\theta \quad (7.1)$$

The shear strain is calculated according to Eqn. (2.21) as:

$$\gamma_{12} = -2\sin\theta \cos\theta \varepsilon_x + 2\sin\theta \cos\theta \varepsilon_y + (\cos^2\theta - \sin^2\theta)\gamma_{xy} \quad (7.2)$$

Unlike stresses, the strains  $\varepsilon_x \neq 0$  because specimens were fixed only on top and bottom. Apart from balanced laminates (0° and 45°) where there is no stretching/shearing coupling the  $\gamma_{xy} \neq 0$ .

Therefore to measure the shear strain  $\gamma_{12}$ , all three global strain had to be measured. To calculate  $\gamma_{xy}$ , strains at  $45^\circ$  directions ( $\varepsilon_{45}$ ) were measured. According to Eqn. (2.21):

$$\varepsilon_1 = \cos^2\theta\varepsilon_x + \sin^2\theta\varepsilon_y + 2\sin\theta\cos\theta\gamma_{xy} \quad (7.3)$$

Inserting  $\theta = 45^\circ$  into this equation gives  $\gamma_{xy}$  as function of  $\varepsilon_x$ ,  $\varepsilon_y$  and strain at  $45^\circ$   $\varepsilon_1 = \varepsilon_{45}$ .

$$\gamma_{xy} = -\varepsilon_x + 2\varepsilon_{45} - \varepsilon_y \quad (7.4)$$

Figure 7.3 shows the measured strain of  $\varepsilon_x$ ,  $\varepsilon_y$  and  $\varepsilon_{45}$  on  $15^\circ$  specimen.

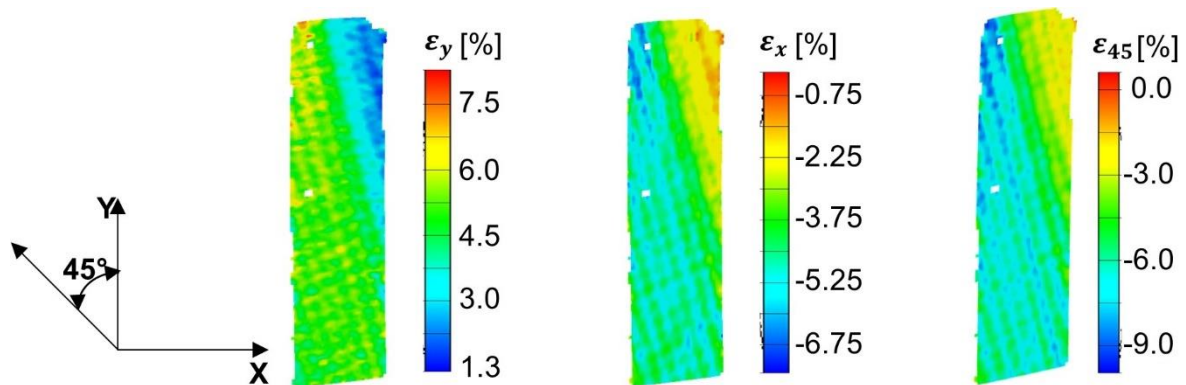


Figure 7.3 Strain measurement on  $15^\circ$  specimen at average longitudinal strain  $\varepsilon_y = 4.5\%$

After the stress-strain transformation, the shear stress-strain results were plot as shown in Figure 7.4.

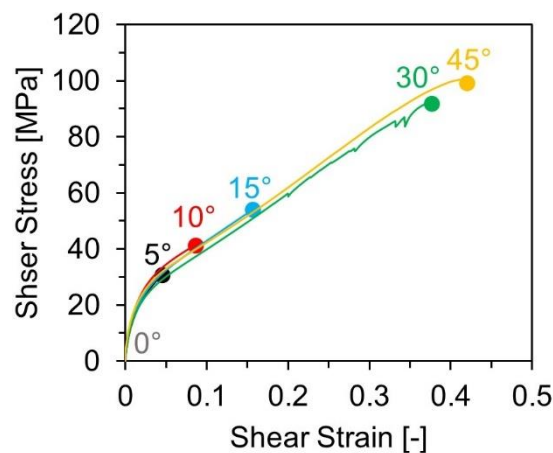


Figure 7.4 Shear stress-strain calculated by stress-strain transformation from off-axis specimens. The end of every curve is marked by a circle for better illustration

The results in Figure 7.4 show that even though the laminate response in Figure 7.2 was different, but shear stress strain plot from different off axis specimens match perfectly. However, the maximum shear-stress/strain was different. A comparison of longitudinal strength and maximum shear stress and their counterpart strains is given in Figure 7.5.

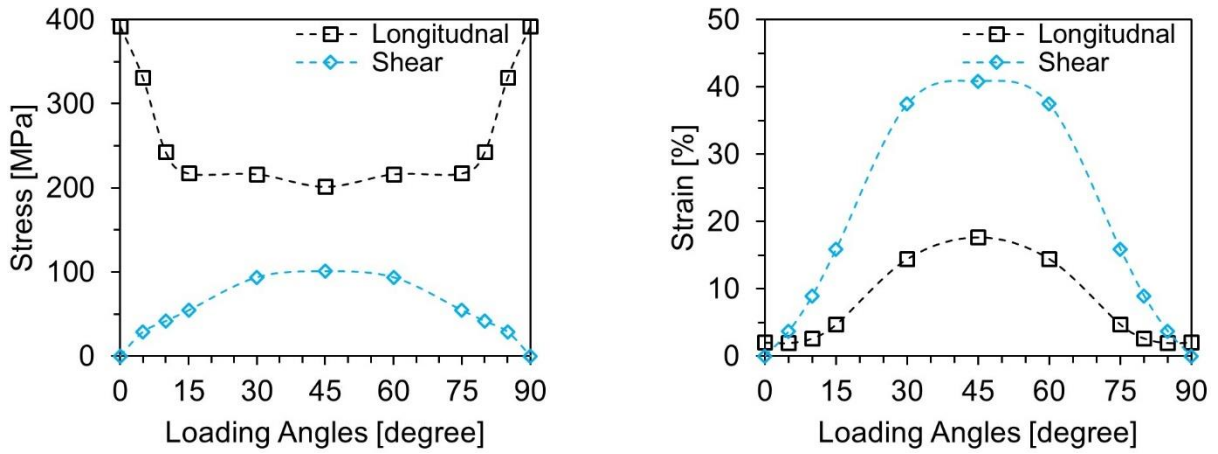


Figure 7.5 Maximum longitudinal and shear stress of different fiber angle of specimen (left) and maximum longitudinal/shear strain at different loading angles (right)

As it can be seen from Figure 7.5 that the laminate strength drops significantly from 0° to 10° at the expense of increasing shear stress. And the laminate failure strain increase drastically between 15° to 45° contributed due to the high shear strains. To analyze the data, the normalized stress (stress to max. stress ratio) and normalized strain (strain to max. strain ratio) is given in Figure 7.6.

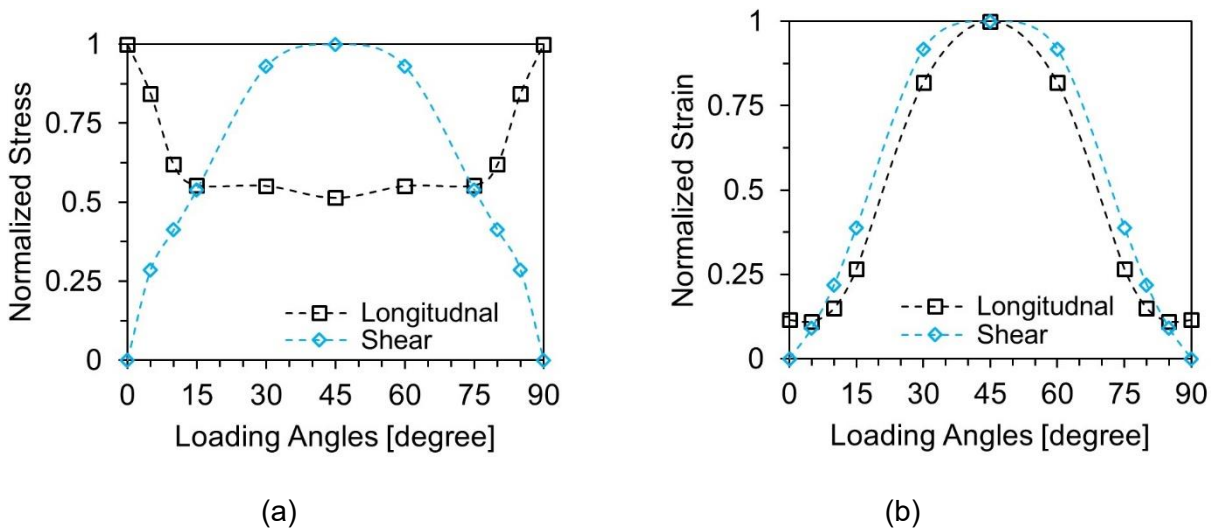


Figure 7.6 (a) Normalized longitudinal and shear stress with different fiber angle of specimen and (b) normalized longitudinal/shear strain at different loading angles

It can be seen that when shear stress is zero ( $\theta = 0^\circ$  or  $90^\circ$ ), the strength of laminate is highest (Figure 7.6a) and the failure strain is minimum (Figure 7.6b). Similarly, when shear stress is highest ( $\theta = 45^\circ$ ), the strength of laminate is minimum (Figure 7.6a) and the failure strain is maximum (Figure 7.6b). So it can be concluded that the presence of shear stress reduces the load bearing capacity of woven composite material significantly. And the maximum stress-criterion used for simulations in previous chapters is not able to predict the exact failure of 102-RG600.

Just like shear stress-strain, the transformation matrix in Eqn. (2.17) can also be used to calculate normal stress-strains in fiber direction. The results are shown in Figure 7.7.

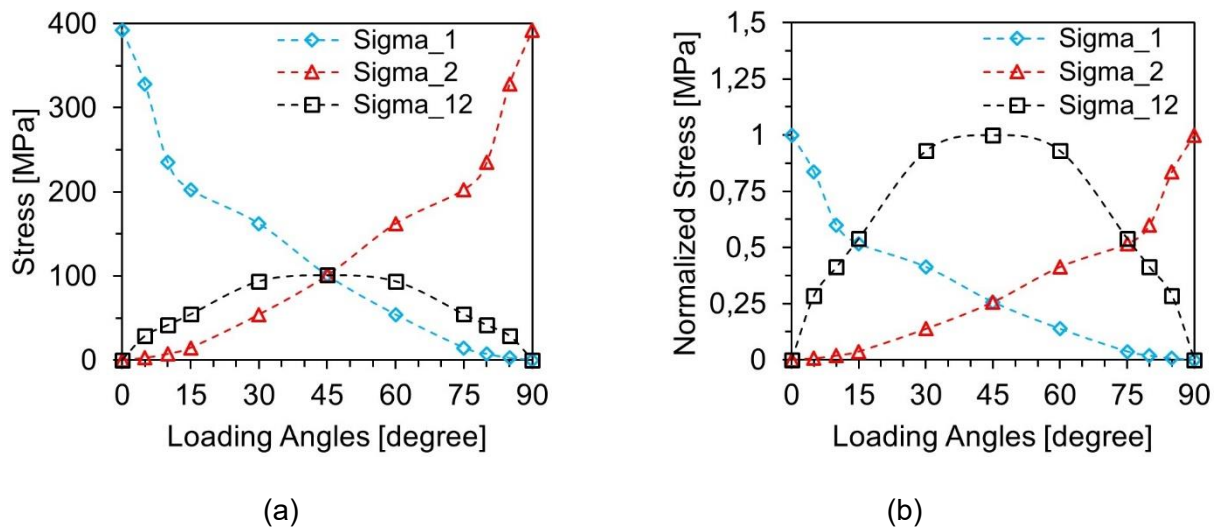


Figure 7.7 (a) Normal and shear stresses in lamina as function of loading angle and (b) Normalized stresses in lamina as function of loading angle

Note that values determined in Figure 7.7 are based on linear elastic transformation without considering the fiber-rotation, bending and locking in woven fabric. The fiber rotation plays major role in evaluated results and it should be considered in future. Even though the fiber rotation has been neglected, the data acquired from tests with lower angle rotation ( $0^\circ$ ,  $5^\circ$  and  $10^\circ$ ) has little fiber rotation. The normalized failure point data of three normalized stress values from Figure 7.7.b is used to represent 2D-stress envelope as shown in Figure 7.8.

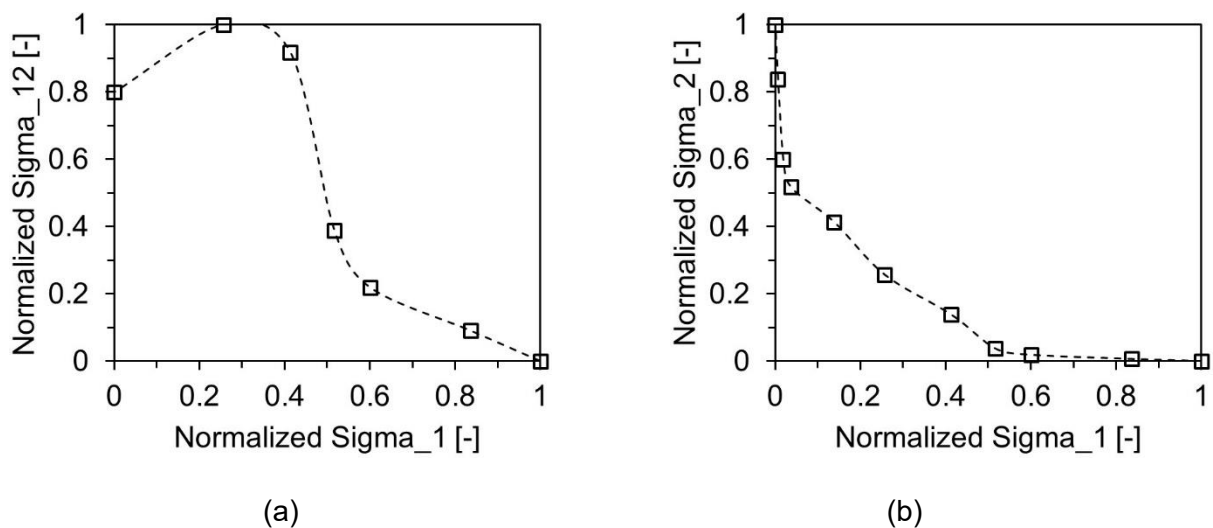


Figure 7.8 (a) Biaxial failure envelope  $\sigma_1$  vs.  $\tau_{12}$  and (b)  $\sigma_1$  vs.  $\sigma_2$

Note that the failure points shown in Figure 7.8 are not purely under biaxial load. Instead a varying value of normal stress  $\sigma_2$  is present in Figure 7.8(a) which is not shown. Similarly shear stress  $\tau_{12}$  is not shown in Figure 7.8(b). Anyhow, it is concluded from Figure 7.8 that failure stress value does not remain constant in presence of multi-stress state. And multi-stress state leads to early failure of the material as opposed to maximum failure criterion.

## 7.2 Conclusion

- Off-axis tests were used to acquire data in first quadrant of  $\sigma_1$  vs.  $\tau_{12}$  and  $\sigma_1$  vs.  $\sigma_2$  biaxial failure envelope;
- Linear stress and strain transformation was used for calculation of stress and strains in material coordinates;
- More test data with cylindrical specimens and cruciform specimen is required for proposal of suitable failure criterion;
- Multistress-state reduces the load bearing capacity of 102-RG600 in comparison to uniaxial loading;
- The maximums stress and maximum strain failure criterion are not exact representation of failure surface of 102-RG600.

## 8 Size effect

In chapter 4.4 the quasi-static simulation of simple rectangular specimens and U-profile predicted the strength lower than experimentally measured strength. Similarly for high speed crashing of closed U-profile in chapter 6.3 the maximum force predicted was lower than experimentally measured data even though strain rate effects were incorporated in user-material model. The reason behind this is that usually the input parameter for the simulation were measured from uni-axial tensile tests. The tensile strength of composite materials is lower than flexural strength. The CDM material models wrongly predict the flexural strength of these elastic brittle materials equal to their tensile strength.

In this chapter, the experimental investigations on size effect of 102-RG600(4) are carried out. In section 8.1, tensile tests on different size of specimens are carried out. In section 8.2 flexural tests are carried out over a range of specimen sizes and results are compared with tensile results. For flexural strain measurement, pin-end buckling tests were carried out. Finally in section 8.3, a method is proposed on how size effect can be incorporated in user-material subroutine.

### 8.1 Size effect in tension

In order to investigate the size effect on tensile strength, tensile tests were done with different gauge lengths specimens. These tests were carried out according to test details discussed in chapter 3.2. All specimens were 25 mm wide and 2 mm thick and glued with 50 mm x 25 mm x1.5 mm end tabs. Specimens with seven different gauge length (5mm, 10mm, 20mm, 50mm, 100mm, 150mm and 200mm) were prepared. The tests were carried out on Zwick Z100 with loading along the fiber direction. The surface strains were measured with ARAMIS as explained in chapter 3.2. In order to minimize potential influence of strain rate, all lengths were tested at the same nominal strain rate. The speed of testing for every gauge length was different and was calculated by keeping a constant strain rate.

$$\dot{\epsilon}(t) = \frac{d\epsilon}{dt} = \frac{d}{dt} \left( \frac{L(t) - L_0}{L_0} \right) = \frac{1}{L_0} \frac{dL}{dt}(t) = \frac{v(t)}{L_0} \quad (8.1)$$

The test results are summarized in Table 8-1, Figure 8.1 and Figure 8.2.

Gauge length [mm]	No. of tests	Test speed [mm/min]	E-modulus [GPa]	Tensile strength [MPa]
5	5	0.05	16.70	369.88
10	5	0.1	18.64	369.24
20	5	0.2	16.94	378.38
50	5	0.5	18.91	387.30
100	5	1.0	18.21	356.22
150	5	1.5	19.02	371.18
200	5	2.0	18.03	371.13

Table 8-1 Tensile test results with different gauge length of 102-RG600(4)

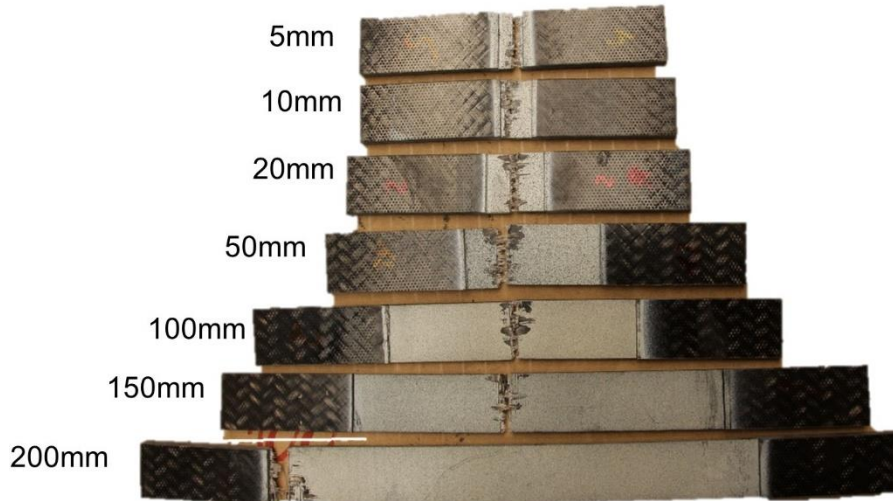


Figure 8.1 Tensile specimens of different gauge lengths after test

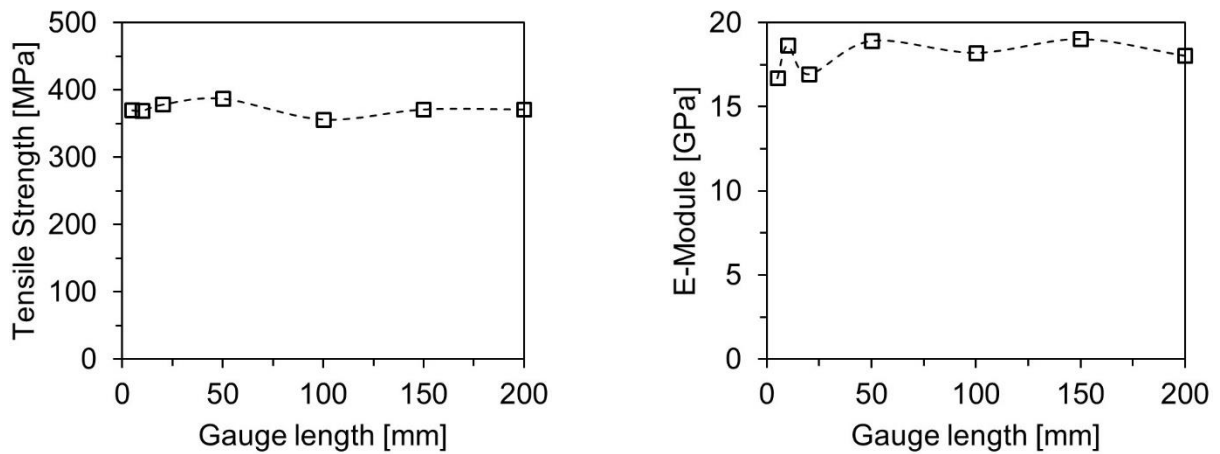


Figure 8.2 Effects of specimen gauge length on tensile strength (left) and E-module (right)

As evident from Figure 8.2, the tensile strength is not influenced much by the size of specimen. So it can be established that the tensile strength remains constant irrespective of the specimen size.

## 8.2 Size effect in bending

Three-point bending tests were carried out with span lengths of 60 mm, 80 mm and 100 mm. All specimens were cut from 2 mm thick sheet in 25 mm width. The specimens were placed on supports of 15 mm radius with fibers running in length direction. An impactor with radius of 5 mm was impacted at speed of 5 mm/min until the specimen failed. Photos of specimens are shown in Figure 8.3.

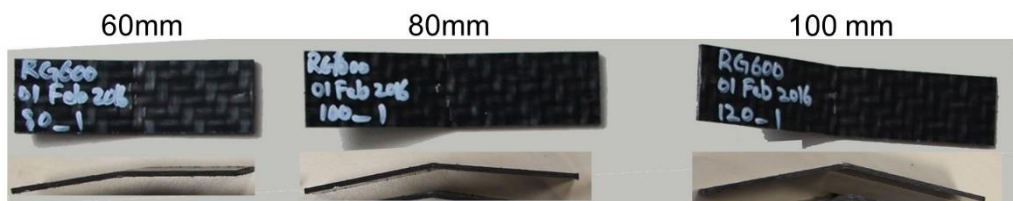


Figure 8.3 Three point bending specimens tested at different span lengths

The force and deformation was measured on Zwick Z100. The flexural stress  $\sigma_b$  and flexural strain  $\varepsilon_b$  can be calculated by:

$$\sigma_b = \frac{3FL}{2bh^2} \quad (8.2)$$

$$\varepsilon_b = \frac{6h\delta}{L^2} \quad (8.3)$$

$F$ : Force measured

$L$ : Span length of the specimen

$b$ : Width of the specimen

$h$ : Thickness of the specimen

$\delta$ : Deformation applied by the impactor

The measured force-deformation and calculated flexural stress-strain plot are shown in Figure 8.4.

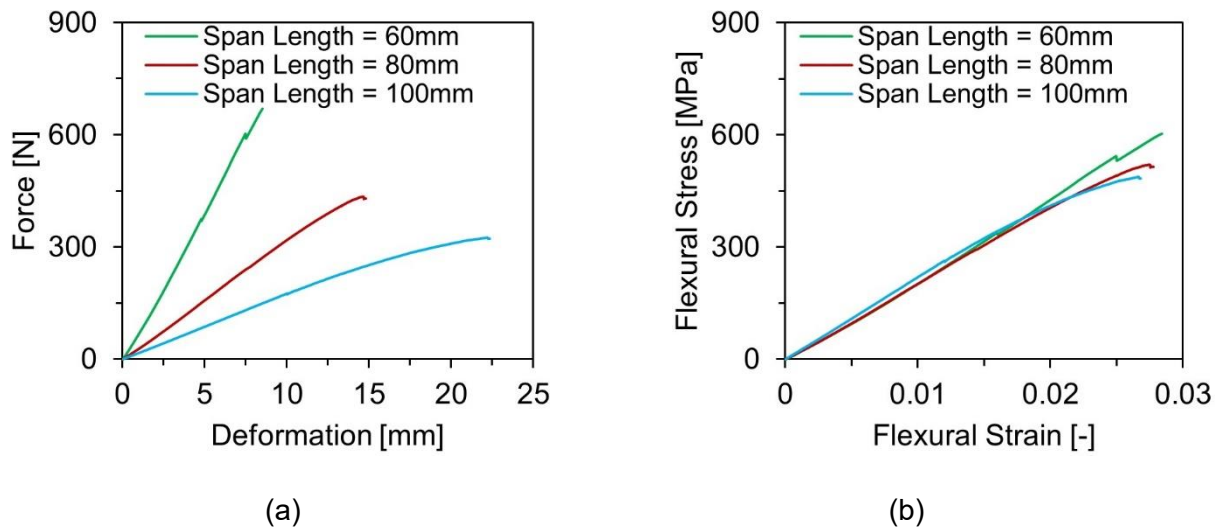


Figure 8.4 (a) Measured force-deformation in three point bending tests and (b) their respective flexural stress-strain plot

Even though the force-deformation response for different tests at different span lengths is different, but their stress-strain response match except the flexural strength. The non-linearity in measured response also increases with increasing span length. The average of results are summarized in Table 8-2 and Figure 8.5.

Span length [mm]	No. of tests	Flexural modulus [GPa]	Tensile strength [MPa]
60	5	18.6	559.58
(St. deviation)		(0.488)	(33.52)
80	5	18.31	497.13
(St. deviation)		(0.415)	(18.46)
100	5	21.1	479.11
(St. deviation)		(0.526)	(7.6)

Table 8-2 Three point bending test results

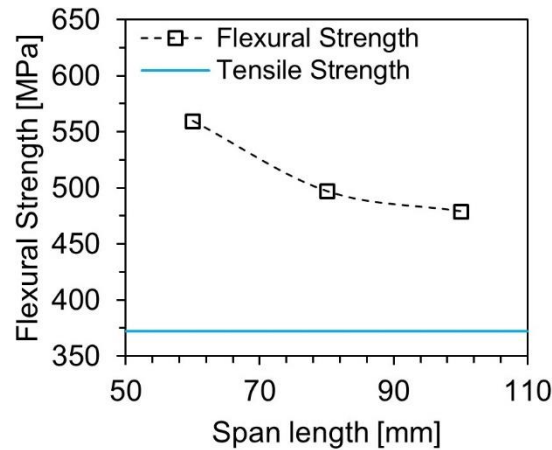


Figure 8.5 Decreasing flexural strength of 102-RG600(4) over span length

It is evident from the results that flexural strength is decreasing with increasing span length. The flexural modulus is not influenced by the specimen size. Regardless of the specimen size, the flexural strength is always higher than tensile strength.

### 8.2.1 Pin-end buckling test

In three-point bending tests, as the span length increases, the maximum amount of deformation required to break the specimen also increases (see Figure 8.4a). At large deformations, span length does not remain constant due to high inward bending of specimens causing non-linearity. The Eqn. (8.2) and (8.3) cannot be used for high deformations with non-linear response. Furthermore, a direct measurement of strain on three-point bending specimen was not possible with GOM Aramis. The reason behind this was that the impactor on upper side and support base on lower side makes it impossible to capture images with GOM camera (see Figure 4.16). Therefore, pin-end buckling test was used to verify the size effect in bending which is a direct method of strain measurement in bending.

In pin-end buckling test, specimen is fixed in rollers which have slots for specimen in it. These slots are a little off-set from the center so that the buckling direction of specimen is predetermined before the experiment. These rollers sit in roller holder where they are free to rotate. When the crosshead of machine moves downwards, the specimen buckles and strain can be measured on any side of the specimen. The measured force has no meaning because it includes the frictional effect between the roller surface and the seat in which they fit. Therefore, only strain will be measured using the digital image correlation apparatus ARAMIS. The test setup is shown in Figure 8.6 and 2D drawings of this fixture are given in Annex 12.3.5.

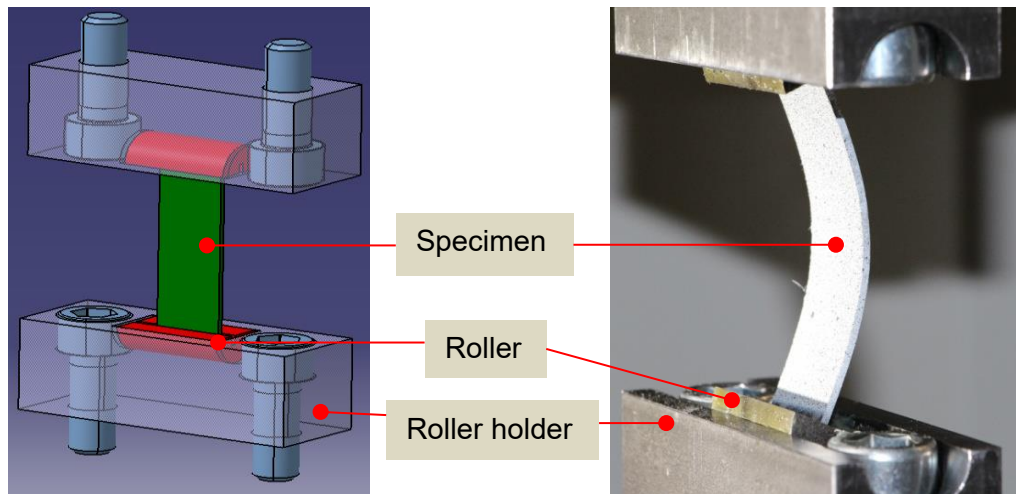


Figure 8.6 Pin-end buckling test

Three different specimen lengths (60mm, 80mm, 100mm) were tested. Specimen dimension were  $L \times 25\text{mm} \times 2\text{mm}$ . The tests were carried out on Zwick Z100. The specimen was fixed in the slots of rollers. Then roller was placed on the lower roller holder and machine cross head was moved downward till the upper roller was also positioned in upper roller holder. Then tests were carried out by moving the cross-head downward at speed of 5mm/min and strains were measured in longitudinal direction. Since with one DIC setup, the strain can be measured only on one side of specimen, so different specimens had to be used for measuring strain on outer (tensile) and inner (compressive) side of bending specimens. Images were captured with GOM 5M camera at frame rate of 1 fps and resolution of 500 x 1632 pixels. The failure of the specimen was just like in 3-point bending. The test results are shown in Figure 8.7- Figure 8.9.

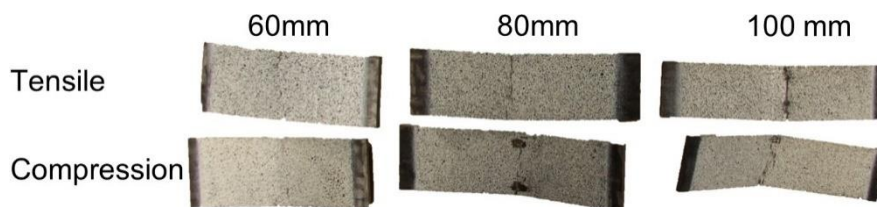


Figure 8.7 Specimen after pin end buckling test

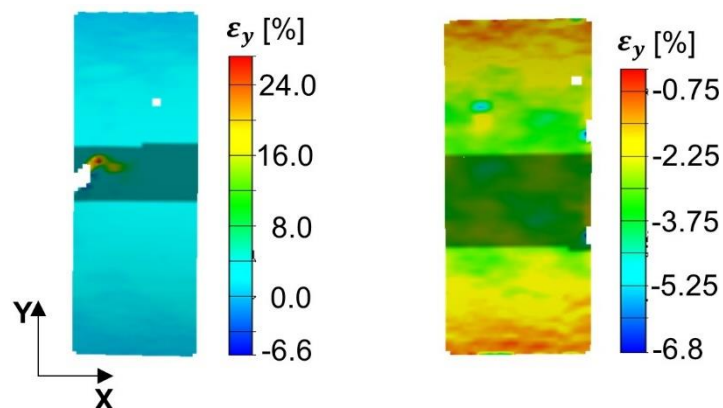


Figure 8.8 Surface strain measured on 80 mm specimen on tensile side (left) and compressive side (right). The shaded region represents where average strain was calculated

Span length [mm]	No. of tests	Tensile failure strain [%]
60 (St. deviation)	3	3.58 (0.3037)
80 (St. deviation)	5	3.34 (0.262)
100 (St. deviation)	5	2.68 (0.5)

Table 8-3 Measured strain on the outer side of pin-end buckling specimens

Span length [mm]	No. of tests	Compression failure strain [%]
60 (St. deviation)	5	4.05 (0.629)
80 (St. deviation)	4	3.26 (0.127)
100 (St. deviation)	5	3.52 (0.493)

Table 8-4 Measured strain on the inner side of pin-end buckling specimens

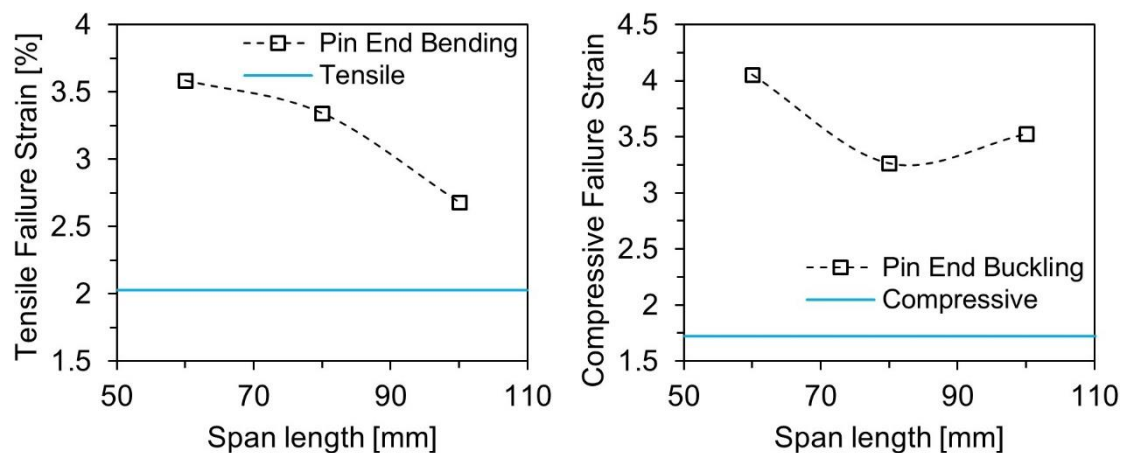


Figure 8.9 Effect of specimen size on the failure strain in Pin End buckling test of 102-RG600(4)

The tensile failure strain measured on the outer surface of specimens in bending in Figure 8.9 verifies the phenomenon of size effect and it is completely in accordance with flexural strength behavior in Figure 8.5. The failure strain in bending is higher than failure strain in tension and it is decreasing with increasing specimen size.

The compressive failure strain results in Figure 8.9 are at one data point dubious somehow. The compressive failure strain is higher than compressive failure strain measured in a combined loading compression test which is completely in accordance with size effect theory. However, the compressive failure strain measured in pin-end-buckling test decreases and then increases for 100mm long specimen which is not in agreement with size effect theory. Because the flexural specimens fail in tension, it is possible that compressive failure strain has little meaning here.

### 8.3 Proposed method for scaling strength in user-material subroutine

It has been seen experimentally that size effect diminished in tensile specimens due to large volume of material under constant stress. However, in bending only small volume of material is under stress so material strength is higher. Automotive structures under crash loading rarely undergo pure tensile loading. Rather most of the deformations are due to bending/buckling for which the strength of the material has to be scaled up. For reference, the three-point bending simulation shown in Figure 4.17 were repeated by manually changing the strength calculated from the 3-point bending test. The results are shown in Figure 8.10.

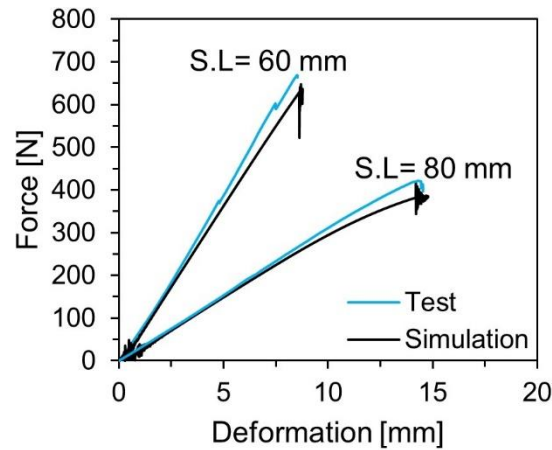


Figure 8.10 Three-point bending simulations by changing the tensile strength with flexural strength

The results in Figure 8.10 are obtained by manually changing the strength in the input file of simulation. For a full scale simulation, however the material model should be able to scale up the strength automatically. For this purpose, a method is proposed on how the Weibull modulus  $m$  in Eqn. (2.4) can be calculated from 3-point bending tests.

Consider Figure 8.11 where three point bending specimen of 102-RG600 with 4 plies is under three-point bending load. Due to bending, the upper ply of the material is under compression stress and lower ply is under tensile stress. The stress state is highest in the middle of plies due to bending moment and zero at the supports. The flexural stress increases linearly over the length of specimen. Because the specimen always fails in the middle at stress value higher than tensile strength, so we define a length  $a$  in the middle, where the flexural stress is higher than tensile strength at the time of failure. The length of  $a$  can be determined graphically by using the fact that stress at supports is zero and maximum at center. By connecting the support point with center point value with a linear line will give the stress value along the length of specimen.

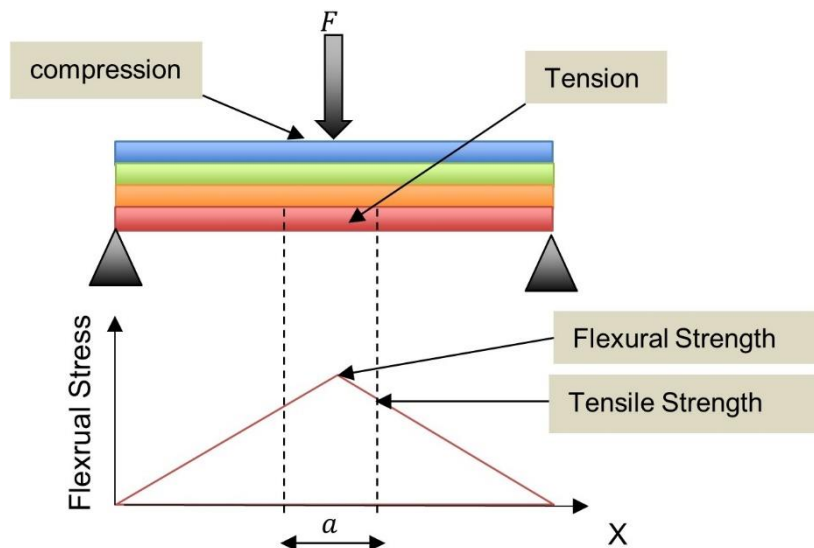


Figure 8.11 Bending Moment/Flexural stress along the length of 3-point bending specimen

The length  $a$  can be used to calculate the volume  $V$  which corresponds to the flexural strength.

$$V = a * \text{ply thickness} * \text{specimen width} \quad (8.4)$$

The same procedure can again be repeated with another test of different span length or different width to determine Weibull modulus  $m$ . Figure 8.12 shows the data points plotted using this methodology. A value of  $m=1.8$  has been calculated for 102-RG600(4).

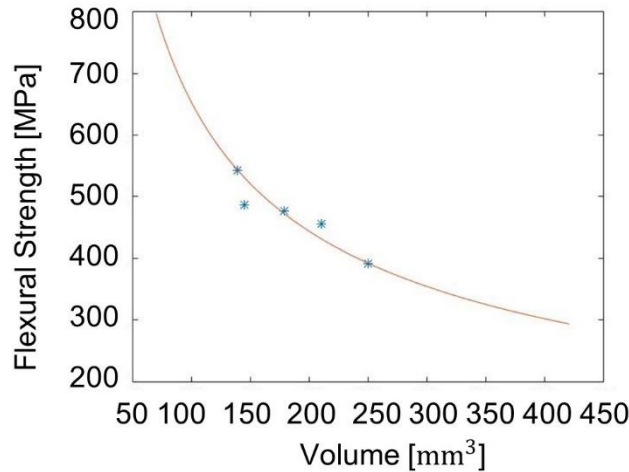


Figure 8.12 Weibull modulus  $m$  calibration

In user-material model the same approach can be adopted. An algorithm must be implemented which calculates the volume of material with stress higher than tensile strength around every integration point. With the calculation of volume, strength scaling can be implemented according to Eqn. (2.4).

#### 8.4 Conclusion

In this chapter the influence of the specimen size on the tensile and flexural strength has been investigated. It was found that

- Flexural strength of 102-RG600(4) is higher than their tensile strength;
- The flexural strength also increases by reducing the specimen size;
- Measured surface tensile failure strain in flexural specimens is also higher than tensile failure strain which means that increase in flexural strength is not due to stress gradient effect rather size effect;
- Similar to tensile failure strain, compressive failure strain in bending is also higher than compressive failure strain measured in simple compression test;
- With simulation of three-point bending test, it is shown that the scaling up of the strength according to specimen size is necessary;
- The size effect must be incorporated in material models by considering the volume of material under load;
- Methodology has been proposed for calculating Weibull's modulus for incorporation in user-material model.

## 9 Axial crush simulation

It was shown in chapter 3.6 that energy absorption by axial crushing of corrugate specimens was due to delamination. The delamination of composite materials cannot be modelled with conventional shell elements such as S4R. The reason behind this result is that shell elements cannot split in thickness direction and hence energy abortion due to delamination cannot be calculated. And all tests (tension, compression) do not characterize the delamination behavior. Therefore, more specific methods have to be adopted.

A considerable research work has been done on predicting the delamination growth in composite materials through fracture mechanics approach. The Linear Elastic Fracture Mechanics (LEFM) and Virtual Crack Closure Technique (VCCT) have limited usage due to the problems of inability to crack initiation and progressive crack propagation [81]. Camanho et al [82] Suggest the use of cohesive elements for prediction of delamination grown in composite materials. These cohesive elements are implemented in Abaqus. In this chapter, the viability of cohesive elements for prediction of crush energy absorption is investigated.

In section 9.1 the inter-laminar fracture energies in mode I and mode II are measured experimentally. The measured fractured energies are used as input parameters for calibration of cohesive elements in section 9.2. The input variables are validated by comparing the simulation with fracture energy measurement test data in section 9.3. Finally, in section 9.4 the simulation of corrugated specimen with cohesive elements between shell elements is done and the results are compared with the experimental data.

### 9.1 Inter-laminar fracture energy measurement

There are three different fracture modes (one normal and two shear fracture modes) in which a delamination in composite materials can occur. These concepts are necessarily the same as considered in any fracture mechanics study.

1. Crack opening mode (mode-I)
2. Shearing mode (mode-II)
3. Tearing mode (mode-III)

A graphical illustration of three modes is given in Figure 9.1.

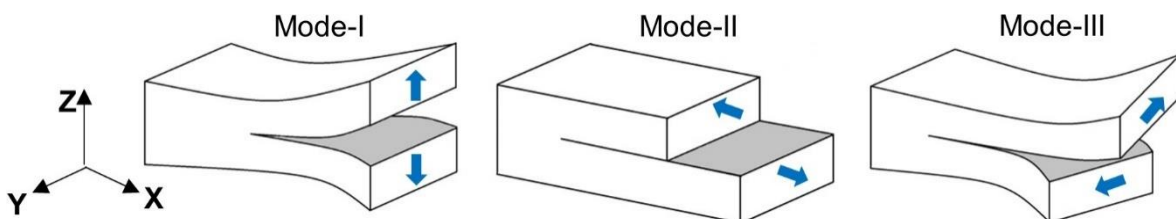


Figure 9.1 Three inter-laminar fracture modes in composites

The fracture energies associated with the mode-I and mode-II were measured experimentally by Double Cantilever Beam (DCB) test and End Notch Flexural (ENF) test respectively. The fracture

energy for mode-III was supposed to be equal to fracture energy of mode-II because of the resemblance.

### 9.1.1 DCB test

DCB test was carried out according to ISO-15024 [83]. A pre-cracked specimen was pulled on opposite edges and delamination propagates as a results of Mode-I loading. The specimens were of rectangular geometry with dimensions of 125 mm x 25 mm x 5 mm. A 63 mm long and 50 $\mu$ m thick film of Kapton HN10 was inserted at mid-plane which act as pre-crack/delamination. When specimen was loaded, the crack front moved forward and hence delamination propagated. The specimen geometry is shown in Figure 9.2.

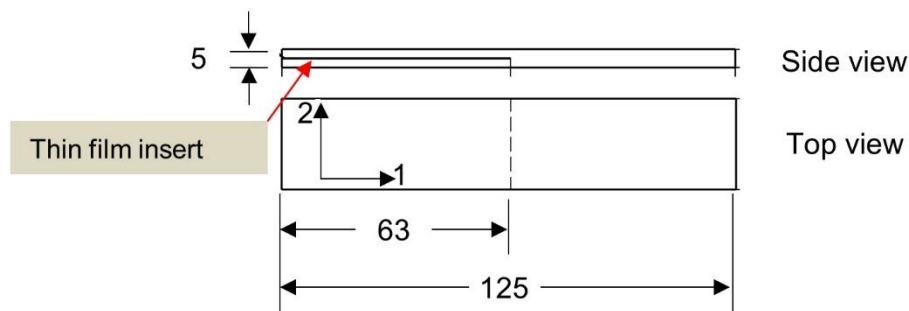


Figure 9.2 Double Cantilever Beam Specimen

The specimens were prepared by Bond Laminates, Germany. To prepare multiple specimens, it was not feasible to manufacture every specimen separately. Therefore, two panels of 2.5 mm thickness were heated. The non-adhesive film was place in the middle and the panels were joined. Afterwards, the specimens were cut on water jet cutting machine. Figure 9.3 shows schematic representation of specimen cutting.

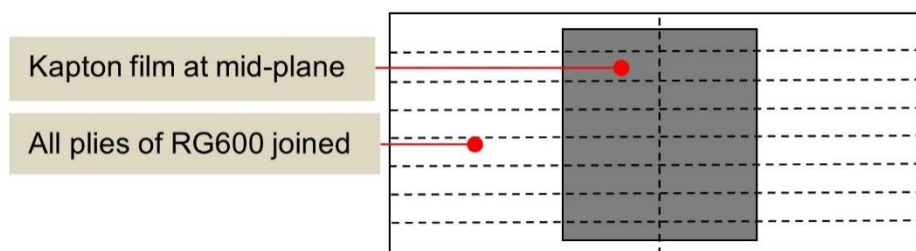


Figure 9.3 Schematic of panel with dashed lines showing the water jet cutting lines

In order to pull apart the two side of specimen, two hinges DIN 7954D-25x38 were glued on upper and lower side of specimen on thin film insert side. Hinges allowed the free rotation of the specimen ends during loading. The adhesive used was Sicomet-77 and surface of the specimen was roughened by P-240 sand paper before gluing the hinges. To measure the delamination growth, the side of specimen was painted white with water soluble correction fluid and every millimeter was marked with help of gauge ruler. The total delamination length is distance between the hinge and crack front. When the head of machine moved and delamination propagates, the force and the deformation was recorded by Zwick 100. Images were recorded at 1 frame/sec and resolution of 2195 x 125 pixels during the test to identify the delamination propagation. Strain was not measured so no stochastic spray was needed on the specimen. Figure 9.4 shows the specimen during test.

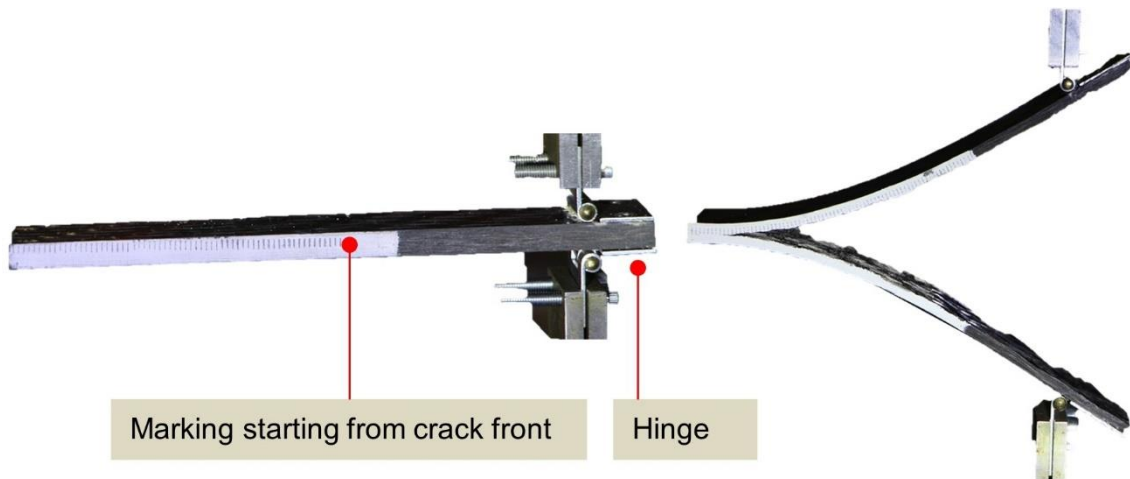


Figure 9.4 DCB specimen at start of test (left) and after delamination propagation (right)

The specimen was loaded and unloaded repeatedly. The purpose of loading and unloading was that the non-adhesive film insert was  $50\mu\text{m}$  thick and a real crack would not have a  $50\mu\text{m}$  crack front. During the loading phases, the delamination propagated which created a natural crack front. The specimen was loaded with speed of  $5\text{mm}/\text{min}$  till crack propagates and then unloaded with speed of  $25\text{mm}/\text{min}$ . The recorded force-deformation data is shown in Figure 9.5. The deformation  $\delta$  here corresponds to the cross-head movement of Z100. The force levels  $P$  at which delamination propagated, were visually identified from synchronized images. Total delamination length  $a$  was determined from the marking on the specimen. These values are given in Annex 12.1.7.

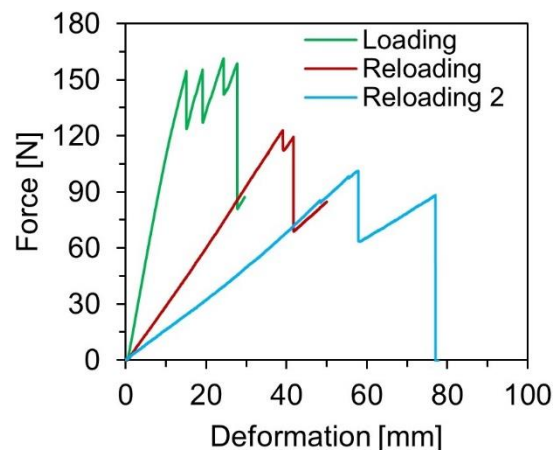


Figure 9.5 Load-Deformation curve of loading and unloading of DCB specimen

For every crack propagation, the value force  $P$ , deformation  $\delta$  and delamination length  $a$  was acquired. From this data two methods were used to calculate the critical fracture energy. The methods are named according to ISO-15024 [83] as:

1. Corrected Beam Theory (CBT)
2. Modified Compliance Calibration (MCC)

The details of these two methods are described in the following.

### Corrected Beam Theory Method

To measure  $G_{IC}$  according to CBT, the compliance  $C$  was calculated which is the ratio of the deformation  $\delta$  to applied load  $P$ . These values were determined for every crack propagation giving different values of delamination length  $a$ . Then a relation between the delamination length  $a$  and compliance was established by plotting the cube-root of the compliance  $C^{1/3}$  as shown in Figure 9.6. This relation was used to calculate the  $\Delta$  which is x-intercept of plot.

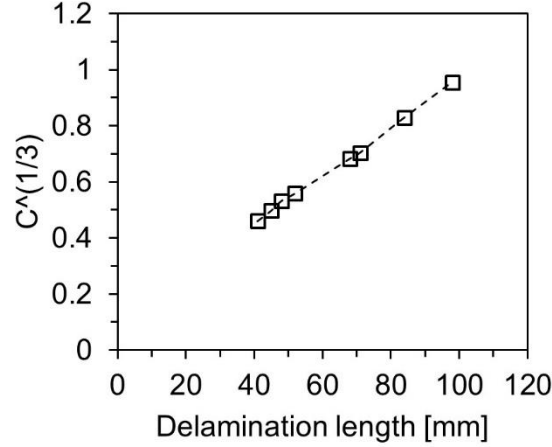


Figure 9.6 Determination of correction factor  $\Delta$  by curve fitting

The critical fracture energy  $G_{IC}$  from DCB test according to CBT was calculated by:

$$G_{IC} = \frac{3P\delta}{2b(a + |\Delta|)} \times F \quad (9.1)$$

$b$  is the width of specimen;  $a$  is the total delamination length which is identified by images taken by camera.  $\Delta$  is the x-intercept of plot in in Figure 9.6.  $F$  is correction factor for hinge calculated by:

$$F = 1 - \frac{3}{10} \left( \frac{\delta}{a} \right)^2 - \frac{2}{3} \left( \frac{\delta l_1}{a^2} \right) \quad (9.2)$$

In which  $l_1$  is the distance from the center of the loading pin of hinge to the mid-plane of the specimen (see Figure 9.4) . The result values are shown in Figure 9.8.

### Modified Compliance Calibration Methods

MCC is just another way to calculate the  $G_{IC}$  using the same measured values as used for CBT. To calculate  $G_{IC}$  according to MCC, the slop  $m$  of plot between thickness-normalized delamination length  $a/2h$  and width-normalized cub root of the compliance  $(bC)^{1/3}$  was measured. The plot is shown in Figure 9.7.

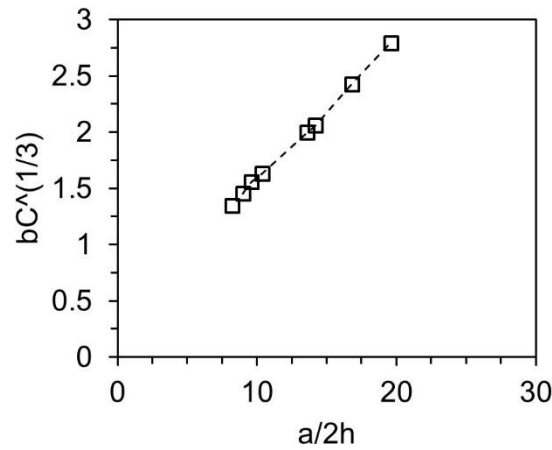


Figure 9.7 Determination of slop  $m$  by curve fitting

And the critical energy release rate was measured by according to:

$$G_{IC} = \frac{3m}{2(2h)} \times \left(\frac{P}{B}\right)^2 \times \left(\frac{bC}{N}\right)^{2/3} \times F \tag{9.3}$$

Here  $m$  is the slop calculated from Figure 9.7.  $2h$  is the thickness of specimen.  $P$  is the force value,  $B$  is the width and  $C$  is compliance.  $N$  is a correction factor which is equal to 1 for hinges.  $F$  has already explained above in Eqn.(9.2).

The results of critical inter-laminar fracture energy calculated by CBT and MCC are plotted for every crack propagation in Figure 9.8. A complete result sheet of the test results and observations can be found in Annex 12.1.7.

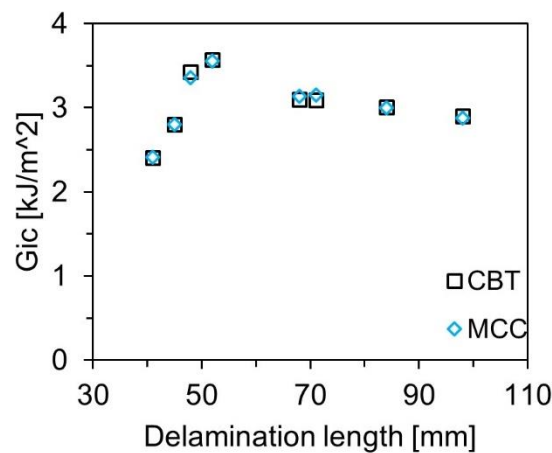


Figure 9.8 Delamination resistance curve calculated by CBT and MCC methods

Both methods have produced same results of  $G_{IC}$ . Eight crack propagation values were determined among which first measured value of critical fracture energy was not measured from a natural crack growth. The average value of fracture energy release rate for Mode-I fracture is  $3.036\text{kJ/m}^2$ .

### 9.1.2 ENF test

End Notch Flexural Test was used to measure Mode-II critical fracture energy according to ASTM D7905 [84]. A pre-cracked specimen was subjected to flexural loading. In bending, the upper half of specimen experience compression and lower half of specimen experience tensile loading. Due to this difference a shear force exists between the plies. Therefore, stress concentration at crack front exists and crack propagates under mode-II loading. The Mode-II and Mode-III failure described as shear and tear mode correspond to the type of loading where the two plies of composite separate from each other in a sliding mode. Due to the same nature of failure, their critical fracture energy values were considered equal.

The ENF specimens were also prepared just like DCB specimens by using non-adhesive layer in mid-plane acting as pre-crack. The specimen dimensions are given in Figure 9.9.

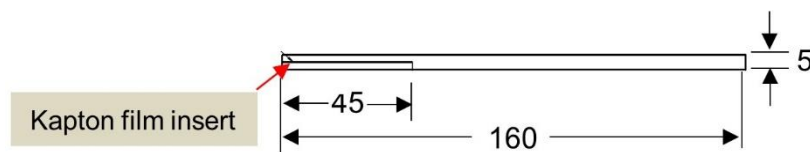


Figure 9.9 End Notch Flexural Specimen

The edges of specimens were painted with white water based typewriter correction fluid to visually locate the delamination tip. Visual detection and marking of delamination tip needed careful observation under magnifying glass. From the delamination tip, three compliance calibration markings at distance of 20 mm, 30 mm and 40 mm were marked. The specimens were placed on the supports rollers of 5 mm. The impactor of 5 mm radius was exactly in the middle of the supports. The distance between the supports was 100 mm. The test setup is shown in Figure 9.10.

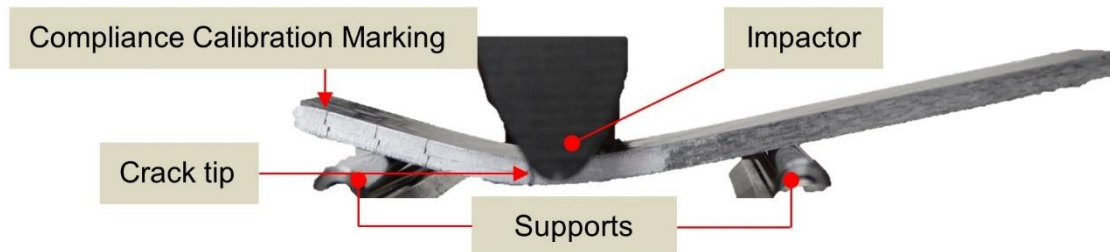


Figure 9.10 ENF specimen under loading

ENF test method uses compliance calibration method to measure  $G_{IIC}$  where the compliances of specimen were measured for difference crack lengths  $a_1=20\text{mm}$ ,  $a_0=30\text{mm}$ ,  $a_2=40\text{mm}$ . And then specimen is loaded with crack length  $a_0=30\text{mm}$  till delamination propagates and maximum force  $P_{max}$  in force-displacement ( $P-\delta$ ) plot is used to calculate  $G_{IIC}$ . So the test procedure consisted of three steps.

1. The specimen was placed such that crack tip was 20 mm from the left support. Thus 20 mm compliance calibration marking was exactly on the left support. The specimen was loaded to 50% of the force at which the crack would propagate and unloaded. This force value corresponds to the 25%  $G_{IIC}$  value. This curve was recorded as blue curve in Figure 9.11.

2. Then specimen was moved towards right so that 40 mm crack length marking was on top of impactor. The same procedure repeated as step 1 and **green curve** was recorded in Figure 9.11.
3. Finally, the specimen was placed such that 30 mm marking was on top of impactor. In Figure 9.10, 30 mm marking is shown exactly on the top of left support. This time the specimen was loaded until crack propagated. The crack propagation was recognized from drop in force value of **red curve** in Figure 9.11.

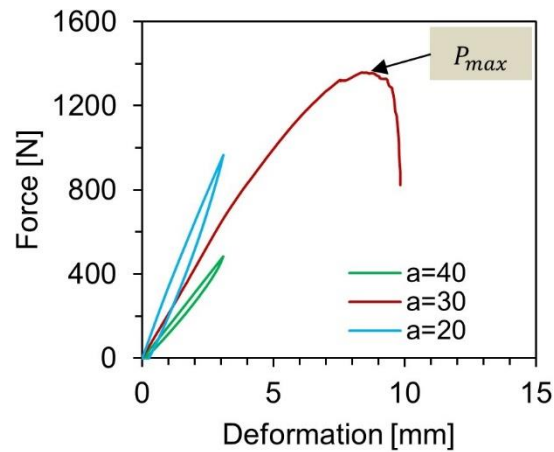


Figure 9.11 Loading, unloading and final loading of ENF curve with 20mm, 40mm and 30mm delamination lengths

To calculate the value of  $G_{IIC}$ , data points of cube of delamination length  $a^3$  and compliance  $C$  for each loading were plotted as shown in Figure 9.12. This plot was used to establish a relation between  $a^3$  and compliance  $C$  resulting in slope  $m$ , intercept on y-axis  $A$  and correlation coefficient  $r^2$ .

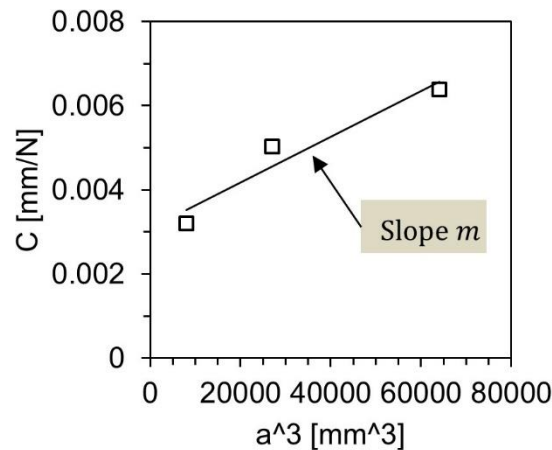


Figure 9.12 Compliance Coefficient determination of ENF

The fracture energy was determined as:

$$G_Q = \frac{3mP_{Max}^2a_0^2}{2B} \quad (9.4)$$

Here  $B$  is the width of specimen. Note, that in Eqn. (9.4), the value of so called candidate fracture energy  $G_Q$  is calculated. The candidate fracture energy is accepted as fracture energy  $G_{IIC}$  only if the

condition  $15 < \%G_{Q,j} < 35$  was fulfilled. Therefore, a percentage of  $G_Q$  ( $\%G_Q$ ) was evaluated according to:

$$\%G_{Q,j} = \left[ \frac{100(P_j a_j)^2}{P_{max} a_o} \right]; j = 1,2 \quad (9.5)$$

Where  $P_j$  is the force at which compliances were measured and  $P_{max}$  is the force values at which crack propagated in Figure 9.11. If the  $15 < \%G_{Q,j} < 35$  was satisfied, then  $G_Q$  was accepted as  $G_{IIC}$ . Therefore, every test for which  $G_Q$  was calculated, two values of  $\%G_Q$  were also measured and the two values had to be between 15 and 35.

As shown in Figure 9.9, the 50 $\mu$ m thick Kapton HN thin foil was used in specimens to mimic the crack. But this makes the crack front thicker than natural crack. So two values of  $G_{IIC}$  were measured. Non-Pre-cracked (NPC)  $G_{IIC}$  was determined when the crack propagated for the first time. Once the crack has propagated, the new crack front acts as natural crack. Pre-cracked (PC)  $G_{IIC}$  values were measured after delamination has advanced from pre-implanted insert and delamination tip mimic the natural crack. Five test were carried out and the average value of pre-cracked specimens  $G_{IIC}$  was 5.96 kJ/m<sup>2</sup>. A complete result sheet according to ASTM D7905 is given in Annex. 12.1.8.

## 9.2 Delamination modeling

For modeling the delamination in plies of composites, 3D solid cohesive elements COH3D8 are used which is available in Abaqus [85]–[87]. A layer of cohesive elements is defined between the two layer of shell elements of composite materials.

Consider a composite material with four plies and delamination has to be modelled between upper two and lower two plies. The composite material is modelled as two layer of shell elements, each containing two plies, parallel to each other. The two layers are joined by placing cohesive elements in between them. The top and bottom face of cohesive elements are joined to shell elements by merging their nodes. By merging the nodes, the mesh of the cohesive layer and adjacent elements share their nodes with each other. Therefore, it is important that the cohesive layer and the shell elements have matching meshes. If their meshed are not structured, then elements can be joined by means of tie constraints.

When the bottom and upper faces of cohesive elements are subjected to traction, the elements behave according to constitutive behavior under the applied tractions.

### 9.2.1 Constitutive model of cohesive elements

The constitutive response of cohesive elements starts with elastic region which is linear elastic until it reaches damage initiation point. At the damage initiation point, the damage in material is zero and starts to increase unless the elements stiffness reverts to zero. The area under traction-separation curve is the fracture energy which equal to fracture energies measured by DCB or ENF tests depending upon the load case. A graphical illustration is given in Figure 9.13.

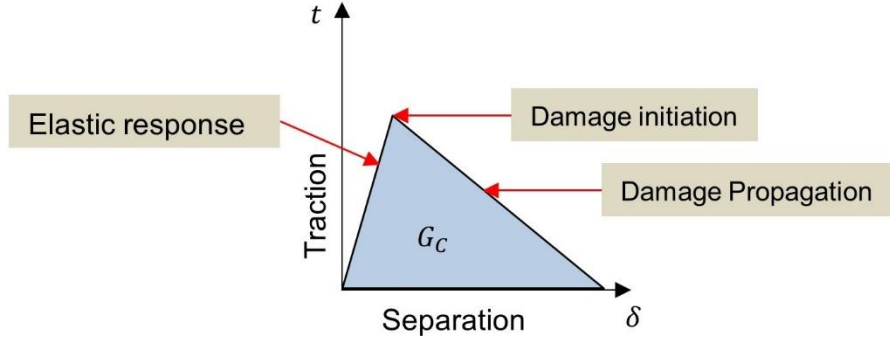


Figure 9.13 traction-separation response of cohesive elements [88]

### Elastic behavior

The traction separation law assumes linear elastic behavior. The traction vector  $\mathbf{t}$  is composed of three components  $t_n$ ,  $t_s$  and  $t_t$ , correspond to Mode-I, Mode-II and Mode-III failure respectively. The relation of traction with nominal strain  $\boldsymbol{\varepsilon}$  with similar components can be written as:

$$\mathbf{t} = \begin{Bmatrix} t_n \\ t_s \\ t_t \end{Bmatrix} = \begin{bmatrix} E_{nn} & E_{ns} & E_{nt} \\ E_{ns} & E_{ss} & E_{st} \\ E_{nt} & E_{st} & E_{tt} \end{bmatrix} \begin{Bmatrix} \varepsilon_n \\ \varepsilon_s \\ \varepsilon_t \end{Bmatrix} = \mathbf{E} \boldsymbol{\varepsilon} \quad (9.6)$$

Because the constitutive model is based on the displacement (see Figure 9.13) and not strain so numerical thickness of elements is set equal to 1. This would mean that strain and displacement values are the same and elastic properties are also equal to young's modulus.

In simulations, uncoupled behavior is used which means that off-diagonal terms in elasticity matrix of Eqn.(9.6) are equal to zero.

### Damage initiation

Damage initiation determines the point at which degradation of material starts. This damage initiation criterion could be based on stresses or strains. Then there are simple stress/strain criteria e.g. Maximum Stress/Strain criteria or Quadratic Stress/Strain Criterion. In simulations, Quadratic Stress criterion was used.

$$\left\{ \frac{\langle t_n \rangle}{t_n^o} \right\}^2 + \left\{ \frac{t_s}{t_s^o} \right\}^2 + \left\{ \frac{t_t}{t_t^o} \right\}^2 = 1 \quad (9.7)$$

Here  $t_n^o$ ,  $t_s^o$  and  $t_t^o$  represent the peak traction values.

### Damage evolution

Once the damage initiation criterion has been met, the degradation of material starts. Damage evolution determines the rate at which the degradation occurs. Damage evolution methods can be based on displacement or energy. In this chapter Benzeggagh-Kenane (BK) [89] method was used which is recommended if Mode-II and Mode-III critical fracture energy values are same. BK is an energy based damage evolution method. According to BK damage evolution, when a combination of normal and shear crack opening load is applied, the area under traction deformation curve is equal to  $G^C$  defined as:

$$G^C = G_n^C + (G_s^C - G_n^C) \left\{ \frac{G_s + G_t}{G_n + G_s + G_t} \right\}^\eta \quad (9.8)$$

Based on the  $G^C$  value, a linear or exponential damage evolution function can be chosen. A graphical illustration of the constitutive behavior used in the simulations of this chapter is shown in Figure 9.14.

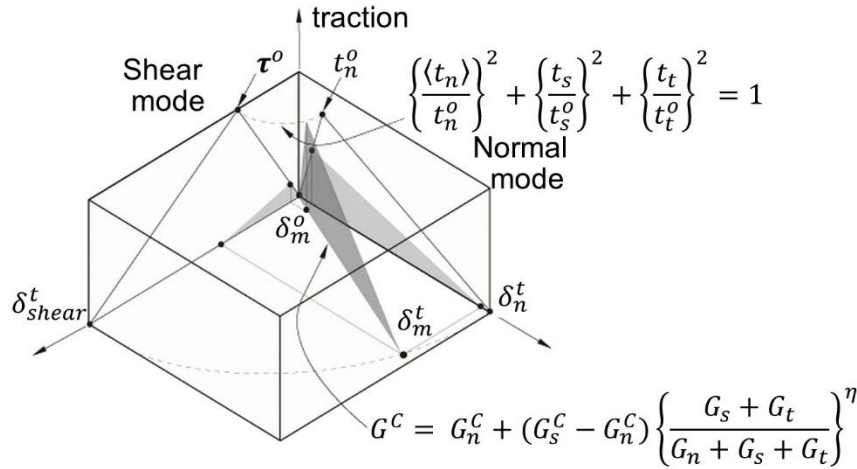


Figure 9.14 Constitutive response of cohesive element with quadratic damage initiation criterion and BK-damage evolution function [88]

Quadratic stress law maps damage initiation and mix-model critical  $G^C$  maps damage growth. For a pure mode-I loading [Normal mode] the curve mapped on the traction- $\delta_n^t$  plane will be followed. For mode-II and mode-III the curve mapped on the traction- $\delta_{shear}^t$  will be followed by the cohesive element. If an element experiences both normal as well as shear loading at the same time, then damage initiation criterion and BK-fracture criterion maps the response (the shaded curve in middle of Figure 9.14).

### 9.2.2 Parameter calibration

The constitutive Eqn. (9.6) and (9.7) require the elastic and strength properties of the matrix material. The matrix material in 102-RG600 is PA6 and its elastic properties are summarized in Table 9-1.

Young's modulus E	2.76 GPa
Tensile strength	82.7 MPa
Poisson's ratio	0.39
Shear modulus = $G = \frac{1}{2(1+\nu)} E$	0.992 GPa
Shear strength	75.8 MPa

Table 9-1 Mechanical properties of PA6 [90], [91]

For a successful FEM simulation with cohesive elements, it is important the element size is less than cohesive zone length  $l_{cz}$  [92]. According to Travesa [81], "The length of the cohesive zone  $l_{cz}$  is defined as the distance from the crack tip to the point where the maximum cohesive traction is attained". Suppose a layer of cohesive elements is modelled in a DCB specimen as shown in Figure 9.15 (also see Figure 9.4, Figure 9.26 and Figure 9.27). The Mode-I crack opening load is applied on the left side of specimen. As the cohesive elements undergo deformation, cohesive elements on the left side start to fail. Cohesive elements in which damage has initiated but are not fully damaged is named as cohesive zone. and some of them are being damaged. The length of the elements in this cohesive zone is called cohesive zone length.

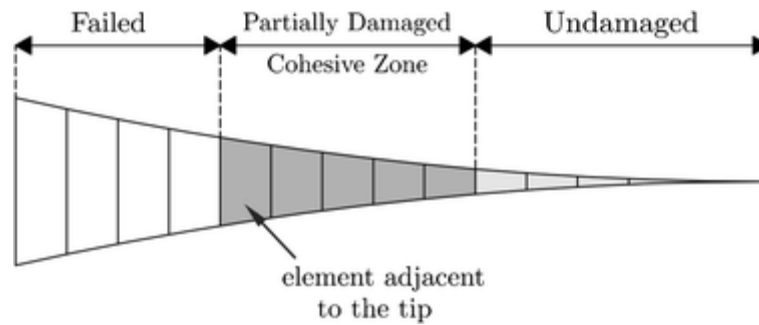


Figure 9.15 Graphical illustration of cohesive zone length [93]

The cohesive zone length is calculated as [81]:

$$l_{cz} = ME \frac{G_c}{(\tau^0)^2} \quad (9.9)$$

Here  $M=1$ ,  $E$  is young's modulus,  $G_c$  is the fracture energy (Mode-I and Mode-II) and  $\tau^0$  is respective maximum strength value. It is recommended that at least three elements should fit into the cohesive zone length. Using the above formula and material properties of PA6, the  $l_{cz}$  is calculated:

- Cohesive zone length for Mode-I = 1.22mm
- Cohesive zone length for Mode-II and Mode-III = 1.03056mm

These cohesive zone lengths mean that the mesh size should be roughly 0.3mm which is too small for feasible simulation time. Travesa [81] devised a method in which he changed the material strength properties to increase the cohesive zone length. He has shown that only fracture energy value dictates the simulation results, and changing the strength of matrix material does not influence the simulation results. By reducing the strength values  $\tau^0$  the cohesive zone length  $l_{cz}$  can be increased and hence the mesh size can also be increased (see Figure 9.16).

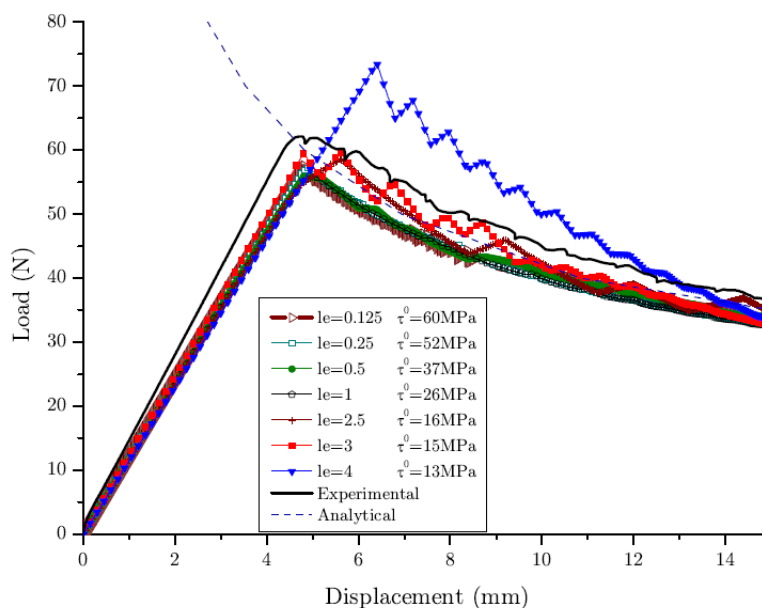


Figure 9.16 Load displacement curves for DCB simulation with modified interface strengths and mesh sizes showing no influence on the results [92]

Travesa [81] also provided guidelines how the modified strength value  $\bar{\tau}^o$  can be calculated.

$$\bar{\tau}^o = \sqrt{\frac{9\pi E G_c}{32 N_e^o l_e}} \quad (9.10)$$

Where  $N_e^o$  and  $l_e$  are number of element and length of element in cohesive zone length. This equation was used to calculate the strength of the cohesive element  $\bar{\tau}_o$  for FE-simulations. It was calculated from the E-modulus, critical fracture energy value  $G_c$ , number of cohesive elements in cohesive zone length  $N_{eo}$  length of cohesive zone  $l_e$ . This value ensures that there are enough number of finite elements in cohesive zone length.

With mesh size of  $l_e = 2 \text{ mm}$  and three elements in cohesive zone length  $N_e^o = 3$ , the modified strength  $\bar{\tau}^o$  for cohesive elements were calculated as:

- Modified Interfacial strength for Mode-I = 20.3MPa
- Modified Interfacial strength for Mode-II and Mode-III = 17.04MPa

Now with all the material parameters determined, the simulation can be carried out.

### 9.2.3 Single-element simulation

To verify the parameters of cohesive elements, a single brick element was created and allocated cohesive element properties. Then the single element was loaded in crack opening mode just by restricting all DOF at bottom and applying displacement BC at the top as shown in Figure 9.17 and the traction separation plot was requested in output as shown in Figure 9.18.

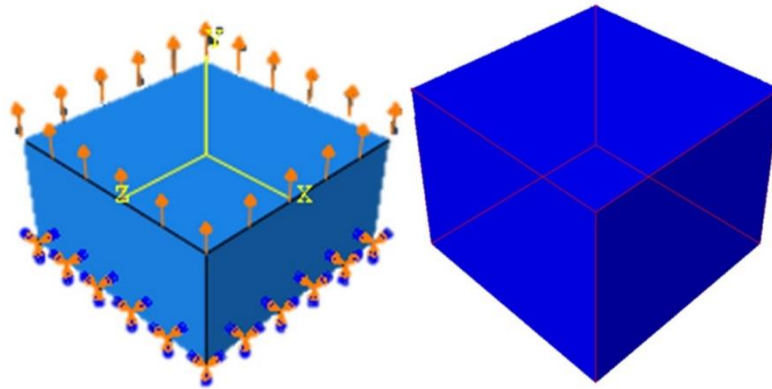


Figure 9.17 Single cohesive element under Mode-I boundary condition (left) and resulting deformation (right)

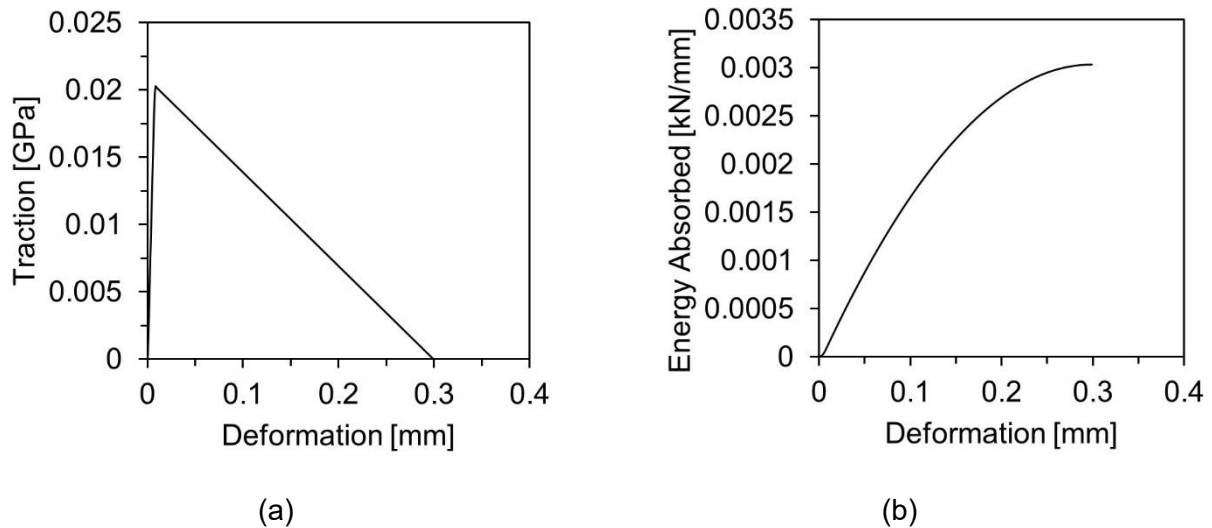


Figure 9.18 (a) Single cohesive element response in Mode-I and (b) Energy absorption over the deformation

The results shown in Figure 9.18a that the maximum traction value is  $0.023 \text{ GPa} = 20.3 \text{ MPa}$  which is the modified strength value for mode-I. Figure 9.18b is calculated by integrating the curve in Figure 9.18a which is the area under traction-deformation curve. The maximum value of energy absorbed is equal to  $0.003036 \text{ kN-mm/mm}^2 = 3.036 \text{ kJ/m}^2$  which is equal to mode-I fracture energy measured by DCB test.

In mode-II the applied displacement boundary condition was perpendicular to the thickness direction. All degrees of freedom at bottom were restricted. The deformation and resulting response are shown in Figure 9.19 and Figure 9.20.

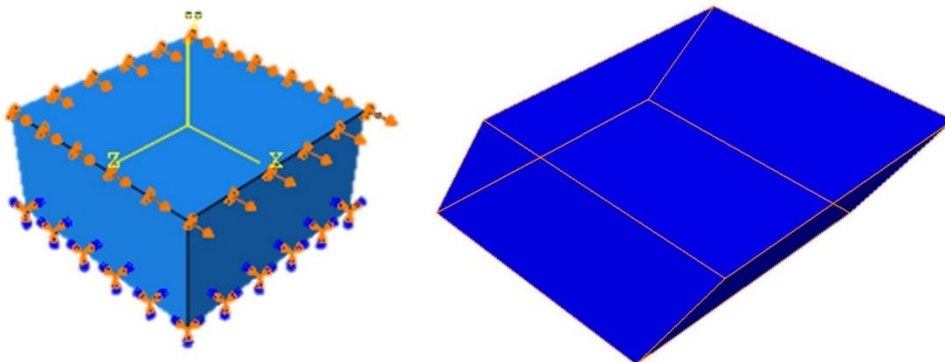


Figure 9.19 Single cohesive element under Mode-II boundary condition (left) and resulting deformation (right)

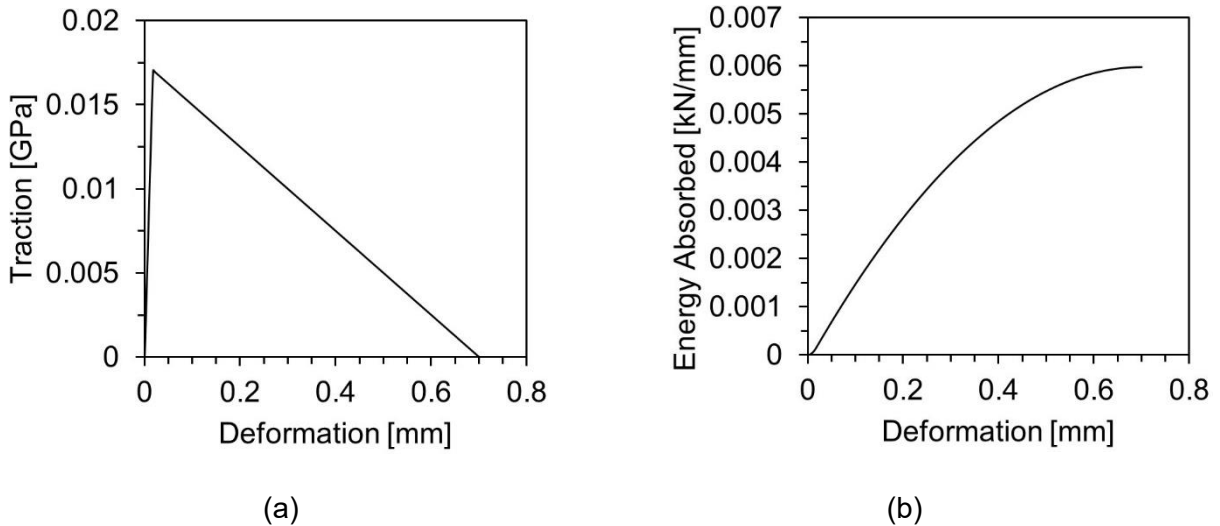


Figure 9.20 (a) Single Element simulation response in Mode-II (b) Energy absorption over the deformation

Similar to Mode-I response, the single element simulation response in Mode-II also matches with input parameters. And area under traction-deformation curve is equal to Mode-II fracture energy measured by ENF test.

**9.2.4 Influence of cohesive modeling on composite response**

The objective of using cohesive elements is that the in-plane response of composite materials does not change. I.e. in-plane stiffness of cohesive elements is zero. Therefore, if cohesive elements are used to model the composite material then composite material response by applying direct membrane strains or in plane shear strains should remain unchanged. This was verified by tensile simulation of a model with and without cohesive elements and comparing their results.

Two simulation models were created. One without cohesive elements for reference purpose and second with cohesive elements between the plies. Model without cohesive elements was modeled with shell elements containing 4 plies, each 0.5mm thick in it. The model with cohesive elements was modeled with two different section, each containing 2 plies of 0.5 thickness. These two shell elements layers were 1 mm offset from each other and joined by 1 mm thick cohesive elements. A schematic diagram of the two models is shown Figure 9.21.

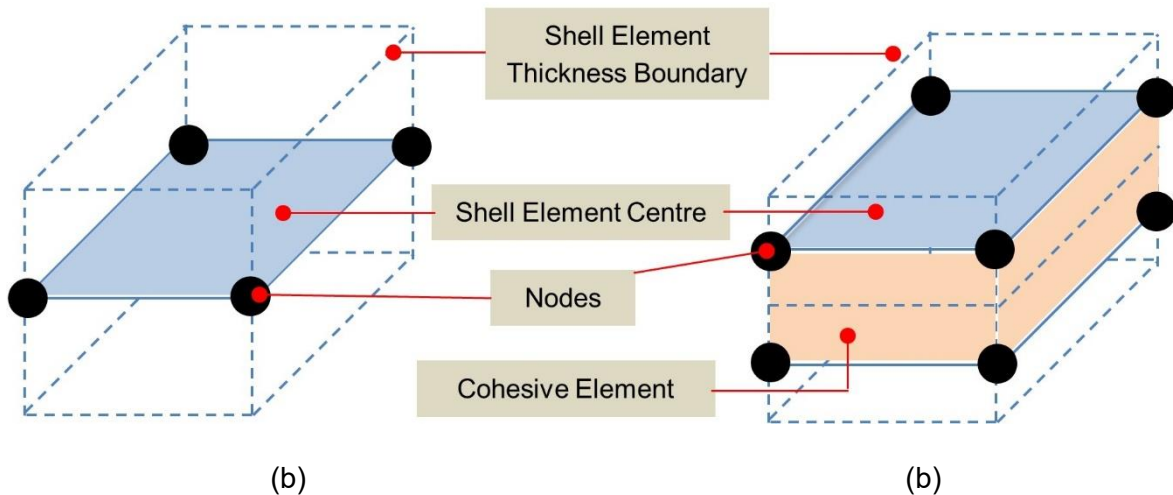


Figure 9.21 (a) Single Shell element containing four plies and (b) two shell elements offset from center and joined with cohesive element

To create cohesive elements on specimen level, all of the pre-processing was automated by a Python-Scripting. The simulation models are shown in Figure 9.22 and simulation results are compared in Figure 9.23.

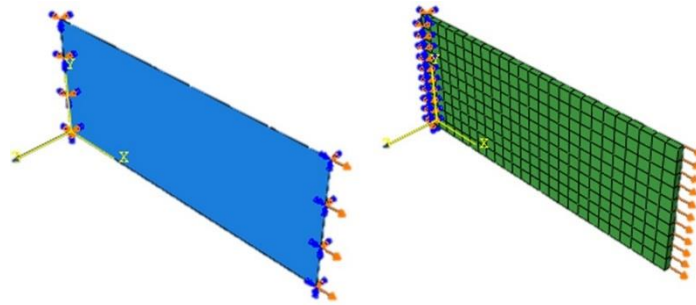


Figure 9.22 Tensile Simulation without cohesive elements (left) and with cohesive elements (right)

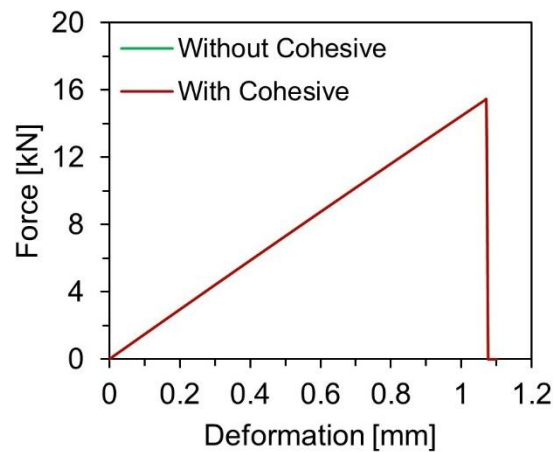


Figure 9.23 Tensile response of a simulation model with and without cohesive elements

It is seen in Figure 9.23 that there is no influence of cohesive elements on the tensile response of laminate.

Similar to tensile behavior, the influence of cohesive elements on flexural response was compared. Three-point bending simulation of 50mmx20mmx2mm specimen was done with and without cohesive elements. The supports of 5mm radius were modelled 40mm apart from each other and an impactor of 5mm radius was impacted at the center with smooth loading step. The simulation models are shown in Figure 9.24 and their results are shown in Figure 9.25.

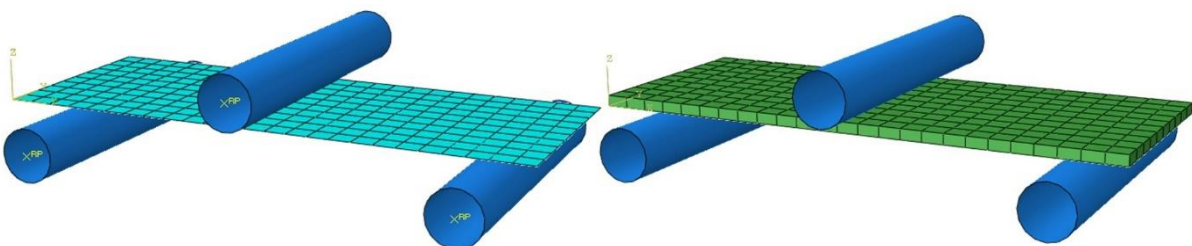


Figure 9.24 Three point bending without (left) and with (right) cohesive elements

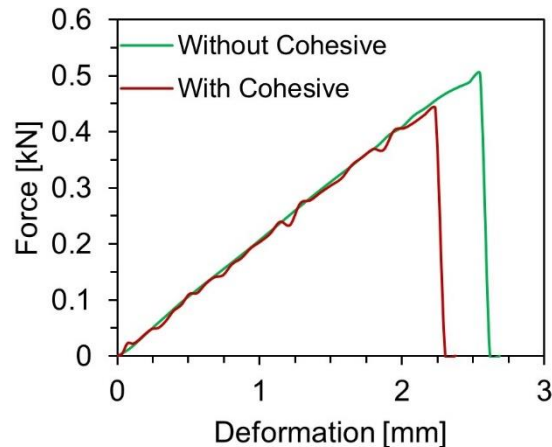


Figure 9.25 Difference in flexural behavior with and without cohesive elements

Figure 9.25 shows that flexural strength predicted with cohesive elements is less than flexural strength predicted without cohesive modeling. In bending, lower half of composite plies experience tensile loading and upper half experience compression loading. When all plies are modeled in single shell elements, the inter-ply load transfer in the thickness direction is dictated by through-thickness shear stiffness. When cohesive elements are present between the plies, the shear/tear properties of cohesive elements dictate the load transfer between plies. If the shear stiffness of cohesive element is not enough then load might not be transferred enough between the plies. If plies on one side of cohesive element take higher load, and other half does not take as much load then maximum load bearing capacity of whole laminate is reduced.

### 9.3 Validation

With the cohesive element material properties calibrated on single element, the modelling approach was validated by the simulation of two tests from which fracture energy values were calculated.

#### 9.3.1 DCB simulation

DCB specimen was modeled by the two parallel layers of shell elements 2.5 mm offset from each other. Each layer of shell elements was assigned five plies, with each ply of 0.5 mm thickness. The shell elements of pre-cracked region (thin film insert) were left without any joining technique. And rest of the model was joined with cohesive elements. Because the two layer of shell elements were 2.5 mm offset from each other so the thickness of cohesive elements was also 2.5 mm. To reduce the no. of elements, the mesh was structured such that there was only one element along the width of specimen. Due to delamination propagation along the length of the specimen, the element width size did not matter and the total number of elements reduced significantly. The mesh along the length of specimen was 2 mm. The simulation model is shown in Figure 9.26.

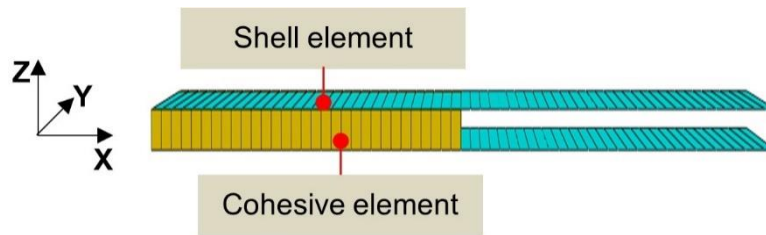


Figure 9.26 DCB simulation model

To apply the B.C. of hinge, one reference point was defined for each hinge at the point of rotation of hinge. This reference point was tied to the region where hinge was glued. The bottom reference point was fixed in all degree of freedom except rotation around y-axis. The upper reference point was restricted in all degrees of freedom except rotation around y-axis and translation along z-axis. Displacement boundary condition was applied to upper reference point with a smooth step to minimize the inertial effects. The cohesive elements were subjected to Mode-I loading and delamination propagated. The results are shown in Figure 9.27 and Figure 9.28.



Figure 9.27 DCB simulation showing mode-I stress in cohesive elements

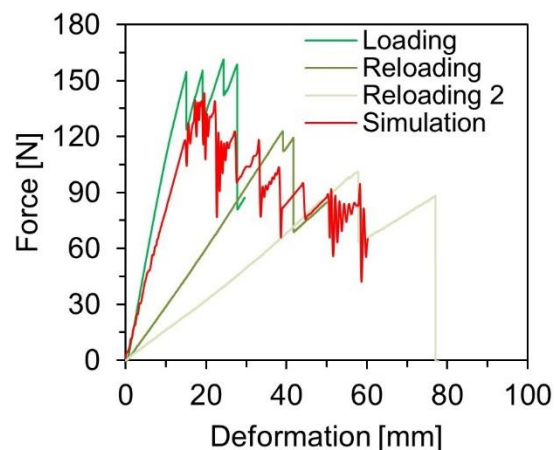


Figure 9.28 Force-displacement plot of DCB simulation compared with test data

Unlike experimental, simulation was run without unloading/reloading for faster results. The simulation results of Figure 9.28 show that the initial stiffness is little lower than experimental data and the delamination propagated at a slightly lower level than experimentally data. However, it can be seen that propagation in DCB simulation has been predicted reasonably well.

### 9.3.2 ENF simulation

Similar to DCB simulation, the pre-cracked ENF specimen was modeled with two parallel layers of shell elements each 2.5 mm thick. The two layers were 2.5 mm offset from each other. The region of specimen where there was no thin film insert (no delamination) were joined by cohesive elements of 2.5 mm thickness. The nodes of shell elements and cohesive elements were merged. The impactor and supports were modelled as 3D analytical rigid parts. Figure 9.29 shows the simulation model.

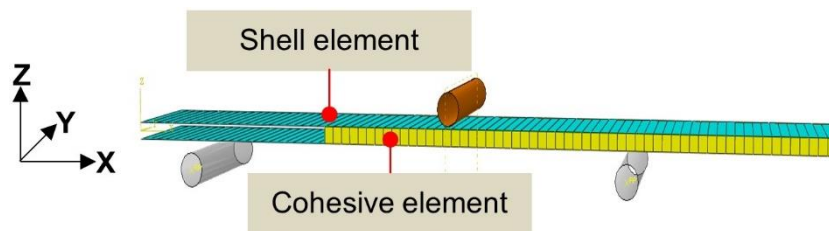


Figure 9.29 ENF simulation model

The bottom supports were fixed in all degrees of freedom. The impactor was restricted in all degree of freedoms except translation in z-direction. The impactor was given displacement boundary condition to apply in 3-point bending load. The results are shown in Figure 9.30 and Figure 9.31.

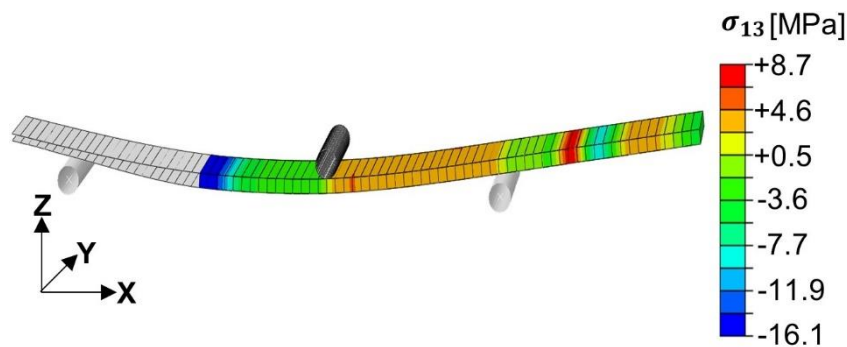


Figure 9.30 Simulation results showing shear (mode-II) stress in cohesive elements

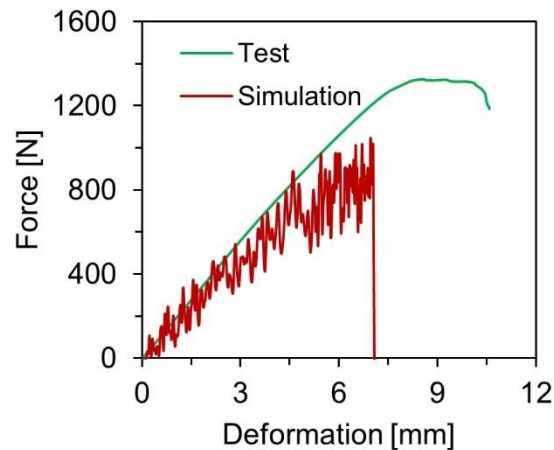


Figure 9.31 ENF simulation results compared with experimental data

In Figure 9.31 the simulation results are shown without filtering the data. The predicted stiffness is in good agreement. However, the shell failed before cohesive elements and hence the force level could not reach experimentally determined force level. This early failure of shell elements in simulation can again be related to the size effect in bending. Before the maximum shear stress in cohesive elements, the shell element failed due to bending stress.

#### 9.4 Axial crush simulation

The objective of modeling cohesive elements in this chapter was to simulate the axial crush phenomenon. Although no good results were seen in ENF simulation but still the corrugated specimen with cohesive elements was modelled.

The total thickness of corrugated specimen was 2 mm made up of four plies. The specimen was modelled with two parallel layers of S4R shell elements with mesh size of 1 mm. Each shell contained two plies of 0.5 mm thickness. The parallel layers were 1 mm offset from each other. Because the two layers of shell elements were 1 mm apart from each other so they were joined by solid cohesive element with dimension of 1 mm in each direction. The impactor and support were modeled as 3D analytical rigid part. The simulation model is shown in Figure 9.32.

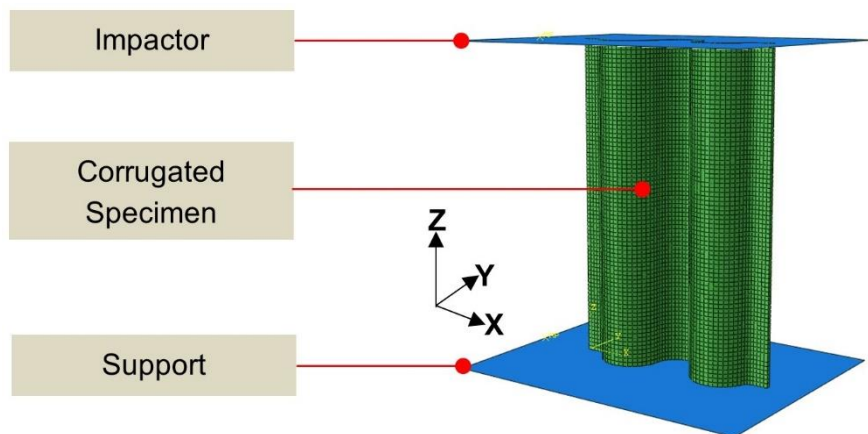


Figure 9.32 Simulation model for axial crushing of corrugated specimen

The support was fixed in all degrees of freedom. The impactor was restricted in all degrees of freedom except translation along Z-axis. The displacement boundary condition was applied to impactor due which corrugated specimen underwent compressive loading. The simulation results are shown in Figure 9.33.

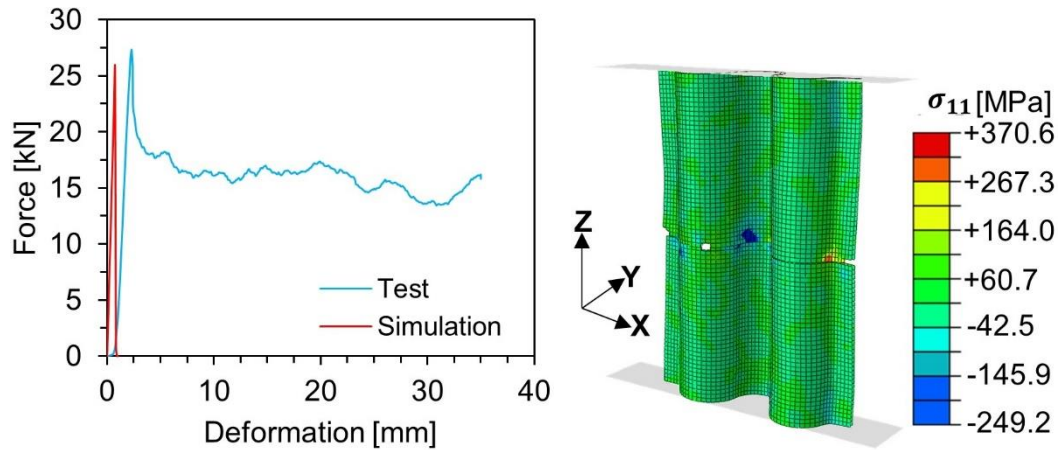


Figure 9.33 Axial crushing of corrugated specimen with and without cohesive element approach

The simulation results show that a corrugated specimen failed in the middle. This is completely in contrast to deformation morphology seen in experiments (see Figure 3.27). Due to failure in the shell elements at the middle of specimen, the progressive crushing behavior could not be achieved. And hence the constant force level output could not be predicted.

#### 9.4.1 Conclusion

In this chapter, the cohesive elements were used to model the delamination in axial crushing of corrugated specimen.

- The DCB and ENF tests were carried out to measure inter-laminar fracture energies in Mode-I and mode-II respectively;
- Simulation on single solid element were used to calibrate the interfacial cohesive elements;
- Simulations of DCB and ENF test were carried out to validate the cohesive modeling approach;
- A full scale corrugated specimen with cohesive elements was modeled for axial crushing;
- The objective of the modelling the composite material with interfacial cohesive elements was to achieve progressive crushing which could not be achieved.

It is recommended to use phenomenological crush modelling technique CZone (an add-on in Abaqus) for the axial crushing simulations. The “crushing stress” measured from coupon tests is the input to the CZone for the crushing region of composite materials. CZone can predict a constant level of force by crushing of the composite laminates at significantly reduced computation time [94].

## 10 Summary and Outlook

### 10.1 Summary

In order to facilitate the use of woven fabric thermoplastic composite materials in passenger cars, while retaining the crash safe behavior, predicting the crash behavior in FEM simulation is required. For precise crash simulations, the knowledge of mechanical behavior is important. In this work the mechanical properties of woven glass fabric thermoplastics were investigated. And a material model based on continuum damage mechanics coupled with fracture mechanics was improved.

The composite materials behave linear elastically along the fiber direction both in tensile and compression. The simulations using classical continuum damage mechanics produce mesh dependent results. The mesh dependency is eliminated by combining the fracture mechanics with continuum damage mechanics where energy is smeared over the whole element.

Unlike tensile and compression, the composite material along inplane shear is highly non-linear. The loss of stiffness and presence of inelastic strains require it to be modeled as elastoplastic material. The effect of fiber- rotation and the reduced stability in compression also influences the measured shear behavior. This was taken care of by inputting two set of parameters for shear behavior depending on the tensile or compression loading. A user-material subroutine was implemented in Fortran and successfully used to prove the improvement in results.

The woven glass fabric thermoplastic composite was proved to be highly strain rate dependent. The tensile and shear strength increased significantly when tested at high speeds. Strain rate dependent strength along fiber direction and strain rate dependent shear damage onset were used to implement the strain rate dependency in user material model in the form of exponential equation. The results were verified on single element and component level test. A clear improvement in simulation results was seen for drop tower crash test of u-profiles.

Failure criterion and size effect were two important aspects which were not implemented in user-material subroutine. However, the need for its improvement was shown by experimental data. A series of tensile tests at different fiber angle were carried out and stress-strain transformation was used to calculate the stress-strain in material coordinates. The presence of even small shear stress lead to strong reduction in the load bearing capacity of laminate. Maximum stress or maximums strain criteria used for the woven fabric composites is therefore regarded as insufficient for use in simulations. However, more tests must be done to determine to appropriate failure criterion.

One of the most underrated problem had been identified experimentally that flexural strength of organo-sheets is higher than tensile strength. Similarly, the material undergoes higher strain levels both in tension and compression during bending as compared to uniaxial tensile or compression loading. The so called size effect is also observed when testing different size of flexural specimens. It was recommended that the size effect be implemented in user-material subroutine which will greatly improve the accuracy of crash simulations.

And last but not least, the cohesive elements were used between the plies to model the axial crushing of corrugated specimens. The cohesive element parameter calibration was done on single element level. The cohesive elements predicted the delamination propagation reasonably well for mode-I delamination propagation. The validation of mode-II loading was not complete due to size effect playing the role in bending of end-notch flexural specimen. Still it is expected that on coupon level

the cohesive elements work quite well. However, for axial crush simulations, the viability for use of cohesive elements could not be proved. The absorbed energy was well under the experimentally measured absorbed energy under axial loading due to unstable failure of the corrugated specimen.

The improvement in the state-of-the art within framework of this thesis are summarized:

1. Shear damage evolution equation has been improved based on the experimental evidence by using exponential form instead of logarithmic;
2. For tensile shear and compression shear separate parameters are calculated. In state of the art only one curve for inplane shear behavior was modelled. User-material-subroutine is capable of automatically detect the type of loading in combination of inplane shear load;
3. Strain rate dependency of tensile behavior along fiber direction has been investigated experimentally and strain rate dependent strength function was implemented in user-material subroutine;
4. Strain rate dependent inplane shear behavior was investigated experimentally and damage onset as function of strain was implement in user material subroutine;
5. The difference in flexural strength and tensile strength was measured quantitatively;
6. Off-axis tensile tests were carried out to find out the validity of maximum stress failure criterion;
7. Cohesive element approach for modelling axial energy absorption was not successful.

## 10.2 Outlook

The work done in this thesis is a step towards better understanding of mechanical properties of organo-sheet and therefore an improved material model. Huge amount of time was invested in achieving a functioning user-material subroutine which worked at the same speed as built-in material models in Abaqus. With the Fortran code available, the changes in material models can be made quickly and desired effects can be modelled relatively easy.

One most important step towards improved results would be the implementation of size effect which has already been investigated experimentally. Implementation of size effect is expected to improve the results as much as implementation of strain rate dependency.

Further experimental investigation is required on some aspect which were not done in the scope of this thesis.

1. The off-axis tensile tests and respective stress-strain transformation is a crude approach to determine the failure points under multi-axial stress state. Biaxial testing setup should be used to determine the failure points. Other composite materials which resemble the weaving architecture of organo-sheet, if available in cylindrical forms can be used to test and determine points on the failure surface;
2. The adiabatic heating effect was not considered in high speed test along fiber direction as well as inplane shear. The temperature on the specimen should be measured with infrared cameras and correspondingly the user-material model be improvised;
3. Strain rate dependent compression behavior was not evaluated. The user-material subroutine assumes strain rate dependent compression parameters equal to the tensile. High speed compression tests cannot be performed on Zwick HTM. With successful experience of modified combined loading fixture, a fixture should be designed for high speed compression testing on drop tower test. And the corresponding results be used to compare

---

with tensile strain rate dependency. The differences must be accounted for in user-material subroutine;

4. Similar to high speed tensile shear, compressive shear behavior at high speed should also be investigated. In user-material subroutine the strain rate dependent damage onset constants are assumed to be equal to strain rate dependent tensile shear damage onset;
5. The possible relation between high speed and size effect should be investigated;
6. Intra-laminar fracture energies in compression and tension were assumed to be constant in user-material subroutine. No analytical methods have yet been developed for measuring the fracture energies in tension and compression. A new method will be needed to account for strain rate dependent crack propagation in compact tension and compact compression tests.

Finally, more composite materials with different fabric architecture, fiber ratio, fiber material and matrix material should be tested and simulated for the validity of user-material model.

## 11 Bibliography

- [1] Regulation (EU) 2019/631 of the European Parliament and of the Council of 17 April 2019 setting CO<sub>2</sub> emission performance standards for new passenger cars and for new light commercial vehicles, and repealing Regulations (EC) No 443/2009 and (EU) No 510/2011 (Text with EEA relevance.), vol. 111. 2019.
- [2] F. Dirschmid, "Application of CFRP within BMW i and BMW 7 -series," presented at the NAFEMS Seminar: Simulation of Composites -Ready for Industrie 4.0?, Hamburg, Germany, Nov. 2016.
- [3] "Composite insert as a structural reinforcement for A-pillars," Bond Laminates, Sep. 24, 2019.
- [4] "The European New Car Assessment Programme | Euro NCAP." <https://www.euroncap.com:443/en> (accessed Jul. 26, 2020).
- [5] G. Oberhofer, M. Vogler, H. Gese, and H. Dell, "Modeling endless fiber reinforced polymers in crashworthiness simulation," presented at the 5th MATFEM Conference, Hohenkammer, Jul. 2019.
- [6] X. F. Fang and M. Grote, "Development of a material model for organic sheets for the simulation of FRP-components in full vehicle crash," presented at the NAFEM World Congress, San Diego, Jun. 2015.
- [7] J. Coulton, "CAE of Thermoplastic Woven Glass Composite," presented at the 11th LS-DYNA Forum, Ulm Germany, Sep. 2012.
- [8] P. K. Mallick, *Fiber-Reinforced Composites: Materials, Manufacturing, and Design*, Third Edition. CRC Press, 2007.
- [9] H. Schürmann, *Konstruieren mit Faser-Kunststoff-Verbunden*. Springer-Verlag, 2006.
- [10] L. Peroni, M. Avalle, and G. Belingardi, "Experimental Investigation of the Energy Absorption Capability of Continuous Joined Crash Boxes," presented at the 20th ESV, Lyon, France, 2007, Accessed: Dec. 22, 2016. [Online]. Available: <http://porto.polito.it/1638706/>.
- [11] "BOND LAMINATES Data Sheets." <http://bond-laminates.com/downloads/data-sheets/> (accessed Apr. 30, 2020).
- [12] M. A. Jiménez, A. Miravete, E. Larrodé, and D. Revuelta, "Effect of trigger geometry on energy absorption in composite profiles," *Compos. Struct.*, vol. 48, no. 1–3, pp. 107–111, Jan. 2000, doi: 10.1016/S0263-8223(99)00081-1.
- [13] S. D. Lazarus, "Energy absorption for crashworthiness in carbon-fibre braided composite structures," Thesis, Cranfield University, 2004.
- [14] P. H. Thornton, "Energy Absorption in Composite Structures," *J. Compos. Mater.*, vol. 13, no. 3, pp. 247–262, Jul. 1979, doi: 10.1177/002199837901300308.
- [15] P. H. Thornton and P. J. Edwards, "Energy Absorption in Composite Tubes," *J. Compos. Mater.*, vol. 16, no. 6, pp. 521–545, Nov. 1982, doi: 10.1177/002199838201600606.
- [16] G. Barnes, I. Coles, R. Roberts, D. O. Adams, and D. M. Garner, "Crash Safety Assurance Strategies for Future Plastic and Composite Intensive Vehicles (Pcivs)," U.S. Department of Transportation, DOT-VNTSC-NHTSA-10-01, Jun. 2010.
- [17] X. Xiao, "Simulation of Composite Tubes Axial Impact with a Damage Mechanics Based Composite Material Model," presented at the 10th International LS-DYNA Users Conference, Detroit, 2008.
- [18] P. Feraboli, "Development of a Corrugated Test Specimen for Composite Materials Energy Absorption," *J. Compos. Mater.*, vol. 42, pp. 229–256, Feb. 2008, doi: 10.1177/0021998307086202.
- [19] P. Feraboli, "Development of a Modified Flat-plate Test Specimen and Fixture for Composite Materials Crush Energy Absorption," *J. Compos. Mater.*, vol. 43, no. 19, pp. 1967–1990, Jul. 2009, doi: 10.1177/0021998309343025.
- [20] G. R. Baran, J. I. McCool, K. G. Boberick, and H. Q. Zhang, "Size effect in resin/glass composite flexure strengths," *J. Oral Rehabil.*, vol. 26, no. 10, pp. 775–780, Oct. 1999.
- [21] M. R. Wisnom, "Size effects in the testing of fibre-composite materials," *Compos. Sci. Technol.*, vol. 59, no. 13, pp. 1937–1957, Oct. 1999, doi: 10.1016/S0266-3538(99)00053-6.

- 
- [22] W. Weibull, *A statistical theory of the strength of materials*. Stockholm: Generalstabens litografiska anstalts förlag, 1939.
- [23] J. M. Hodgkinson, *Mechanical Testing of Advanced Fibre Composites*. Elsevier, 2000.
- [24] C. Kassapoglou, *Design and Analysis of Composite Structures: With Applications to Aerospace Structures*. John Wiley & Sons, 2011.
- [25] M. J. Hinton, A. S. Kaddour, and P. D. Soden, *Failure Criteria in Fibre Reinforced Polymer Composites: The World-Wide Failure Exercise*. Elsevier, 2004.
- [26] M. J. Hinton and A. S. Kaddour, "Triaxial test results for fibre-reinforced composites: The Second World-Wide Failure Exercise benchmark data," *J. Compos. Mater.*, p. 0021998312459782, Sep. 2012, doi: 10.1177/0021998312459782.
- [27] P. D. Soden, M. J. Hinton, and A. S. Kaddour, "Biaxial test results for strength and deformation of a range of E-glass and carbon fibre reinforced composite laminates: failure exercise benchmark data," *Compos. Sci. Technol.*, vol. 62, no. 12–13, pp. 1489–1514, Sep. 2002, doi: 10.1016/S0266-3538(02)00093-3.
- [28] A. Smits et al., "A Review of Biaxial Test Methods for Composites," in *Experimental Analysis of Nano and Engineering Materials and Structures*, 2007, doi: [https://doi.org/10.1007/978-1-4020-6239-1\\_464](https://doi.org/10.1007/978-1-4020-6239-1_464).
- [29] S. T. Pinho, "Modelling failure of laminated composites using physically-based failure models," Department of Aeronautics, Imperial College London, 2005.
- [30] S. W. Tsai, "Strength Characteristics of Composite Materials," National Aeronautics and Space Administration, Washington D.C., Technical NASA CR-224, 1965. [Online]. Available: [www.dtic.mil/cgi-bin/GetTRDoc?AD=ADA307777](http://www.dtic.mil/cgi-bin/GetTRDoc?AD=ADA307777).
- [31] Z. Hashin, "Failure Criteria for Unidirectional Fiber Composites," *J. Appl. Mech.*, vol. 47, no. 2, pp. 329–334, Jun. 1980, doi: 10.1115/1.3153664.
- [32] S. W. Tsai and E. M. Wu, "A General Theory of Strength for Anisotropic Materials," *J. Compos. Mater.*, vol. 5, no. 1, pp. 58–80, Jan. 1971, doi: 10.1177/002199837100500106.
- [33] F. Paris, "A Study of Failure Criteria of Fibrous Composite Materials," NASA Langley Technical Report Server, Hampton, Virginia, NASA/CR-2001-210661, Mar. 2001. [Online]. Available: <http://ntrs.nasa.gov/archive/nasa/casi.ntrs.nasa.gov/20010035883.pdf>.
- [34] K. Rohwer, "Models for Intralaminar Damage and Failure of Fiber Composites - A Review," presented at the NAFEMS World Congress 2015, San Diego, CA, USA, Jun. 2015, Accessed: Mar. 21, 2016. [Online]. Available: <http://elib.dlr.de/97632/>.
- [35] C. G. Davila, P. P. Camanho, and C. A. Rose, "Failure Criteria for FRP Laminates," *J. Compos. Mater.*, vol. 39, no. 4, pp. 323–345, Feb. 2005, doi: 10.1177/0021998305046452.
- [36] Z. Hashin and A. Rotem, "A Fatigue Failure Criterion for Fiber Reinforced Materials," *J. Compos. Mater.*, vol. 7, no. 4, pp. 448–464, Oct. 1973, doi: 10.1177/002199837300700404.
- [37] A. Puck and H. Schürmann, "Failure analysis of FRP laminates by means of physically based phenomenological models," *Compos. Sci. Technol.*, vol. 58, no. 7, pp. 1045–1067, Jul. 1998, doi: 10.1016/S0266-3538(96)00140-6.
- [38] A. K. Pickett, "Review of Finite Element Simulation Methods Applied to Manufacturing and Failure Prediction in Composites Structures," *Appl. Compos. Mater.*, vol. 9, no. 1, pp. 43–58, 2002, doi: 10.1023/A:1012667427575.
- [39] R. Talreja, "Physical modelling of failure in composites," *Philos. Trans. R. Soc. Math. Phys. Eng. Sci.*, vol. 374, no. 2071, p. 20150280, Jul. 2016, doi: 10.1098/rsta.2015.0280.
- [40] D. Fanteria and E. Panettieri, "A non-linear model for in-plane shear damage and failure of composite laminates," *Aerotec. Missili Spaz.*, vol. 93, no. 1, pp. 17–24, Jan. 2014, doi: 10.1007/BF03404672.
- [41] L. L. Yaw, "Nonlinear Static - 1D Plasticity - Various Forms of Isotropic Hardening." Jan. 25, 2012, Accessed: Aug. 30, 2016. [Online]. Available: <https://gab.wallawalla.edu/~louie.yaw/plasticitypublications/>.
- [42] J. C. Simo and T. J. R. Hughes, *Computational Inelasticity*, vol. 7. Springer-Verlag New York, Inc., 1998.

- 
- [43] ISO 527-4:1997, "Plastics - Determination of tensile properties -- Part 4: Test conditions for isotropic and orthotropic fibre-reinforced plastic composites." Accessed: Nov. 18, 2016. [Online]. Available: [http://www.iso.org/iso/catalogue\\_detail.htm?csnumber=4595](http://www.iso.org/iso/catalogue_detail.htm?csnumber=4595).
- [44] ISO 14126:1999, "Fibre-reinforced plastic composites -- Determination of compressive properties in the in-plane direction." .
- [45] ASTM D6641 / D6641M - 14, "Standard Test Method for Compressive Properties of Polymer Matrix Composite Materials Using a Combined Loading Compression (CLC) Test Fixture." .
- [46] ISO 14129:1997, "Fibre-reinforced plastic composites -- Determination of the in-plane shear stress/shear strain response, including the in-plane shear modulus and strength, by the plus or minus 45 degree tension test method." .
- [47] A. F. Johnson, "Modelling fabric reinforced composites under impact loads," *Compos. Part Appl. Sci. Manuf.*, vol. 32, no. 9, pp. 1197–1206, Sep. 2001, doi: 10.1016/S1359-835X(00)00186-X.
- [48] "VUMAT for Fabric Reinforced Composites." Dassault Systemes, 2008.
- [49] P. Ladeveze and E. LeDantec, "Damage modelling of the elementary ply for laminated composites," *Compos. Sci. Technol.*, vol. 43, no. 3, pp. 257–267, 1992, doi: 10.1016/0266-3538(92)90097-M.
- [50] A. Matzenmiller, J. Lubliner, and R. L. Taylor, "A constitutive model for anisotropic damage in fiber-composites," *Mech. Mater.*, vol. 20, no. 2, pp. 125–152, Apr. 1995, doi: 10.1016/0167-6636(94)00053-0.
- [51] S. T. Pinho, P. Robinson, and L. Iannucci, "Fracture toughness of the tensile and compressive fibre failure modes in laminated composites," *Compos. Sci. Technol.*, vol. 66, no. 13, pp. 2069–2079, Oct. 2006, doi: 10.1016/j.compscitech.2005.12.023.
- [52] R. T. Bubsey, M. H. Jones, and W. F. Brown, *Clevis Design for Compact Tension Specimens Used in Plane-strain Fracture Toughness Testing*. National Aeronautics and Space Administration, 1969.
- [53] P. Maimí Vert, P. M. P. R. de C. Camanho, J. A. Mayugo Majó, and C. G. Dávila, "A Thermodynamically Consistent Damage Model for Advanced Composites," *Natl. Aeronaut. Space Adm. Langley Res. Cent. Hampton Va.*, 2006, Accessed: Jun. 24, 2015. [Online]. Available: <http://dugi-doc.udg.edu/handle/10256/7898>.
- [54] "LS-Dyna keyword user's manual volume II." Livermore Software Technology Corporation, Mar. 18, 2015, [Online]. Available: [http://ftp.lstc.com/anonymous/outgoing/jday/manuals/LS-DYNA\\_Manual\\_Volume\\_II\\_R8.0.pdf](http://ftp.lstc.com/anonymous/outgoing/jday/manuals/LS-DYNA_Manual_Volume_II_R8.0.pdf).
- [55] J. J. Skrzypek and A. Ganczarski, *Modeling of Material Damage and Failure of Structures: Theory and Applications*. Springer Science & Business Media, 2013.
- [56] L. Kachanov, *Introduction to continuum damage mechanics*. Springer Science & Business Media, 2013.
- [57] K. Schweizerhof, K. Weimar, T. Munz, and T. Rottner, "Crashworthiness analysis with enhanced composite material models in LS-DYNA-Merits and Limits," 1998, Accessed: Mar. 16, 2016. [Online]. Available: [https://www.dynasupport.com/howtos/material/composite-models/composite\\_paper.pdf](https://www.dynasupport.com/howtos/material/composite-models/composite_paper.pdf).
- [58] I. Lapczyk and J. A. Hurtado, "Progressive damage modeling in fiber-reinforced materials," *Compos. Part Appl. Sci. Manuf.*, vol. 38, no. 11, pp. 2333–2341, Nov. 2007, doi: 10.1016/j.compositesa.2007.01.017.
- [59] Z. P. Bažant and B. H. Oh, "Crack band theory for fracture of concrete," *Matér. Constr.*, vol. 16, no. 3, pp. 155–177, May 1983, doi: 10.1007/BF02486267.
- [60] S. T. Pinho, L. Iannucci, and P. Robinson, "Physically based failure models and criteria for laminated fibre-reinforced composites with emphasis on fibre kinking. Part II: FE implementation," *Compos. Part Appl. Sci. Manuf.*, vol. 37, no. 5, pp. 766–777, May 2006, doi: 10.1016/j.compositesa.2005.06.008.
- [61] W. Van Paepegem, I. De Baere, and J. Degrieck, "Modelling the nonlinear shear stress–strain response of glass fibre-reinforced composites. Part I: Experimental results," *Compos. Sci. Technol.*, vol. 66, no. 10, pp. 1455–1464, Aug. 2006, doi: 10.1016/j.compscitech.2005.04.014.

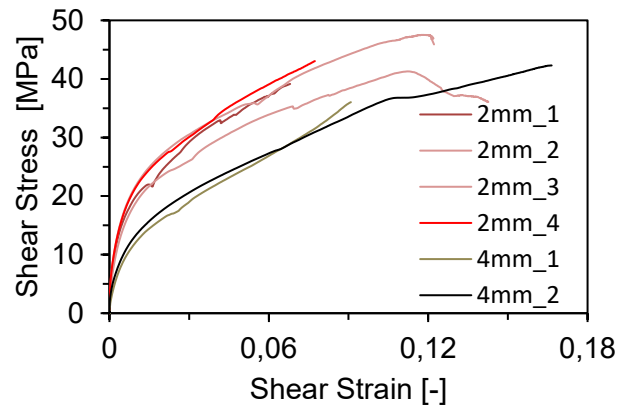
- 
- [62] W. Van Paepegem, I. De Baere, and J. Degrieck, "Modelling the nonlinear shear stress–strain response of glass fibre-reinforced composites. Part II: Model development and finite element simulations," *Compos. Sci. Technol.*, vol. 66, no. 10, pp. 1465–1478, Aug. 2006, doi: 10.1016/j.compscitech.2005.04.018.
- [63] O. Cousigné, D. Moncayo, D. Coutellier, P. Camanho, and H. Naceur, "Numerical modeling of nonlinearity, plasticity and damage in CFRP-woven composites for crash simulations," *Compos. Struct.*, vol. 115, pp. 75–88, Aug. 2014, doi: 10.1016/j.compstruct.2014.04.017.
- [64] U. Mandel, R. Taubert, and R. Hinterhölzl, "Mechanism based nonlinear constitutive model for composite laminates subjected to large deformations," *Compos. Struct.*, vol. 132, pp. 98–108, Nov. 2015, doi: 10.1016/j.compstruct.2015.04.029.
- [65] C. T. Herakovich, R. D. Schroedter III, A. Gasser, and L. Guitard, "Damage evolution in  $[\pm 45]_s$  laminates with fiber rotation," *Compos. Sci. Technol.*, vol. 60, no. 15, pp. 2781–2789, Nov. 2000, doi: 10.1016/S0266-3538(00)00091-9.
- [66] A. Tabiei and I. Ivanov, "Fiber Reorientation in Laminated and Woven Composites for Finite Element Simulations," *J. Thermoplast. Compos. Mater.*, vol. 16, no. 5, pp. 457–474, Sep. 2003, doi: 10.1177/0892705703032853.
- [67] J. Schulte et al., "Isogeometric analysis of fiber reinforced composites using Kirchhoff–Love shell elements," *Comput. Methods Appl. Mech. Eng.*, vol. 362, p. 112845, Apr. 2020, doi: 10.1016/j.cma.2020.112845.
- [68] R. Basan, "Untersuchung der intralaminaren Schubeigenschaften von Faserverbundwerkstoffen mit Epoxidharzmatrix unter Berücksichtigung nichtlinearer Effekte," 2011.
- [69] ASTM D5448 / D5448M - 16, "Standard Test Method for Inplane Shear Properties of Hoop Wound Polymer Matrix Composite Cylinders." .
- [70] ASTM D5379 / D5379M - 19, "Standard Test Method for Shear Properties of Composite Materials by the V-Notched Beam Method." .
- [71] DIN SPEC 4885:2014-01, "Fibre-reinforced plastic composites - Shear test method using a shear frame for the determination of the in-plane shear stress/shear strain response and shear modulus." .
- [72] ASTM D4255 / D4255M - 01, "Standard Test Method for In-Plane Shear Properties of Polymer Matrix Composite Materials by the Rail Shear Method." .
- [73] J. Li and X. Fang, "Stress Wave Analysis and Optical Force Measurement of Servo-Hydraulic Machine for High Strain Rate Testing," *Exp. Mech.*, vol. 54, no. 8, pp. 1497–1501, Aug. 2014, doi: 10.1007/s11340-014-9929-4.
- [74] X. F. Fang and R. Grams, "A novel method for oscillation-free determination of material properties during high speed tests," *ASTM Journal of Material testing and evaluation*, 2019, doi: 10.1520/JTE20180887.
- [75] X. F. Fang and R. Grams, "Neue Entwicklungen in der Materialprüfung bei sehr hohen Dehnraten," presented at the DGM/DVM Conference Werkstoffprüfung, Berlin, Oct. 2017.
- [76] C. Sorini, A. Chattopadhyay, and R. K. Goldberg, "Effects of adiabatic heating on the high strain rate deformation of polymer matrix composites," in *32nd Technical Conference of the American Society for Composites 2017*, Jan. 2017, pp. 438–452, Accessed: Aug. 12, 2020. [Online]. Available: <https://asu.pure.elsevier.com/en/publications/effects-of-adiabatic-heating-on-the-high-strain-rate-deformation->.
- [77] M. H. Lee and D. J. Sordelet, "Evidence for adiabatic heating during fracture of W-reinforced metallic glass composites," *Appl. Phys. Lett.*, vol. 88, no. 26, p. 261902, Jun. 2006, doi: 10.1063/1.2208269.
- [78] C. R. Siviour and J. L. Jordan, "High Strain Rate Mechanics of Polymers: A Review," *J. Dyn. Behav. Mater.*, vol. 2, no. 1, pp. 15–32, Mar. 2016, doi: 10.1007/s40870-016-0052-8.
- [79] C. Sorini, A. Chattopadhyay, and R. K. Goldberg, "Micromechanical modeling of the effects of adiabatic heating on the high strain rate deformation of polymer matrix composites," *Compos. Struct.*, vol. 215, pp. 377–384, May 2019, doi: 10.1016/j.compstruct.2019.02.016.

- 
- [80] J. Cui, S. Wang, S. Wang, G. Li, P. Wang, and C. Liang, "The Effects of Strain Rates on Mechanical Properties and Failure Behavior of Long Glass Fiber Reinforced Thermoplastic Composites," *Polymers*, vol. 11, no. 12, Dec. 2019, doi: 10.3390/polym11122019.
- [81] A. Turon Travesa, "Simulation of delamination in composites under quasi-static and fatigue loading using cohesive zone models," info:eu-repo/semantics/doctoralThesis, Universitat de Girona, Departament d'Enginyeria mecànica i de la construcció industrial, 2006.
- [82] P. P. Camanho, C. G. Dávila, and D. R. Ambur, Numerical simulation of delamination growth in composite materials. National Aeronautics and Space Administration, Langley Research Center, 2001.
- [83] ISO 15024, "Fibre-reinforced plastic composites — Determination of mode I interlaminar fracture toughness for unidirectionally reinforced materials." .
- [84] ASTM D7905/D7905M-14, "Standard Test Method for Determination of Mode II Interlaminar Fracture Toughness of Unidirectional Fiber-Reinforced Polymer Matrix Composites." .
- [85] "Simulation of the Quasi-static Crushing of a Fabric Composite Plate." Abaqus Technology Brief, [Online]. Available: <http://www.3ds.com/fileadmin/PRODUCTS/SIMULIA/PDF/tech-briefs/Aero-Simulation-of-Quasi-static-Crushing-of-Fabric-11.pdf>.
- [86] K. Indermuehle, V. Sokolinsky, and G. Barnes, "Simulating Composites Crush: From the Coupon Level to Full Vehicle Crashworthiness," in 52nd AIAA/ASME/ASCE/AHS/ASC Structures, Structural Dynamics and Materials Conference, American Institute of Aeronautics and Astronautics.
- [87] K. Indermuehle, G. Barnes, S. Nixon, and M. Schrank, "Simulating Composites Crush and Crash Events Using ABAQUS," presented at the 50th AIAA/ASME/ASCE/AHS/ASC Structures, Structural Dynamics, and Materials Conference, Palm Springs, California, May 2009, Accessed: Mar. 09, 2016. [Online]. Available: <http://arc.aiaa.org/doi/abs/10.2514/6.2009-2551>.
- [88] "Abaqus Analysis User's Guide (6.14)." <http://abaqus.software.polimi.it/v6.14/books/usb/default.htm>.
- [89] M. L. Benzeggagh and M. Kenane, "Measurement of mixed-mode delamination fracture toughness of unidirectional glass/epoxy composites with mixed-mode bending apparatus," *Compos. Sci. Technol.*, vol. 56, no. 4, pp. 439–449, 1996, doi: 10.1016/0266-3538(96)00005-X.
- [90] "Mechanical Properties of Plastic Materials." Professional Plastics, Accessed: Jun. 03, 2018. [Online]. Available: [www.professionalplastics.com](http://www.professionalplastics.com).
- [91] "Mechanical properties of PA6." CNC Plastics, Accessed: Nov. 10, 2017. [Online]. Available: <http://www.cncplastics.com>.
- [92] A. Turon, C. G. Dávila, P. P. Camanho, and J. Costa, "An engineering solution for mesh size effects in the simulation of delamination using cohesive zone models," *Eng. Fract. Mech.*, vol. 74, no. 10, pp. 1665–1682, Jul. 2007, doi: 10.1016/j.engfracmech.2006.08.025.
- [93] A. Amiri-Rad and M. Mashayekhi, "A Cohesive Zone Approach for Fatigue-Driven Delamination Analysis in Composite Materials," *Appl. Compos. Mater.*, vol. 24, no. 4, pp. 751–769, Aug. 2017, doi: 10.1007/s10443-016-9543-y.
- [94] "CZone for Abaqus." Simulia, Accessed: Mar. 16, 2016. [Online]. Available: <http://www.3ds.com/products-services/simulia/products/abaqus/add-ons/czone/>.

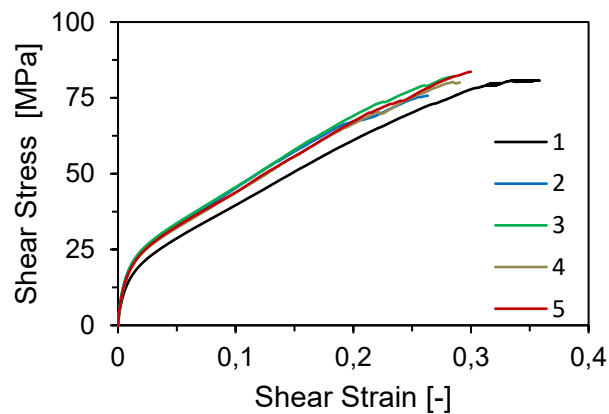
## 12 Annex

### 12.1 Test results data

#### 12.1.1 Frame shear

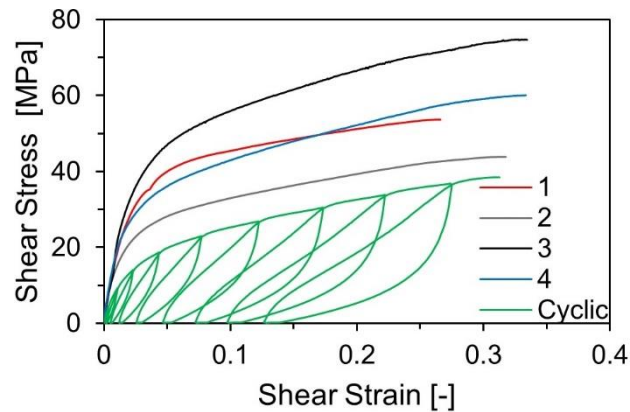


#### 12.1.2 Rail shear



Sr. no.	Thickness [mm]	Test speed [mm/min]	Shear chord modulus [MPa]	Shear strength [MPa]	Failure shear strain [-]
1	1.99	2	1682.5	80.77	0.35
2	1.99	3	2087.5	75.70	0.30
3	1.99	3	2147.2	82.01	0.32
4	1.99	3	2058.7	80.20	0.34
5	1.99	3	1977	83.61	0.31
Average	1.99		1990.58	80.46	0.33
Standard deviation			163.5	2.65	0.016
Co-efficient of variance [%]			8.21	3.29	4.98

### 12.1.3 Compression shear



Sr. no.	Thickness [mm]	Width [mm]	Shear chord modulus [MPa]	Shear strength [MPa]	Failure shear strain [-]
1	4.07	24.94	1988.5	54.21	0.31
2	4.1	24.87	2072.2	43.81	0.32
3	4.08	24.93	1822.4	74.73	0.33
4	4.08	25.12	2055.2	60.05	0.33
Cyclic 1	4.17	25.02	1150.3	38.44	0.31
Average	4.11	24.98	1817.72	54.26	0.32
Standard deviation			385.93	14.25	0.013
Co-efficient of variance [%]			21.23	26.26	4.12

### 12.1.4 High-speed tensile test

Test speed	Nominal strain-rate [1/s]	Specimen no.	Measured strain-rate [1/s]	E- modulus [GPa]	Tensile strength [MPa]	Failure strain [%]
1.5 mm/min	1.67E-4	1	7.323E-5	20.44	391.41	1.91
		2	7.34E-5	18.70	378.92	1.8
		3	8.008E-5	19.05	392.70	2.09
		4	8.001E-5	18.19	389.90	2.14
		5	7.335E-5	18.71	341.15	1.69
Average			7.601E-5	19.02	378.82	1.93
Standard deviation			3.6E-6	0.849	21.75	0.1845
Coefficient of variance (%)			4.84	4.46	5.74	9.53

Test speed	Nominal strain-rate [1/s]	Specimen No.	Measured strain-rate [1/s]	E- modulus [GPa]	Tensile strength [MPa]	Failure strain [%]
2 mm/min	2.22E-4	1	1.104E-4	19.13	411.23	2.09
		2	1.133E-4	18.69	409.20	2.13
		3	1.119E-4	18.73	374.49	1.93

		4	1.12E-4	18.9	387.32	1.98
		5	1.15E-4	16.9	379.65	1.97
Average			1.12E-4	18.48	392.38	2.026
Standard deviation			1.89E-06	0.87	16.92	0.083
Coefficient of Variance (%)			1.68	4.72	4.31	4.13

Test speed	Nominal strain-rate [1/s]	Specimen no.	Measured strain-rate [1/s]	E-modulus [GPa]	Tensile strength [MPa]	Failure strain [%]
1m/sec	6.67	1	3.25	19.74	611.97	3.28
		2	2.75	19.93	536.47	2.72
		3			581.00	3.10
		4			577.00	2.41
Average			3.005	19.83	576.61	2.88
Standard deviation			0.349	0.13	30.98	0.388
Coefficient of variance (%)			11.63	0.67	5.37	13.48

Test speed	Nominal strain-rate [1/s]	Specimen no.	Measured strain-rate [1/s]	E-modulus [GPa]	Tensile strength [MPa]	Failure strain [%]
5m/sec	33.33	1	20.69	20.76	611.53	2.98
		2	24.72	19.91	658.96	3.60
		3	22.94	20.38	672.04	3.39
		4	23.78	20.56	628.23	3.28
Average			23.03	20.40	642.69	3.31
Standard deviation			1.72	0.362	27.72	0.26
Coefficient of variance (%)			7.47	1.77	4.31	7.91

Test speed	Nominal strain-rate [1/s]	Specimen no.	Measured strain-rate [1/s]	E-modulus [GPa]	Tensile strength [MPa]	Failure strain [%]
10m/sec	66.66	1	57.51	19.87	678.61	3.68
		2	59.97	19.91	704.11	3.71
		3	65.09	19.26	702.41	3.77
Average			60.85	19.68	695.04	3.72
Standard deviation			3.86	0.362	14.25	0.047
Coefficient of variance (%)			6.35	1.84	2.05	1.27

Test speed	Nominal strain-rate [1/s]	Specimen no.	Measured strain-rate [1/s]	E-modulus [GPa]	Tensile strength [MPa]	Failure strain [%]
15m/sec	100	1	78.65	23.35	761.25	4.08

	2	90.04	21.05	763.13	3.96
	3	82.86	24.20	705.06	3.81
	4	88.10	23.13	696.80	3.87
Average		84.91	22.93	731.56	3.93
Standard deviation		5.16	1.33	35.53	0.12
Coefficient of variance (%)		6.07	5.83	4.85	3.05

Test speed	Nominal strain-rate [1/s]	Specimen no.	Measured strain-rate [1/s]	E-modulus [GPa]	Tensile strength [MPa]	Failure strain [%]
20m/sec	133.33	1	115.96	23.68	732.05	3.942
		2	120.89	25.83	773.24	4.11
		3	104.97	22.95	723.48	3.97
Average			113.94	24.16	742.92	4.01
Standard deviation			8.14	1.49	26.60	0.088
Coefficient of variance (%)			7.15	6.19	3.58	2.205

### 12.1.5 High-speed shear test

Test speed	Specimen no.	Measured strain-rate [1/s]	Shear strength [MPa]	Failure shear strain [%]
1.5mm/min	1	3.17E-4	94.39	47.05
	2	3.15 E-4	94.97	48.20
	3	3.16 E-4	95.56	47.98
	4	3.08E-4	89.79	42.38
	5	3.18 E-4	96.65	48.54
Average		3.15 E-4	94.27	46.83
Standard deviation		3.99E-06	2.64	2.54
Coefficient of variance (%)		1.26	2.80	5.44

Test speed	Specimen no.	Measured strain-rate [1/s]	Shear strength [MPa]	Failure shear strain [%]
2mm/min	1	4.07E-4	98.99	39.16
	2	4.22 E-4	100.49	42.03
	3	4.01 E-4	101.80	41.21
	4	3.95 E-4	101.66	40.97
Average		4.06 E-4	100.73	40.84
Standard deviation		1.14E-05	1.302	1.20
Coefficient of Variance (%)		2.81	1.29	2.95

Test speed	Specimen no.	Measured strain-rate [1/s]	Shear strength [MPa]	Failure shear strain [%]
27mm/min	1	5.16E-3	117.64	45.06

	2	5.01E-3	118.63	43.11
	3	5.15E-3	118.49	46.36
Average		5.11E-3	118.25	44.84
Standard deviation		8.50E-05	0.538	1.63
Coefficient of Variance (%)		1.66	0.455	3.65

Test speed	Specimen no.	Measured strain-rate [1/s]	Shear strength [MPa]	Failure shear strain [%]
1m/s	1		143.06	36.22
	2		153.57	44.05
	3	16.86345438	138.46	39.98
Average		16.86345438	145.03	40.08
Standard deviation			7.74	3.91
Coefficient of Variance (%)			5.34	9.77

Test speed	Specimen no.	Measured strain-rate [1/s]	Shear strength [MPa]	Failure shear strain [%]
5m/s	1	68.21	168.67	46.65
	2	69.42	163.43	46.65
	3	68.83	154.88	41.30
Average		68.82	162.33	44.87
Standard deviation		0.609	6.96	3.09
Coefficient of Variance (%)		0.88	4.28	6.88

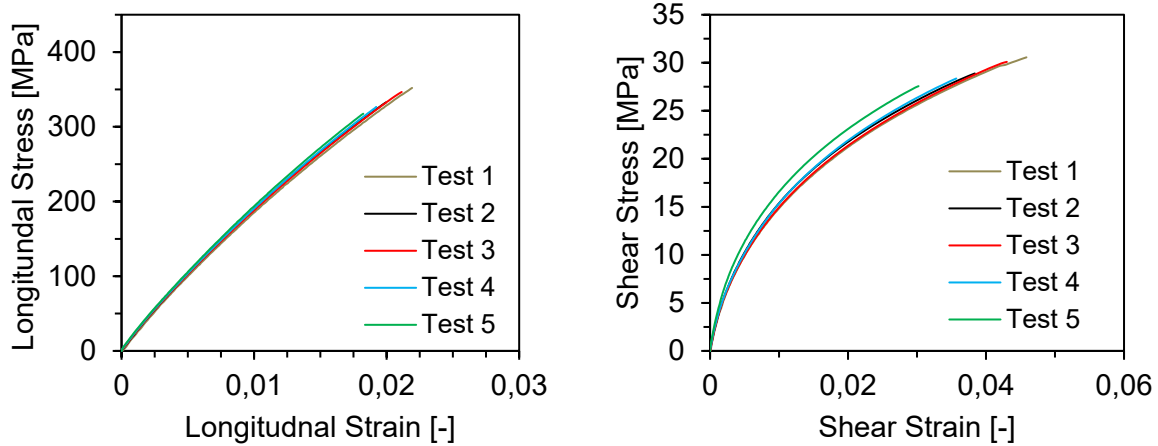
Test speed	Specimen no.	Measured strain-rate [1/s]	Shear strength [MPa]	Failure shear strain [%]
10m/s	1	127.30	166.16	44.30
	2	136.41	172.88	46.38
	3	135.19	160.81	41.09
Average		132.97	166.62	43.92
Standard deviation		4.94	6.04	2.66
Coefficient of Variance (%)		3.71	3.62	6.05

Test speed	Specimen no.	Measured strain-rate [1/s]	Shear strength [MPa]	Failure shear strain [%]
15m/s	1	235.95	165.49	41.52
	2	235.99	163.15	43.42
	3	244.55	164.00	43.04
Average		238.83	164.21	42.66
Standard deviation		4.95	1.18	1.00
Coefficient of Variance (%)		2.07	0.71	2.34

Test speed	Specimen no.	Shear strength [MPa]	Failure shear strain [%]
2mm/min	Cyclic 1	103.78	43.69
4mm/min	Cyclic 2	99.16	34.68
27mm/min	Cyclic 3	97.81	42.33

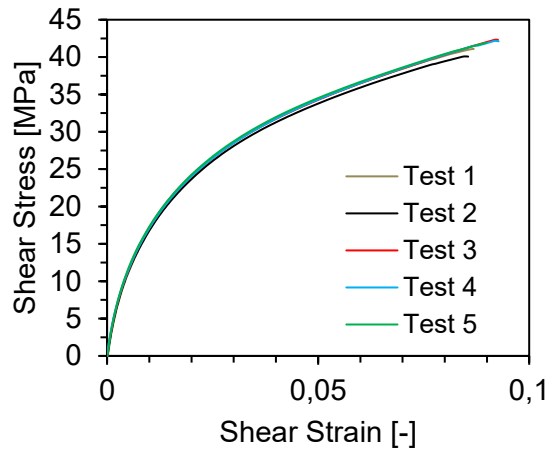
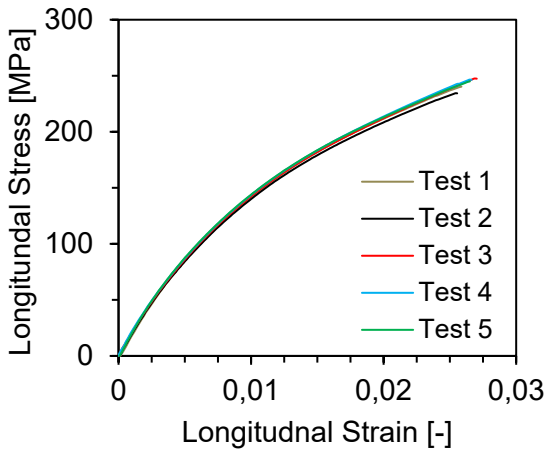
### 12.1.6 Off-axis tests

5°



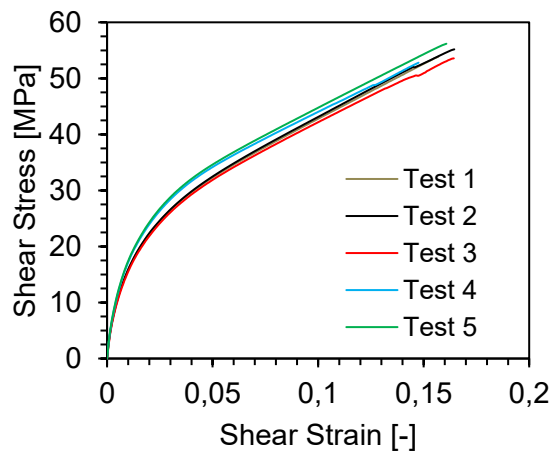
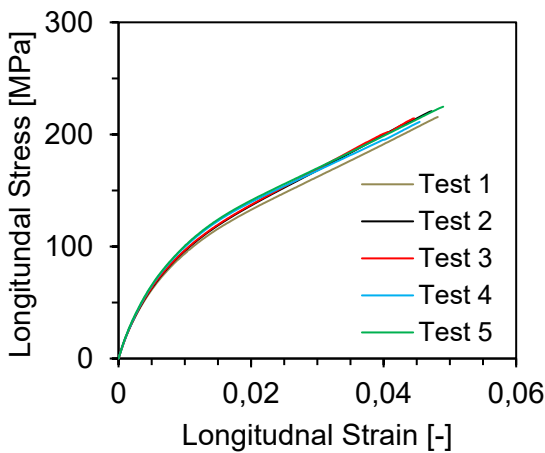
Specimen No.	Thickness [mm]	Width [mm]	Longitudinal strength [MPa]	Longitudinal failure strain [%]
1	1.94	25.04	352.02	2.19
2	1.91	25.35	332.67	1.99
3	1.94	25.21	346.59	2.11
4	1.93	25.07	326.61	1.92
5	1.9	25	317.46	1.82
Average	1.92	25.09	330.83	1.95
Standard deviation			14.20	0.14
Coefficient of variance [%]			4.29	7.53

10°



Specimen No.	Thickness [mm]	Width [mm]	Longitudinal strength [MPa]	Longitudinal failure strain [%]
1	1.91	25.13	240.29	2.58
2	1.91	25.05	234.42	2.55
3	1.9	25.08	247.54	2.70
4	1.9	25.05	246.58	2.66
5	1.91	26.54	244.99	2.65
Average	1.92	25.09	242.84	2.64
Standard deviation			5.43	0.059
Coefficient of variance [%]			2.23	2.26

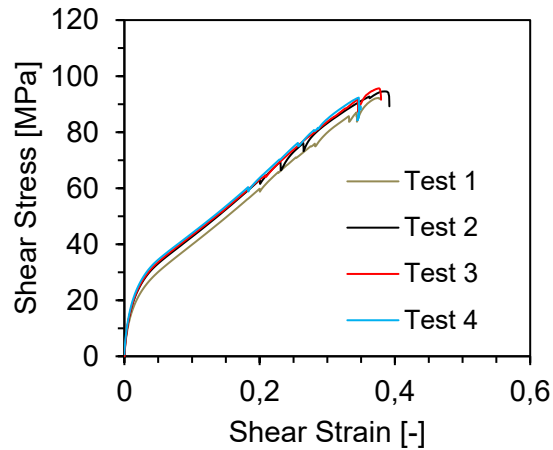
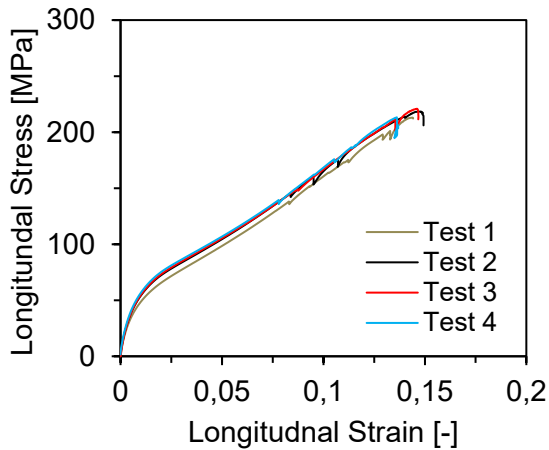
15°



Specimen No.	Thickness [mm]	Width [mm]	Longitudinal strength [MPa]	Longitudinal failure strain [%]
1	1.95	24.77	215.51	4.81
2	1.99	24.78	220.72	4.72
3	1.97	24.81	214.26	4.46
4	2.02	24.81	211.17	4.54

5	2	24.76	224.72	4.89
Average	1.995	24.79	217.28	4.68
Standard deviation			5.40	0.183
Coefficient of variance [%]			2.48	3.90

30°



Specimen No.	Thickness [mm]	Width [mm]	Longitudinal strength [MPa]	Longitudinal failure strain [%]
1	2.05	24.895	212.96	14.41
2	2.05	24.835	218.34	14.93
3	2.03	24.84	220.86	14.68
4	2.05	24.83	213.23	13.68
Average	2.045	24.85	216.35	14.42
Standard deviation			3.89	0.538
Coefficient of variance [%]			1.80	3.73

### 12.1.7 DCB test

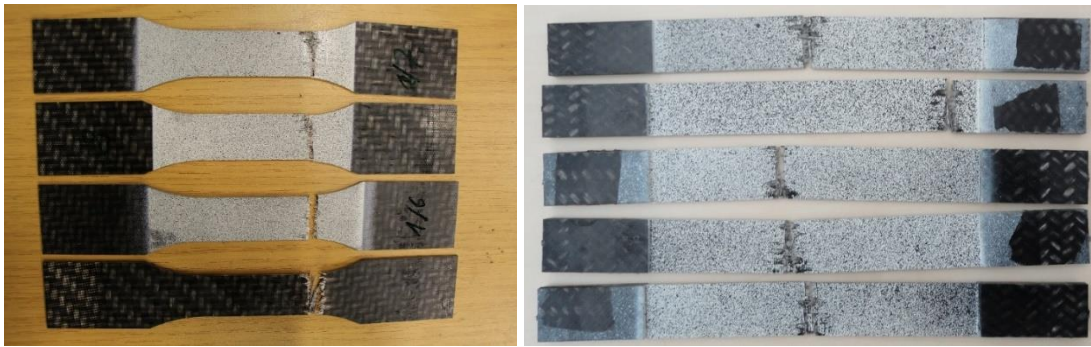
DCB mode I ISO 15024			Material			
Specimen identification	2		Tapex-Dynalite 102-RG600(10)47%B			
Test laboratory	FLB		No. of specimens			Test Date
Laminte Manufactured	Bond Laminate		Test personnel			Fibre Manufacturer
Resin Manufacturer						
Specimen length	l (mm)	125	Load Introduction	Hinge	DIN 7954 D-25x38	Average NL±σ
Average thickness	2h(mm)	5	Hinge thickness	H(mm)	0.8	CV NL
Max. Thickness variation	Δ(2h)(mm)		Hinge length	l3(mm)	-	Average VIS ±σ
Specimen width	b (mm)	25	Block/hinge width	(mm)	25	CV VIS
Insert material	Kapton HN	17705 B 0.05x600	Surface preparation	Sand Paper	P240	Av. 5%/MAX±σ
Insert thickness	(μm)	50	Adhesive	Sicomet 77	Ethyl-. 2-cyanoacrylate	CV5%MAX
Insert length	A (mm)	60	Conditioning temperature	Td (°)		
Mould release agent			Conditioning duration	td (h)		
Precrack length	a0 (mm)	41	Test temperature	T (°)	20	
Max. cure temperature	Tmc (°)		Relative humidity	rh (%)		
Cure duration	tc (h)		Loading/unloading rates	(mm/min)	5/25	
Max. delamination length	amax (mm)		Distance I1 and I2	(mm)	4.5	2
% change in complinace	(%)		Correction			



Precracked Test Results														
Material	Date	Operator	a0(mm)	a1[a_min for CC](mm)	a2[a_max for CC](mm)	r1(mm)	r2(mm)							
	2/05/2017		30	20	40	5	5							
Description of precracking method: For specimen no. 2, visualization method has been used. For all rest of specimens, a_calc is used														
DATA														
Spe. No.	CC load (N)		Compliances (mm/N)			A (mm/N)	m 1/(Nmm <sup>2</sup> )	r <sup>2</sup>	Pmax (N)	Gq (kJ/m <sup>2</sup> )	%Gq (a=a1)	%Gq (a=a2)	Accept? (Y/N)	GIIc (kJ/m <sup>2</sup> )
	At a1	At a2	C(a1)	C(a2)	C(a0)									
1														
2	966	483	0.00320737	0.00639656	0.00504414	0.00309548	5.42E-08	0.92836566	1358.28735	5.35E+00	22.4795918	22.4795918	Y	5.35E+00
3													Y	
4	966	483	0.00235127	0.00505622	0.00346776	0.00205536	4.76E-08		1632.68164	6.79E+00	15.5585355	15.5585355	Y	6.78648095
5	966	483	0.00244224	0.00499607	0.0032928	0.00199824	4.68E-08	0.99977418	1490.04602	5.67E+00	18.6798064	18.6798064	Y	5.66592692
6	966	483	0.00238802	0.00500388	0.00324022	0.00199824	4.68E-08	0.99977418	1479.21082	5.53E+00	18.9544675	18.9544675	Y	5.53468674
7	966	483	0.0023419	0.00482639	0.0032585	0.00202051	4.41E-08	0.9988927	1653.90613	6.51E+00	15.1617741	15.1617741	Y	6.51311971
Mean													5.96918408	
SD													0.63900661	
CV													10.7050915	
No. Spec.													5	
Max													6.78648095	
Min													5.34570607	

## 12.2 Specimen photos

### 12.2.1 Tensile test specimens



### 12.2.2 Compression tests specimens



### 12.2.3 Tensile-shear test specimens



### 12.2.4 Intralaminar fracture energy specimens

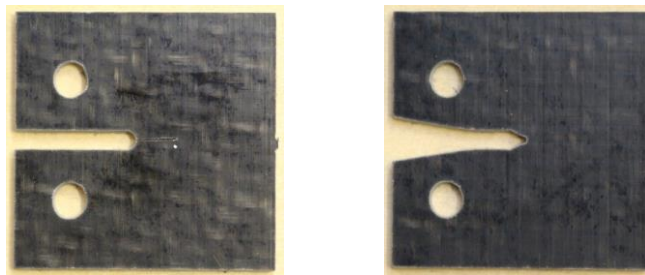


Figure 12.1 Compact Tension (left) and compact compression (right) specimen before test



Figure 12.2 Compact Tension (left) and Compact Compression specimen after test

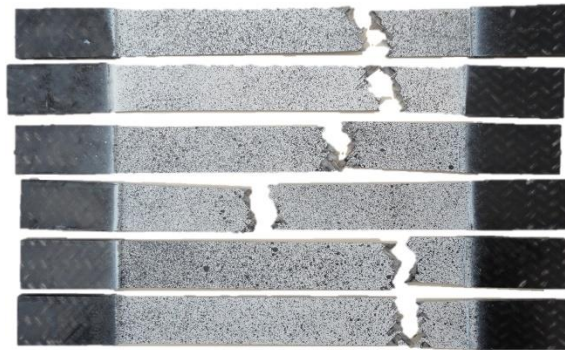
### 12.2.5 Axial crush of corrugated specimens



### 12.2.6 Rail shear tests specimens



### 12.2.7 Tensile shear specimens



### 12.2.8 Compression shear specimen



### 12.2.9 High speed tensile test specimens

1m/sec



**5m/s**



**10m/s**



**15m/s**



**20m/s**



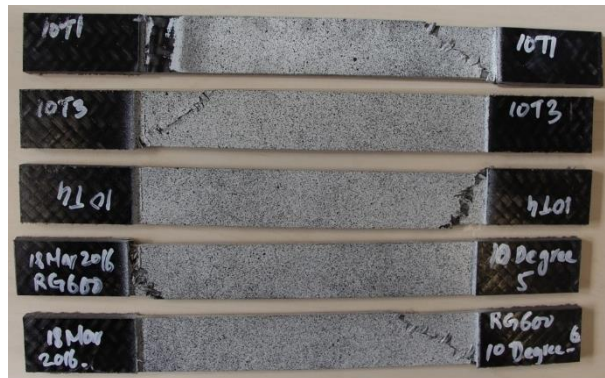
**12.2.10 High-speed shear specimen****1m/s****5m/s****10m/s****15m/s**

**12.2.11 Off-axis tensile test specimen**

**5° test specimen**



**10° test specimen**



**15° test specimen**



**30° test specimen**



### 12.3 CAD drawings

#### 12.3.1 CLC fixture

**Front view**      **Left view**

**Top view**      **Isometric view**

**Bill of Material: CLC Modified**

No.	Part Name	Quantity	Definition	Source
1	LowerLeft	1	Lower Left Block	Made
2	LowerRight	1	Lower Right Block	Made
3	UpperLeft	1	Upper Left Block	Made
4	UpperRight	1	Lower Right Block	Made
5	ISO 2338 PIN 4x35 STEEL PARALLEL UNHARDENED	4	Dowell Pin	Bought
6	ina_kh14-pp	4	Linear Ball Bearing	Bought
7	INA-W14h6-Cf53-90	4	Guide Shaft	Bought
8	ISO 4762 SCREW M8x70 STEEL HEXAGON SOCKET HEAD CAP	8	Bolt	Bought

Material:	Surface Finish: DIN ISO 1302	Tolerance: ISO 2768-MK	Scale: 1:1	Dimensions: mm	Mass: kg
				Model Name: Modified CLC Fixture	
		Appr: Checked Standard	Date	Modified CLC Fixture Assembly	
		FLB			Drawing No. 1
Resp: Change	Date	Name		Paper:	BL

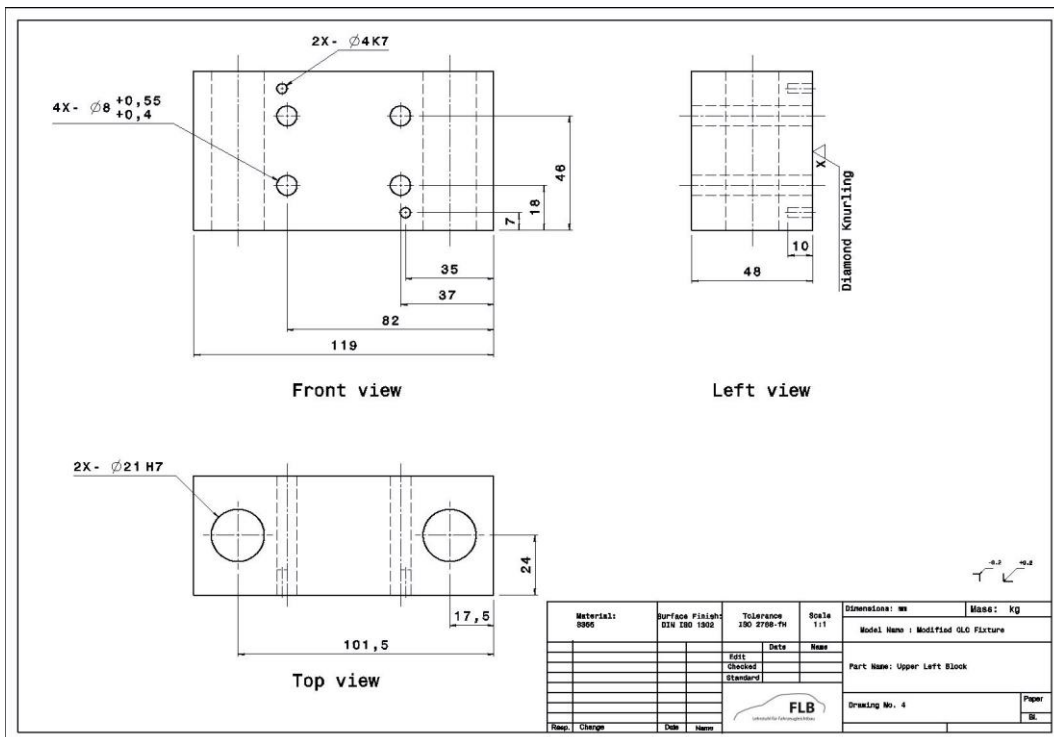
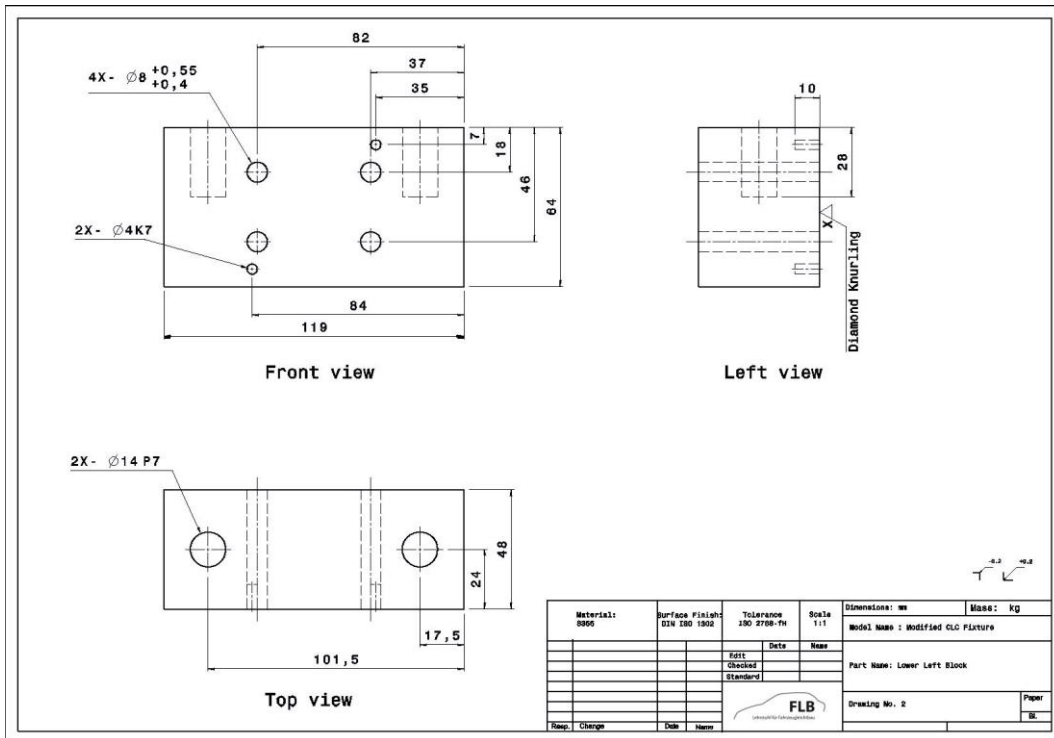
**Front view**      **Left view**

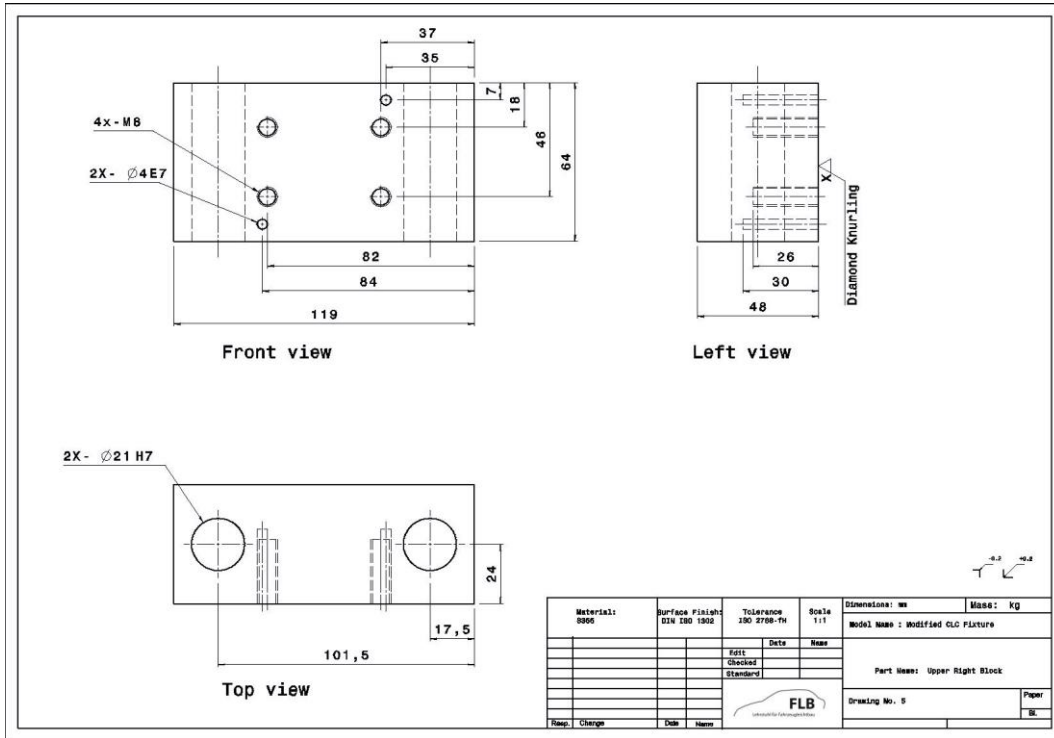
**Top view**

**Dimensions:**  
 4X-  $\varnothing 8^{+0,55}_{+0,4}$   
 2X-  $\varnothing 4K7$   
 2X-  $\varnothing 14 P7$   
 82, 37, 35, 7, 18, 46, 64, 119, 84, 101,5, 17,5, 24, 48, 10, 28, 17,5

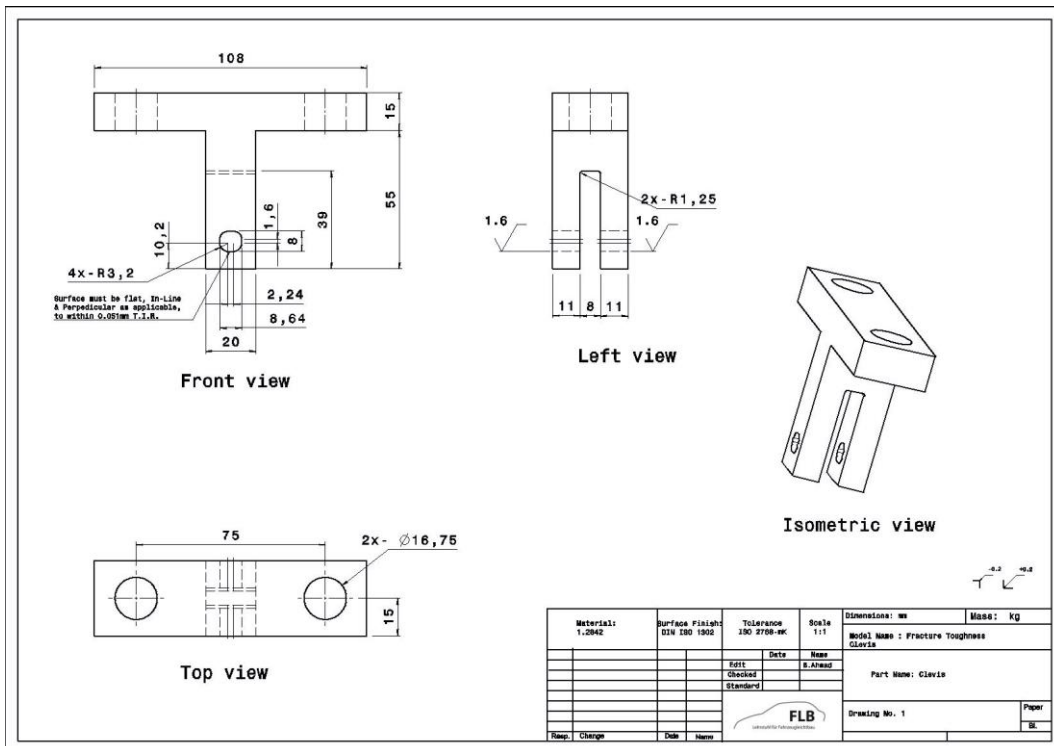
**Left view:** Diamond Knurling

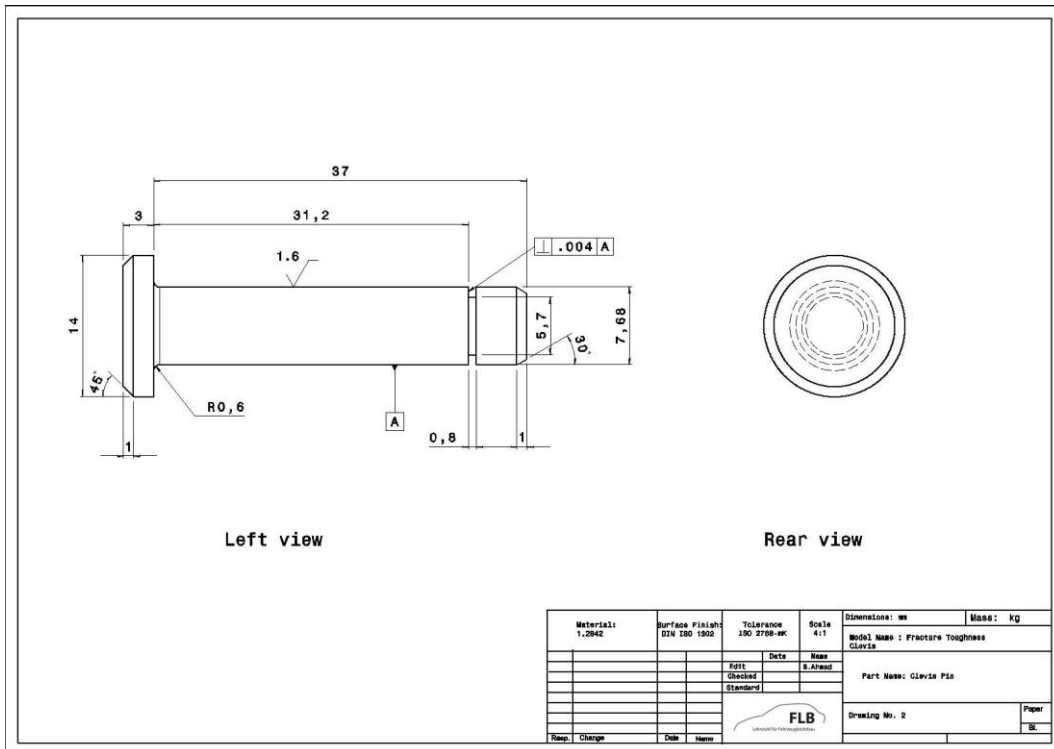
Material:	Surface Finish: DIN ISO 1302	Tolerance: ISO 2768-MK	Scale: 1:1	Dimensions: mm	Mass: kg
8005				Model Name: Modified CLC Fixture	
		Appr: Checked Standard	Date	Part Name: Lower Left Block	
		FLB			Drawing No. 2
Resp: Change	Date	Name		Paper:	BL



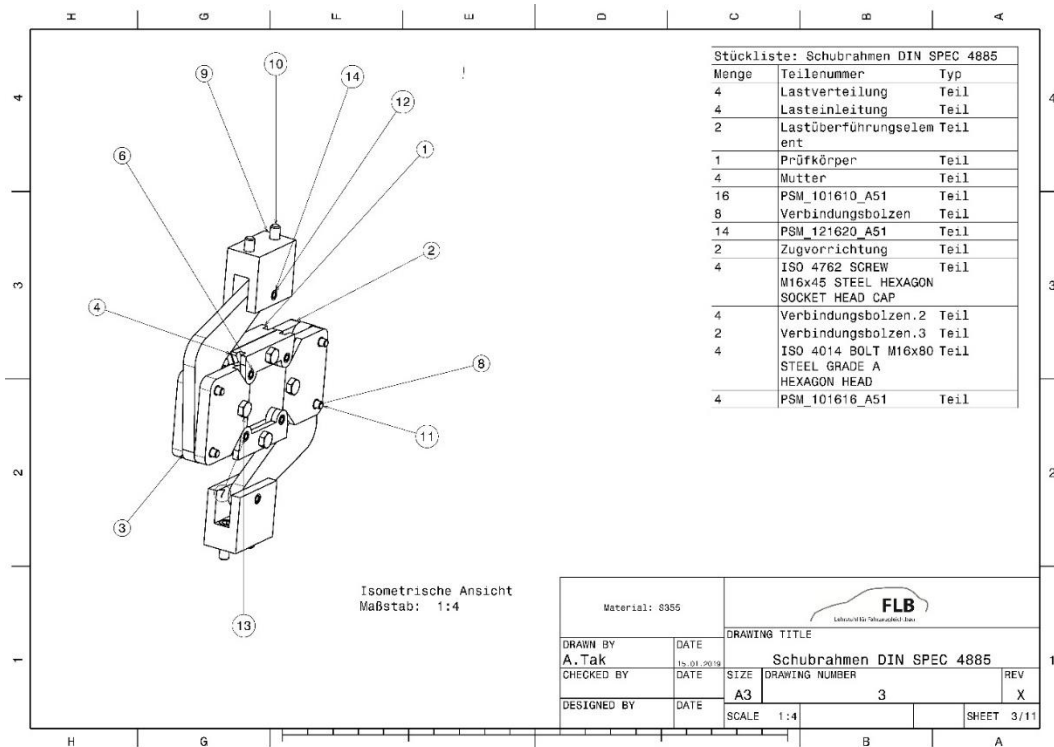


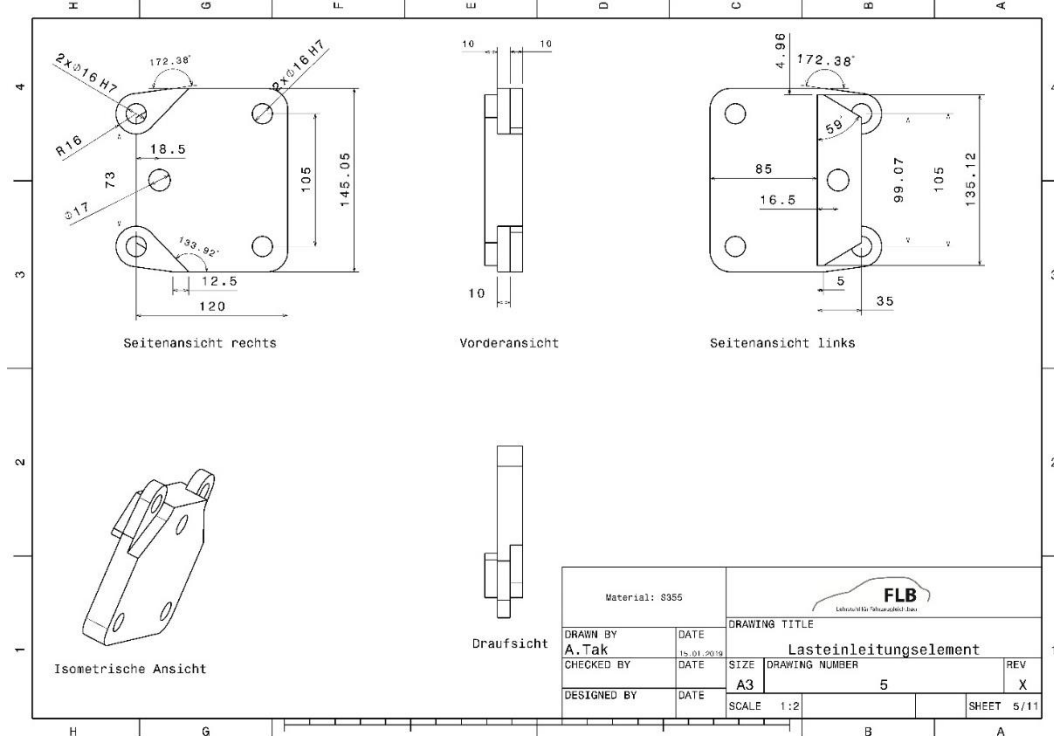
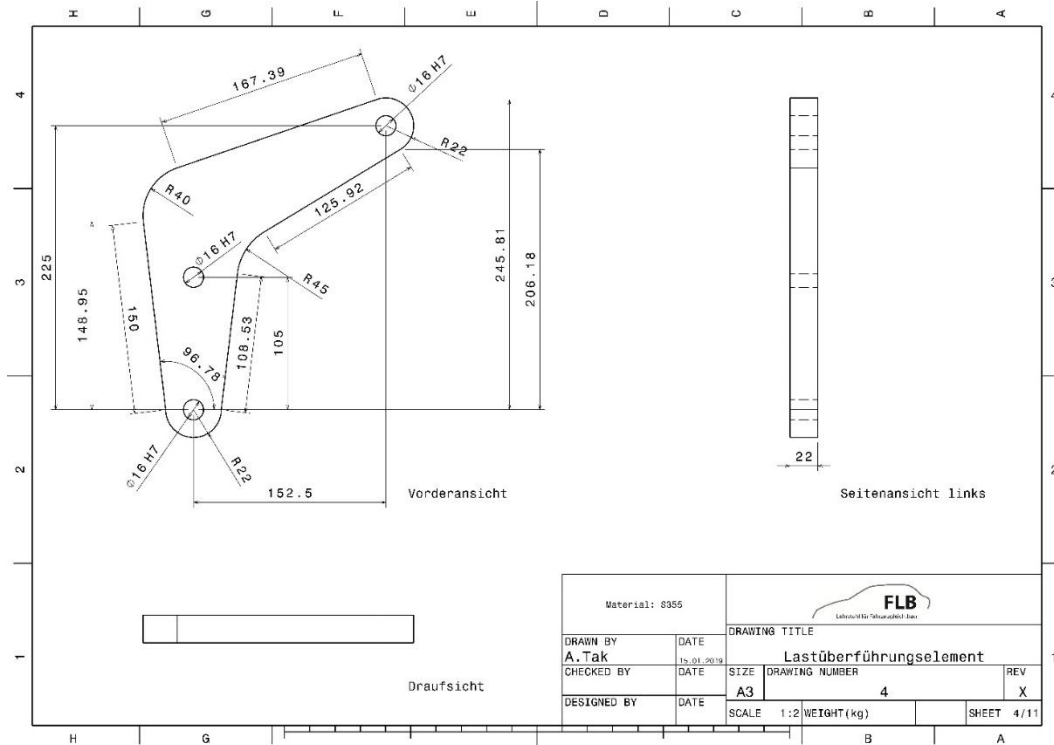
12.3.2 Clevis design for intra-laminar fracture energy

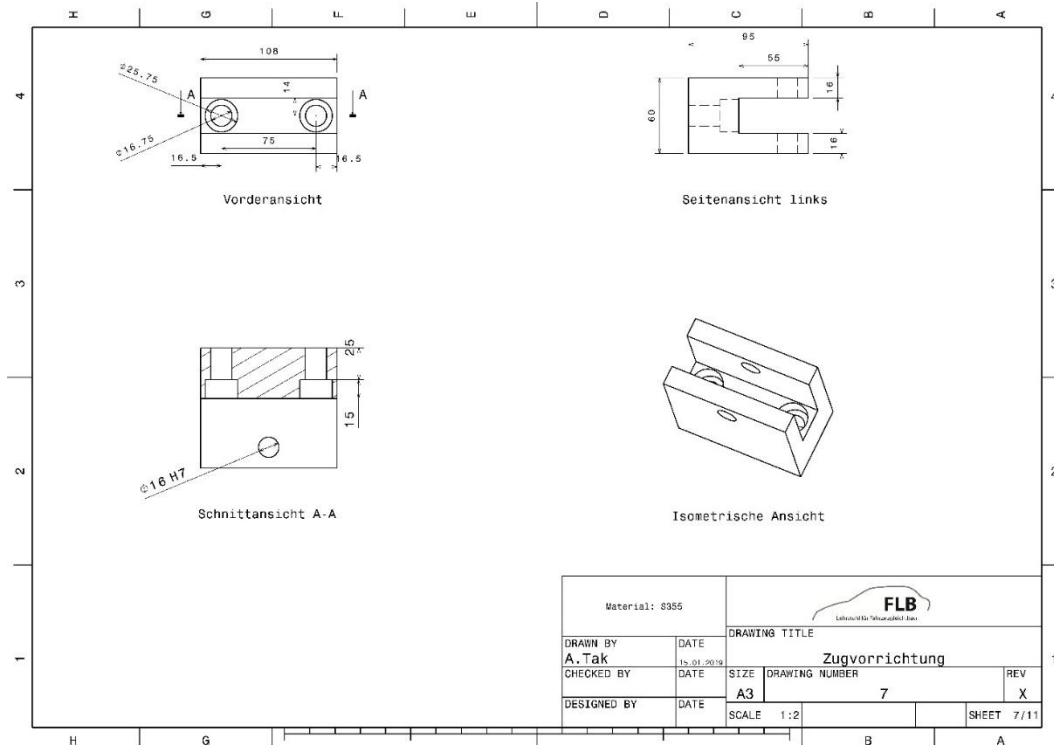
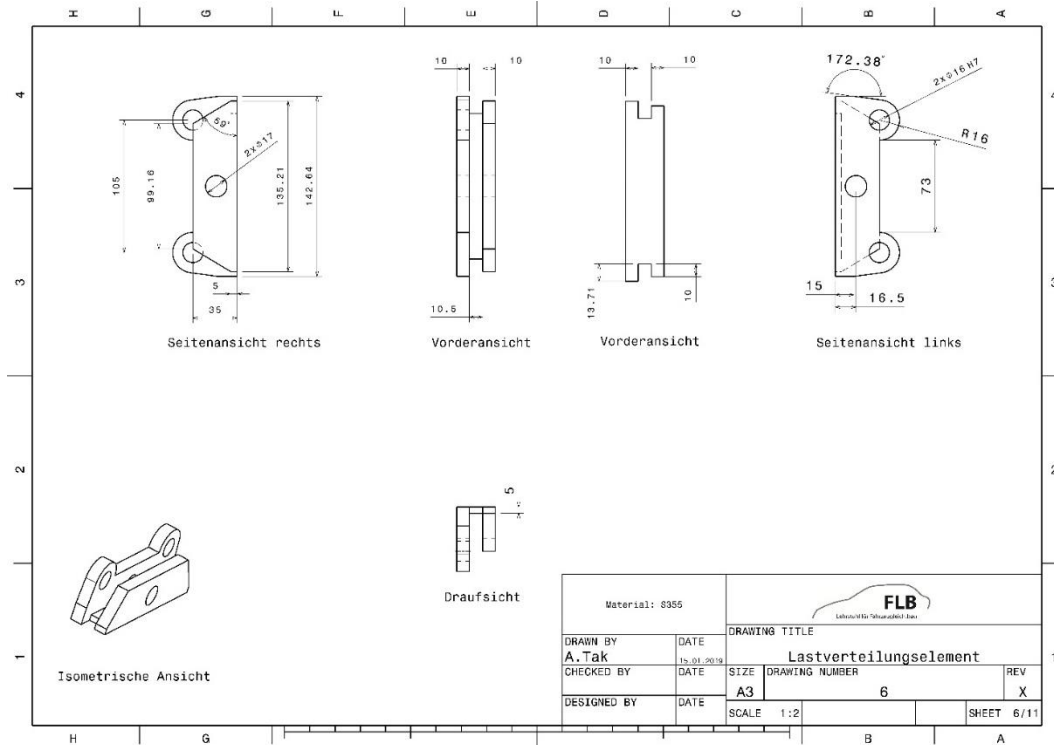


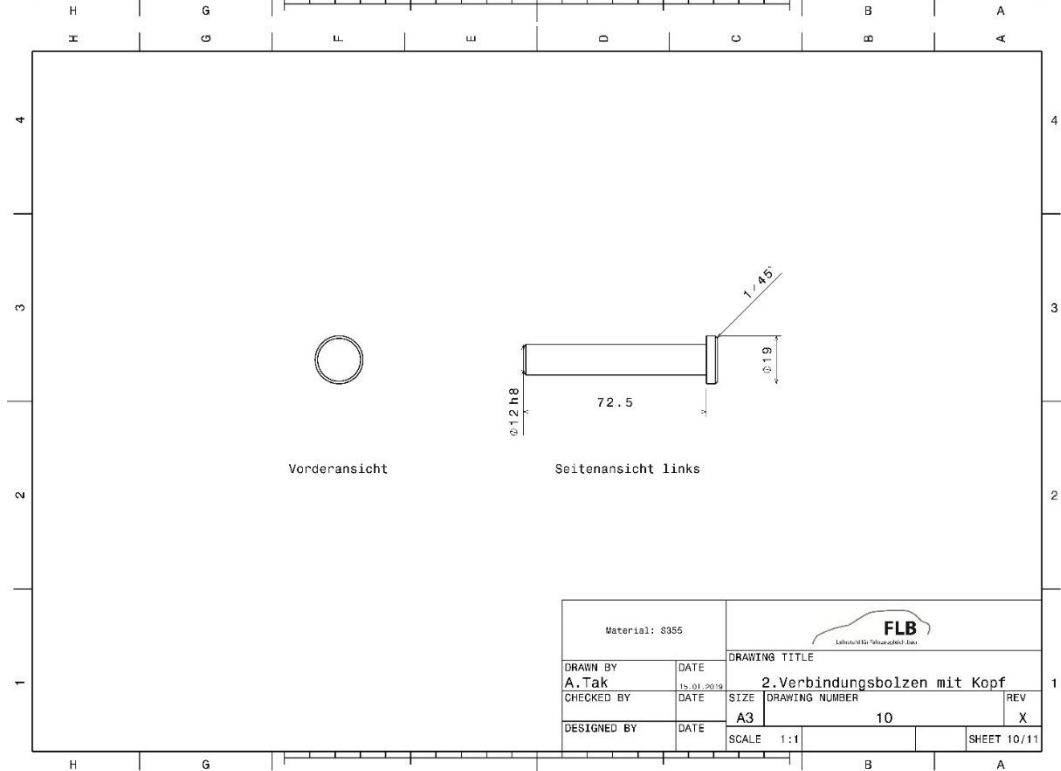
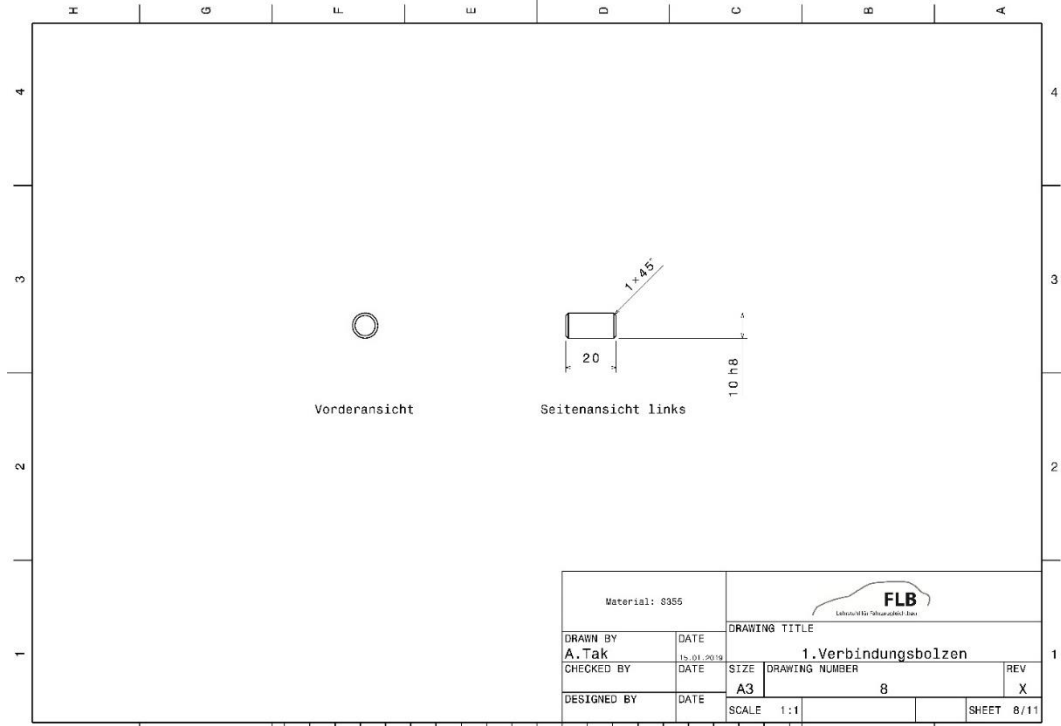


12.3.3 Frame shear fixture

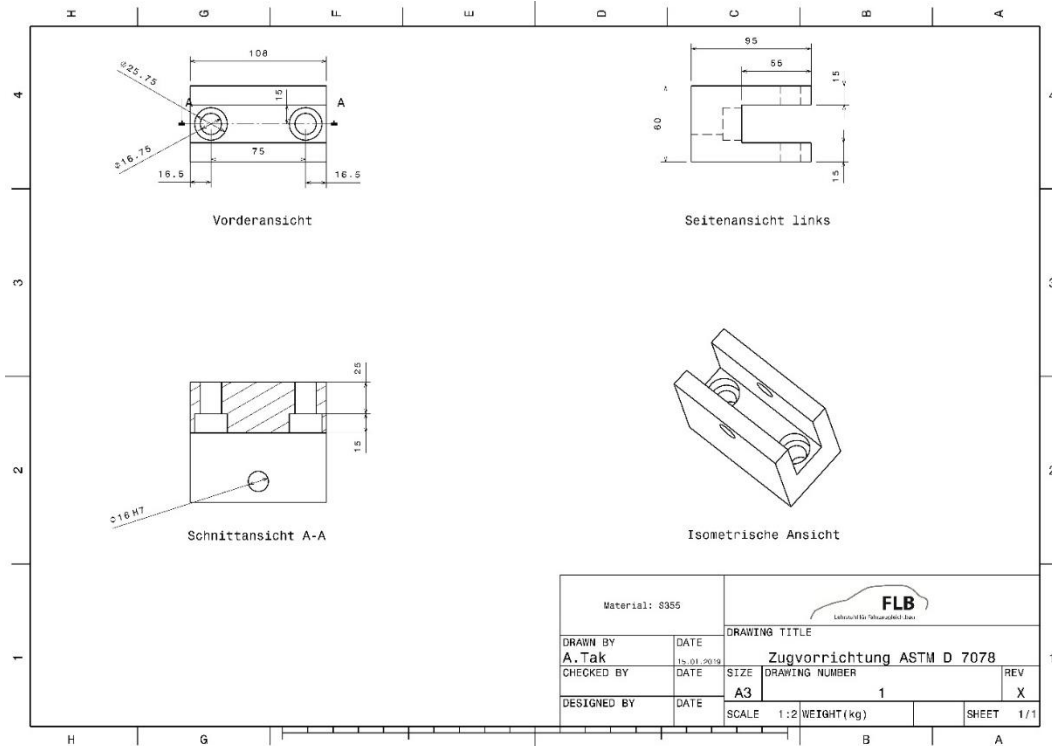
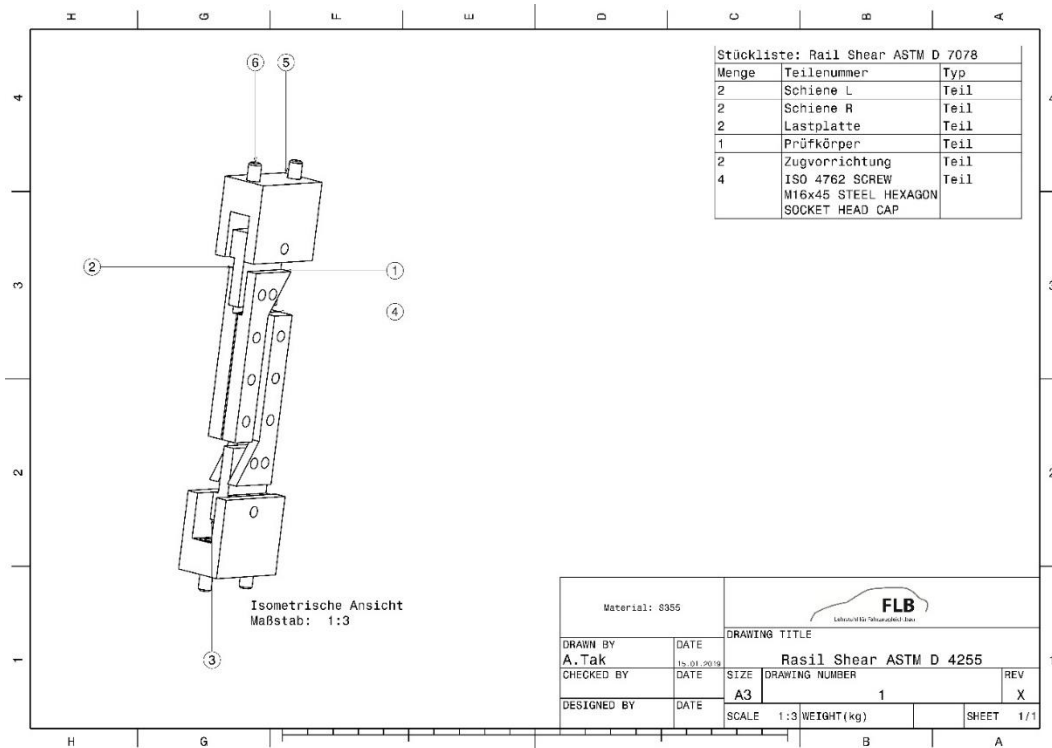


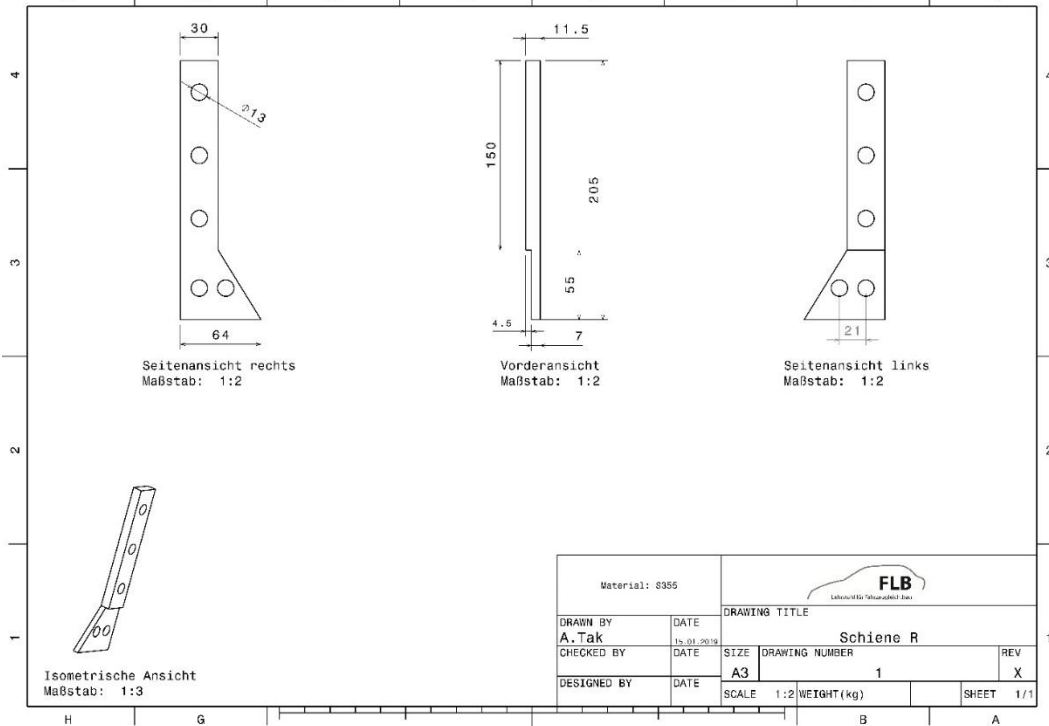
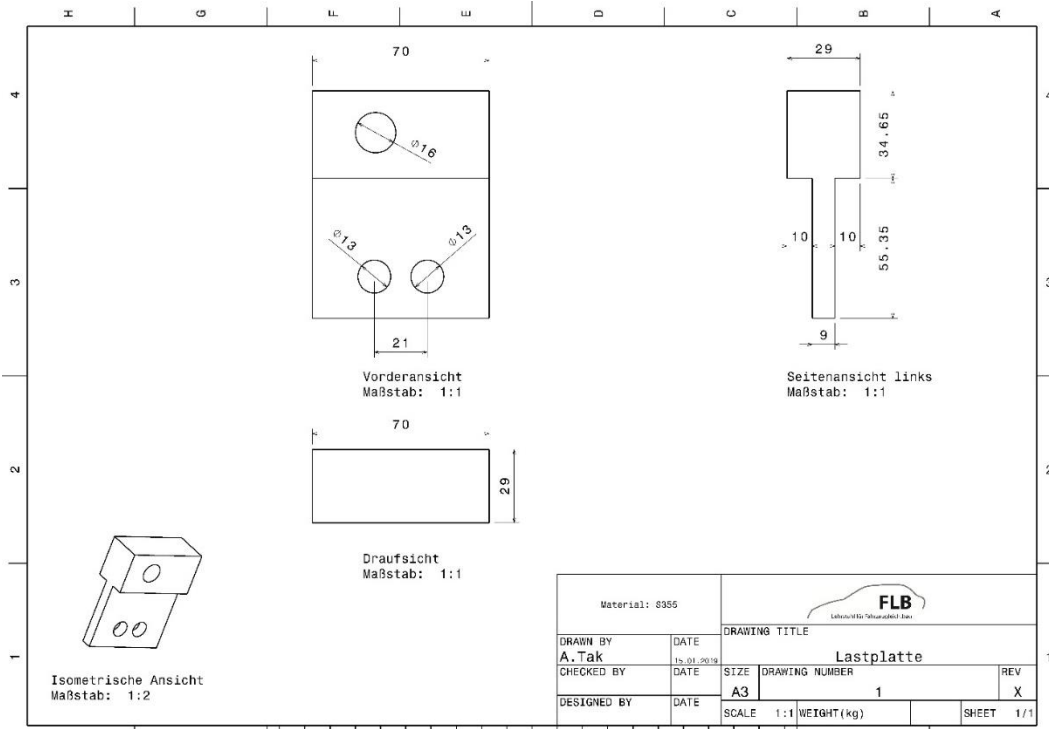


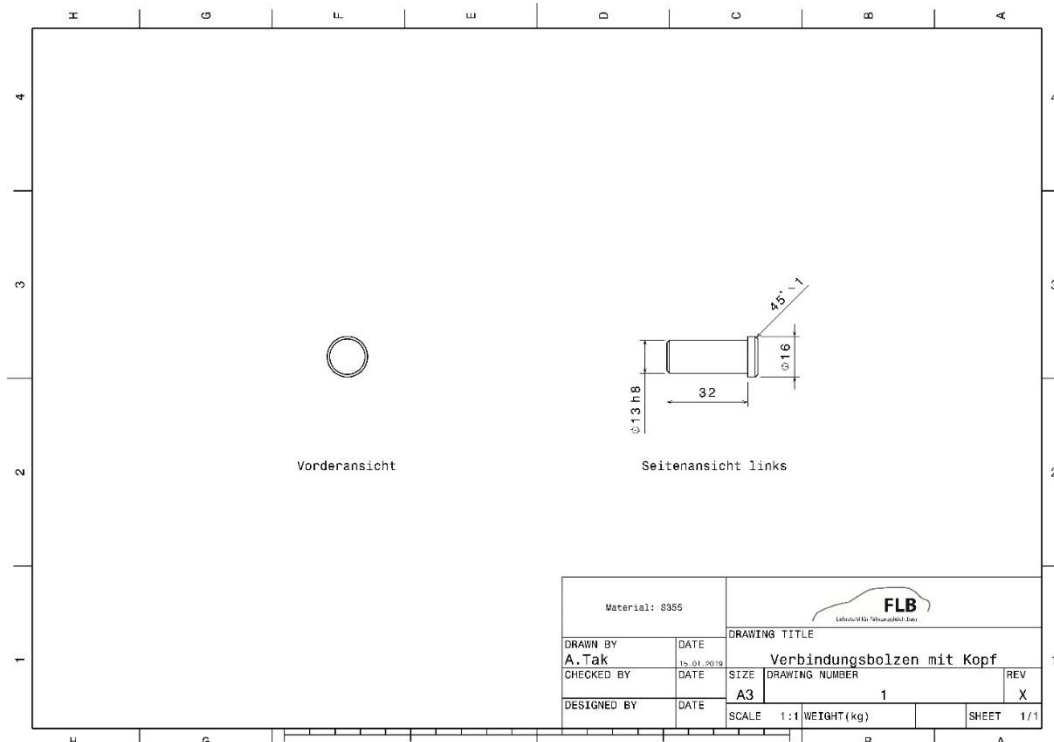
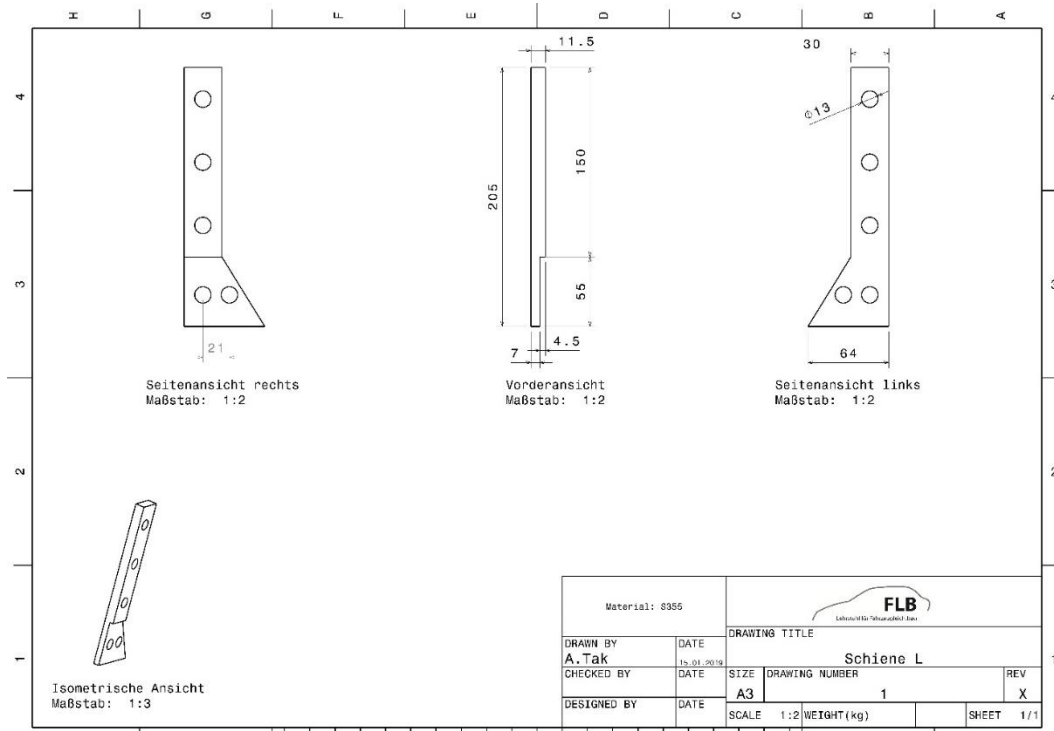




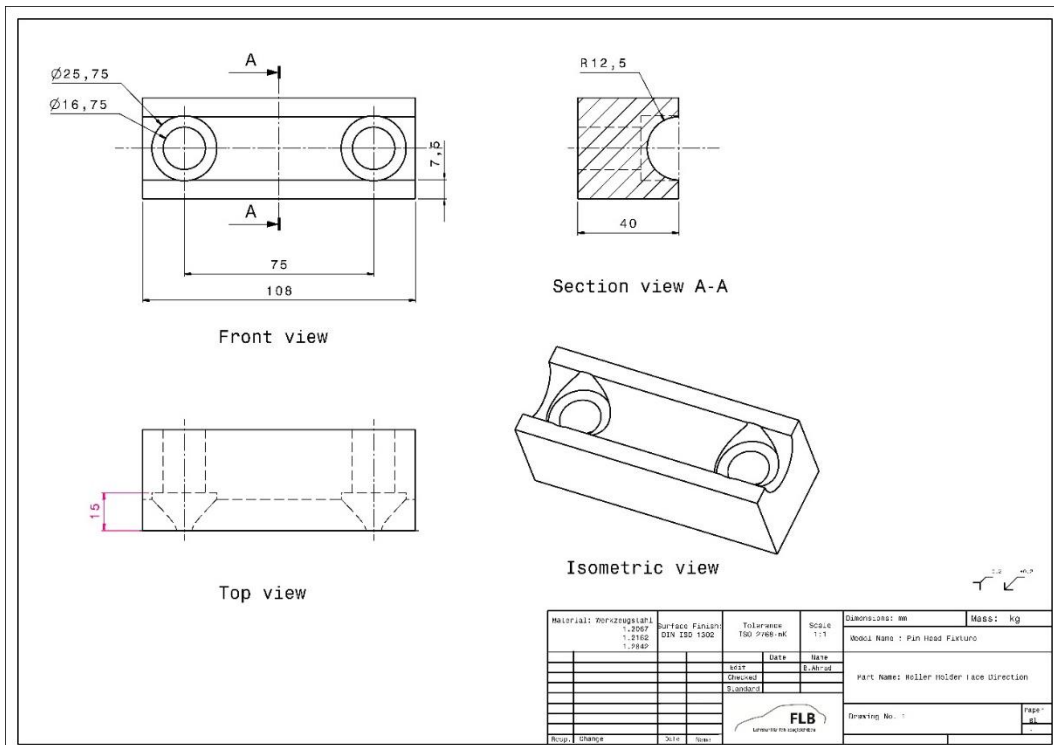
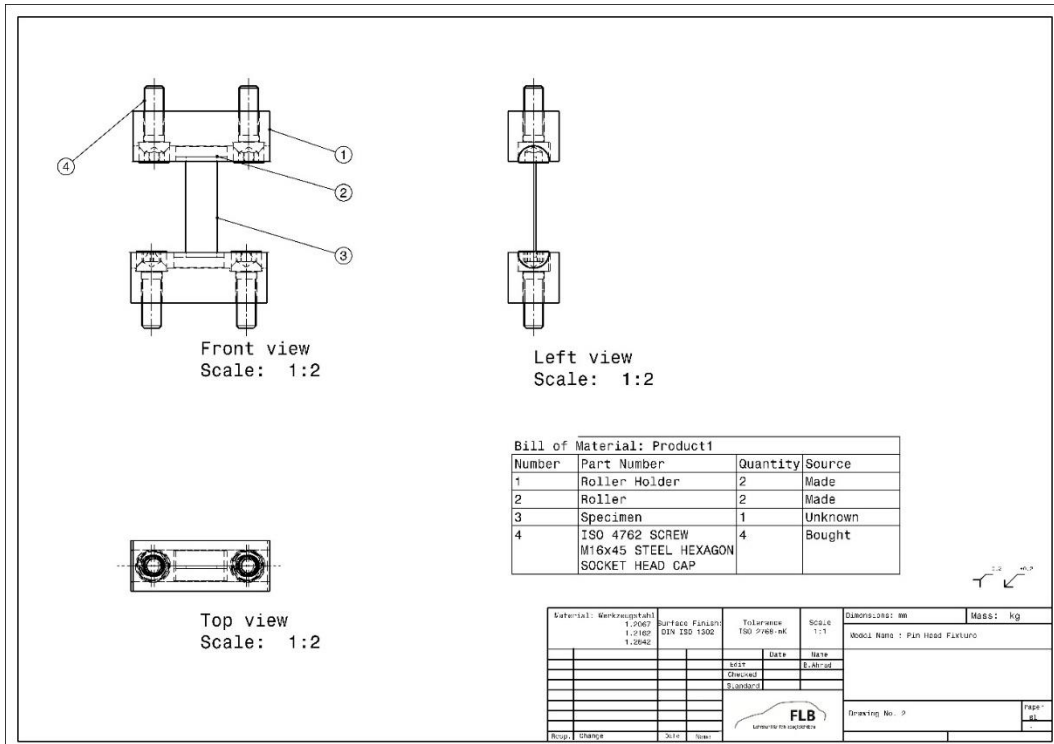
12.3.4 Rail shear fixture

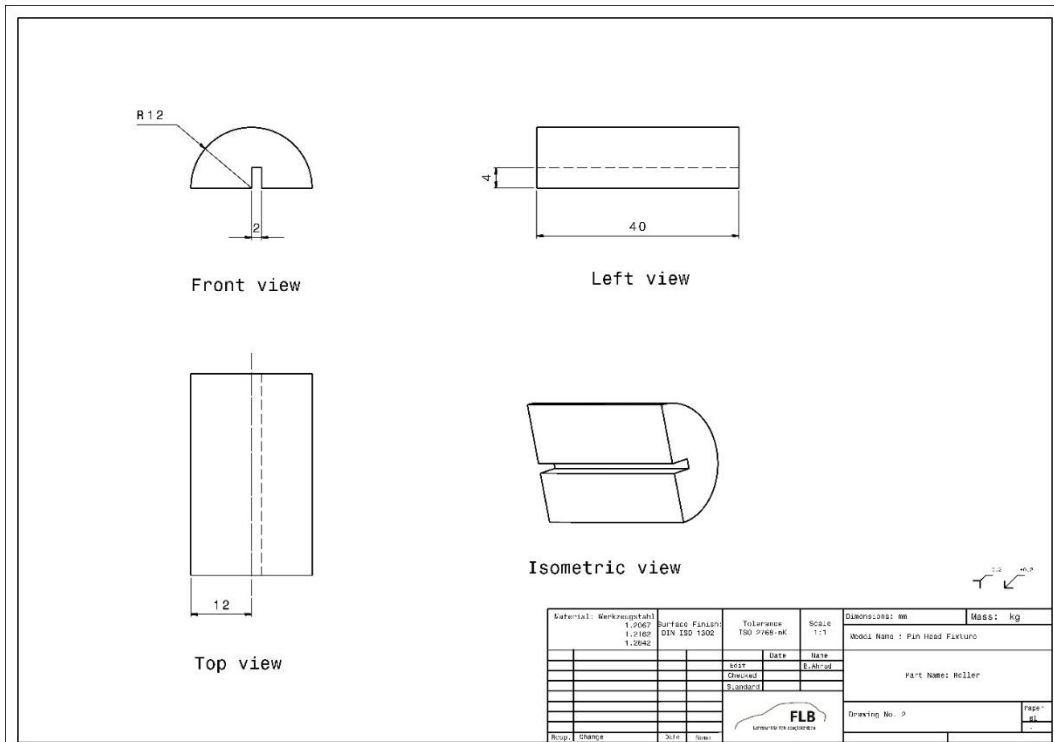






12.3.5 Pin-end buckling fixture





**Die „Siegener Schriftenreihe Automobiltechnik“ präsentiert die Dissertationen des Lehrstuhls für Fahrzeugleichtbau (FLB) der Universität Siegen. Die Beiträge befassen sich mit der Entwicklung von Methoden und Prinzipien sowie neuen Leichtbautechnologien zur effizienten Gestaltung des Leichtbaus in Karosserie- und Fahrwerkstrukturen.**

**Die Reihe erscheint in unregelmäßigen Abständen.**

**Mit neuen Methoden zu  
leichten Lösungen**